



HELLENIC
MEDITERRANEAN
UNIVERSITY



université
BORDEAUX



Erasmus+

The European Commission support for the production of this publication does not constitute an endorsement of the contents which reflects the views only of the authors, and the Commission cannot be held responsible for any use which may be made of the information contained therein.

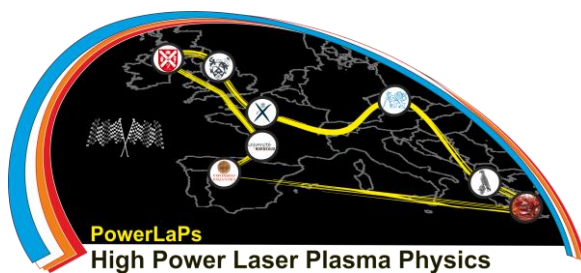
Co-funded by the
Erasmus+ Programme
of the European Union



PowerLaPs

Innovative Education & Training in High Power Laser Plasmas

High Power Laser Matter Interactions/High Energy Density Physics - Theory and Experiments



Erasmus+

Output Identification: O2

Output Title: High Power Laser Matter Interactions/High Energy Density Physics - Theory and Experiments



O2 - High Power Laser Matter Interactions/High Energy Density Physics

O2 - Theory

1. Basic laser physics.....	7-12
<i>B. Dromey</i>	
1.1 Spontaneous vs Stimulated emission	
1.2 Designer light vs ordinary light	
2. Making laser pulses—real light waves, Fourier series & coherence.....	13-19
<i>B. Dromey</i>	
2.1 The ideal wave equation	
2.2 Real light pulses and Fourier's Theorem	
2.3 Coherence	
2.4 Partial Coherence	
3. Designer light.....	20-24
<i>B. Dromey</i>	
3.1 Cavities and the use of stimulated emission to engineer the properties of light	
3.2 Gain coefficient	
3.3 Controlling laser performance in cavity – the principle	
4. Basics of linear laser matter interaction.....	25-28
<i>N. Papadogiannis</i>	
4.1 Semi-classical Absorption and Emission, Einstein Coefficients	
4.2 Linear Propagation of a laser electric field	
5. Evolution of laser technology.....	29-33
<i>N. Papadogiannis</i>	
5.1 Theoretical background of Stimulated emission	
6. Basics of ultrafast and intense laser technology.....	34-46
<i>N. Papadogiannis</i>	
6.1 Introduction to ultrafast and intense lasers	
6.2 Chirp pulse amplification	
6.3 Characterization of laser pulse temporal profile	
7. Basics of non-linear laser matter interaction.....	47-52
<i>N. Papadogiannis</i>	
7.1 Polarization for relative higher laser intensities and electric fields	
7.2 Non-linear Kerr effect and the Self Phase Modulation (SPM)	



8. Ultrafast laser solid surfaces interactions.....53-58
N. Papadogiannis

- 8.1 Main regimes of laser solid matter interaction
- 8.2 Nanosecond laser pulses interaction with matter
- 8.3 Femtosecond laser pulses interaction with matter

9. Coherent laser driven XUV sources.....59-69
M. Young

- 9.1 Attosecond pulse trains
- 9.2 High harmonic generation in gases
- 9.3 High harmonic generation from plasma surfaces

10. Basics of laser-atom interactions and atomic processes in plasma....70-97
M. Benis

- 10.1 Single electron atoms in weak electromagnetic fields
- 10.2 Atomic and molecular processes in intense laser fields
- 10.3 Bibliography

11. Inertial Confinement Fusion implosion hydrodynamics and indirect drive.....98-108
J. Pasley

- 11.1 Implosion
- 11.2 Indirect-drive ICF
- 11.3 Conclusions

12. Generation and characterisation of warm dense matter in the laboratory.....109-130
D. Riley

- 12.1 Introduction
- 12.2 Shock or ramp compression
- 12.3 Volumetric heating
- 12.4 Diagnostics

13. Fast electron beam transport: theory and bibliographic overview.....131-169
J.J. Santos

- 13.1 Introduction: Matter at extreme conditions driven by intense electron currents
- 13.2 Intense laser interaction with over-dense matter
- 13.3 Fast electron beam transport in dense matter
- 13.4 Detection of fast electron beams in dense matter
- 13.5 Bibliography

14. Laser driven ion acceleration.....170-183
M. Borghesi

- 14.1 Introduction



- 14.2 Sheath acceleration
- 14.3 TNSA scaling and optimization
- 14.4 Radiation Pressure Acceleration
- 14.5 Relativistic transparency regimes

15. From perfect gas to QMD: applications to planetary physics.....184-186
M. Koenig

- 15.1 Plasma theoretical description leading to Equation Of State (EOS)
- 15.2 Description of internal structure of planets by Equation Of State (EOS)
- 15.3 Exercises

O2 - Experiments

1. EXP 1. Study of laser breakdown on solid targets.....188-201
D. Batani, E. d'Humières, J.J. Santos, V.T. Tikhonchuk

- 1. A phenomenological approach to laser breakdown
- 2. A few important plasma parameters
- 3. Work to be done

2. EXP 2. Measure the coherence length/Time of flight - Determine the concentrations of metals in unknown alloys using X-ray absorption.....202-203
S. White, B. Dromey

3. EXP 3. TW Ultrafast laser system and laboratories.....204-221
I. Fitis, K. Kosma, Y. Orphanos, S. Petrakis, A. Grigoriadis

- 1. Description of the 40TW laser system at CPPL
- 2. Operation of the 40TW laser system at CPPL
- 3. Laser-matter interactions experiments at CPPL

4. EXP 4. Interaction of TW laser pulses with metal targets.....222-231
I. Fitis, A. Grigoriadis

- 1. Interaction of TW laser pulses with metal targets
- 2. Experimental work

O2 – Annex

Supplementary educational material.....232

- **O2-A1-High power lasers** (*B. Dromey*)
- **O2-A2-Designer light** (*B. Dromey*)
- **O2-A3-Basic Laser Physics** (*B. Dromey*)
- **O2-A4-Making the shortest laser pulses** (*B. Dromey*)
- **O2-A5-Ultrafast laser matter interactions** (*N. Papadogiannis*)
- **O2-A6-Introduction to Solid-State Lasers and applications** (*Mauricio Rico*)
- **O2-A7-Coherent laser driven XUV sources** (*M. Young*)



- **O2-A8-Coherent XUV sources** (*N. Papadogiannis*)
- **O2-A9-Basics on laser-atom interactions and atomic processes in plasma** (*M. Benis*)
- **O2-A10-Inertial Confinement Fusion implosion hydrodynamics and indirect drive** (*J. Pasley*)
- **O2-A11-Generation and characterisation of warm dense matter in the laboratory** (*D. Riley*)
- **O2-A12-Energy transport by laser-generated fast electron beams in dense matter** (*J.J. Santos*)
- **O2-A13-Laser-driven ion acceleration** (*M. Borghesi*)
- **O2-A14-Laser plasma particle acceleration** (*E. Clark*)
- **O2-A15-Introduction to laser-plasma diagnostics** (*L. Volpe*)
- **O2-A16-Ion stopping power in extreme state of plasmas** (*L. Volpe*)
- **O2-A17-Equation of state of dense matter** (*M. Koenig*)
- **O2-A18-Toward planetary interiors physics using lasers** (*M. Koenig*)
- **O2-A19-Hydrodynamic instabilities and implications in ICF and astrophysics** (*L. Masse*)



HELLENIC
MEDITERRANEAN
UNIVERSITY



UNIVERSITÉ
BORDEAUX



Erasmus+

O2 – Theory



HELLENIC
MEDITERRANEAN
UNIVERSITY



universit 
BORDEAUX



UNIVERSITY
of York



Erasmus+

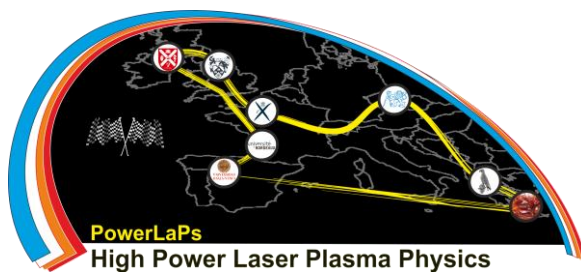
PowerLaPs

Innovative Education & Training in High Power Laser Plasmas

High Power Laser Matter Interactions/High Energy Density Physics - Theory and Experiments

Chapter 1: Basic Laser Physics

B. Dromey



Erasmus+



Queen's University
Belfast

1. Basic Laser Physics

Lasers offer the ability produce light with highly specified properties that allow highly tailored applications from the generation of laser produced plasmas to probing matter on the characteristic response times of the medium. We can think of this laser light as ‘designer light’. On the other hand the emission of light from light bulbs/incandescent sources/LEDs and many others do not organically produce light of a highly specified nature. These sources of light are termed “ordinary light” for the purposes of the discussion below.

1.1 Spontaneous vs Stimulated emission

To understand the fundamental difference between “ordinary light” and laser light it is important to first understand the basic interaction of light and matter –photoabsorption – and how matter, in turn, responds to this.

Photoabsorption (or absorption) is the process whereby an electron is excited from a lower energy level E_1 to a higher energy level E_2 by absorbing a photon with $h\nu = \Delta E = E_2 - E_1$. A schematic of this process for a simple two level system initially in equilibrium/ground state (i.e. lowest energy levels filled first) is shown in Fig 1.1.

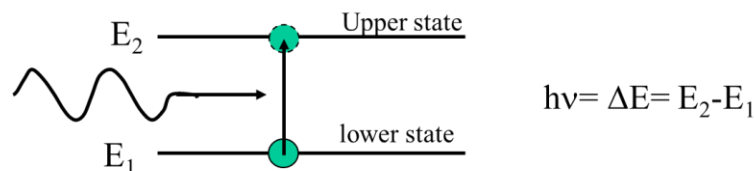


Figure 1.1 Photoabsorption in a simple two level system

What is the photoabsorption rate?

Absorption depends on lower state density (N (cm^{-3})), absorption cross section for a transition from level 1 to 2 (σ_{12} (m^2)) **and incident PHOTON FLUX I**: Intensity in photons per second per m^2

$$\frac{dN_1}{dt} = \sigma_{12} I N_1 = W_{12} N_1 \quad (\text{where } \sigma_{12} I = W_{12})$$

The important thing to recognise here is that absorption only happens in the presence of an incident photon and the rate depends directly on the number of photons arriving per second. Once absorption has occurred our simple two level system is now in an “excited state” (Fig 1.1) and one way it can return to the ground state is via the emission of a photon. This

emission, however, can occur via two very different mechanisms that dominate under very different conditions – spontaneous and stimulated emission.

I. Spontaneous emission is a statistical (random) process whereby an electron in an excited energy state relaxes to the lower energy state under emission of a photon. Spontaneous emission is the source of all ‘normal’ light.

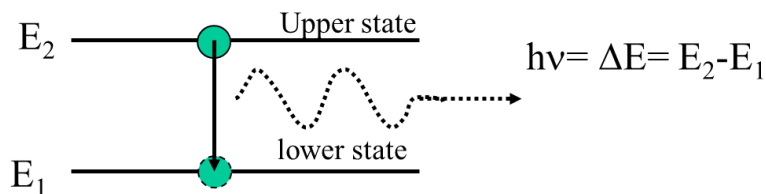


Figure 1.2 Spontaneous emission in a simple two level system. This system has now relaxed to the equilibrium/ground state with the emission of ONE photon of characteristic energy ΔE

What is the lifetime of the upper-state (or rate) of spontaneous emission?

For each atom the process is random and can't be predicted. However the average lifetime can be described in the same way as other random processes (e.g. radioactive decay), by a decay time constant - the natural lifetime τ_{sp} .

$$N_2(t) = N_2(0) \exp\left(-\frac{t}{\tau_{sp}}\right) \quad (\leftarrow \text{cross reference Radioactive decay})$$

$$\frac{dN_2}{dt} = \frac{-N_2(t)}{\tau_{sp}} = -AN_2 \quad (N_2 \text{ density in upper state, A: Einstein A-coefficient})$$

Typical decay times: $10^{-11}\text{s} < \tau_{sp} < \text{seconds}$

What is the frequency spread of spontaneous emission?

The natural linewidth $\Delta\nu_{sp}$ is determined by Heisenberg's uncertainty theorem

$$\Delta\nu_{sp} = \frac{1}{2\pi\tau_{sp}}$$

This is the minimum frequency bandwidth for the spontaneous emission transition. Note: many mechanisms exist to broaden the line further (e.g. Doppler broadening, collisional broadening) but fundamentally the energy level system.

What are the properties of spontaneous emission?

- Directionality - Random into 4π steradian (any direction)
- Polarisation - Random
- Phase - Random

The combination of these properties show that broadly spontaneous emission is determined by the properties of radiative decay.

II. Stimulated emission is the process by which an electron in an excited energy state relaxes to the lower energy state under emission of a photon (light) in the presence of a photon corresponding to the transition energy ΔE . In this sense the incident photon 'stimulates' the excited atom to undergo a transition.

Stimulated emission is the source of all **LASER** light. (Light Amplification by Stimulated Emission of Radiation).

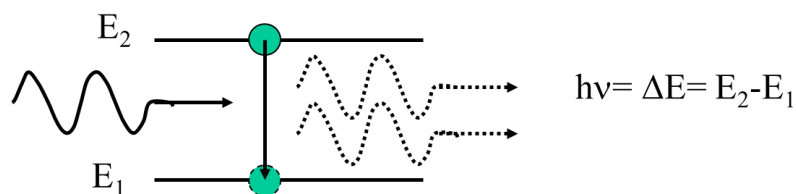


Figure 1.3 Spontaneous emission in a simple two level system. This system has now relaxed to the equilibrium/ground state with the emission of ONE photon of characteristic energy ΔE .

What is the rate of stimulated emission?

It is immediately obvious from Fig 1.3 that photons are required to drive stimulated emission and that the rate of this will be closely linked to the flux of incident photons.

$$\frac{dN_2}{dt} = \sigma_{21} I N_2 = W_{21} N_2 \quad (\text{where the minus sign indicates a transition from level 2 to 1})$$

Note: If $I = 0 \rightarrow \frac{dN_2}{dt} = 0$

Stimulated emission is the inverse process of absorption i.e. $W_{21} = W_{12}$

What is the frequency spread of spontaneous emission?

The frequency spread for stimulated emission $\Delta \nu_{\text{stim}}$ is the same as that of the driving photon.

What are the properties of spontaneous emission?

- Directionality – same as the driving photon
- Polarisation - same as the driving photon
- Phase - same as the driving photon

Since the emitted photons has the same properties as the driving photons stimulated emission can be thought of as a coherent process.

Stimulated Emission and amplification (gain)

Stimulated emission and absorption compete with each other: $\frac{dI}{dt} = \sigma_{12}I(N_2 - N_1)$

Clearly from this, there must be more electrons in the upper state (or more excited atoms) for stimulated emission to dominate. This scenario is known as a population inversion.

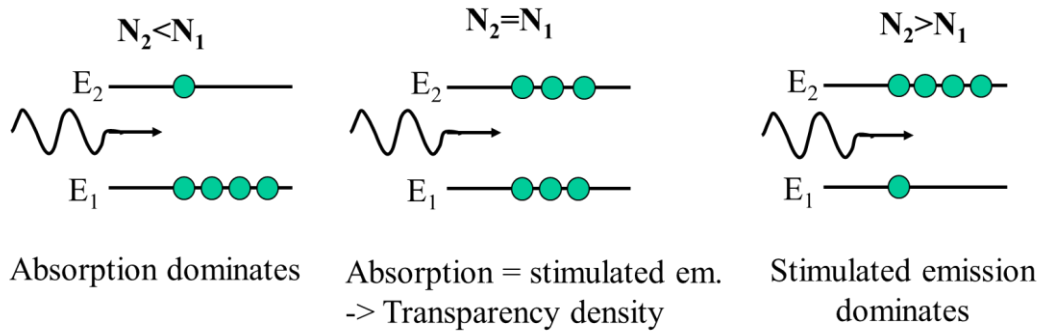


Figure 1.4. How relative populations of electrons in energy levels effect the dominant process. For $N_2 < N_1$, $dI/dt < 1$ and absorption dominates i.e. more photons absorbed than emitted reducing intensity with respect to time. For $N_2 > N_1$, $dI/dt > 1$ and stimulated emission dominates i.e. more photons emitted respect to time – gain condition. For $N_2 = N_1$, stimulated emission matches absorption meaning that dI/dt is a constant (transparency condition)

1.2 Designer light vs ordinary light

The properties described above can be summarised in the table below

Spontaneous/Ordinary vs Stimulated/Designer Emission

Emission rate:	λN_2	Emission rate:	$\sigma_{21}IN_2$
Frequency:	Mean Energy ΔE ,	Frequency:	As incident photon
Bandwidth:	$\Delta\nu \geq 1/2\pi\tau_{sp}$	Bandwidth:	As incident photons
Directionality:	Isotropic (4π steradian).	Directionality:	As incident photon
Polarisation:	Random.	Polarisation:	As incident photon
Phase:	Random	Phase:	As incident photon

Stimulated emission produces ‘cloned’ photons.

In practice what does this imply? Ultimately these properties suggest that by careful selection of the properties of the initial, or ‘seed’, photons and the type of level transitions, laser light can be controlled to an exceptionally high degree of accuracy:

- Monochromatic
 - Very small spread of frequencies
- Broadband
 - Very small broad spread of frequencies



- Coherent
 - Spatially
 - Temporally
- Polarised
- Directional
 - A beam of laser light can be made to be very close to parallel
- High brightness
 - High power per unit area per unit solid angle.
- Short pulse durations achievable.

But this raises the question - are these properties really limited to stimulated emission?

- Yes and no...

Can 'ordinary light' be made monochromatic?

- YES

Take a neon-lamp. The emission consists of a few discrete lines. Filtering the emission one can achieve a quasi-monochromatic source with a linewidth of

$\Delta\lambda \sim 0.1 \text{ \AA} - 1 \text{ nm} \Rightarrow \Delta\nu \sim 10^{12} - 10^{14} \text{ Hz}$ (Spontaneous emission linewidth:

$$\Delta\nu_{sp} = 1 / 2\pi\tau_{sp})$$

This is very monochromatic compared to white light ($\Delta\nu \sim \nu \sim 10^{15} \text{ Hz}$)

How monochromatic can lasers be designed?

- A typical frequency spread is $< 1 \text{ nm}$
- Calculate the frequency spread using $\Delta\omega / \omega = \Delta\lambda / \lambda$:
For a Diode Laser @ $630 \text{ nm} \rightarrow \omega = 3 \times 10^{15} \text{ s}^{-1} \rightarrow \Delta\omega = 10^{13} \text{ s}^{-1}$.
- Lowest possible spread is about 1 Hz !! (for Gravitational Wave Observatories, LIGOs)
 - NOT possible with a spontaneous light source

Are all lasers monochromatic?

- NO.
 - Many lasers operated on several lines at once (e.g. Ar⁺-lasers)
 - Short pulse lasers must have a large bandwidth
 \rightarrow A 5 fs ($5 \times 10^{-15} \text{ s}$) laser has around 200 nm bandwidth
Note: that is almost the entire visible spectrum.



HELLENIC
MEDITERRANEAN
UNIVERSITY



universit 
BORDEAUX



UNIVERSITY
of York



Erasmus+

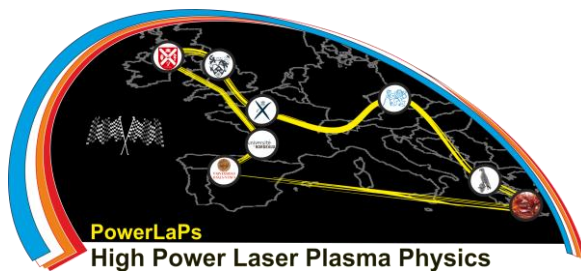
PowerLaPs

Innovative Education & Training in High Power Laser Plasmas

High Power Laser Matter Interactions/High Energy Density Physics - Theory and Experiments

Chapter 2: Making laser pulses – real light waves, Fourier series and coherence

B. Dromey





2. Making laser pulses – real light waves, Fourier series and coherence

It seems spontaneous emission can have similar properties to many lasers – so what is the key difference? To understand this we must first look at the basics of waves and their implications on what we can observe in the laboratory.

2.1 The Ideal wave equation

A plane wave at a single frequency ω propagating in $+r$ direction for all times t and all space r

$$E(\mathbf{r}, t) = E_0 \cos(\omega t - \mathbf{k} \cdot \mathbf{r})$$

What is a single frequency plane wave?

- A plane wave is infinite in the spatial dimensions perpendicular to r
- The surfaces of equal phase are planes perpendicular to r
- There is only one frequency ω present.
 - ⇒ The wave has constant amplitude for all times t .
 - ⇒ The light 'pulse' is infinitely long.

Such a light wave has perfect coherence and it is not very realistic. For example, it is difficult to imagine manmade light source that has been 'on' forever from an infinitely large source. The implication of this impracticality is that light from a manmade (and in fact any conceivable) source must be thought of on its most basic level as a pulse – i.e. finite aperture in space and time. Therefore, we need to understand how to describe real light pulses/beams.

2.2 Real light pulses and Fourier's Theorem

Real beams and pulses of light are described by a superposition (addition) of many individual sine and cosine waves of spatially and temporally limited extent.

Fourier's theorem states that if $f(x)$ is a finite, single valued, function of period 2π (0 to 2π or $-\pi$ to $+\pi$) it can be expanded in a trigonometrical series given by:

$$f(t) = \frac{a_0}{2} + \sum_1^{\infty} a_n \cos(nt) + \sum_1^{\infty} b_n \sin(nt)$$

A full discussion of Fourier theory is beyond the scope of this lecture series, but suffice to say the important concept to grasp is that all physically realisable waveforms can be described as a sum of harmonic cosine and sine terms with weighted amplitudes (a_n and b_n in the equation above are known as the Fourier Coefficients).

2.3 Coherence

In general terms one gets a feel for what (full) coherence means by thinking of it as the ability to predict the properties of a function at any point in space and time from the knowledge of the function in one point and one time.

For example, we can clearly predict the value $E(t)$ of the monochromatic plane wave from section 2.1

$$E(t) = E_0 \cos(\omega t - \mathbf{k} \cdot \mathbf{r})$$

for all times t since it is fully coherent. The reason for this is because there is a fixed phase difference between two points r_1 and r_2 for all times t . But what happens if this correlation is not perfect for all times t ?

One easy way to think of this is as follows: How likely is it that you know the weather in Crete if you know what the weather is like in your city/town? What about making the same prediction the next nearest town/city to you? Clearly there is some correlation over short distances – but it fails over longer distances. The same is true of time – if we know the weather today how well can we predict the weather at an exact time next week or next month?

Clearly the weather IS correlated (coherent) over short distances/time frames but not over longer ones. This is an example of partial coherence. How can we quantify partial coherence?

How does one measure coherence

- If we interfere two coherent waves (or one wave with itself) we will observe an interference pattern that doesn't vary with time -> Any detector can see it, no matter how slow its response
- Maxima occur for a phase difference $\Delta\phi = (\omega t_1 - \mathbf{k} \cdot \mathbf{r}_1) - (\omega t_2 - \mathbf{k} \cdot \mathbf{r}_2) = 2n\pi$
- Minima occur for $\Delta\phi = (\omega t_1 - \mathbf{k} \cdot \mathbf{r}_1) - (\omega t_2 - \mathbf{k} \cdot \mathbf{r}_2) = (2n-1)\pi$

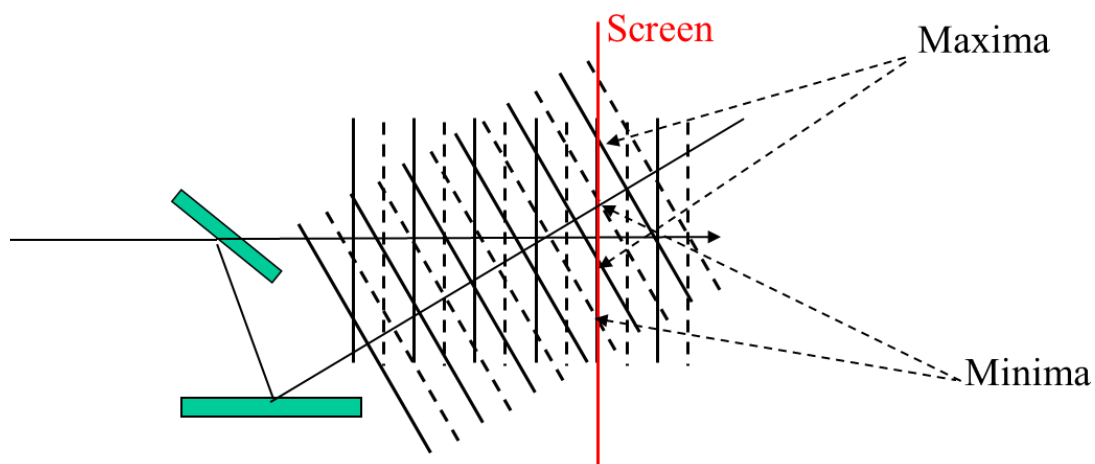


Figure 2.1 Schematic for measuring coherence

If the wave is incoherent the relative phase will be random and maxima and minima will occur at rapidly varying position. This can only be seen with a *very* fast detector. A slow detector simply observes uniform illumination - the time average. If, on the other hand, the source is coherent.

Thought experiment: Assuming a coherent source is incident how can this setup be modified to mimic an incoherent source at the measurement screen. Hint it has to be continuously modified.

2.4 Partial Coherence

Partial coherence can be quantified by calculating the coherence length for two waves i.e. the distance or time over which two waves add coherently. Let's look at the coherence between two ideal cosine waves:

$$E_1 = \cos(\omega_1 t - k_1 x)$$

$$E_2 = \cos(\omega_2 t - k_2 x)$$

Looking at the superposition of the two waves:

$$E = E_1 + E_2 = 2 \cos(\Delta\omega t - \Delta k x) \cos(\omega t - kx) \text{ with}$$

$$\Delta\omega = (\omega_1 - \omega_2)/2, \Delta k = (k_1 - k_2)/2, \omega = (\omega_1 + \omega_2)/2, k = (k_1 + k_2)/2.$$

Immediately it is clear that there will be two different frequencies present in the solution, a schematic of which is given in Figure 2.2.

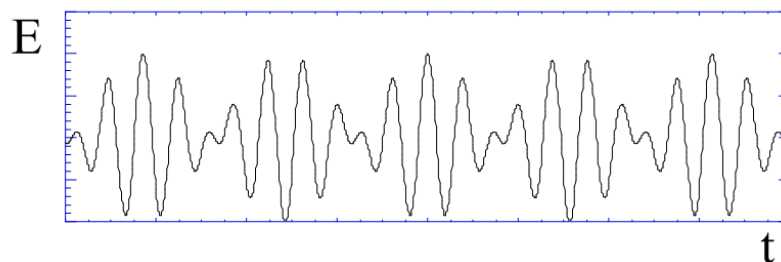


Figure 2.2 Beat pattern from the superposition of two waves with different frequency

Even from this simple example it is clear that the superposition of two waves of different frequency results in a carrier frequency (the fast oscillation) and a modulation frequency (slow oscillation). This gives the overall effect of a beat pattern and is the basis for all pulse formation in laser systems. It should also be clear that this 'beating' is occurring since the two waves E_1 and E_2 are running in and out of phase with each other – they are partially coherent. Therefore, the beating or pulse duration is a direct measure of the partial coherence of the light beam.



Let's take the difference between the nodes of the superposition function/beat pattern as the time taken for the two waves to run completely out of phase with each other and define this as the 'coherence time', t_c . This occurs for the following condition: $\Delta\omega t_c = \pi/2$ or $t_c = \pi/(2\Delta\omega) = 1/\Delta\nu$

The coherence length is then given by $L_c = ct_c$ where c is the speed of the wave. The significance of this should now be clear. By virtue of the fact that real light beams can only be described by a superposition of many individual sine and cosine waves of spatially and temporally limited extent there will ALWAYS be partial coherence, or a finite coherence length, associated with the beam. This places several fundamental limits on real light beams/pulses:

A. The Transform Limit: What is the coherence length for a continuous spread of frequencies?

Assuming a Gaussian spectrum we get the same result as above:

$$L_c = ct_c = c/\Delta\nu = \lambda^2/\Delta\lambda \quad (\Delta\nu : \text{Full width at half maximum frequency bandwidth and } t_c = 1/\Delta\nu)$$

This makes intuitive sense - when significant components first run out of phase the coherence will be compromised.

⇒ But the minimum pulse duration $\Delta\tau$ of a Gaussian is just $\Delta\tau \sim 1/\Delta\nu$ (approximately)

⇒ $\Delta\tau = t_c$: the pulse duration is just the coherence length!

A pulse which has the shortest possible duration for its bandwidth $\Delta\nu$ is called "Transform Limited" and has a coherence length equal to its pulse duration. (The exact relationship is $\Delta\tau > 0.441$ for a Gaussian spectrum).

B. The Diffraction Limit: Can a beam of finite diameter have $\Delta k = 0$?

Another way to ask this question is can a beam of finite diameter be truly parallel and therefore never expand?

From the above discussion we know that real, finite diameter beams can only be represented by a superposition of many individual sine and cosine waves of spatially limited extent. That implies that $\Delta k \neq 0$, or that there will always be a spread of spatial frequencies. To better understand the implications of this consider the case presented in Figure 2.3.

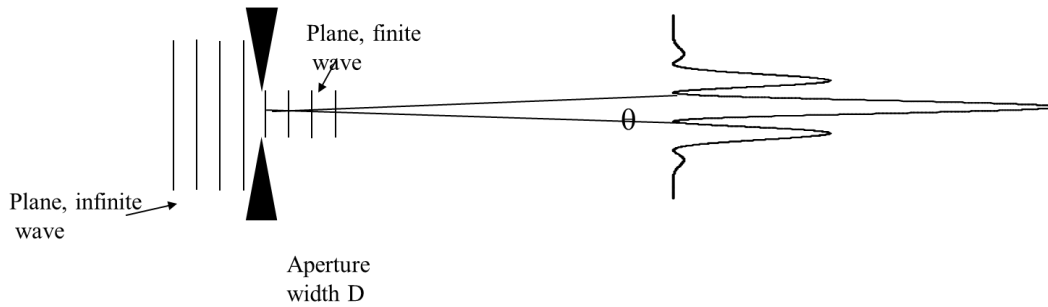


Figure 2.3 Aperturing an infinite plane wave

An infinite plane wave with $\Delta k=0$ is incident from the left side of an aperture with finite width D . However, the aperture introduces a spread of spatial frequencies such that $\Delta k \neq 0$. Essentially this is just a single slit experiment (cross reference: Huygens' wavelets interfering).

⇒ The wave does not stay at width D but expands due to diffraction.

⇒ Different parts of the beam now propagate in different directions: $\Delta k \neq 0$.

The angular separation between the first minima is $\theta_{DL}=\lambda/D$ and defines the direction limited divergence for the beam. This places a fundamental limit on the beam and makes the concept of a geometric focus impossible for finite beams (Figure 2.4)

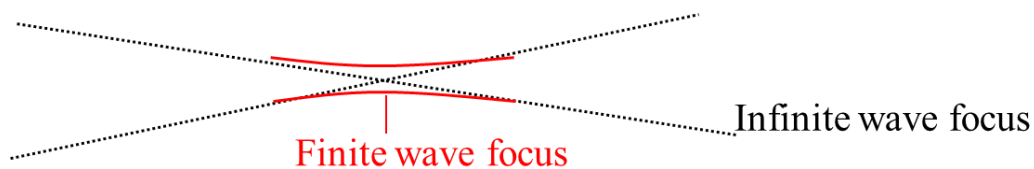


Figure 2.4 Focusing schematic for finite (red) and infinite (dotted) plane wave beams

A finite wave focuses to a spot of finite size. Why?

Explanation A) when the beam gets sufficiently small diffraction effects outweighs the focusing by the lens.

Explanation B) the finite beam has a spread of k -vectors (propagation directions) and these focus in different points

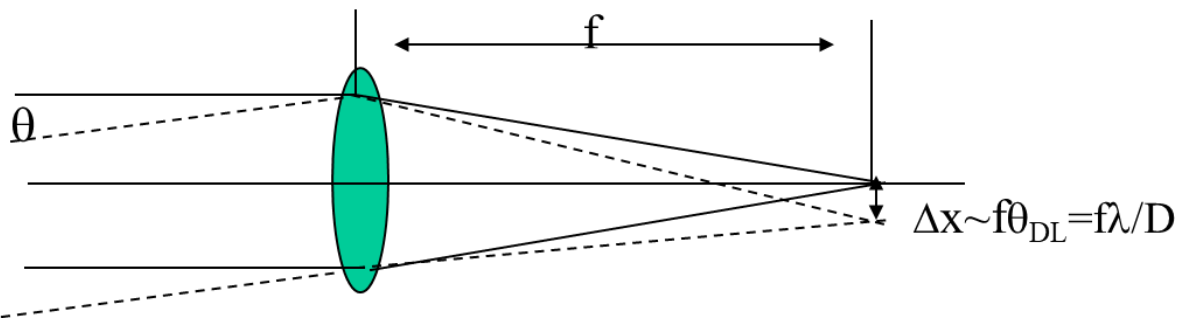


Figure 2.5 Diffraction limited focusing for finite beams



HELLENIC
MEDITERRANEAN
UNIVERSITY



UNIVERSITÉ
BORDEAUX



UNIVERSITY
of York



Erasmus+

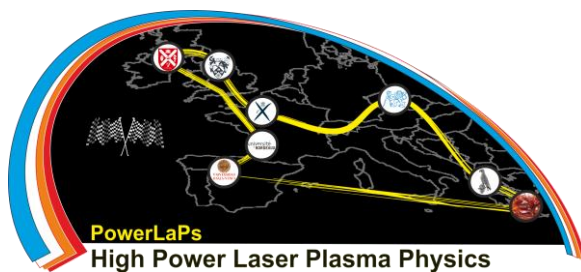
PowerLaPs

Innovative Education & Training in High Power Laser Plasmas

High Power Laser Matter Interactions/High Energy Density Physics - Theory and Experiments

Chapter 3: Designer Light

B. Dromey



Erasmus+



Queen's University
Belfast

3. Designer light

Stimulated emission allows the efficient production of light with very well defined properties

- Laser approach: Select photons with the desired properties and amplify them ('clone them') using stimulated emission.
- This contrasts to the inefficient 'shot gun' approach one would have to use with spontaneous emission.
- The losses make highly controlled light sources completely impractical to achieve.
 - Laser light is, in effect, uniquely different from spontaneously emitted light
(cf. also quantum entanglement).
- However Lasers are not more efficient at producing light per se:
 - Most efficient lasers have efficiencies of $\sim 0.5-0.7$ (Laser diodes)
(but more typically a 0.1% - a few %)
 - Most efficient standard sources have efficiencies of $\sim 0.5-0.7$
(more typically $\sim 10\%$)

The catch is simply that capitalising on the gain mechanism provided by stimulated emission allows preferential growth of desired properties. This has the overall effect of making the process vastly more efficient than if spontaneous emission was used.

3.1 Cavities and the use of stimulated emission to engineer the properties of light

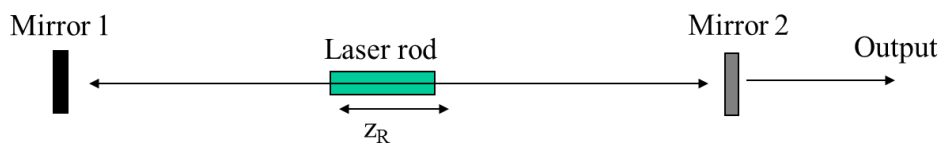


Figure 3.1 Simple cavity schematic

How does a cavity generate laser output?

Initially the laser medium is pumped to produce emission on the lasing transitions. The basic cavity operation is as follows:

- One of the mirrors is a partial reflector with reflectivity $R < 1$
- In steady state there will be a constant number of photons oscillating in the cavity

- The output of each roundtrip will be
 $E_{osc} \cdot (1 - R) = E_{osc} \cdot T$, where E_{osc} = cavity energy content, T = transmission)
- The power will be $P_{out} = E_{osc} \cdot \frac{T}{t_R}$ (where t_R is the cavity roundtrip time)

The typical output of this extremely simple cavity is

- Frequency space: Multiple frequencies (temporal modes) oscillate
- K-space: Multiple spatial modes oscillate, beam is not diffraction limited

Immediately we see that this is far from the idea of designer light described above. However, the use of a cavity is not without a reason. First, we can remove unwanted spatial modes by inserting a spatial filter giving full control of the spatial coherence of the light in the cavity. In this scheme (Figure 3.2) all rays that fall outside θ_{DL} (the diffraction limit) will be rejected by the aperture. On the next pass the majority of photons propagating in the cavity will only have θ_{DL} and since stimulated emission is effectively a cloning mechanism for photons this directionality (of diffraction limited performance) will dominate the spatial mode of the cavity.

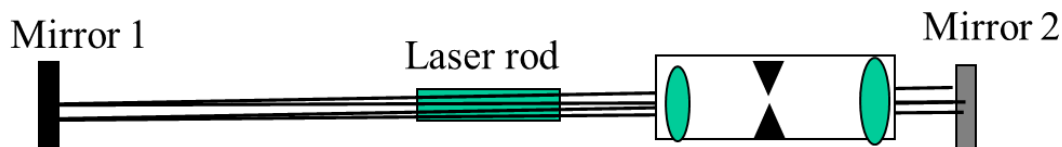


Figure 3.2 Spatial filter to control spatial coherence within the cavity

The discussion above allows the simple operation of a cavity to be understood – introduce loss mechanisms into the cavity for “undesired” properties of the light while at the same time allowing “desired” properties to freely propagate within the cavity and experience gain due to stimulated emission in the laser medium.

3.2 Gain coefficient

From the above discussion it is clear that gain is required to enhance the desired properties of the light within the cavity. For a given length of lasing material the gain can be best be described by studying the increase in intensity as it travels along the lasing medium. This is given by

$$dI = \sigma_{12}(N_2 - N_1)I(z)dz$$

which allows us to define the gain coefficient

$$g = \sigma_{12}(N_2 - N_1)$$

such that

$$\frac{dI}{dz} = gI(z)$$

a solution of which is

$$I(z) = I_0 e^{gz}$$

Finally, the total gain per pass G can be defined as

$$G = \frac{I(z)}{I_0} = e^{gz}$$

3.3 Controlling laser performance in cavity – the principle

Even very low gain systems can be made to lase once stimulated emission dominates. The condition for this to occur is that the number of photons increases every round trip.

Starting with a gain per pass G :

$$G = \frac{I(z)}{I_0} = e^{gz}$$

To satisfy this condition we need $G > 1$ (i.e. an optical gain medium with $N_2 > N_1$ will achieve this). Of course for a real cavity we want to get some light out so they will have inherent losses. For the mirrors in Figure 3.1. Mirror 1 and 2 with reflectivities R_1 and R_2 respectively we can define the cavity reflectivity as $R = R_1 R_2 < 1$

If the mirrors have a reflectivity $R < 1$ then we require $GR > 1$ to achieve lasing i.e. the gain must be large enough to offset losses due to getting some light out every round trip. From this we can define the threshold gain

$$G = \frac{1}{R}$$

Once a cavity is **above** threshold i.e. $GR > 1$ it will amplify photon numbers by stimulated emission leading to an exponential increase of photons

Conversely if a cavity is **below** threshold i.e. $GR < 1$, photon numbers will decrease exponentially.

Therefore, the approach discussed in 3.1 above can be quantified as follows: Add design features that increase the loss L for unwanted photons such that

$$GRL_{unwanted} < 1$$

Ensure that desirable photons are above threshold

$$GRL_{desired} > 1$$



HELLENIC
MEDITERRANEAN
UNIVERSITY



université
BORDEAUX



Erasmus+

This is the simple principle of operation for laser cavities. This principle allows careful selection of temporal frequency bandwidth and spatial frequencies/modes such that the transform limited pulse duration with diffraction limited performance (discussed in 2.2 above) can be achieved. This provides the basis of ultrashort pulse laser systems.



HELLENIC
MEDITERRANEAN
UNIVERSITY



université
BORDEAUX



UNIVERSITY
of York



Erasmus+

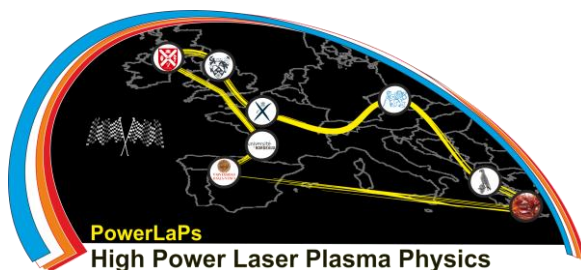
PowerLaPs

Innovative Education & Training in High Power Laser Plasmas

High Power Laser Matter Interactions/High Energy Density Physics - Theory and Experiments

Chapter 4: Basics of linear Laser Matter Interaction

N. Papadogiannis



Erasmus+

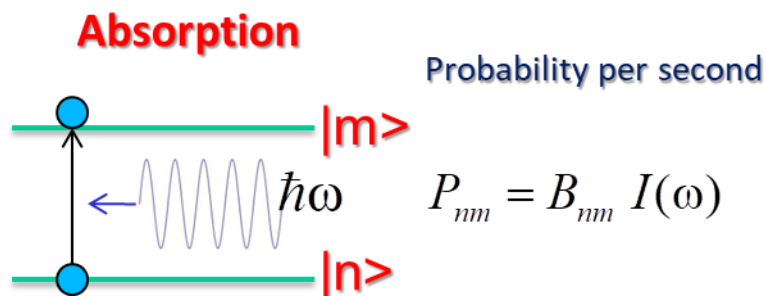
HELLENIC
MEDITERRANEAN
UNIVERSITY

4. Basics of linear Laser Matter interaction

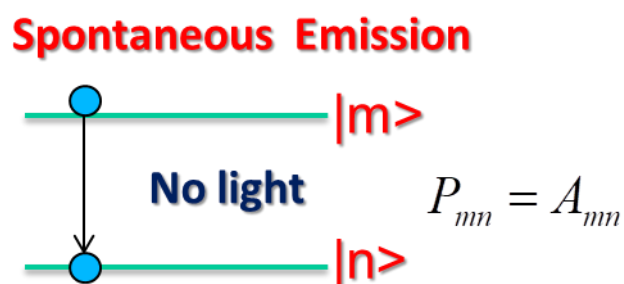
4.1 Semi-classical Absorption and Emission, Einstein Coefficients

In a two-stage quantum system three linear phenomena generally occur when a laser of low energy and low intensity interacts with matter. In these linear phenomena only one photon participates and for this reason these phenomena are also entitled as single-photon processes.

The first phenomenon is the linear resonance absorption of light where a photon with energy equal with the energy difference between the two stages of the quantum system is absorbed and the quantum system is excited in the excitation stage.

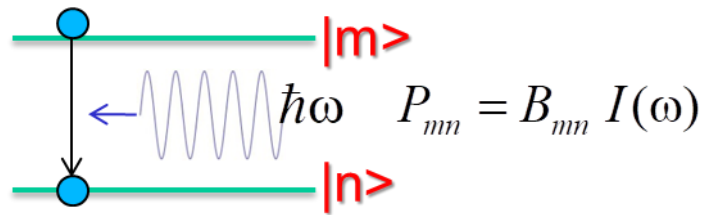


The second linear phenomenon is the spontaneous emission where the quantum system is initially excited and because of the so-called quantum fluctuations the system is de-excited and emits a photon with energy equal with the difference of the stages.

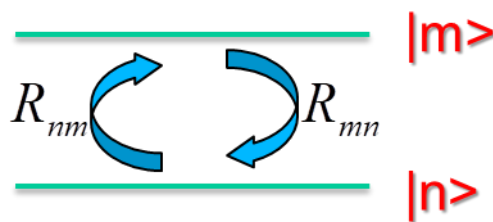


The third phenomenon is the stimulated emission where in the presence of a photon with energy equal to the energy difference of the two quantum stages an already excited atom is de-excited and emits a second photon with the same energy and k-vector as the initial one.

Stimulated Emission



In an equilibrium condition where the number of absorbed photons is equal with the number of the spontaneously emitted photons it happens:



Where R_{nm} and R_{mn} are the absorption and emission rates and N_n , N_m the number of atoms in n and m state at temperature T . Therefore:

$$R_{nm} = N_n B_{nm} I(\omega)$$

$$R_{mn} = N_m [A_{mn} + B_{mn} I(\omega)]$$

In equilibrium steady-state condition:

$$N_n B_{nm} I(\omega) = N_m [A_{mn} + B_{mn} I(\omega)]$$

$$N_n \propto e^{-\frac{E_n}{kT}} \quad N_m \propto e^{-\frac{E_m}{kT}}$$

$$I(\omega) = \frac{A_{mn}}{B_{nm} e^{-\frac{\hbar\omega}{kT}} - B_{mn}} \quad \left. \begin{array}{l} B_{mn} = B_{nm} \\ A_{mn} = \frac{\hbar\omega^3}{\pi^2 c^2} B_{nm} \end{array} \right\}$$

$$I(\omega) = \frac{\hbar\omega^3}{\pi^2 c^2} \frac{1}{e^{\frac{\hbar\omega}{kT}} - 1}$$

4.2 Linear Propagation of a laser electric field

By combining Maxwell equations and considering only the dipole response of the material it holds

$$\nabla \times \nabla \times \vec{E}(r, t) + \frac{1}{c^2} \frac{\partial^2}{\partial t^2} \vec{E}(r, t) = -\frac{1}{\varepsilon_0 c^2} \frac{\partial^2}{\partial t^2} \vec{P}(r, t)$$

where ε_0 is the permittivity of the free space and $\vec{P}(r, t)$ is the polarization of the medium.

For low laser intensities and electric fields (laser electric field orders of magnitudes less than the electric field that connects electrons with the nucleus)

$$\vec{P}(r, t) = \varepsilon_0 \chi^{(1)} \vec{E}(r, t)$$

where $\chi^{(1)}$ is the linear susceptibility tensor, which is a scalar quantity for an isotropic material. Assuming an instantaneous material response (e.g. no ferroelectricity)

$$\nabla^2 \vec{E}(r, t) + \frac{n_0^2}{c^2} \frac{\partial^2}{\partial t^2} \vec{E}(r, t) = 0, \quad n_0 = \sqrt{1 + \chi^{(1)}} \quad (4.1)$$

where n_0 is the refractive index of the material. To derive Equation 5.1 it is assumed no free charges and spatial independent susceptibility. The above wave equation governs all the linear optical propagation phenomena inside the matter and can be solved for certain material and geometrical schemes. For a short laser pulse (which have broad frequency spectrum) and because the index of diffraction depends on wavelength, dispersion occurs simultaneous with the pulse propagation. As a final effect the laser pulse duration increases (chirp phenomena-color dispersion).



HELLENIC
MEDITERRANEAN
UNIVERSITY



universit 
BORDEAUX



Queen's University
Belfast



Erasmus+

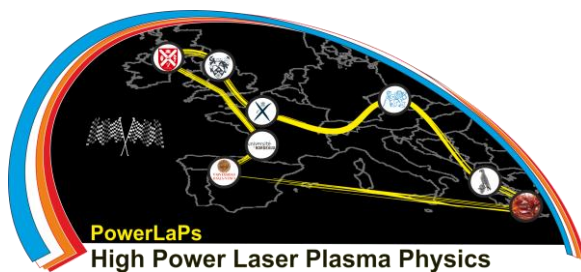
PowerLaPs

Innovative Education & Training in High Power Laser Plasmas

High Power Laser Matter Interactions/High Energy Density Physics - Theory and Experiments

Chapter 5: Evolution of laser technology

N. Papadogiannis



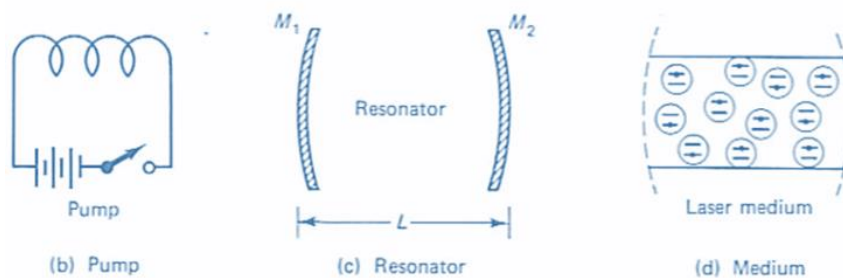
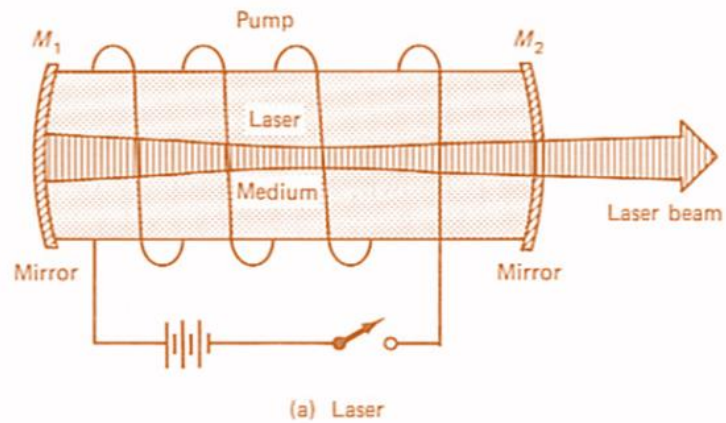
Erasmus+

HELLENIC
MEDITERRANEAN
UNIVERSITY

5. Evolution of laser technology

5.1 Theoretical background of Stimulated emission

The theoretical background of Stimulated emission was presented by Einstein in 1916. First Maser ("M" → Microwave) was presented by Charles H. Townes and coworkers in 1954. The first laser was a solid-state Ruby laser and was discovered by Theodore H. Maiman in 1960.



The Lasing Process can be described by the following steps:

- Population inversion—Through pumping and the existence of a metastable state.
- Seed photons—From spontaneous emission and initiate the stimulated emission process.
- Optical cavity—Resonant enhancement and define the output wavelength.
- Gain saturation—Population inversion decreases as stimulated emission increases.
→Steady state
- Output coupling—Let some of the photons out at each round trip.

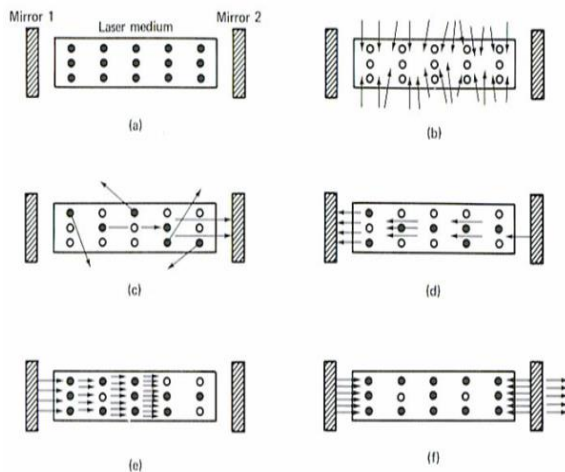
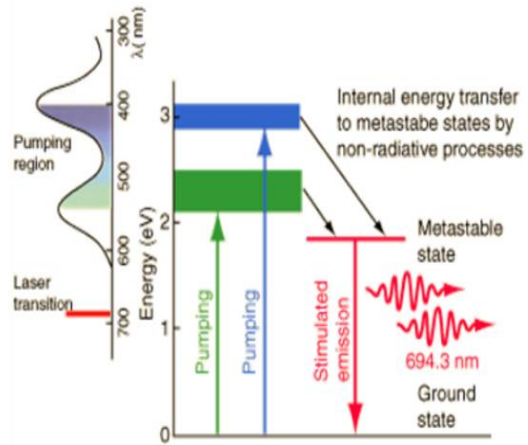


Figure 21-7 Step-by-step development of laser oscillation in a typical laser cavity. (a) Quiescent laser. (b) Laser pumping. (c) Spontaneous and stimulated emission. (d) Light amplification begins. (e) Light amplification continues. (f) Established laser operation.



Ruby laser example.

The first method for pulsed laser operation was the Q-switching. A Variable attenuator inserts inside the laser's optical resonator (light which leaves the gain medium does not return, and lasing cannot begin). This produces a population inversion, but laser operation cannot yet occur since there is no feedback from the resonator. Since the rate of stimulated emission is dependent on the amount of light entering the medium, the amount of energy stored in the gain medium increases as the medium is pumped. Due to losses from spontaneous emission and other processes, after a certain time the stored energy will reach some maximum level; the medium is then gain saturated.

At this point, the Q-switch device quickly changes, allowing feedback and the process of optical amplification by stimulated emission to begin. Because of the large amount of energy already stored in the gain medium, the intensity of light in the laser resonator builds up very quickly; this also causes the energy stored in the medium to be depleted almost as quickly. The net result is a short pulse of light output from the laser, known as a giant pulse, which may have a very high peak intensity.

The two known techniques of Q-switching are the active and the passive. The active Q-Switching is an externally-controlled technique through a variable attenuator. This may be a mechanical device such as a shutter, chopper wheel, or spinning mirror/prism placed inside the cavity, or (more commonly) it may be some form of modulator such as an acousto-optic device or an electro-optic device - a Pockels cell or Kerr cell. The reduction of losses (increase of Q) is triggered by an external event, typically an electrical signal. The pulse repetition rate can therefore be externally controlled. In the passive Q-Switch the Q-switch is a saturable absorber, a material whose transmission increase when the intensity of light exceeds some



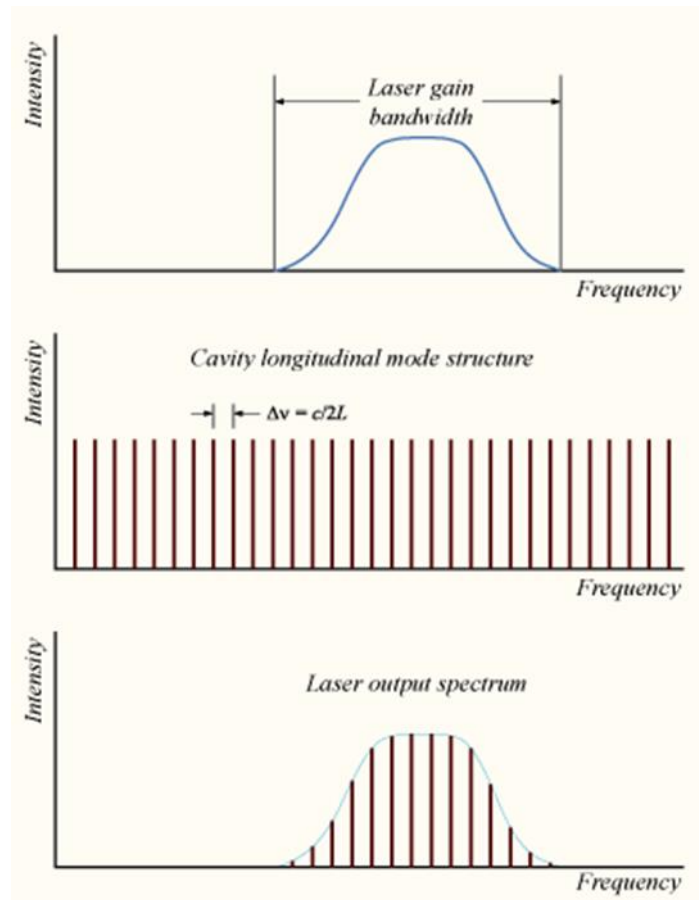
threshold. A typical Q-switched laser (e.g. a Nd:YAG laser) with a resonator length of e.g. 10 cm can produce light pulses of several tens of nanosecond duration. Even when the average power is well below 1 W, the peak power can be many kilowatts. Large-scale laser systems can produce Q-switched pulses with energies of many joules and peak powers in the gigawatt region.

The other method of pulsed laser operation is the Mode-locking technique. Natural Bandwidth of the material laser gain bandwidth. The Laser Cavity supports quantized longitudinal standing wave modes ($\Delta f=c/2L$). There is a convolution of the above that results to a laser output spectrum. In a simple laser, each of these modes will oscillate independently (randomly), with no fixed relationship between each other due to thermal changes in materials of the laser. In lasers with only a few oscillating modes, interference between the modes can cause beating effects in the laser output, leading to random fluctuations in intensity; In lasers with many thousands of modes, these interference effects tend to average to a near-constant output intensity, and the laser operation is known as a c.w. or continuous wave.

If oscillating modes operate with a fixed phase will periodically all constructively interfere producing an intense burst (pulse of light). Such a laser is named to be mode-locked or phase-locked. These pulses occur separated in time by $\tau = 2L/c$, where τ is the time taken for the light to make exactly one round trip of the laser cavity (laser repetition rate). This time corresponds to a frequency exactly equal to the mode spacing of the laser, $\Delta f = 1/\tau$. The pulse duration of the laser burst depends on the number of mode lock modes

$$\Delta t = a / (N \times \Delta f) \quad (5.1)$$

where a is a constant that depends on the pulse shape (0.441 for Gaussian and 0.315 for sech square), N is number of mode locked modes and Δf is the mode spacing. There are also two types of mode-locking the Active Mode Locking (e.g. with acousto-optical modulator) and the Passive Mode Locking (e.g. saturable absorber).



Typical Q-switched laser performance are the femtosecond laser oscillators that utilizing the Kerr effect).



HELLENIC
MEDITERRANEAN
UNIVERSITY



universit 
BORDEAUX



Erasmus+

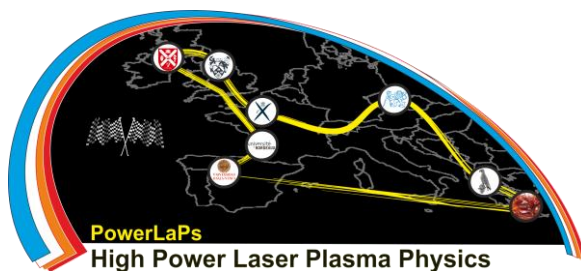
PowerLaPs

Innovative Education & Training in High Power Laser Plasmas

High Power Laser Matter Interactions/High Energy Density Physics - Theory and Experiments

Chapter 6: Basics of ultrafast and intense laser technology

N. Papadogiannis



Erasmus+

HELLENIC
MEDITERRANEAN
UNIVERSITY

6. Basics of ultrafast and intense laser technology

6.1 Introduction to ultrafast and intense lasers

Different time scales are used for the study of different physical phenomena.

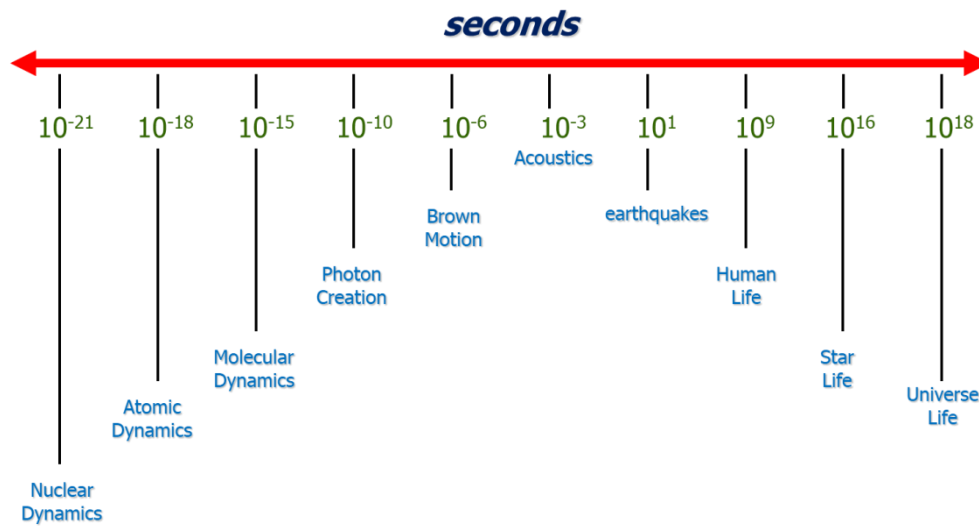
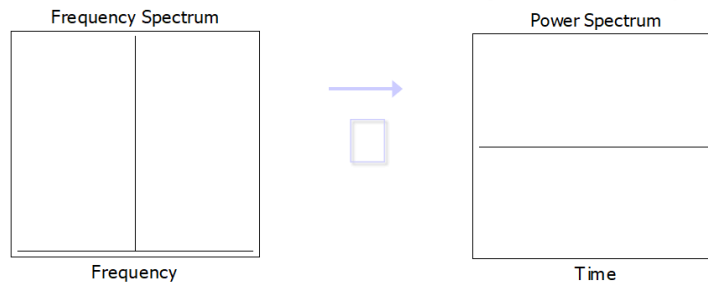


Figure 6.1 The time scales

In fast phenomena the pulsed laser light offers a significant advantage. Pulsed laser operation means that at the same time the power spectrum of the laser is broad. Therefore, in time-frequency analysis a δ -function in time corresponds to flat spectrum in all frequencies and vice versa.

Continuous Beam (Ideal Case)



Ultrashort Pulses (Ideal Case)

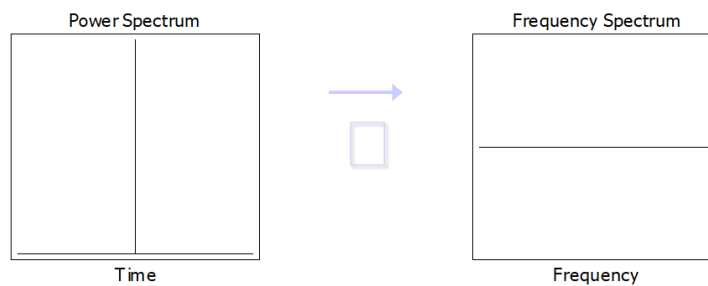
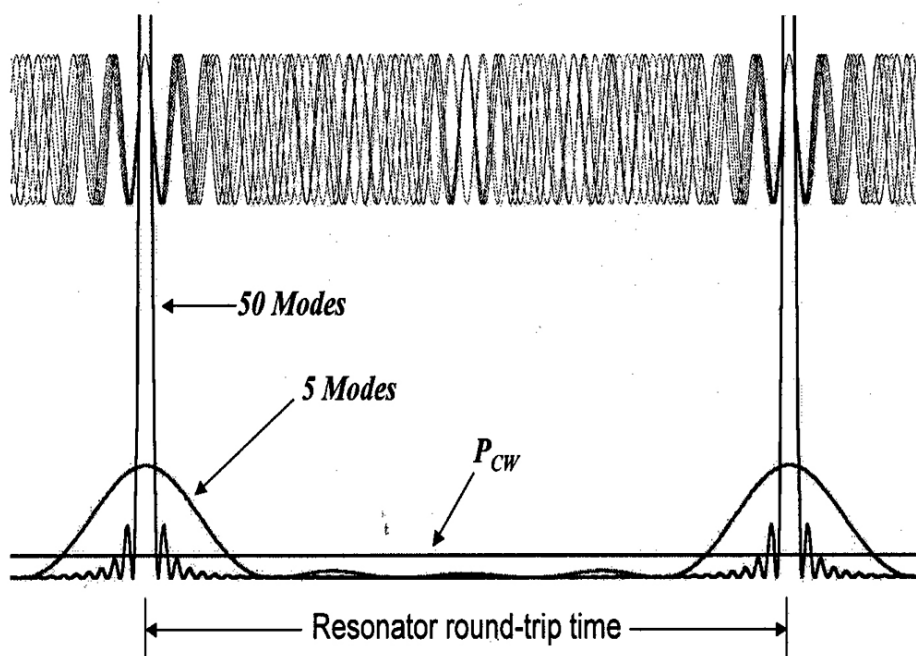


Figure 6.2 Time vs frequency

Ultrafast lasers are nothing else than the coherent superposition of thousand longitudinal modes of a laser cavity.



M. Didomenico, *J. Appl. Phys. Lett.* **35**, 2870 (1964); L. Hargrove *et al.*, *Appl. Phys. Lett.* **5**, 4 (1964)

Figure 6.3 Superposition of longitudinal modes

In order to understand the mathematical description of a pulsed laser in time and in frequency domain let's start to describe the AC electric field of a Laser. The e-Field Fourier transform gives

$$E(t) = \frac{1}{2\pi} \int_{-\infty}^{+\infty} \mathbf{E}(\omega) e^{i\omega t} d\omega \xrightarrow{\text{F.T.}} \mathbf{E}(\omega) = \int_{-\infty}^{+\infty} E(t) e^{-i\omega t} dt$$

If $E(t)$ is a real function, which it will be whenever it represents an actual physical observable then $E(\omega) = E^*(-\omega)$, only the positive spectrum at $\omega > 0$ remains.

$$\begin{aligned} \mathbf{E}(\omega \geq 0) &= |\mathbf{E}(\omega)| e^{-i\theta(\omega)} \\ \mathbf{E}(\omega < 0) &= 0 \end{aligned} \xrightarrow{\text{F.T.}} \begin{aligned} E(t) &= \frac{1}{2\pi} \int_{-\infty}^{+\infty} E(\omega) e^{i\omega t} dt = |E(t)| e^{i\vartheta(t)} \\ \vartheta(t) &= \omega_0 t + \phi(t) \end{aligned}$$

We know that the instantaneous intensity $I(t)$ of a pulse whose electric field profile is $E(t)$ is proportional to $|E(t)|^2 = E(t)E^*(t)$. According to Parseval's theorem

$$\int_{-\infty}^{+\infty} E(t) E^*(t) dt = \frac{1}{2\pi} \int_{-\infty}^{+\infty} \mathbf{E}(\omega) \mathbf{E}^*(\omega) d\omega$$

Therefore, the time-integrated intensity is equal to the frequency-integrated intensity, except for a multiplicative factor. For this reason, the quantity is called the power spectral density. $|E(\omega)|^2 = E(\omega)E^*(\omega)$.

Let's consider now the Laser AC Electric Field in the Frequency domain:

$$\mathbf{E}(\omega \geq 0) = |\mathbf{E}(\omega)| e^{-i\theta(\omega)} = \mathbf{E}_0(\omega) e^{-i\theta(\omega)}$$

$\omega_0 = \text{central frequency}$

Taylor expansion around the central frequency

$$\theta(\omega) = \sum_{n=0}^{\infty} \frac{1}{n!} (\omega - \omega_0)^n \left. \frac{d^n \theta(\omega)}{d\omega^n} \right|_{\omega=\omega_0}$$

$$\theta(\omega) = \theta(\omega_0) + \sum_{n=1}^{\infty} \frac{1}{n!} (\omega - \omega_0)^n \left. \frac{d^n \theta(\omega)}{d\omega^n} \right|_{\omega=\omega_0}$$

\downarrow
 Constant Phase

\downarrow
 Sum of n-order phase chirp terms

The corresponding laser AC electric field in time domain is:

$$E(t) = \frac{1}{2\pi} \int_{-\infty}^{+\infty} E(\omega) e^{i\omega t} dt = |E(t)| e^{i\mathcal{G}(t)}$$

$$e(t) = \text{Re}[E(t)] = |E(t)| \cos[\mathcal{G}(t)]$$

$$\text{Instant Frequency: } \omega(t) = \frac{d\mathcal{G}(t)}{dt}$$

Taylor expansion around pulse center, $t=0$

$$\mathcal{G}(t) = \sum_{n=0}^{\infty} \frac{1}{n!} t^n \left. \frac{d^n \mathcal{G}(t)}{dt^n} \right|_{t=0} = \mathcal{G}(t=0) + \sum_{n=1}^{\infty} \frac{1}{n!} t^n \left. \frac{d^n \mathcal{G}(t)}{dt^n} \right|_{t=0}$$

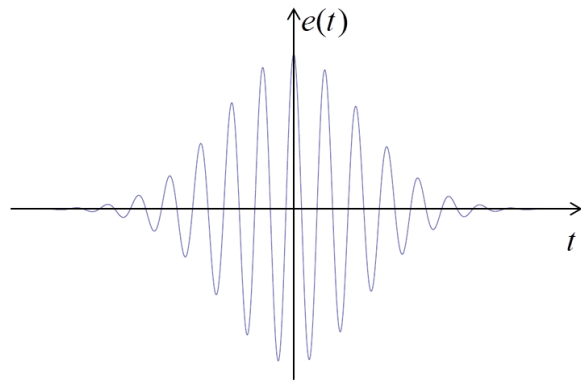
$$\mathcal{G}(t) = \phi_0 + \omega(t=0)t + t^2 \left. \frac{d^2 \mathcal{G}(t)}{dt^2} \right|_{t=0} + t^3 \left. \frac{d^3 \mathcal{G}(t)}{dt^3} \right|_{t=0} + \dots$$

Constant initial phase

Frequency at $t=0$

Second order Chirp

Third order Chirp

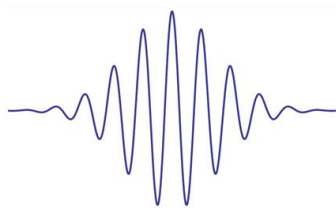


If now we introduce the laser pulse Chirp in time domain we have:

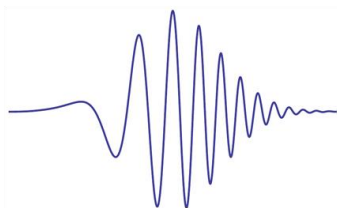
$$e(t) = \text{Re}[E(t)] = |E(t)| \cos[\mathcal{G}(t)] = |E(t)| \cos[\omega t + \phi_0 + at^2 + bt^3 + \dots]$$

$$\mathcal{G}(t) = \phi_0 + \omega(t=0)t + t^2 \left. \frac{d^2 \mathcal{G}(t)}{dt^2} \right|_{t=0} + t^3 \left. \frac{d^3 \mathcal{G}(t)}{dt^3} \right|_{t=0} + \dots$$

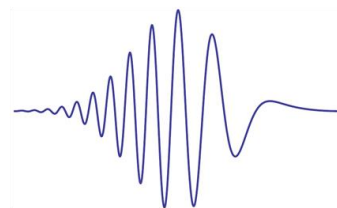
$$a = \frac{d^2 \mathcal{G}(t)}{dt^2}, b = \frac{d^3 \mathcal{G}(t)}{dt^3}$$



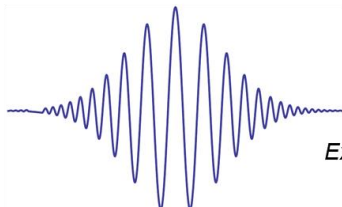
No chirp



Positive second order chirp $a > 0$



Negative second order chirp $a < 0$



Example of Third order chirp $a=0, b > 0$

Another important parameter is to introduce the laser intensity in the time and frequency domains

Temporal intensity (W/cm^2), time domain

$$I(t) = \varepsilon_0 c n \frac{1}{T} \int_{t-\frac{T}{2}}^{t+\frac{T}{2}} e(t') dt' = \varepsilon_0 c n |E(t)|^2$$

Spectral intensity (W/cm^2), frequency domain

$$I(\omega) = \varepsilon_0 c n |E(\omega)|^2$$

Total pulse Energy per unit area (J/cm^2)

$$W = \int_{-\infty}^{+\infty} T(t') dt'$$

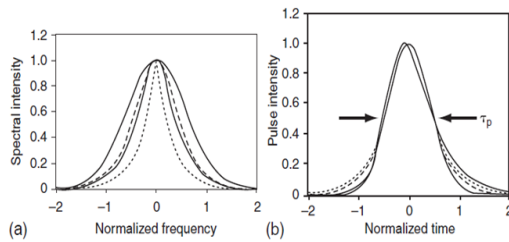


Figure 1.3 Temporal pulse profiles and the corresponding spectra (normalized).

—	Gaussian pulse	$\mathcal{E}(t) \propto \exp[-1.385(t/\tau_p)^2]$
- - - -	Sech pulse	$\mathcal{E}(t) \propto \text{sech}[1.763(t/\tau_p)]$
⋯⋯⋯	Lorentzian pulse	$\mathcal{E}(t) \propto [1 + 1.656(t/\tau_p)^2]^{-1}$
—	Asymm. sech pulse	$\mathcal{E}(t) \propto [\exp(t/\tau_p) + \exp(-3t/\tau_p)]^{-1}$

Experimental estimation of Peak Intensity =Max of $I(t)$

$$I_0 = \text{Max}\{I(t)\} = \frac{En}{At_p}$$

Where En = total laser energy (energy meter), A =Laser focus area, t_p =laser pulse duration

Table 1.1

Examples of standard pulse profiles. The spectral values given are for unmodulated pulses. Note that the Gaussian is the shape with the minimum product of mean square deviation of the intensity and spectral intensity.

Shape	Intensity profile $I(t)$	τ_p FWHM	Spectral profile $S(\Omega)$	$\Delta\omega_p$ FWHM	c_B	$(\tau_p)(\Delta\Omega_p)$ MSQ
Gauss	$e^{-2(t/\tau_G)^2}$	$1.177\tau_G$	$e^{-\left(\frac{\Omega\tau_G}{2}\right)^2}$	$2.355/\tau_G$	0.441	0.5
Sech	$\text{sech}^2(t/\tau_S)$	$1.763\tau_S$	$\text{sech}^2\frac{\pi\Omega\tau_S}{2}$	$1.122/\tau_S$	0.315	0.525
Lorentz	$[1 + (t/\tau_L)^2]^{-2}$	$1.287\tau_L$	$e^{-2 \Omega \tau_L}$	$0.693/\tau_L$	0.142	0.7
Asym. sech	$[e^{t/\tau_a} + e^{-3t/\tau_a}]^{-2}$	$1.043\tau_a$	$\text{sech}\frac{\pi\Omega\tau_a}{2}$	$1.677/\tau_a$	0.278	
Square	1 for $ t/\tau_r \leq 1$, 0 elsewhere	τ_r	$\text{sinc}^2(\Omega\tau_r)$	$2.78/\tau_r$	0.443	3.27

$$\Delta\omega_p t_p \geq 2\pi C_B$$

Where $\Delta\omega_p$ is the spectral bandwidth (FWHM),

t_p is the pulse duration (FWHM),

C_B is a dimensionless parameter of the order of 1

depending on the actual laser pulse profile (see Table).

The inequality becomes equality when the pulse is Fourier limited.

Now we consider the case where a laser pulse is propagating inside a medium with index of diffraction equal to $n(\omega)$.

$$E(z, t) = \frac{1}{2\pi} \int_{-\infty}^{+\infty} \mathbf{E}(\omega - \omega_0) e^{i(\omega t - kz)} d\omega \quad \text{where} \quad k(\omega) = \frac{2\pi n(\omega)}{\lambda_0} \quad \begin{array}{l} n(\omega) \text{ is the index of diffraction of the mater} \\ \lambda_0 \text{ is laser central wavelength in vacuum} \\ \omega_0 \text{ is the laser carrier frequency} \end{array}$$

$$\text{Taylor expansion of } k(\omega) \text{ around } \omega_0 \quad k(\omega) = k_0 + \left(\frac{dk}{d\omega}\right)_{\omega=\omega_0} (\omega - \omega_0) + \frac{1}{2!} \left(\frac{d^2k}{d\omega^2}\right)_{\omega=\omega_0} (\omega - \omega_0)^2 + \frac{1}{3!} \left(\frac{d^3k}{d\omega^3}\right)_{\omega=\omega_0} (\omega - \omega_0)^3 + \dots$$

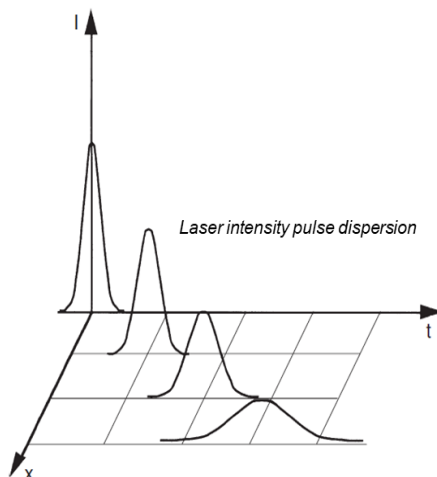
$$k_0 = \frac{2\pi}{\lambda_0} \quad \text{is the laser wavevector in vacuum}$$

$$\frac{dk}{d\omega} = \frac{1}{v_g} \quad \text{is the reverse of the group velocity}$$

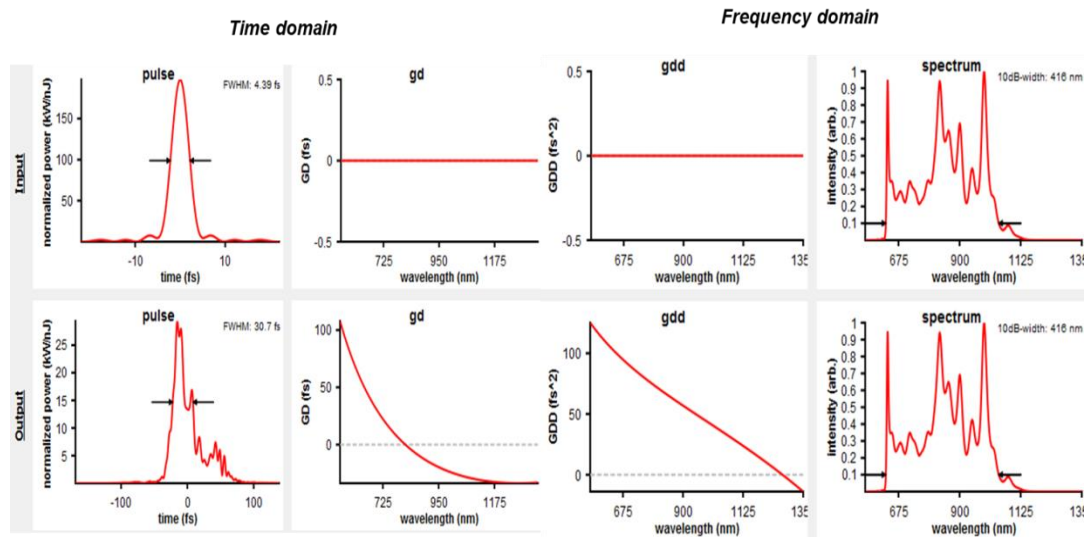
$$\frac{d^2k}{d\omega^2} \quad \text{is the reverse of the group velocity dispersion (GVD)}$$

$$\text{The Fourier transform of a Gaussian laser pulse is } \mathbf{E}_0(\omega) = e^{-\frac{(\omega - \omega_0)^2}{4\Gamma}}$$

$$\text{Then, keeping two terms } \mathbf{E}(\omega, z) \propto e^{-ik_0 z - ik'z(\omega - \omega_0) - \left(\frac{1}{4\Gamma} + \frac{i}{2}k''\right)(\omega - \omega_0)^2}$$

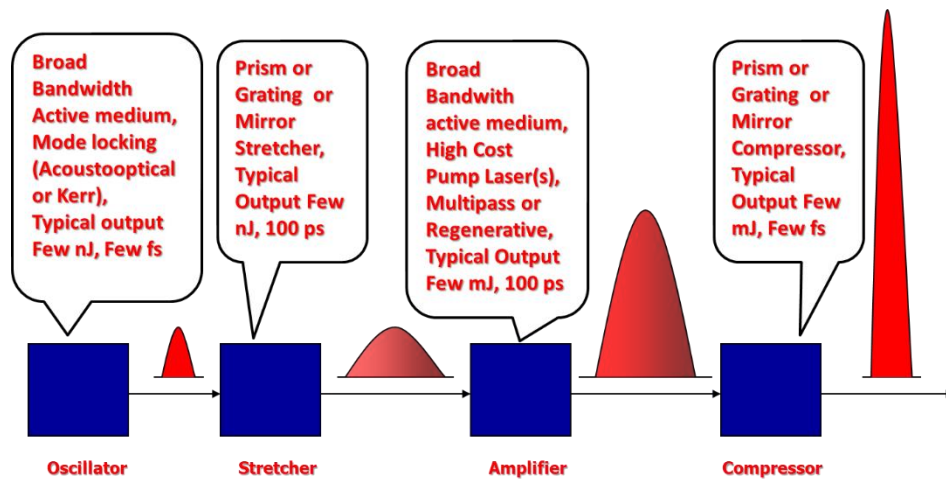


In this frame let's calculate the dispersion of a 4.4 fs laser pulse that propagates in a 2 mm fused silica plate as an example using the freeware program v-chirp®.

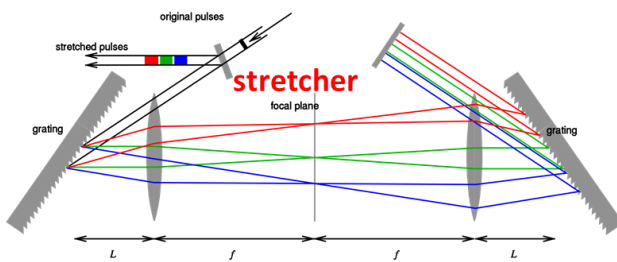
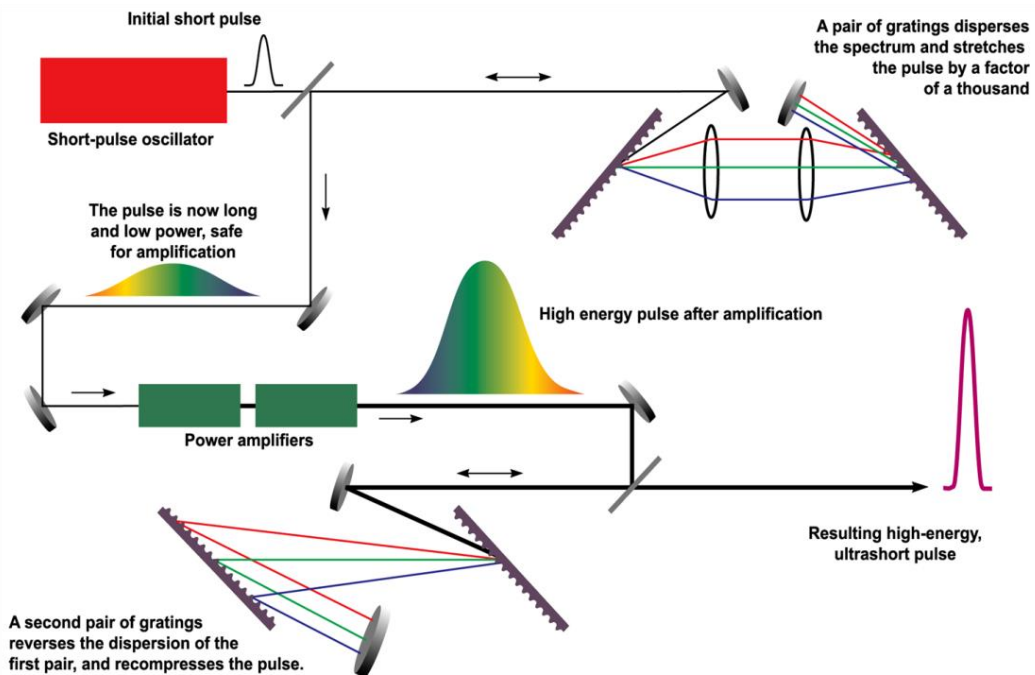


6.2 Chirp pulse amplification

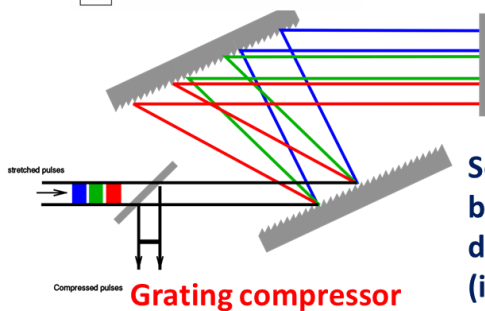
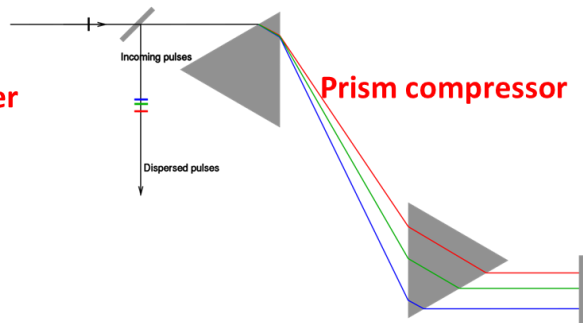
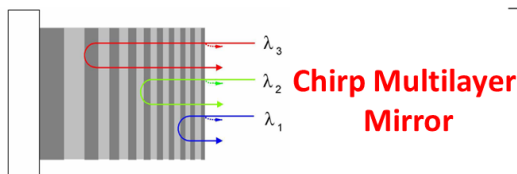
The main method back of the high energy ultrashort laser pulse is the Chirp Pulse Amplification (CPA) which is presented schematically in the figure below:



In the following two figures two CPA techniques are illustrated based in optical designs based in optical stretcher and optical compressors.



Schematic layout of a grating-based stretcher. If $L < f$ leads to a positive dispersion, i.e. the long wavelengths (in red) come first



Schematic layout of prism and grating-based compressor with negative dispersion, i.e. the short wavelengths (in blue) come out first

6.3 Characterization of laser pulse temporal profile

The next important step, in the technology of ultrafast laser pulses, is the method to measure and characterize the laser pulses. The introduction of the definition of the correlated functions is important towards the step of ultrafast laser pulse characterization [[https://en.wikipedia.org/wiki/Optics & /Optical_autocorrelation](https://en.wikipedia.org/wiki/Optics_%26_%2FOptical_autocorrelation)].

Assume n distinct light pulses with real electric field amplitude:

$$E_j(t) = \zeta(t) \cos[\omega_j t + \phi_j(t)]$$

then, we define the nth order fast autocorrelation function with background:

$$g_B^{(n)}(\tau_1, \tau_2, \dots, \tau_{n-1}) = \frac{\int_{-\infty}^{+\infty} [E_1(t) + E_2(t + \tau_1) + \dots + E_n(t + \tau_{n-1})]^{2n} dt}{\int_{-\infty}^{+\infty} [E_1^{2n}(t) + E_2^{2n}(t) + \dots + E_n^{2n}(t)] dt}$$

And nth order fast background free autocorrelation function:

$$g_0^{(n)}(\tau_1, \tau_2, \dots, \tau_{n-1}) = \frac{\int_{-\infty}^{+\infty} [E_1(t)E_2(t + \tau_1) \dots E_n(t + \tau_{n-1})]^n dt}{\int_{-\infty}^{+\infty} [E_1^n(t)E_2^n(t) \dots E_n^n(t)] dt}$$

And the respectively the slow autocorrelation functions

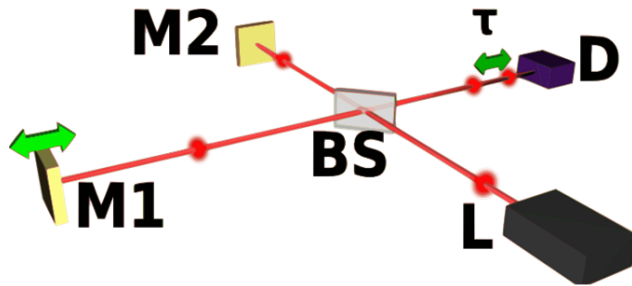
$$G_B^{(n)}(\tau_1, \tau_2, \dots, \tau_{n-1}) = \langle g_B^{(n)}(\tau_1, \tau_2, \dots, \tau_{n-1}) \rangle_{\tau, n}$$

$$G_0^{(n)}(\tau_1, \tau_2, \dots, \tau_{n-1}) = \langle g_0^{(n)}(\tau_1, \tau_2, \dots, \tau_{n-1}) \rangle_{\tau, n}$$

Where $\langle \rangle$ denotes time and order average

The fast first order autocorrelation pulse is able only to measure the power spectrum of the pulse and not the pulse duration.

Field Autocorrelation (Fast 1st order)



Setup for a field autocorrelation, based on a Michelson interferometer. L: Ultrafast laser, BS: beam splitter, M1: moveable mirror providing a variable delay line, M2: fixed mirror, D: linear energy detector

$$g_B^{(1)}(\tau) = \frac{\int_{-\infty}^{+\infty} [E(t) + E(t + \tau)]^2 dt}{\int_{-\infty}^{+\infty} E^2(t) dt}$$

$$g_0^{(1)}(\tau) = \frac{\int_{-\infty}^{+\infty} E(t)E(t + \tau) dt}{\int_{-\infty}^{+\infty} E^2(t) dt}$$

$$g_B^{(1)}(\tau) = 2 [1 + g_0^{(1)}(\tau)]$$

Wiener-Khinchin Theorem:

The Spectral Intensity is proportional to the Fourier Transform of the Field Autocorrelation

$$I(\omega) \propto F \{g_B^{(1)}(\tau)\}$$

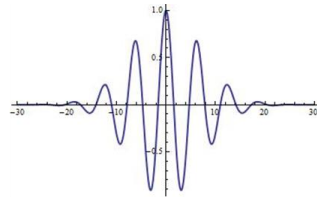
Wiener-Khinchin Theorem :

$$\mathcal{F} \left\{ \int_{-\infty}^{\infty} f(t) f^*(t - \tau) dt \right\} = |\mathcal{F}\{f(t)\}|^2$$

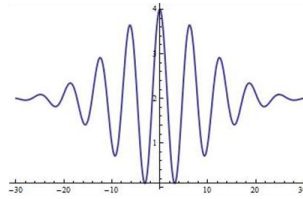
$$\begin{aligned} \mathcal{F} \left\{ \int_{-\infty}^{\infty} f(t) f^*(t - \tau) dt \right\} &= \int_{-\infty}^{\infty} \int_{-\infty}^{\infty} f(t) f^*(t - \tau) dt \exp(-i\omega\tau) d\tau \\ &= \int_{-\infty}^{\infty} f(t) \int_{-\infty}^{\infty} f^*(t - \tau) \exp(-i\omega\tau) d\tau dt = \int_{-\infty}^{\infty} f(t) \left[\int_{-\infty}^{\infty} f(t - \tau) \exp(i\omega\tau) d\tau \right]^* dt \\ &= \int_{-\infty}^{\infty} f(t) \left[\int_{-\infty}^{\infty} f(\tau' + t) \exp(-i\omega\tau') d\tau' \right]^* dt = \int_{-\infty}^{\infty} f(t) [F(\omega) \exp(i\omega t)]^* dt \\ &= \int_{-\infty}^{\infty} f(t) \exp(-i\omega t) dt F^*(\omega) = F(\omega) F^*(\omega) = |F(\omega)|^2 = |\mathcal{F}\{f(t)\}|^2 \end{aligned}$$

In the next figure are illustrated some examples of Field (1st order) autocorrelation functions for some laser pulse duration profiles [[https://en.wikipedia.org/wiki/Optics & /Optical_autocorrelation](https://en.wikipedia.org/wiki/Optics_%26/Optical_autocorrelation)].

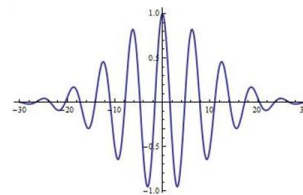
$$E(t) = e^{-\frac{t^2}{10}} \cos[t]$$



$$g_B^{(1)}(\tau) = \frac{\int_{-\infty}^{+\infty} [E(t) + E(t + \tau)]^2 dt}{\int_{-\infty}^{+\infty} E^2(t) dt}$$



$$g_0^{(1)}(\tau) = \frac{\int_{-\infty}^{+\infty} E(t)E(t + \tau) dt}{\int_{-\infty}^{+\infty} E^2(t) dt}$$

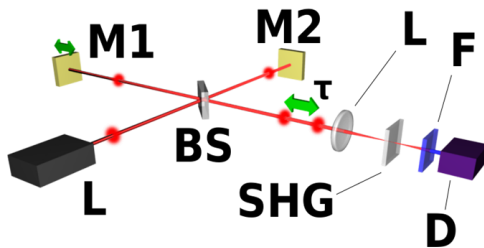


Field Autocorrelator:

- Provide the laser pulse coherence time
- Provide the spectrum of the laser pulse by Fourier Transforming itself
- Do not Provide any phase information
- Cannot Provide the pulse duration, temporal envelop function (e.g. asymmetries)

If we want to measure the laser pulse duration we have to measure the second order autocorrelation function (interferometric autocorrelation).

$$g_B^{(2)}(\tau) = \frac{\int_{-\infty}^{+\infty} [E(t) + E(t + \tau)]^4 dt}{\int_{-\infty}^{+\infty} E^4(t) dt} = 2 + 4 \frac{\int_{-\infty}^{+\infty} E^2(t)E(t + \tau) dt}{\int_{-\infty}^{+\infty} E^4(t) dt} + 4 \frac{\int_{-\infty}^{+\infty} E(t)E^2(t + \tau) dt}{\int_{-\infty}^{+\infty} E^4(t) dt} + 6 \frac{\int_{-\infty}^{+\infty} E^2(t)E^2(t + \tau) dt}{\int_{-\infty}^{+\infty} E^4(t) dt}$$



Typical Setup for a field autocorrelation, based on a Michelson interferometer. L: Ultrafast laser, BS: beam splitter, M1: moveable mirror providing a variable delay line, M2: fixed mirror, D: linear fast second harmonic detector, SHG: Second harmonic Crystal

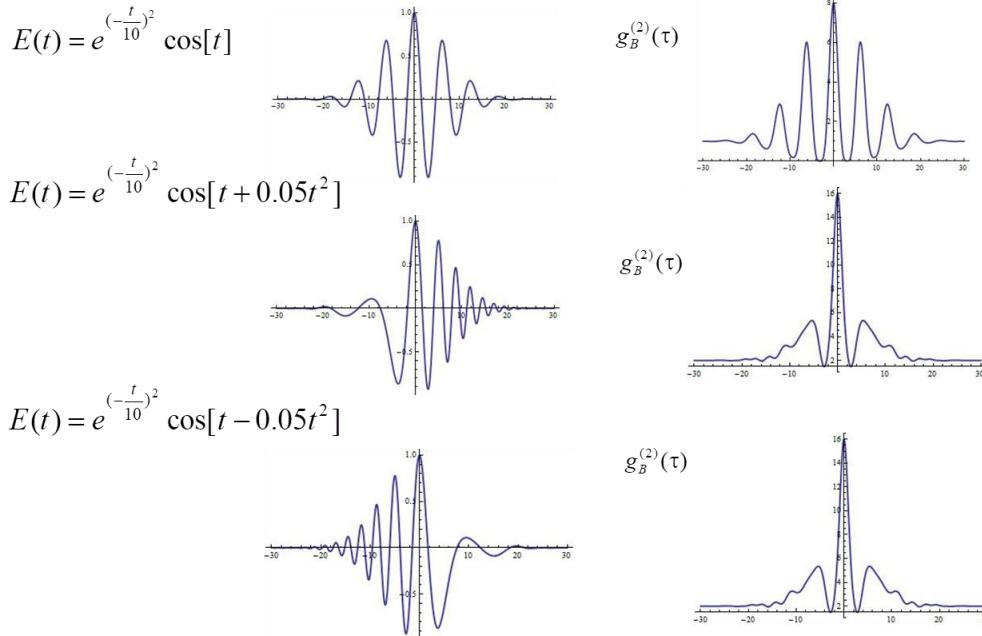
$$\frac{g_B^{(2)}(0)}{g_B^{(2)}(\infty)} = \frac{8}{1}$$

$$g_0^{(2)}(\tau) = \frac{\int_{-\infty}^{+\infty} E^2(t)E^2(t + \tau) dt}{\int_{-\infty}^{+\infty} E^4(t) dt}$$

In the next figure is illustrated some examples of Interferometer (2st order) autocorrelation functions of some laser pulse duration profiles.

Interferometric Autocorrelator (Fast 2th order) Example

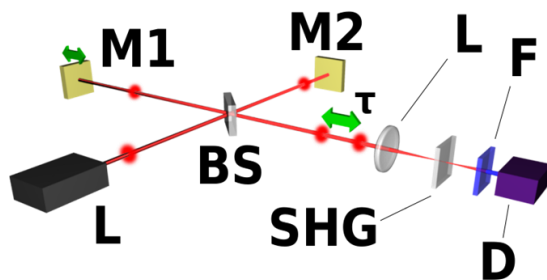
- Provide phase chirp indication (no information for positive or negative)
- Provide the pulse duration, assuming a symmetric temporal envelope function



The laser pulse duration (FWHM) can be also measured with a rigorous way by the second order slow autocorrelation function (intensity autocorrelation) [[https://en.wikipedia.org/wiki/Optics & /Optical_autocorrelation](https://en.wikipedia.org/wiki/Optics#/Optical_autocorrelation)].

Intensity Autocorrelator (Slow 2th order)

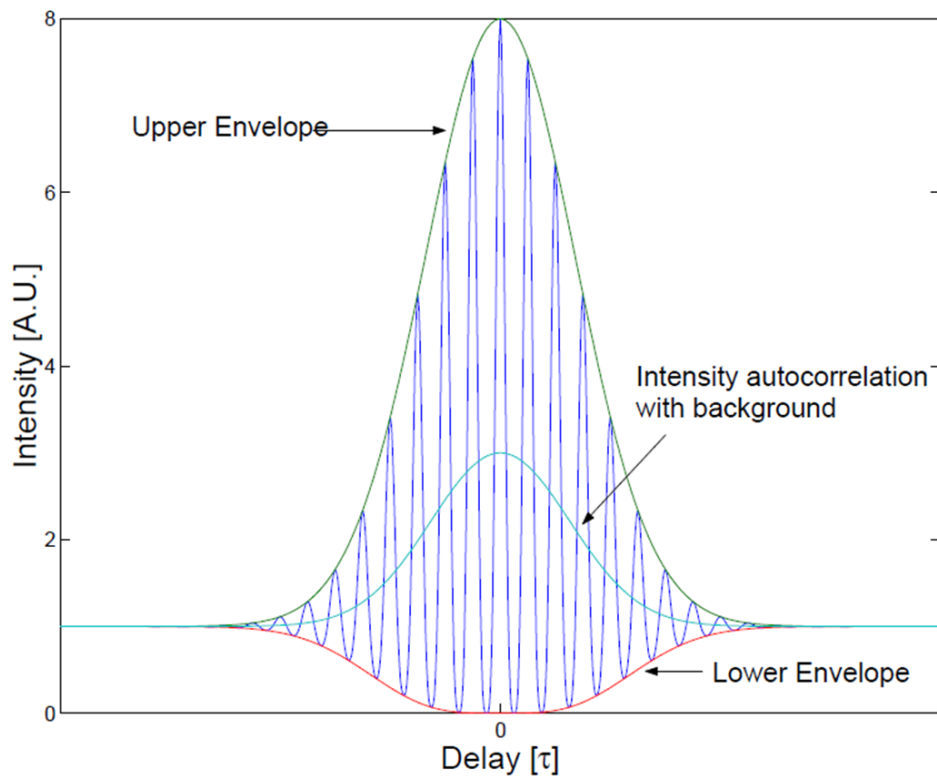
$$G_B^{(2)}(\tau) = \langle g_B^{(2)} \rangle_\tau = 2 + 4 \frac{\int_{-\infty}^{+\infty} E^2(t)E^2(t+\tau)dt}{\int_{-\infty}^{+\infty} E^4(t)dt} = 2 + 4 \frac{\int_{-\infty}^{+\infty} I(t)I(t+\tau)dt}{\int_{-\infty}^{+\infty} I^2(t)dt} = 2 + 4G_0^{(2)}(\tau)$$



$$G_0^{(2)}(\tau) = \frac{\int_{-\infty}^{+\infty} \xi^2(t)\xi^2(t+\tau)dt}{\int_{-\infty}^{+\infty} \xi^4(t)dt} = \frac{\int_{-\infty}^{+\infty} I(t)I(t+\tau)dt}{\int_{-\infty}^{+\infty} I^2(t)dt}$$

Typical Setup for a field autocorrelation, based on a Michelson interferometer. L: Ultrafast laser, BS: beam splitter, M1: moveable mirror providing a variable delay line, M2: fixed mirror, D: linear slow second harmonic detector, SHG: Second harmonic Crystal

$$\frac{G_B^{(2)}(0)}{G_B^{(2)}(\infty)} = \frac{3}{1}$$





HELLENIC
MEDITERRANEAN
UNIVERSITY



universit 
BORDEAUX



UNIVERSITY
of York



Queen's University
Belfast



Erasmus+

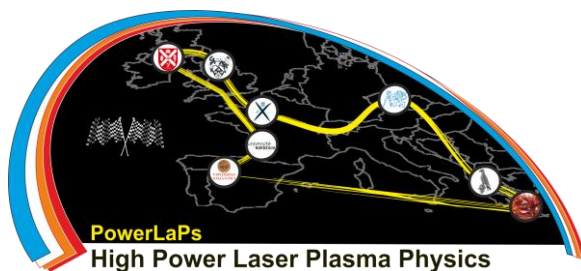
PowerLaPs

Innovative Education & Training in High Power Laser Plasmas

High Power Laser Matter Interactions/High Energy Density Physics - Theory and Experiments

Chapter 7: Basics of non-linear laser matter interaction

N. Papadogiannis



Erasmus+

HELLENIC
MEDITERRANEAN
UNIVERSITY

7. Basics of non-linear laser matter interaction

7.1 Polarization for relative higher laser intensities and electric fields

For relative higher laser intensities and electric fields (laser electric field less than the electric field that connects electrons with the nucleus) the polarization has non-linear terms of the electric field:

$$P(t) = \varepsilon_0 \left[\chi^{(1)} E(t) + \chi^{(2)} E^2(t) + \chi^{(3)} E^3(t) + \dots \right]$$

Then, there are terms in the polarization that oscillates with higher harmonic frequencies for example 2ω :

$$E(t) = E_0 e^{i\omega t} + E_0^* e^{-i\omega t}$$

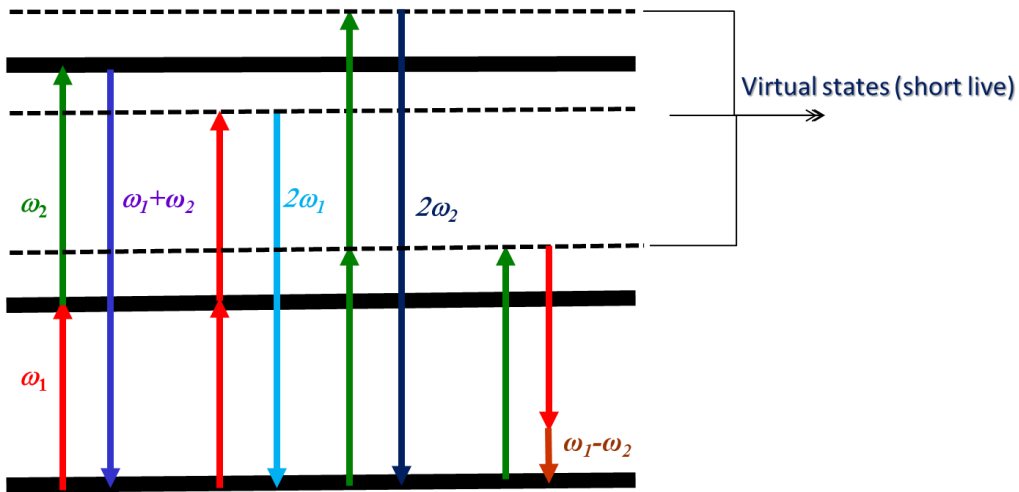
$$E^2(t) = 2|E_0|^2 + E_0^2 e^{i2\omega t} + E_0^{2*} e^{-i2\omega t} \quad \leftarrow \text{Second harmonic generation}$$

Now, adding two fields **with** different frequencies we have:

$$E(t) = E_{10} e^{i\omega_1 t} + E_{10}^* e^{-i\omega_1 t} + E_{20} e^{i\omega_2 t} + E_{20}^* e^{-i\omega_2 t}$$

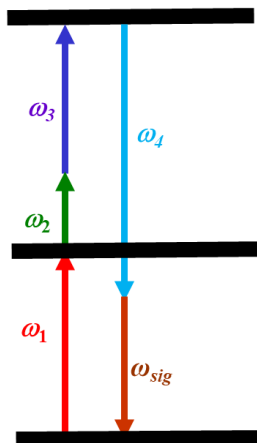
$$\begin{aligned} E^2(t) \propto & E_{10}^2 e^{i2\omega_1 t} + E_{10}^{2*} e^{-i2\omega_1 t} \quad \leftarrow \text{Second harmonic generation} \\ & + 2E_{10}E_{20} e^{i(\omega_1+\omega_2)t} + 2E_{10}^*E_{20}^* e^{-i(\omega_1+\omega_2)t} \quad \leftarrow \text{Sum frequency generation} \\ & + 2E_{10}E_{20}^* e^{i(\omega_1-\omega_2)t} + 2E_{10}^*E_{20} e^{-i(\omega_1-\omega_2)t} \quad \leftarrow \text{difference frequency generation} \\ & + 2|E_{10}|^2 + |E_{20}|^2 \quad \leftarrow \text{DC Term} \end{aligned}$$

In the above figure an example of resonant absorption of two different laser frequencies ω_1 and ω_2 and emission of photons with frequencies $\omega_1 + \omega_2$ (sum frequency generation), $2\omega_1$, $2\omega_2$ (second harmonic generation) and $\omega_1 - \omega_2$ (difference frequency generation) is illustrated.

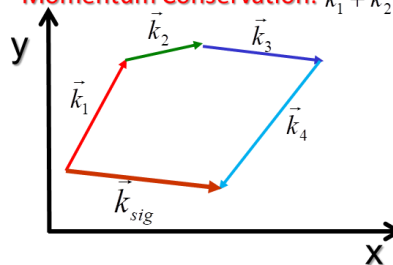


In these multiphoton schemes and for efficient processes it is important to fulfill at the same time the energy and the momentum conservation. This is nothing else than the phase matching condition.

Energy Conservation: $\hbar\omega_1 + \hbar\omega_2 + \hbar\omega_3 - \hbar\omega_4 = \hbar\omega_{sig}$



Momentum Conservation: $\vec{k}_1 + \vec{k}_2 + \vec{k}_3 - \vec{k}_4 = \vec{k}_{sig}$



Phase Matching condition for SHG:

$$\hbar\omega_1 + \hbar\omega_1 = \hbar\omega_{sig} \Rightarrow 2\omega_1 = \omega_{sig}$$

$$\vec{k}_1 + \vec{k}_1 = \vec{k}_{sig} \Rightarrow 2\vec{k}_1 = \vec{k}_{sig} \Rightarrow 2 \frac{\omega_1}{c_0} n(\omega_1) = \frac{\omega_{sig}}{c_0} n(\omega_{sig})$$

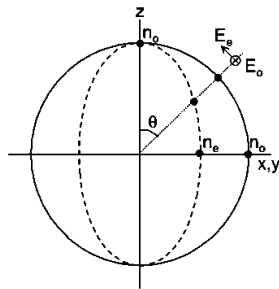
$$2 \frac{\omega_1}{c_0} n(\omega_1) = \frac{2\omega_1}{c_0} n(2\omega_1) \Rightarrow \boxed{n(\omega_1) = n(2\omega_1)}$$

The phase matching condition is very important in the second harmonic generation in birefringent non-linear crystals.

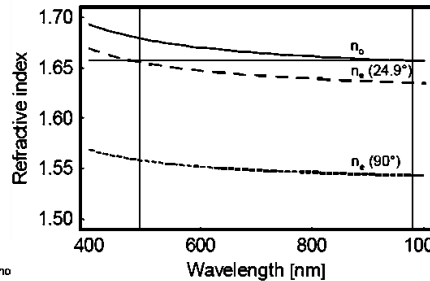
In a normal medium $n(2\omega) > n(\omega)$ so phase matching is impossible

Solution: Birefringence Crystals

Ordinary and extra-ordinary refractive index at a single wavelength for different propagation directions. A line from the origin corresponds to propagation at an angle θ relative to the crystalline c-axis.

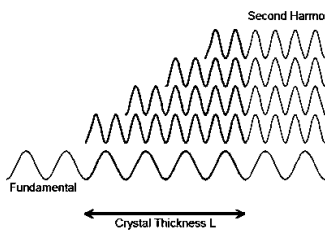


$$\frac{1}{n_e^2(\theta, \lambda)} = \frac{\sin^2 \theta}{n_e^2(\lambda)} + \frac{\cos^2 \theta}{n_o^2(\lambda)}$$



Example:

Refractive index as a function of optical wavelength for BBO. The lines in the figure correspond to the ordinary and extra-ordinary refractive index. Also indicated is the index calculated for $\theta = 24.9^\circ$ that yields perfect phase matching for frequency doubling of 980 nm light.



Concept of phase matching: The fundamental wave at frequency ω has a well defined phase and amplitude everywhere in the crystal. The induced dipoles all radiate at a frequency 2ω with a phase dictated by the fundamental wave. The picture shows the case where all dipoles radiate in phase in the forward direction so that all contributions add up constructively.

$$I_{2\omega} = C^2 I_\omega^2 \frac{L^2}{\pi w_0^2}$$

Intensity of the second harmonic is proportional to the square of intensity of the fundamental. w_0 is the beam waste of the Gaussian focusing.

7.2 Non-linear Kerr effect and the Self Phase Modulation (SPM)

Another important phenomenon in non-linear laser matter interaction is the non-linear Kerr Effect and the Self Phase Modulation (SPM).

Linear index of refraction : $n_0 = \sqrt{1 + \chi^{(1)}}$

Non-linear index of refraction: $n = \sqrt{1 + \chi^{(1)} + \chi^{(3)} |E|^2} = \sqrt{n_0^2 + \chi^{(3)} |E|^2} = n_0 \sqrt{1 + \frac{\chi^{(3)} |E|^2}{n_0^2}}$

Assuming that $\chi^{(3)} |E|^2 \ll n_0^2$ we have: $n \approx n_0 \left(1 + \frac{1}{2} \frac{\chi^{(3)} |E|^2}{n_0^2} \right) = n_0 + n_2 I$

Where I is the laser intensity ($I \sim |E|^2$) and n_2 the nonlinear refractive index defined as: $n_2 = \frac{1}{2} \frac{\chi^{(3)}}{n_0^2}$

$$E(t, z) = E_0(t) e^{i(\omega_0 t - kz)}$$

Spatiotemporal profile of the laser Electric field

$$E(t, z) = E_0(t) e^{i\left(\omega_0 t - \frac{\omega_0 n_0 z}{c} - \frac{\omega_0 n_2 I(t) z}{c}\right)}$$

Including the non-linear refractive index

$$\theta(t, z) = \omega_0 t - \frac{\omega_0 n_0 z}{c} - \frac{\omega_0 n_2 I(t) z}{c}$$

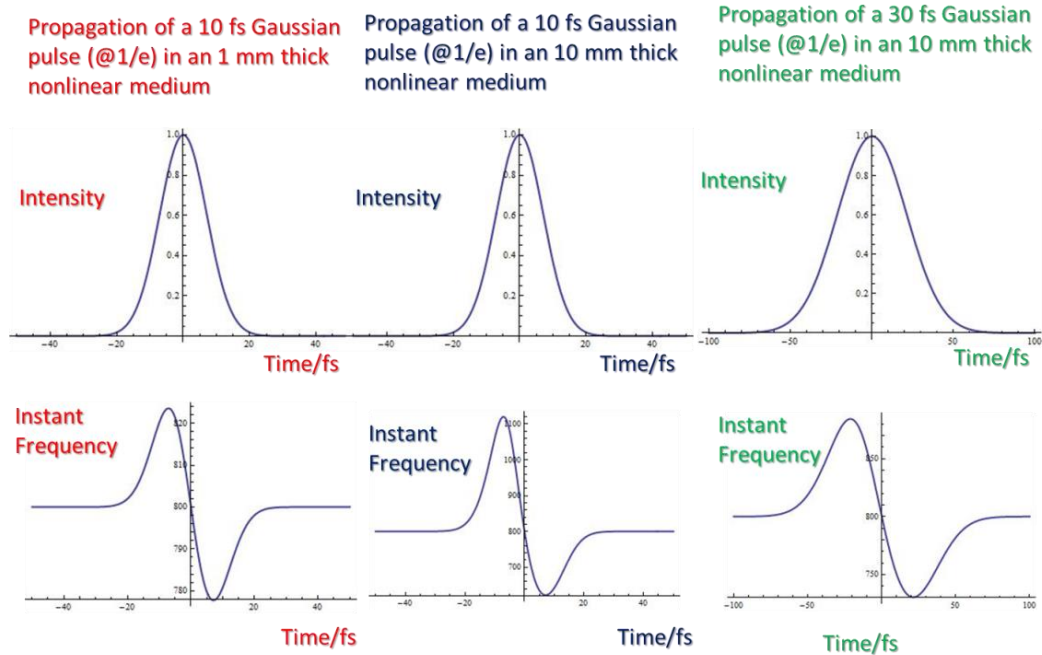
Spatiotemporal overall phase of the field

$$\omega(t, z) = \frac{\partial \theta}{\partial t} = \omega_0 - \frac{\omega_0 n_2 z}{c} \frac{dI(t)}{dt}$$

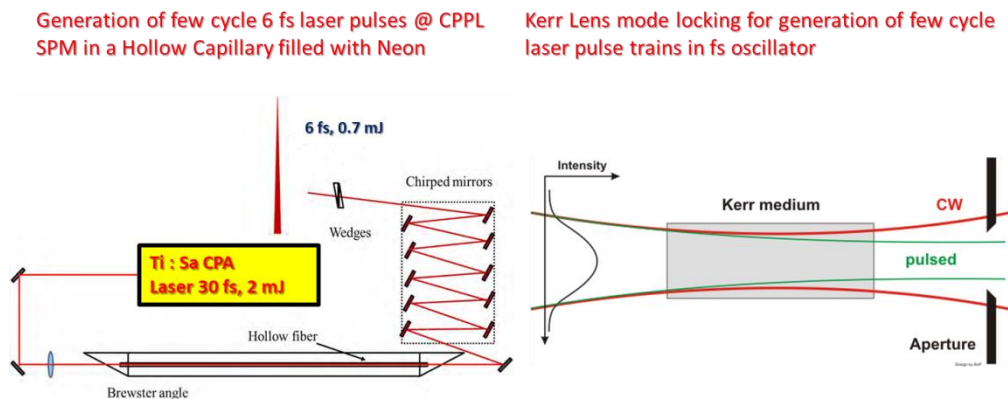
Spatiotemporal frequency of the field

**Final Conclusion : Generation of new frequencies
Phenomenon known as Self Phase Modulation (SPM)**

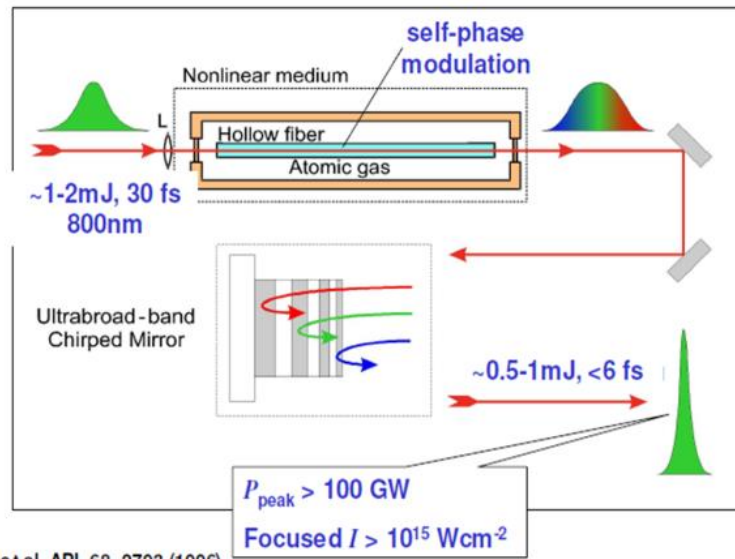
In the above figure some numerical examples of self-phase modulation of two different pulse duration pulses that propagates inside a non-linear medium are illustrated. The generation of new frequencies is obvious, especially in the case of the shorter pulse and wide non-linear medium.



Also in the next figure an application of Kerr effect in the technology of ultrafast laser pulse generation is illustrated.



The self-phase modulation is used also in the generation of few cycle laser pulses where the bandwidth of the laser is needed to be few hundreds of nanometers.



M. Nisoli et al. APL 68, 2793 (1996)



HELLENIC
MEDITERRANEAN
UNIVERSITY



universit 
BORDEAUX



UNIVERSITY
of York



Erasmus+

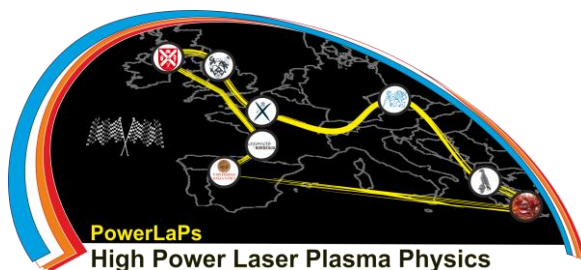
PowerLaPs

Innovative Education & Training in High Power Laser Plasmas

High Power Laser Matter Interactions/High Energy Density Physics - Theory and Experiments

Chapter 8: Ultrafast laser solid surfaces interaction

N. Papadogiannis



Erasmus+

HELLENIC
MEDITERRANEAN
UNIVERSITY

8. Ultrafast laser solid surfaces interaction

8.1 Main regimes of laser solid matter interaction

The two main regimes of laser solid matter interaction is the thermoelastic and the ablation/plasma regime and the physical phenomena that are investigated can be categorized to:

- **Thermoelastic Regime** (Picosecond Ultrasonics, non-linear photoemission, harmonic generation, non-linear absorption, electron and phonon relaxation processes, plasmons, THz Light generation)
- **Ablation/Plasma regime** (Ponderomotive force, Higher Harmonic generation, intense attosecond pulses, particle acceleration, X-ray generation, Thomson Scattering)

In the thermoelastic regime

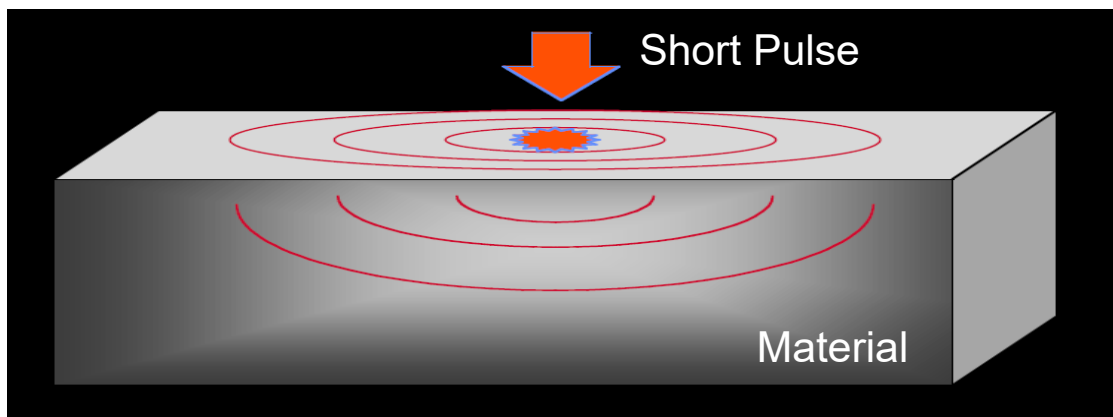
- Absorption of the laser pulse results in an increased localized temperature below the melting point of the material
- Local thermal expansion generates thermal stresses and material vibrations
- Only electrons and photons are the secondary generated products of the interaction
- The material fully recovers in its initial condition after a characteristic time depending on material nature and laser pulse characteristics

In the ablation/plasma regime

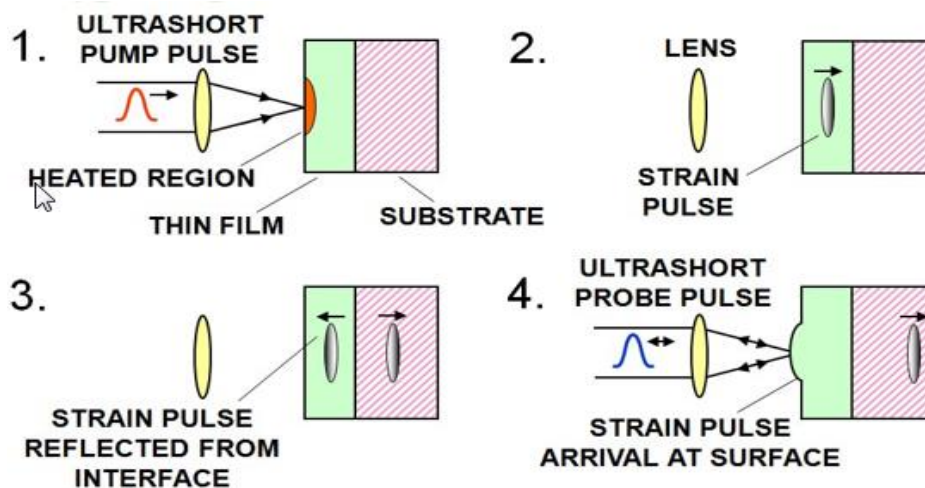
- Absorption of the laser pulse results in an increased localized temperature above the melting point of the material
- Some material is evaporated (typically some nanometres) and vibrations are generated mainly by the recoil effect of the expanding evaporated material.
- A plasma is often formed above the material surface and its expansion can make a substantial contribution to the ultrasonic generation.
- Ions, Electrons and Photons are the secondary generated products of the interaction
- The material never recovers in its initial condition in the place of the interaction

When a material is irradiated with a short-laser pulse for laser fluence below the ablation threshold

- Absorption of the laser pulse results in an increased localized temperature
- Local thermal expansion, thermal stresses
- Generation of ultrasonic waves in the solid in all directions from the generation site.



A typical generation and detection scheme for ultrasounds in the thermoelastic regime.
[Orphanos Y. et al, "Short-pulse laser-generated surface nano-acoustic waves", Micro and Nano 2012]



- An ultrashort laser pulse (pump) is focused onto a thin opaque film on a substrate, the optical absorption results in a thermal expansion that launches an elastic strain pulse. This strain pulse mainly consists of longitudinal acoustic phonons that propagate directly into the film as a strain pulse
- The strain pulse returns to the film surface after acoustic reflection from the film-substrate interface
- This can be detected by a delayed optical probe pulse through optical reflectance or transmittance changes.

8.2 Nanosecond laser pulses interaction with matter

When nanosecond laser pulses interact with matter the Electron and Lattice are in thermodynamic equilibrium and they described by a common temperature, T , and the following equations describe the physical phenomena that occur

Thermal conduction equation:
$$\frac{\partial T}{\partial t} = \left(\frac{\kappa}{\rho c}\right) \nabla^2 T + \frac{Q}{\rho c} - \frac{T_0 \varepsilon}{\rho c} \nabla \left(\frac{\partial u}{\partial t}\right)$$

T is the transient temperature function, T_0 the reference temperature.

κ , ρ and c constants are respectively thermal conductivity, density and specific heat of the sample

ε is the thermal acoustic coupling constant.

Q represents the heat source, which is specified as the absorbed energy per volume unit per second.

The final term in the thermal conductive equation describes the heat induced by mechanical oscillations in the material which is negligible compared to the heat absorbed from laser energy, thus this term can be neglected.

Wave propagation equation:
$$\rho \frac{\partial^2 u}{\partial t^2} = \mu \nabla^2 u + (\lambda + \mu) \nabla(\nabla u) - \varepsilon \nabla T$$

u is the displacement vector of thermal induced elastic waves

λ , μ are the Lamé constants

Laser heat source Q :
$$Q(r, z, t) = I_0 (1 - R) F(t) S(r) a e^{-\alpha z}$$

I_0 is the incident laser power density (laser pulse energy per unit area per second),

R is the optical reflectivity of the sample

α is the optical absorption coefficient ($1/\alpha$ is the optical penetration depth).

Laser temporal and spatial distribution described by the functions $F(t)$ and $S(r)$, respectively

$$F(t) = e^{-2.77(t/t_0)^2}$$

$$S(r) = e^{-(r/r_0)^2}$$

t_0 is the FWHM laser pulse duration and r_0 is the beam radius on the sample surface

8.3 Femtosecond laser pulses interaction with matter

When femtosecond laser pulses interact with matter the Electron and Lattice are initially in non-thermal equilibrium and the following equations describe the physical phenomena that occur

Anisimov Coupled Equations:

$$c_e \frac{\partial T_e(z,t)}{\partial t} = \frac{\partial}{\partial t} \left(k \frac{\partial T_e(z,t)}{\partial z} \right) - g_{ep} (T_e - T_i) + S(z,t)$$

$$c_i \frac{\partial T_i(z,t)}{\partial t} = g_{ep} (T_e - T_i)$$

T_e, T_i are the transient electron and lattice temperature function

c_e, c_i are the electron and lattice heat capacities

k is thermal conductivity,

g_{ep} is the electron-phonon energy coupling constant

S represents the laser heat source $S(z,t) = (1-R)\Phi P(t) \alpha e^{-\alpha z}$

where R is the reflectivity, Φ is the laser fluence, $P(t)$ the laser temporal function, α is the absorption coefficient

Calculation of the thermoelastic waves (picosecond ultrasonics):

$\delta\sigma$ is the tension (Wright et al): $\delta\sigma = -(\gamma_i c_i \delta T_i + \gamma_e c_e \delta T_e) \Rightarrow \frac{\partial \sigma}{\partial t} = (\gamma_i c_i \frac{\partial T_i}{\partial t} + \gamma_e c_e \frac{\partial T_e}{\partial t})$
 γ_i and γ_e are the Gruneisen coefficients

$\eta(z,t)$ is the strain (Thomsen et al):

$$\eta(z,t) = -\frac{(1-R)\Phi\alpha}{2\rho v^2} e^{-\alpha(z-vt)} + \frac{1}{2\rho v^2} \int_0^\infty dt' \int_0^\infty dz' \frac{\partial \sigma}{\partial t} \delta(z' - z + v(t-t')) \quad z > vt$$

$$\eta(z,t) = -\frac{(1-R)\Phi\alpha}{2\rho v^2} e^{-\alpha(z-vt)} + \frac{1}{2\rho v^2} \int_0^\infty dt' \int_0^\infty dz' \frac{\partial \sigma}{\partial t} [\delta(z' - z + v(t-t')) - \delta(z' + z - v(t-t'))] \quad z < vt$$

$u(z,t)$ is the lattice displacement: $u(z,t) = \int_z^\infty \eta(z',t) dz'$



HELLENIC
MEDITERRANEAN
UNIVERSITY



université
BORDEAUX



UNIVERSITY
of York



Erasmus+

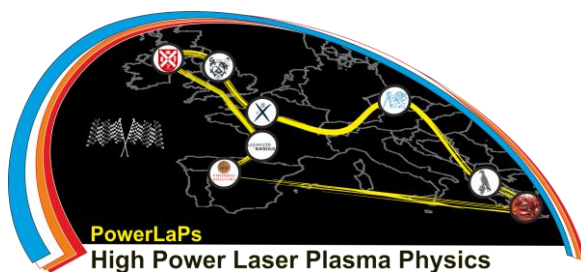
PowerLaPs

Innovative Education & Training in High Power Laser Plasmas

High Power Laser Matter Interactions/High Energy Density Physics - Theory and Experiments

Chapter 9: Coherent laser driven XUV sources

M. Young



Erasmus+





9. Coherent laser driven XUV sources

Laser driven sources of coherent extreme ultraviolet (XUV) radiation can act as ultrafast flashes of light to allow us to probe nature on nanometre spatial scales and femtosecond (10^{-15} s) or even attosecond (10^{-18} s) timescales. The fundamentals of how such pulses can be created by exploiting non-linear interactions with various target media across a range of laser intensities will be discussed. Particular focus will be paid to methods of isolating single pulses from trains of attosecond pulses generated in these interactions.

9.1 Attosecond pulse trains

9.1.1 Why do we need coherent XUV sources?

Studying the dynamics of the microcosm on atomic time scales requires the development of novel radiation sources that can achieve the required spatial and temporal resolution. A camera can be limited by the detector (spatial resolution by lens quality and temporal resolution by shutter time) or potentially by the properties of the camera flash itself (ultimate spatial limit is the wavelength of the light, in a dark room the temporal resolution can be the duration of the camera flash).

The ultimate limit to the temporal duration of a laser pulse is the length of a single cycle, one period of the electromagnetic wave, which for radiation in the visible range of the spectrum is on the order of femtoseconds (10^{-15} s). Whilst very short and still useful for studying a range of molecular dynamics physics, to study dynamics of atomic bound electrons attosecond (10^{-18} s) resolution, and hence radiation extending into the extreme-ultraviolet (XUV) regime, is needed. Since diffraction limits spatial resolution to the \approx the wavelength used, such radiation is also needed to achieve spatial resolution of nanoscale structures.

Time-frequency relationship

The spectral structure of any light pulse is related to the temporal structure of the electromagnetic fields that form the pulse by the Fourier transform. A useful analogy is the relationship between a slit function and the far-field Fraunhofer diffraction pattern that results from diffraction at a slit which can be found by Fourier transforming the slit function. In this case, a top-hat slit function results in a sinc² function for the angular distribution of the diffracted radiation where the diffraction pattern becomes wider as the slit gets smaller. Likewise, for the spectral domain, a wider frequency bandwidth ($\Delta\nu$) can lead to a shorter pulse (Δt) in the temporal domain according to

$$\Delta\nu\Delta t = \alpha \quad (9.1)$$

Where α is a constant on the order of unity that depends on the shape of the spectral amplitude function. For a Gaussian function we have $\alpha \approx 0.44$.

This, however, is not the full story. It is not sufficient to have enough bandwidth to support a short pulse, we must also consider the relative phase between different spectral components. A flat phase indicates that all the peaks of each wavelength line up at some point and add together to give a short pulse. In this case, the pulse duration is given by equation (1) and we say the pulse is transform limited.

9.1.2 Pulse trains and high order harmonics

The output of a laser is not quite as simple as the single pulse discussed so far. We will have a train of pulses separated by the round trip time of the cavity. In the Fourier domain this will be seen as a frequency comb with a constant frequency spacing. This is analogous to how a diffraction grating relates to a single slit. The diffraction grating pattern will consist of individual diffraction orders with an envelope function determined by the width of each groove. Likewise, a frequency comb in the time domain will (assuming flat phase) be a regularly spaced pulse train as shown in figure 9.1.

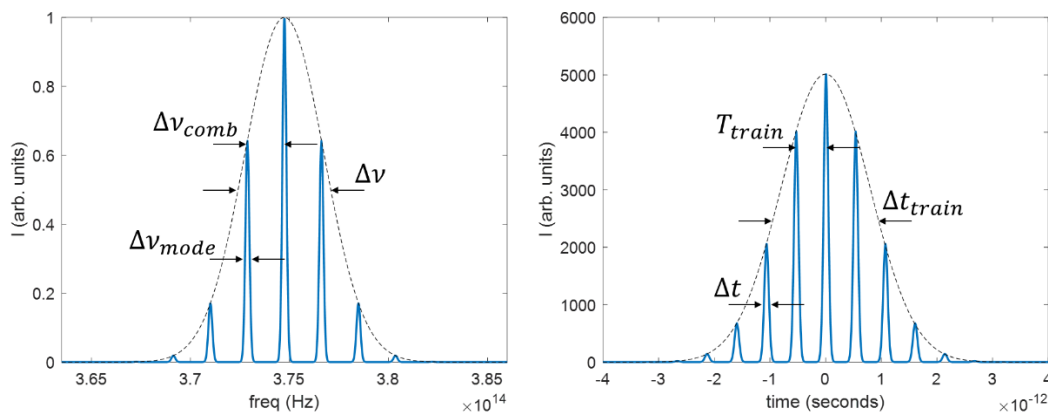


Figure 9.1 An equal spacing frequency comb and its corresponding temporal structure, assuming a flat spectral phase. The width of individual modes and pulses are related to the overall width of the temporal and spectral envelope functions (dashed lines) respectively. The spacing of the frequency comb is also directly related to the spacing of the pulse train.

The spacing of the pulse train will just be the reciprocal of the frequency spacing:

$$T_{train} = \frac{1}{\Delta\nu_{comb}} \quad (9.2)$$

The width of the envelope function of the frequency comb will be related to the width of each individual pulse according to equation (9.1): $\Delta\nu\Delta t = \alpha$ and vice versa for the envelope of the pulse train: $\Delta\nu_{mode}\Delta t_{train} = \alpha$

Harmonics are nothing more than a frequency comb when the spacing of the pulse train is the length of an optical cycle ($T = \lambda/c$). Thus, when we observe harmonics we know this is the signature of interference of individual attosecond pulses in the same way as a diffraction grating pattern results from interference from individual grooves. This will become important for laser driven XUV sources as the period of the driving laser pattern will result in a series of equally spaced pulses resulting in harmonics that can extend into the XUV regime with an overall broad bandwidth sufficient to support attosecond scale pulses. One further challenge will then, of course, be to isolate individual pulses from this pulse train.

9.2 High harmonic generation in gases

9.2.1 Single atom mechanism – the three-step model

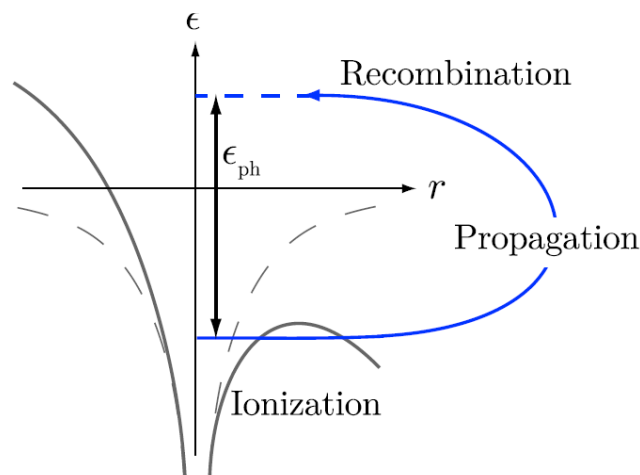


Figure 9.2 The three step model. Following tunnel ionization, the electron is free to move in the laser field where it gains energy before returning to the parent ion where it recombines and gives up this energy as an XUV photon [1]

At sufficiently high laser intensities, the electric field of the laser is sufficiently strong that it can significantly modify the potential well of an atom as shown in figure 9.2. This perturbed shape will allow an electron to quantum tunnel out of the barrier on the suppressed side with a certain probability that will depend on the strength of the laser field at this point. A liberated electron is free to move in the laser field where it can gain energy before returning to the parent ion and recombining and releasing an XUV photon with energy given by

$$\epsilon_{ph} = \epsilon_{ion} + \epsilon_k \quad (9.3)$$

where ϵ_{ion} is the ionisation potential and ϵ_k is the kinetic energy gained by the electron traveling in the laser field.

This so-called 3 step model, first attributed to Corkum [2], allows us to make some powerful predictions about the properties of the resulting radiation. Firstly, we know it will be in the form



of harmonics of the laser frequency. Going further, we say the system has inversion symmetry and the contribution when the electric field is positive will be the same as when it is negative but with opposite sign. This means we will get two pulses per optical cycle with alternating phase, which give us only odd harmonics in the Fourier domain.

Secondly, by modelling the electron trajectory with a simple 1D model where we assume the motion to be dominated by the forces due to the laser electric field, we can determine the possible return velocities of the electron. The kinetic energy corresponding to the maximum return velocity turns out to always have a value of $3.17U_p$ where U_p is the ponderomotive energy of the driving laser which is simply the cycle averaged kinetic energy of a single electron moving in the laser's electric field and is given by

$$U_p = \frac{e^2 E_0^2}{4m_e \omega^2} \quad (9.4)$$

Where e is the electron charge, E_0 is the electric field amplitude, m_e is the electron mass and ω is the angular frequency of the laser.

A typical harmonic spectrum is shown in figure 9.3. Here we see a characteristic plateau extending out to a cutoff region, which approximately corresponds to the maximum return energy just discussed. Notice only odd harmonics are indicated here. Unfortunately, this single atom model does not tell the full picture and we have to also look at the macroscopic picture to develop a full understanding of this mechanism.

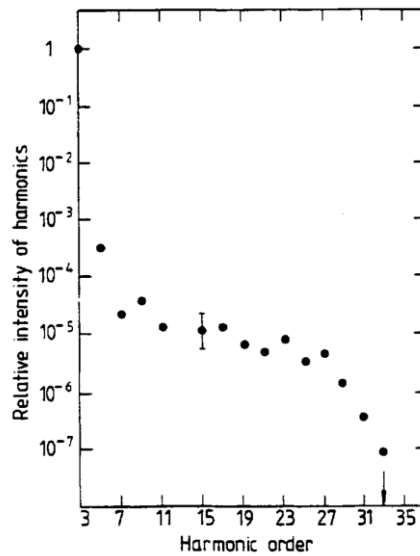


Figure 9.3 A typical spectrum of HHG from gases which closely resembles single atom predictions. A plateau region of harmonics is observed before the efficiency falls off sharply at the cutoff frequency [3]

9.2.2 Macroscopic effects – phase-matching

In any dispersive medium, different frequencies will propagate with different phase velocities and hence, any phase relationship between the pulses at the start of the medium will change as they propagate through. In the ionised gas medium, the dominant effect is typically free electron dispersion due to the variation of the refractive index:

$$\eta = \sqrt{1 - \frac{n_e}{n_c}} \quad (9.5)$$

Where n_e is the electron density and n_c is the critical density that you'll have seen already and which, crucially, depends on the wavelength of light. The high frequency harmonic effectively has a refractive index of 1 but the laser frequency will depend on equation 9.5. As the harmonic and laser relative phase slips, harmonic radiation will be generated out of phase with that co-propagating with the laser leading to destructive interference and a limit to the efficiency. This is often quantified by the coherence length:

$$L_c = \frac{\pi}{\Delta k} \quad (9.6)$$

Where Δk is the mismatch between the wave vector of the harmonic and that of the laser (effectively the phase mismatch per unit length). When the total phase mismatch is π , any further harmonic generation will start to destructively interfere. This can be a complex process with both longitudinal and transverse variation. For low ionisation fractions, the neutral



contribution to the refractive index can partially compensate the free electron dispersion whilst at high ionisation fractions this becomes a negligible contribution. Phase effects due to the 3D propagation of the laser can also be exploited (a phenomenon called the Gouy phase).

9.2.3 Isolating single pulses

Having two pulses for every laser cycle can be restrictive if these pulses are to be used for measurements needing the full temporal resolution of a single attosecond pulse. Thus, we must find some way to gate the emission to only one pulse.

Intensity gating is possible for harmonics near the cut-off and for extremely short laser pulses (FWHM < 5fs). In this case, only a single cycle of the laser pulse reaches sufficient amplitude to drive the HHG process for the higher harmonics and thus if all other spectral components are filtered out, we are left with a single attosecond pulse.

For longer pulses we can exploit the strong dependence of the efficiency of the process on the ellipticity of the driving laser. Budil et al. [4] experimentally verified that elliptically polarised light will strongly suppress the efficiency of the harmonic emission process. This can be intuitively understood by considering that the polarisation direction of an elliptical pulse is constantly changing direction, thus so will the path of the free electron which is then more likely to “miss” the parent ion upon its return. By constructing a laser pulse whose polarisation flips from circular to linear for less than one half cycle to circular again, the harmonic emission will be restricted to only the linear part. This technique is known as polarisation gating and has been widely verified as viable route to isolated attosecond pulses. One possible method of generating a pulse with such a complex polarisation structure using birefringent plates is shown in figure 9.4.

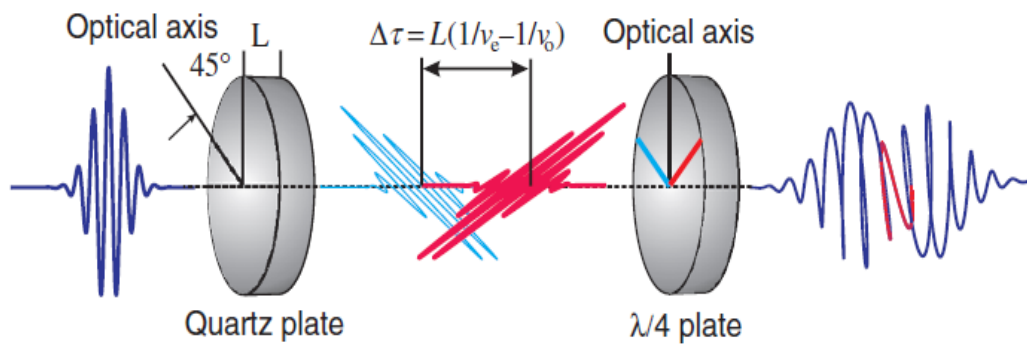


Figure 9.1 Creating a polarisation gate using birefringent plates. The first plate splits the linear pulse into two replicas, separated in time and with orthogonal polarisation. Each pulse replica will now have circular polarisation with opposite handedness. Where these overlap, the pulse will be linear and this part will be the polarisation gate [5].

9.3 High harmonic generation from plasma surfaces

9.3.1 Intense laser-surface interactions

Whilst XUV generation in gas media is a widely used source of coherent attosecond radiation, it is limited by ground state depletion and phase-matching effects as the pulse intensity is increased which limits the efficiency. Going beyond the intensities used for HHG in gases, to intensities $> 10^{18} \text{Wcm}^{-2}$ we reach a regime where we can effectively assume full ionisation of the target. In this regime, a lot of interesting physics takes place during interactions with initially solid targets which become overdense after ionisation (free electron density greater than the critical density which means the plasma reflects the incident laser).

During these intense interactions, we can also get coherent attosecond XUV radiation emitted in the reflected direction, without the same intensity limitations as gaseous media. There are a variety of the possible mechanisms [6] but two key contributors are coherent wake emission and the relativistically oscillating mirror.

9.3.2 Coherent wake emission (CWE)

When the main part of the laser pulse arrives at the target, it will already be ionised due to intense light arriving before the main pulse due to the amplified spontaneous emission or prepulses arising in the laser chain. These need only be tiny fractions of the main pulse intensity in order to generate a plasma on the surface of the target. This will then expand to give an exponential density ramp which the main pulse interacts with.

It is the electrons in this plasma ramp that are the key to the CWE mechanism, which can be efficient for intensities starting at 10^{16}Wcm^{-2} and for a laser field incident obliquely so that



there will be an electric field component normal to the plasma surface. At these intensities, the electrons that are pulled out by the laser field have trajectories that extend significantly into the vacuum region in front of the target. This can be called vacuum heating or the Brunel regime [7].

In an interesting analogy with gas harmonics (although due to a different mechanism) the electrons gain energy in the laser field and return to the plasma density ramp. Here, trajectories of the electrons overlap in space and time inside the ramp and lead to a sharp density spike, which is able to strongly perturb the local plasma medium leading to plasma oscillations [8].

These plasma oscillations are then able to couple into electromagnetic modes propagating in the reflected direction. As this process repeats each laser cycle (once per cycle) this radiation is observed as harmonics of the laser frequency. Since the frequency of these plasmas oscillations depends on the electron density via the plasma frequency, different electromagnetic frequencies originate from different parts of the density ramp, resulting in an inherent chirp of the XUV pulse. A critical feature of this mechanism is then that the maximum XUV frequency observed corresponds to the maximum plasma frequency present in the target which will be given by

$$\omega_m = \sqrt{\frac{n_m}{n_c}} \omega_L \quad (9.7)$$

where ω_L is the laser frequency and n_m is the peak electron density. Typical peak densities are about $400n_c$ for a bulk glass target with 800nm laser radiation which corresponds to a maximum CWE harmonic of $\approx 20^{\text{th}}$.

9.3.3 The relativistically oscillating mirror (ROM) mechanism

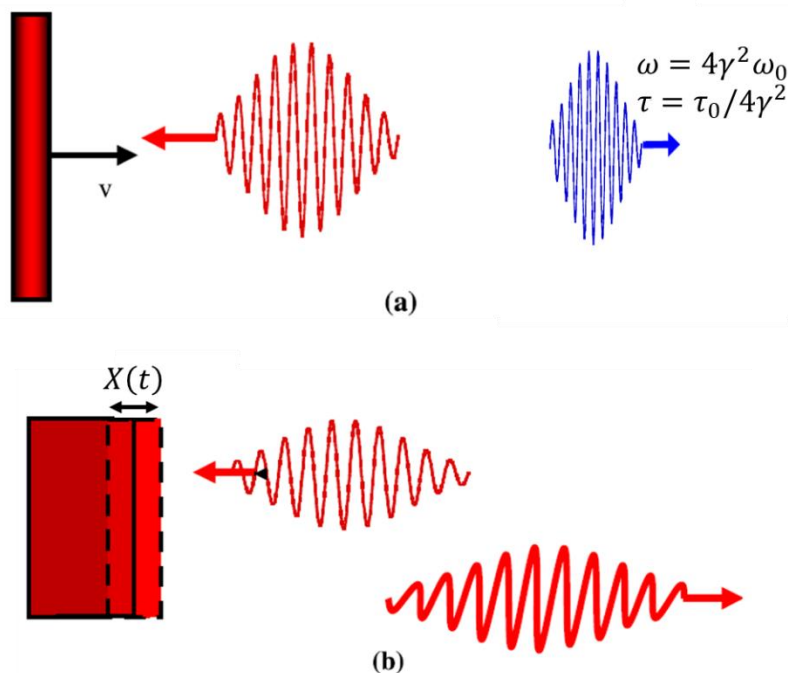


Figure 9.5 Drawing of (a) a laser pulse upshifted in frequency after reflection from a constant velocity mirror and (b) an oscillating mirror periodically upshifting an incident pulse each laser cycle in a model of the interaction with an overdense plasma at very high intensity [9]

As the intensity of the driving laser is increased beyond 10^{18}Wcm^{-2} , the peak velocity of the electrons approaches the speed of light and relativistic effects become important. Consider the reflection of pulse of light from a perfect reflector counterpropagating with a constant velocity as shown in figure 9.5. Einstein's relativity theory tells us that the reflected pulse will experience a Doppler upshift in frequency by a factor of $4\gamma^2$ where γ is the Lorentz factor of the mirror. The reflected pulse will also be compressed in time by the same factor.

During the interaction of a laser pulse, the overdense surface can be modelled as a reflector moving periodically with the laser and Doppler upshifting it each cycle but with a time varying velocity. This oscillatory extension to the ideas of Einstein's moving mirror is the ROM model. This model has been supported by the results of both simulations [10] and experimental observations [11]. As the intensity is increased further, this mechanism is seen to dominate the emission.

Both of these mechanisms (CWE and ROM) are strongly dependent on the size of the plasma ramp that extends in front of the target. For CWE, scale lengths on the order of $\lambda/20$ or less are required for efficient generation. For ROM, an optimum is typically found around $\lambda/10$.



Additionally, as with gas harmonics, both mechanisms result in pulse trains that must be gated if single attosecond pulses are required.

9.3.4 Polarisation gating at relativistic intensities

We have a significant issue with trying to implement polarisation gating schemes for laser systems with sufficient energy to drive ROM processes. This is the accumulation of non-linear phase (called the B-integral) through the required birefringent optics that manipulate the polarisation of the laser. This can lead to undesirable effects such as self-phase modulation in the time domain and deformation of the wavefront in the spatial dimension. Hence, the scheme discussed for gas harmonics would not be applicable in the given form for solid target harmonics.

One small modification to the scheme, however, can reduce the required transmissive optics to just a thin quarter waveplate [12]. We split the beam into two halves and control the delay of each half separately. Each beam is then passed through a quarter waveplate which has a perpendicular axis to the other resulting in one left and one right circularly polarised pulse. When these two beam halves are focused onto a target, they overlap and result in a polarisation gate in time. Experimental results have verified the feasibility of this scheme but, as with gas harmonics, requires an initial laser pulse which is already fairly short (<20fs).

References

- [1] C. Heyl *et al.* J Phys B, 50, (2017) 013001
- [2] P.B. Corkum, PRL, 71, (1993), 1994
- [3] X. Li *et al.* Phys. Rev. A **39** (1989) 5751
- [4] K. Budil *et al.* PRA **48** (1993) R3437
- [5] S. Rykovanov *et al.* NJP **10** (2008) 025025
- [6] Teubner, U. and Gibbon, P., Rev. Mod. Phys. **81** (2009) 445
- [7] F. Brunel, PRL **59** (1987) 52
- [8] F. Quéré *et al.* PRL **96** (2006) 125004
- [9] M. Zepf *et al.* PPCF **49** (2007) B149
- [10] R. Lichters *et al.* Phys. Plasmas **3** (1996) 3425
- [11] B. Dromey *et al.* PRL **99** (2007) 085001
- [12] M. Yeung *et al.* PRL **115** (2015) 193903



HELLENIC
MEDITERRANEAN
UNIVERSITY



université
BORDEAUX



UNIVERSITY
of York



Erasmus+

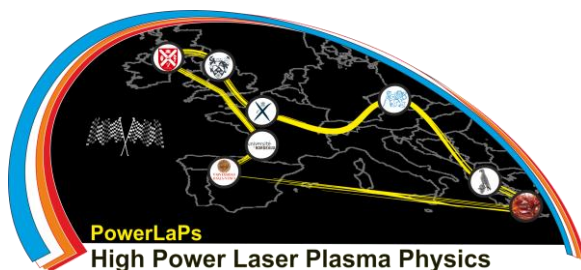
PowerLaPs

Innovative Education & Training in High Power Laser Plasmas

High Power Laser Matter Interactions/High Energy Density Physics - Theory and Experiments

Chapter 10: Basics on laser-atom interactions and atomic processes in plasma

M. Benis



Erasmus+



10. Basics on laser-atom interactions and atomic processes in plasma

10.1 Single electron atoms in weak electromagnetic fields

Here we review the most elemental material in the interactions of hydrogenic atoms with electromagnetic radiation under the concept of perturbation theory. Although this is usually covered in most quantum mechanics courses, it is included here for tracing the various interaction process as the electric or laser of a laser pulse is gradually increased to the non-perturbative conditions.

10.1.1 Transition rates

The Hamiltonian of a spinless particle of charge q and mass m in an electromagnetic field is

$$H = \frac{1}{2m} (\mathbf{p} - q\mathbf{A})^2 + q\Phi \quad (10.1)$$

where \mathbf{p} is the generalized momentum while \mathbf{A} and Φ are the vector and scalar potentials, respectively. Then the Schrödinger equation is written

$$i\hbar \frac{\partial}{\partial t} \Psi(\mathbf{r}, t) = \left[\frac{1}{2m} (\mathbf{p} - q\mathbf{A})^2 + q\Phi - \frac{Ze^2}{(4\pi\epsilon_0)r} \right] \Psi(\mathbf{r}, t) \quad (10.2)$$

or using the Coulomb gauge

$$\nabla \cdot \mathbf{A} = 0 \quad (10.3)$$

and keeping only linear terms in the Hamiltonian

$$i\hbar \frac{\partial}{\partial t} \Psi(\mathbf{r}, t) = \left[-\frac{\hbar^2}{2m} \nabla^2 - \frac{Ze^2}{(4\pi\epsilon_0)r} - \frac{i\hbar e}{m} \mathbf{A} \cdot \nabla \right] \Psi(\mathbf{r}, t) \quad (10.4)$$

This is equivalent to writing it in the terms of

$$i\hbar \frac{\partial \Psi}{\partial t} = [H_0 + H'(t)]\Psi \quad (10.5)$$

where

$$H_0 = -\frac{\hbar^2}{2m} \nabla^2 - \frac{Ze^2}{(4\pi\epsilon_0)r} \quad (10.6)$$

is the time-independent Hamiltonian and

$$H'(t) = -\frac{i\hbar e}{m} \mathbf{A} \cdot \nabla \quad (10.7)$$

the time-dependent Hamiltonian. Assuming that this term is much weaker than the Coulomb term we shall treat the solution under the concept of time-dependent perturbation theory. For this we shall consider known the wavefunctions of the unperturbed Hamiltonian

$$H_0\psi_k = E_k\psi_k \quad (10.8)$$

Then, the solution for the time dependent Hamiltonian is written as a linear combination of the known wavefunctions ψ_k , i.e.

$$\Psi = \sum_k c_k(t)\psi_k e^{-iE_k t/\hbar} \quad (10.9)$$

where, the unknown coefficient $c_k(t)$ are the probability amplitude to find the system in the state ψ_k . By applying the perturbation technique it is proven that, in first order approximation, the amplitude probability of the system to go from the state ψ_a to the state ψ_b is

$$c_b^{(1)}(t) = (i\hbar)^{-1} \int_0^t H'_{ba}(t') e^{i\omega_{ba}t'} dt' = -\frac{e}{m} \int_0^t \langle \psi_b | \mathbf{A} \cdot \nabla | \psi_a \rangle e^{i\omega_{ba}t'} dt' \quad (10.10)$$

where $\omega_{ba} = \frac{E_b - E_a}{\hbar}$. In order to proceed to a realistic calculation we need to know the exact form of the electromagnetic field. As such we may assume a quasi-monochromatic field of a superposition of plane waves of the form

$$\mathbf{A}(\mathbf{r}, t) = \int_{\Delta\omega} A_0(\omega) \hat{\mathbf{e}} [\exp[i(\mathbf{k} \cdot \mathbf{r} - \omega t + \delta_\omega)] + c. c.] d\omega \quad (10.11)$$

Then, the probability amplitude $c_b^{(1)}(t)$ reads

$$c_b^{(1)}(t) = -\frac{e}{m} \int_{\Delta\omega} d\omega A_0(\omega) [e^{i\delta_\omega} \langle \psi_b | e^{i\mathbf{k} \cdot \mathbf{r}} \hat{\mathbf{e}} \cdot \nabla | \psi_a \rangle \int_0^t dt' e^{i(\omega_{ba} - \omega)t'} + e^{-i\delta_\omega} \langle \psi_b | e^{-i\mathbf{k} \cdot \mathbf{r}} \hat{\mathbf{e}} \cdot \nabla | \psi_a \rangle \int_0^t dt' e^{i(\omega_{ba} + \omega)t'}] \quad (10.12)$$

In this relation the first term corresponds to the process of one photon absorption and gets excited to a state with energy $E_b \cong E_a + \hbar\omega$. The second term corresponds to the process of emission of one photon and the system gets de-excited to a state with energy $E_b \cong E_a - \hbar\omega$. In this picture of first order perturbation theory the transition probability is described by the relation

$$P_{ba}(t) = |c_b^{(1)}(t)|^2 \quad (10.13)$$

while the transition rate (a much convenient parameter as it does not depend on time) is described as

$$W_{ba} = \frac{dP_{ba}(t)}{dt} \quad (10.14)$$

After performing the algebra, the transition rate results in

$$W_{ab} = \frac{\pi e^2}{m^2 c \varepsilon_0} \frac{I(\omega_{ab})}{\omega_{ab}^2} |M_{ab}(\omega_{ab})|^2 \quad (10.15)$$

where $I(\omega_{ab})$ is the intensity of the pulse and M_{ab} the transition matrix element

$$M_{ab} = \langle \psi_a | e^{-ik \cdot r} \hat{\varepsilon} \cdot \nabla | \psi_b \rangle = \int \psi_a^*(\mathbf{r}) e^{-ik \cdot r} \hat{\varepsilon} \cdot \nabla \psi_b(\mathbf{r}) d\mathbf{r} \quad (10.16)$$

10.1.2 The Fermi golden rule

The above analysis, even though it was developed for transition between ideal hydrogenic bound states it can be generalized as to include realistic bound states having a physical bandwidth as well as continuum states which in this case correspond to the process of ionization. The result is known as the *Fermi golden rule* and is written as

$$W_{ba} = \frac{2\pi}{\hbar} |H'_{ba}|^2 \rho_b(E) \quad (10.17)$$

where H'_{ba} is the perturbative Hamiltonian of Eq. 10.7, and $\rho_b(E)$ the density of states around the energy E . We should mention once more that all the above are valid for pulse intensities low enough so that the condition $P_{ba}(t) = W_{ba} \cdot t \ll 1$ is fulfilled.

10.1.3 The dipole approximation

So far it becomes clear that for the calculation of a transition rate all that is needed is the calculation of the matrix element of Eq. 10.16. In many realistic problems this is performed by the expansion of the term $e^{ik \cdot r}$ as

$$e^{ik \cdot r} = 1 + (ik \cdot r) + \frac{1}{2!} (ik \cdot r)^2 + \dots \quad (10.18)$$

For optical transitions $kr \ll 1$, and thus the approximation $e^{ik \cdot r} \cong 1$ can be adopted. This is the well known *dipole approximation*. In this case the transition rate is estimated as

$$W_{ba} = \frac{\pi}{\hbar^2 c \varepsilon_0} I(\omega_{ba}) |\hat{\varepsilon} \cdot \mathbf{D}_{ba}|^2 \quad (10.19)$$

where $\mathbf{D} = -e\mathbf{r}$ is the electric dipole moment. The well-known selection rules $\Delta l = \pm 1$ and $\Delta m = 0, \pm 1$ result from the term $\hat{\varepsilon} \cdot \mathbf{D}_{ba}$ of the dipole approximation.

10.1.4 Line shapes and lifetimes

An important feature of an atomic/ionic de-excitation is the shape of the spectral lines. This is obtained by the transition probability. Assuming an exponential decay of the state population then the transition probability is estimated as

$$P_{ba}(t) = |c_b^{(1)}(\omega, t)|^2 \sim \frac{1}{(\omega - \omega_{ba})^2 + 1/4\tau^2} \sim \frac{\Gamma^2/4}{(\hbar\omega + E_a - E_b)^2 + \Gamma^2/4} \quad (10.20)$$

where τ is the *lifetime* of the state. This is a Lorentzian distribution and it is characteristic for the atomic de-excitations. The *lifetime* of an excited state can be obtained as the reciprocal of the transition rate, $\tau = 1/W_{ba}$. However, since the relaxation of an excited state usually involves many de-excitation channels the lifetime of the state is then estimated as

$$\tau = \left(\sum_k W_{ka}^S \right)^{-1} \quad (10.21)$$

The quantity

$$\Gamma = \frac{\hbar}{\tau} \quad (10.22)$$

is the *natural width* of the state.

10.2 Atomic and molecular processes in intense laser fields

10.2.1 Intermediate intensities - Rabi oscillations

Here we shall examine the case where the condition $P_{ba}(t) = W_{ba}t \ll 1$ is not valid. This perturbative case corresponds to weak fields, that among others does not take into account the depletion of the population of the states. In stronger fields the change in the population of the states is not negligible and should be taken into account even in a perturbative approach of the problem. For this, for easiness, we shall assume a two-level atomic system interacting with an external electromagnetic field strong enough to affect the population of the atomic states $|a\rangle$ and $|b\rangle$ (see Fig. 10.1)

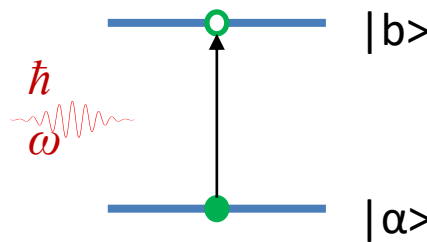


Figure 10.1 Interaction of a two-level atomic system with monochromatic electromagnetic field.

The unperturbed wave function of the system is

$$|\Psi(t)\rangle = c_a|a\rangle e^{-iE_a t/\hbar} + c_b|b\rangle e^{-iE_b t/\hbar} \quad (10.23)$$

where c_a και c_b are the probability amplitudes to find the system in states $|a\rangle$ or $|b\rangle$, respectively. Assuming an external perturbation of an electric field of the form $E = E_0 \cos(\omega t)$, the perturbative Hamiltonian can be written in the dipole approximation as $H' = -erE_0 \cos(\omega t)$. Then the wave function is modified as

$$|\Psi(t)\rangle = c_a(t)|a\rangle e^{-iE_a t/\hbar} + c_b(t)|b\rangle e^{-iE_b t/\hbar} \quad (10.24)$$

satisfying the time-dependent Schrödinger equation

$$(H_0 + H')|\Psi(t)\rangle = i\hbar \frac{\partial}{\partial t} |\Psi(t)\rangle \quad (10.25)$$

where H_0 is the time-independent Hamiltonian for which $H_0|a\rangle = E_a|a\rangle$ and $H_0|b\rangle = E_b|b\rangle$. By replacing Eq. 10.24 into Eq. 10.25 and assuming a linearly polarized field along the x axis, we obtain after some algebra

$$\dot{c}_a(t) = i\frac{\Omega_R}{2}c_b(t)e^{i(\omega_{ab}-\omega)t} + i\frac{\Omega_R}{2}c_b(t)e^{i(\omega_{ab}+\omega)t} \quad (10.26a)$$

$$\dot{c}_b(t) = i\frac{\Omega_R}{2}c_a(t)e^{-i(\omega_{ab}-\omega)t} + i\frac{\Omega_R}{2}c_a(t)e^{-i(\omega_{ab}+\omega)t} \quad (10.26b)$$

where $\omega_{ab} = (E_b - E_a)/\hbar$. Here we have defined the quantity of *Rabi frequency* as

$$\Omega_R \equiv \frac{|\langle a|ex|b \rangle|E_0}{\hbar} \quad (10.27)$$

By applying the rotating wave approximation (RWA), in which the fast oscillating terms $e^{i(\omega_{ab}+\omega)t}$ are omitted, and assuming the initial conditions $c_a(t=0) = 1$ and $c_b(t=0) = 0$ the solution is written as

$$c_a(t) = \left[\cos\left(\frac{\Omega t}{2}\right) - \frac{i(\omega_{ab} - \omega)}{\Omega} \sin\left(\frac{\Omega t}{2}\right) \right] e^{i(\omega_{ab}-\omega)t/2} \quad (10.28a)$$

$$c_b(t) = \frac{i\Omega_R}{\Omega} \sin\left(\frac{\Omega t}{2}\right) e^{i(\omega_{ab}-\omega)t/2} \quad (10.28b)$$

where we have also defined $\Omega \equiv \sqrt{(\omega_{ab} - \omega)^2 + \Omega_R^2}$. From the above solution we conclude the following

- In the case of $\omega_{ab} \neq \omega$ the transition probability $|c_b(t)|^2$ is oscillating with a frequency $\Omega/2$. The maximum transition probability is always smaller than one, reduced to smaller values as departing from the resonance at $\omega_{ab} = \omega$.
- The quantity $W(t) = |c_b(t)|^2 - |c_a(t)|^2$ describes the population inversion, a crucial parameter in laser operation. In the case of $\omega_{ab} \neq \omega$ it is written as

$$W(t) = \frac{(\omega_{ab} - \omega)^2 - \Omega_R^2}{\Omega^2} \sin^2\left(\frac{\Omega t}{2}\right) + \cos^2\left(\frac{\Omega t}{2}\right) \quad (10.29)$$

In the case of resonance, where $\omega_{ab} = \omega$ and $\Omega = \Omega_R$, the population inversion results in

$$W(t) = -\sin^2\left(\frac{\Omega t}{2}\right) + \cos^2\left(\frac{\Omega t}{2}\right) = \cos(\Omega_R t) \quad (10.30)$$

Therefore, the population inversion oscillates between the values -1 and 1 with the Rabi frequency. The more intense is the field the more rapid will be the oscillation and this is actually the physical meaning of the Rabi frequency. It is a measure of the strength of the electromagnetic field. The above are presented graphically in Fig. 10.2.

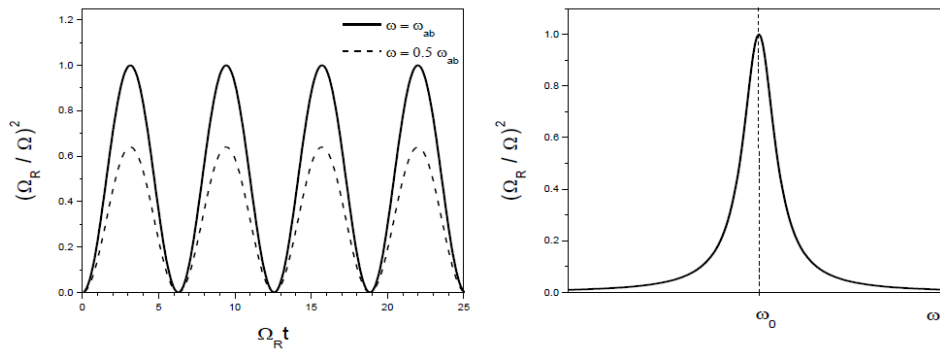


Figure 10.2 [Left]. The transition probability in the cases of resonance $\omega_{ab} = \omega$ and off-resonance $\omega_{ab} \neq \omega$. [Right] The transition probability as a function of the external field frequency.

The Rabi oscillations are very important in Physics, Chemistry and Medicine. In all cases, the behavior of the nuclear magnetic dipole moments in a combination of external constant magnetic field and variable magnetic and/or electric fields are examined to obtain results about the local structure of the specimen under study. In Physics this is known as Nuclear Magnetic Resonance (NMR), while in Medicine it is known as Magnetic Resonant Imaging (MRI).

10.2.2 Strong laser fields

10.2.2.1 The Keldysh parameter and terminology

The ionization of an atom can take place via the absorption of a photon with energy higher than the ionization potential of the atom. However, in conditions of intense laser fields the atom may absorb more than one photons of smaller than the ionization potential energy, I_p , and get ionized. This process is termed *non-linear* as it does not depend linearly on the intensity of the laser pulse. Non-linear processes are present whenever the intensity of the laser field is increased so that the Hamiltonian term of the interaction with the field (see Eq. 10.7) can no longer be considered as a small perturbation. In bibliography, a popular way to classify the intensities range of interaction is through the Keldysh parameter that is a measure of the radiation intensity.

First, we have to introduce the concept of the *ponderomotive energy*. Assuming an electric field of the form $E = E_0 \cos(\omega t)$, the ponderomotive or *quiver energy* is the kinetic energy that a particle of mass m and charge q acquires in this field, i.e.

$$U_p = \left\langle \frac{1}{2} m v^2 \right\rangle = \frac{q^2 E_0^2}{4m\omega^2} = 9.33 \times 10^{-14} I (W cm^{-2}) \lambda^2 (\mu m) \quad (10.31)$$

Then the Keldysh parameter is defined as

$$\gamma = \sqrt{\frac{I_p}{2 U_p}} \quad (10.32)$$

The classification scheme is the following and graphically presented in Fig. 10.3

- $\gamma \gg 1$. *Multiphoton ionization*. Ionization is succeeded through the multiple absorption of photons (Fig. 10.3.a). The electromagnetic field is much stronger than that for single photon ionization but still weak to be treated within the higher order perturbation theory.
- $\gamma < 1$. *Tunelling ionization*. The field is so strong that it cannot be treated perturbatively. Actually it is of the order of the Coulombic field causing its deformation as graphically shown in Fig. 10.3.b. Then the atom is ionized at the peak of the field through the process of tunneling. For example, for a laser field with $\lambda = 800 \text{ nm}$ and an Ar atom with $I_p = 15.8 \text{ eV}$, the condition is fulfilled for intensities $I \geq 3 \times 10^{14} \text{ W/cm}^2$.
- $\gamma \ll 1$. *Over the barrier ionization*. In this case depicted in Fig. 10.3.c, the field has deformed the Coulombic potential so much that the electron escapes the atom without tunneling.

The above classification is not universal but rather academic. It is very popular though as it is valid for optical transitions where most lasers deliver. A more aesthetic approach for the Keldysh parameter can be defined as

$$\gamma = \frac{\text{tunneling time}}{\text{laser period}} \quad (10.33)$$

Indeed, for values of $\gamma > 1$ the laser period is smaller than the tunneling time and therefore tunneling cannot be concluded but rather the multiphoton ionization. For values of $\gamma < 1$, the laser period is longer than the tunneling time and therefore tunneling is promoted. Next we shall examine in detail this classification schemes.

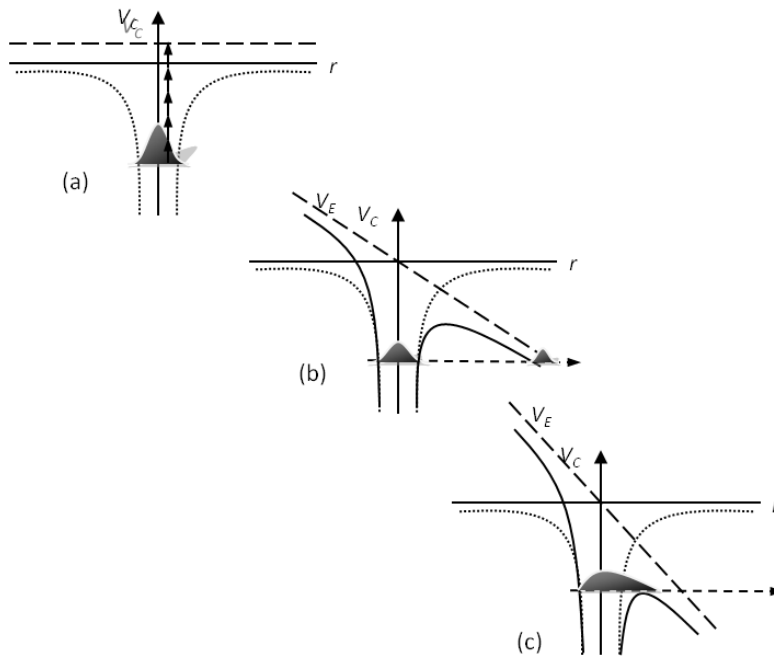


Figure 10.3 [a]. Multiphoton ionization. [b] Tunneling ionization. [c] Over the barrier ionization. V_E and V_C are the laser and Coulombic potentials, respectively.

10.2.2.2 Multiphoton processes ($\gamma \gg 1$)

Multiphoton ionization and above threshold ionization

As already mentioned, in this case the multiphoton ionization (MPI) is succeeded through the multiple absorption of photons. The scaling law for the N-photon ionization rate implies that MPI rate is proportional to the Nth power of the laser photon flux F ($F = I/\hbar\omega$), i.e.

$$W_N = \sigma_N F^N \quad (10.34)$$

where σ_N is the generalized cross section (in units of $cm^{2N} s^{N-1}$). Thus, if the duration of the laser pulse is t_d the probability for the N-photon MPI is

$$P = \int_0^{t_d} W_N(t) dt = \sigma_N t_d F^N \quad (10.35)$$

The MPI rate can be estimated utilizing higher order perturbation theory. The result is a straightforward generalization of the Fermi's Golden Rule

$$W_N = \frac{2\pi}{\hbar} \left(\frac{2e^2}{\varepsilon_0 c} \right)^N I^N \sum_f |M_{i \rightarrow f}^{(N)}|^2 = \sigma_N F^N \quad (10.36)$$

where $M_{i \rightarrow f}^{(N)}$ is the Nth order multiphoton transition matrix element. In the case of linear polarization it has the form

$$M_{i \rightarrow f}^{(N)} = \sum_{j', j'', \dots, j'''} \frac{\langle i | x | j' \rangle \langle j' | x | j'' \rangle \dots \langle j''' | x | f \rangle}{(E_i + \hbar\omega - E_{j'}) (E_i + 2\hbar\omega - E_{j''}) \dots (E_i + (N-1)\hbar\omega - E_{j'''})} \quad (10.37)$$

where the initial state is $|i\rangle$ is usually the ground state of the atom and the final state in the continuum is $|f\rangle$. With the letter j are denoted all the intermediate states (virtual states) that correspond to each photon absorption. The final energy of the emitted electron is $E_i + N\hbar\omega$.

An astonishing feature in the first observations of this process was that the emitted electron may absorb more photons than the necessary number for ionization (e.g. for Ar atoms with $I_p = 15.8 \text{ eV}$ and a laser pulse of wavelength $\lambda = 800 \text{ nm}$ the necessary number of photons with is 11). The process can be observed in the recorded electron spectra as shown in Fig. 10.4 and is known as Above Threshold Ionization (ATI).

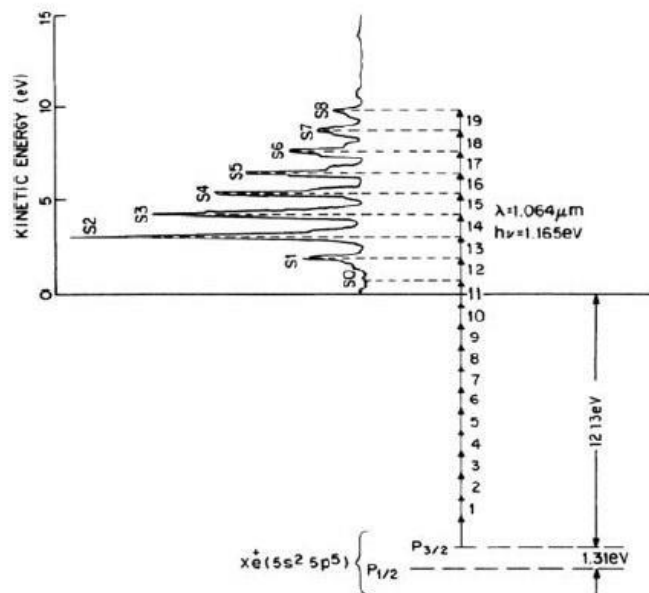


Figure 10.4 Photoelectron energy spectrum for xenon irradiated by 1064 nm light showing many ATI peaks (Phys. Rep. 204, (1991) 331-383).

Low order harmonic generation

When a laser beam propagates through a gaseous medium, the atomic electrons oscillate in response to the laser field. If the laser field is weak enough, the electrons oscillate at the angular frequency of the laser field. However, when stronger laser fields are involved, the electrons oscillate at higher angular frequencies resulting in emission of radiation at these frequencies. The source of radiation is the laser-induced polarization P of the medium. For a low intensity fields the displacement of the electrons is linear, leading to a polarization which is linearly proportional to the laser field, i.e.

$$P = \chi^{(1)}E \quad (10.38)$$

where $\chi^{(1)}$ is the linear susceptibility and E the electric field. For intense laser fields, the electron displacement is highly nonlinear. In this case the polarization is expanded perturbatively and high orders of E should be taken into account as

$$P = \sum_N \chi^{(N)}(\omega)E^N \quad (10.39)$$

where the quantities $\chi^{(N)}$ are the N th order nonlinear susceptibilities of the medium at the fundamental angular frequency ω . The N th order susceptibility $\chi^{(N)}$ is the source of the N th harmonic generation corresponding to the absorption of N photons and emission of one harmonic photon with energy $N\hbar\omega$. In gaseous media only odd orders of harmonics can be generated in this process due to symmetry considerations. Thus, this model is valid for the 3rd to 7th harmonics as for higher harmonics the process of tunneling prevails as will be discussed later on. A graphical energy diagram is shown in Fig. 10.5.

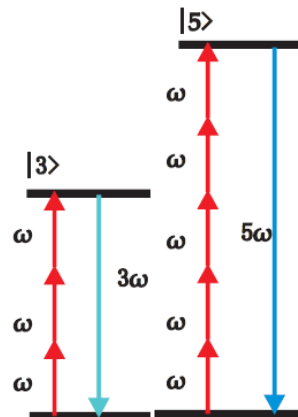


Figure 10.5 Schematic energy diagram depicting the: [Left] Three photon absorption of the fundamental and emission of a third harmonic photon. [Right] Five photon absorption of the fundamental and emission of a fifth harmonic photon.

10.2.2.3 Tunneling ($\gamma < 1$)

In these conditions the potential barrier formed by the core of the atom or molecule and the electric field of the laser becomes small enough for tunneling to become possible. Processes involving individual photons cannot be considered but rather the interaction of the atom with an electric field. Atomic ionization is the simpler process. More complex processes can be described in the concept of the *rescattering model* or *three-step model*. Next we shall examine the processes of higher order harmonics generation (HHG) both in the semi classical approximation as well as in the quantum mechanical approach.

Ionization

A non-perturbative treatment of atomic ionization was reported by Ammosov, Delone and Krainov thereafter known as ADK theory. In their theory, they consider the single-active-electron picture, where only electrons of the outer shells participate in the ionization process. This leads to a simplified ionization picture of an atomic system, where it is characterized only by its ionization potential I_p and an effective quantum number. The theory is effective in atoms, such as rare gasses, whose wave-functions are hydrogenic-like. Although the ADK rate for tunneling ionization can be quite complex, for s-electrons it is

$$W_{ADK} = \left(\frac{3e}{\pi}\right)^{3/2} \frac{Z^2}{n^{*9/2}} \left(\frac{4eZ^3}{E_0 n^{*4}}\right)^{2n^*-3/2} \exp\left(\frac{-2Z^3}{3E_0 n^{*3}}\right) = \frac{A}{\sqrt{I_0}} \exp\left(-\frac{B}{\sqrt{I_0}}\right) \quad (10.40)$$

where Z is the charge of the core and E_0 the amplitude of the laser field and I_0 the peak intensity of the field. n^* is the effective quantum number defined as $n^* = Z/\sqrt{2E_B}$, with E_B the binding energy of the electron. The theory can be applied not only to single ionization but to multiple ionization as well. Typical experimental ionization signals for atoms and molecules described by the ADK model are shown in Fig. 10.6. Note that at the higher intensities the signal scales as $I^{3/2}$ due to laser focusing volume effects.

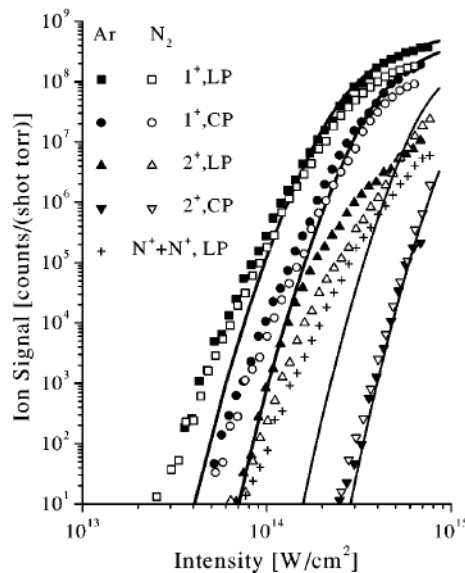


Figure 10.6 Single and double ionization yields for N₂ and Ar using linear (LP) and circular (CP) polarizations. ADK model calculations are depicted by the full curves (Phys. Rev. A 58, (1998) R4271).

The semi classical three-step model

The process is concluded in three steps as graphically depicted in Fig. 10.7:

1. The peak field maximum is considered as the zero time. In the first step the electron is emitted through the tunneling process. The time interval necessary for the emission is called *tunneling time* t_0 .
2. The emitted electron propagates in the field of the laser pulse. The effect of the Coulombic field of the ion is considered negligible. The electron initially is accelerated away from the parent nucleus, decelerated as the field changes its sign, and is accelerated again back towards the parent ion. This time interval is called *travelling time* τ .
3. In the third step the electron is recombined to its ion emitting the gain of energy during its trajectory as harmonic radiation. The sum of the tunneling time and the travelling time is called the *recombination time* t_r , i.e. $t_r = \tau + t_0$.

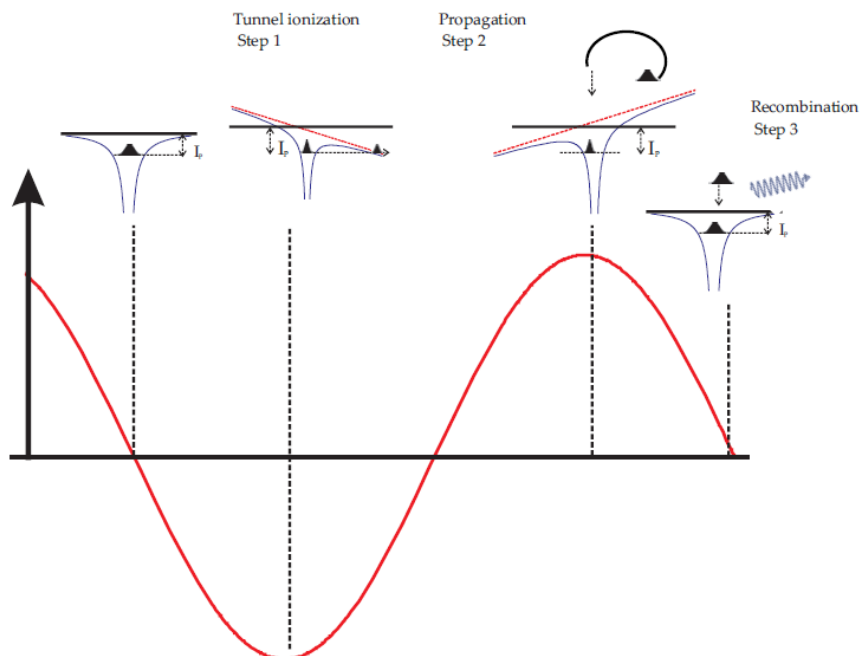


Figure 10.7 Schematic of the dynamics in the three-step model.

In the semi classical three-step model we reach the final results by solving the equation of motion of the electron in the laser field. Thus, assuming a laser pulse of the form of $\mathbf{E} = \hat{x} E_0 \cos(\omega t)$ we have to solve the differential equation

$$m\ddot{x} = e E_0 \cos(\omega t) \quad (10.41)$$

with the initial conditions of $x(t = t_0) = 0$, $v(t = t_0) = 0$. In other words, the electron is emitted at time t_0 with respect to the maximum of the electric field at the position zero with respect to the atom location and with zero velocity. Then the solution for the velocity and the position is

$$v_x = \frac{qE_0}{m\omega} (\sin\omega t - \sin\omega t_0) \quad (10.42)$$

$$x = \frac{qE_0}{m\omega^2} \{(\cos\omega t_0 - \cos\omega t) + (\omega t_0 - \omega t)\sin\omega t_0\} \quad (10.43)$$

In Fig. 10.8 (left) the electron trajectories are plotted for various tunneling times t_0 . The kinetic energy is estimated as $T = \frac{1}{2}mv_x^2$. However, it is of interest to estimate the kinetic energy at the moment of recombination as this energy defines the energy of the harmonic radiation emitted. This can be estimated considering the condition of $x = 0$. The result is shown in Fig. 10.8 (right) where the recombination energy is given as a function of the corresponding times. There it is seen that the electron follows two trajectories: For $\omega t_0 < 0.3$ rad it follows a *long trajectory* while for $\omega t_0 > 0.3$ rad a shorter one the *short trajectory*. The energy of the generated harmonic photon E_{hv} is estimated considering the ionization potential as $E_{h\omega} = T - I_p$. The values are quantized as odd multiples of the fundamental harmonic (due to symmetry considerations), i.e. $E_{h\omega} = T - I_p = q\hbar\omega$, $q = 3, 5, 7, \dots$ justifying the term harmonic generation. The maximum energy corresponds to $\omega t_0 = 0.3 \text{ rad} = 17^\circ$ and has the value of $T_{max} = 3.17U_p + I_p$ where the ionization potential of the atom I_p has been also considered.

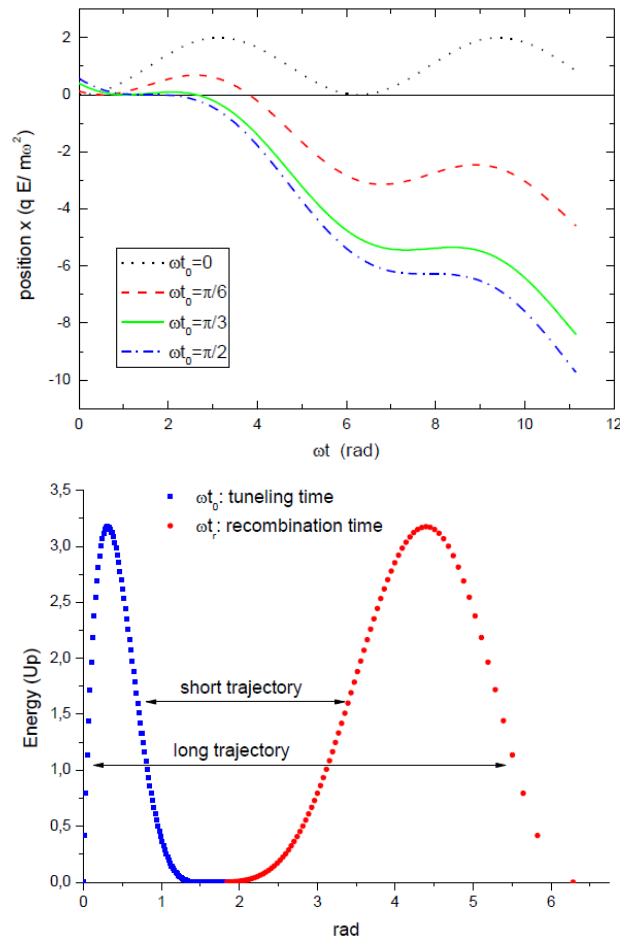


Figure 10.8 [Left] Electron trajectories for various tunneling times t_0 . [Right] The kinetic energy of the emitted electron (in units of ponderomotive energy U_p) as a function of the tunneling and recombination times. The short and long trajectories are depicted.

The quantum mechanical three-step model

The quantum mechanical model is quite complicated and we shall present here only the basics of it as it is instructive to compare the results to the semi classical model. The requirements of the model are similar to the semi classical:

- i. Only the ground state $|0\rangle$ contributes to the process.
- ii. The ground state population depletion is negligible.
- iii. The electron is considered as a free particle in the continuum under the influence of the electric field while the contribution of the Coulombic potential is considered negligible.

Then assuming an electric field linearly polarized in the x direction, $\mathbf{E} = \hat{x} E_0 \cos(\omega t)$, the Schrödinger equation is written as (in the length gauge and atomic units)

$$i \frac{\partial}{\partial t} |\Psi(x, t)\rangle = \left[-\frac{1}{2} \nabla^2 + V(x) - E_0 \cos(t)x \right] |\Psi(x, t)\rangle \quad (10.44)$$

The dipole moment along the x direction, $x(t) = \langle \Psi(t) | x | \Psi(t) \rangle$, is estimated as

$$x(t) = i \int_0^t dt_0 \int d^3\mathbf{p} E \cos(t_0) \mathbf{d}_x(\mathbf{p} - \mathbf{A}(t_0)) \times \mathbf{d}_x^*(\mathbf{p} - \mathbf{A}(t)) \exp[-i S(\mathbf{p}, t, t_0)] + c. c. \quad (10.45)$$

This is the heart of the three-step model. The first term, $E \cos(t_0) \mathbf{d}_x(\mathbf{p} - \mathbf{A}(t_0))$, corresponds to the probability amplitude of an electronic transition to the continuum in time t_0 having a generalized momentum \mathbf{p} . This corresponds to the first step. Then, the electron's wavefunction then propagates until the time t , acquiring a phase factor $\exp[-i S(\mathbf{p}, t, t_0)]$. The quantity S corresponds to the action of the electron along its path.

$$S(\mathbf{p}, t, t_0) = \int_{t_0}^t dt'' \left(\frac{[\mathbf{p} - \mathbf{A}(t'')]^2}{2} + I_p \right) \quad (10.46)$$

The influence of the atomic potential is considered negligible for the time interval between t_0 and t , and therefore the action $S(\mathbf{p}, t, t_0)$ describes the propagation of the free electron in the presence of the laser field with momentum \mathbf{p} . This is the second step. Finally, the electron recombines with the parent ion at the moment t with a probability amplitude $\mathbf{d}_x^*(\mathbf{p} - \mathbf{A}(t))$. This is the third step. The derivatives of the action $S(\mathbf{p}, t, t_0)$ result in the saddle-point equations

$$\nabla_{\mathbf{p}} S(\mathbf{p}, t, \tau) = x(t) - x(t - \tau) = 0 \quad (10.47a)$$

$$\frac{\partial S(\mathbf{p}, t, \tau)}{\partial \tau} = \frac{[\mathbf{p} - \mathbf{A}(t - \tau)]^2}{2} + I_p = 0 \quad (10.47b)$$

$$\frac{\partial S(\mathbf{p}, t, \tau)}{\partial t} = \frac{[\mathbf{p} - \mathbf{A}(t)]^2}{2} - \frac{[\mathbf{p} - \mathbf{A}(t - \tau)]^2}{2} = 2K + 1 \quad (10.47c)$$

where $\mathbf{A}(t) = -E_0 \sin t$, is the vector potential. Eq. 10.47a results in the long and short trajectories of the semi classical model, as only under this condition the integral of Eq. 10.45 does not vanish. The only relevant electron trajectories are those where the electron leaves the nucleus at time $t - \tau$ and returns at time t . The time t corresponds to the recombination time t_r introduced in the semi classical model. Eq. 10.47b has more complicated interpretation. It turns out that it associates the tunneling time (t_0 in the semi classical model) with the imaginary part of the complex time τ . Finally, we may rewrite Eq. 10.47c as

$$\frac{[\mathbf{p} - \mathbf{A}(t)]^2}{2} - I_p = E_{kin}(t) + I_p = 2K + 1 \quad (10.47d)$$

which is actually the energy conservation law. It gives the final kinetic energy of the recombining electron that generates the $(2K + 1)th$ harmonic.

A comparison between the classical and the quantum mechanical result for the harmonic energies and the involved times is presented in Fig. 10.9. The agreement is noteworthy, justifying the popularity of the semi classical rescattering model.

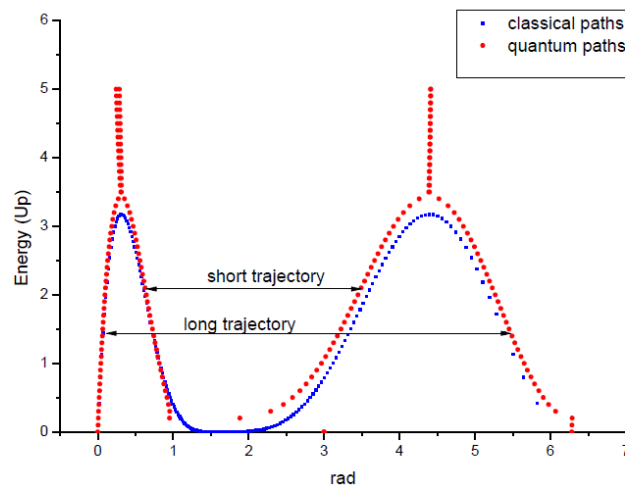


Figure 10.9 Same as in Fig. 10.8 but comparing the semiclassical calculations (blue dots) and the quantum mechanical (red dots).

HHG spectrum

The HHG spectrum consists of three regions as depicted in Fig. 10.10 (up). In low harmonics the spectrum is generated by the multiphoton processes showing a rapid decrease of the harmonic yield at higher harmonics. Then at the tunneling conditions the harmonic spectrum shows a plateau where all the harmonics are generated at a constant yield. Then for the highest harmonics energetically allowed there is a rapid decrease of the yield known as the cut-off. In Fig. 10.10 (bottom) these characteristics are seen also in experimental data.

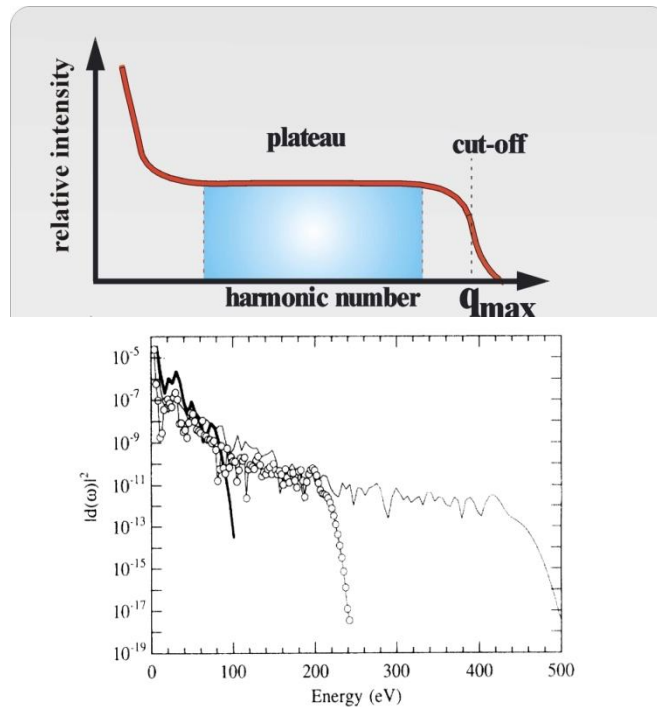


Figure 10.10 [up] Typical HHG spectra. [bottom] Experimental HHG spectra (Phys. Rev. Lett. 68, (1992) 3535).

Attosecond pulses

Perhaps the most important application of the HHG is the formation of attosecond pulses (1 asec = 10⁻¹⁸ sec). Attosecond pulses take advantage of the coherence of the generated harmonics. Adding coherently the amplitudes of a number of the generated harmonics results in pulses with durations close to the Fourier Transform Limited (FTL) value that corresponds to attosecond durations. The mathematical description is simply

$$I = \left| \sum_q A_q \sin(q\omega t + q\omega t_r) \right|^2 \quad (10.48)$$

where q is the number of harmonics in use, A_q the amplitude of the q th harmonic and t_r the recombination time. An artificial example of the formation of attosecond pulses known as pulse train is given in Fig. 10.11. Attosecond pulses is currently the fastest camera that can record the electron dynamics in atoms, molecules and solid state materials.

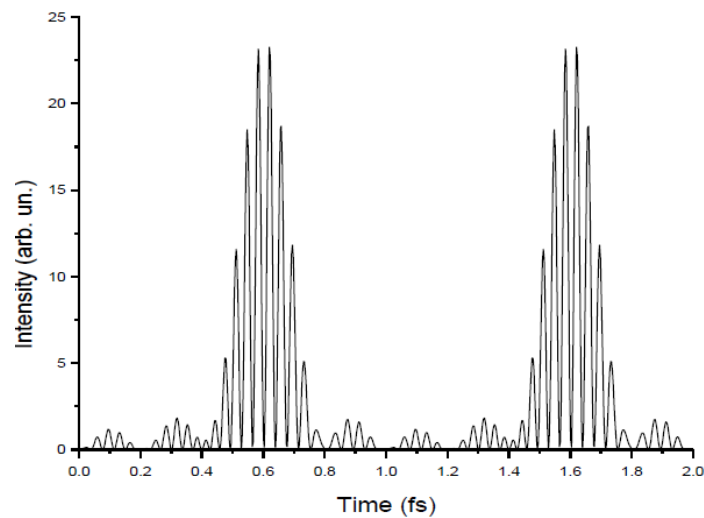


Figure 10.11 Formation of an attosecond pulse train by superimposing harmonics of the orders 23-31 for a laser pulse with wavelength $\lambda=800$ nm and period $T=2.6$ fs.

ATI spectrum

The generation of ATI electrons in the tunneling regime is described by the same quantum mechanical rescattering model as the HHG. It shares similar features with HHG as for example the plateau in the tunneling region. A typical experimental spectrum is shown in Fig. 10.12 where these characteristics are seen.

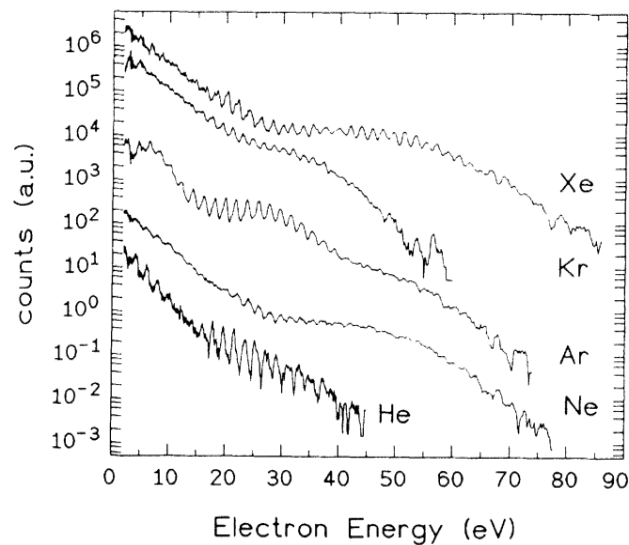


Figure 10.12 ATI spectra for various atomic gases (Phys. Rev. Lett. 72, (1994) 2851)

10.2.2.4 Over the barrier ($\gamma \ll 1$)

When the laser intensity exceeds the values for the tunneling processes the third ionization scenario appears. In this case the laser field severely distorts the potential barrier as illustrated in Fig.10.3c. The outer electron is no longer bound and it can classically overcome the barrier. This case is known as over the barrier ionization (OTBI). The threshold intensity above which OTBI occurs is described by

$$I_{OTBI} = \frac{c\varepsilon_0\pi^2 I_p^4}{2Z^2 e^6} = 4 \times 10^9 I_p^4 (eV) Z^2 (W cm^{-2}) \quad (10.49)$$

10.2.3 Molecular dissociation

The molecular behavior in strong fields can be quite complicated. For this reason we shall restrict this chapter to the study to diatomic molecules. Multiphoton or tunneling ionization are similar to the atomic cases and will not be repeated. Instead, the fundamental dissociation processes in the tunneling regime will be examined. A benchmark molecule for this is the hydrogen molecular ion H_2^+ . When H_2^+ interacts with a low-frequency field, the $1s\sigma_g$ ground state couples strongly to the repulsive $2p\sigma_u$ state but weakly to all other states. Therefore, the molecule can be in principle treated as a two-level system as shown in Fig. 10.13 (left).

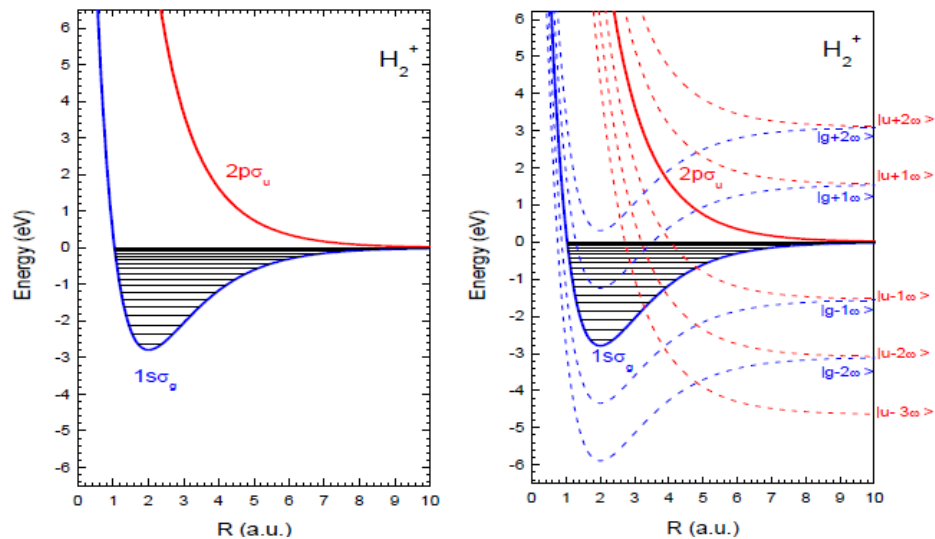


Figure 10.13 [Left] Energy level diagram of H_2^+ . The black lines are the vibrational levels. [Right] The H_2^+ dressed in the laser field photon states.

The Floquet picture

The detailed quantum mechanical description of the dynamics of the H_2^+ molecule in strong laser fields requires solving the time-dependent Schrödinger equation utilizing numerical techniques. If the laser period is considerably shorter than the nuclear motion, a typical condition for lasers, then the dissociating wavepacket hardly changes position on that timescale, one may refer to another model, that of the *field-dressed states* or as popularly known as the *Floquet picture*.

A laser pulse can be described as a coherent superposition of a large number of photon-number states, $|n\rangle$ centered on a large photon number N (of the order of 10^{10}). Thus, the photon states $n = N, N \pm 1, N \pm 2, \dots$ are occupied. Dressed states are products of molecular

states and photon-number states. When the $1s\sigma_g$ state of the H_2^+ molecule is dressed with the photon states, one will thus obtain a large series of parallel potential curves, $|g, n\rangle$, that are separated by the photon energy. The same is true for $2p\sigma_u$ that leads to $|g, n\rangle$ dressed states. The situation is shown in Fig. 10.13 (right). It is seen that when the excited molecular state is dressed with less photons than the molecular ground state, the two dressed states cross each other. For example the $|g, N\rangle$ and the $|g, N - 1\rangle$ states differ in energy by exactly the photon energy at the position where the two states cross each other. A transition between the two states is exactly resonant at this point.

These curves are the so-called diabatic curves. They do not include the coupling between the states. The coupling is proportional to the laser-field strength and the dipole matrix element between the two molecular states. Including the coupling between the states results in the adiabatic energies illustrated by the avoided crossing at the area of the diabatic crossings as shown in Fig. 10.14 (right). The size of the gap at the avoided crossings depends sensitively on the laser intensity and the order of the crossing. It appears that for H_2^+ in intense laser fields at wavelengths in the ultraviolet to near-infrared regime, only the one-photon and three-photon crossings play a role. Since for each photon the parity of the molecular state must change, there are no two-photon crossings.

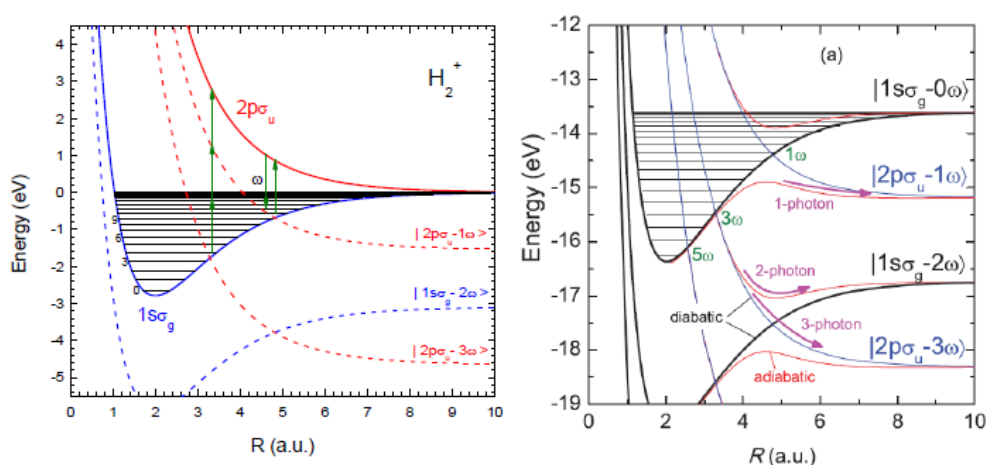


Figure 10.14 [Left] The H_2^+ dressed in the laser field photon states showing the one- and three-photon transitions at the crossings. [Right] Equivalent picture showing the diabatic curves and the adiabatic avoided crossings (Phys. Rev. A 85, (2012) 023405).

Bond softening

For small field intensities (or at the falling edge of the pulse) the vibrational states of the $1s\sigma_g$ ground state above the diabatic crossing point will be unstable allowing for the excitation to the $2p\sigma_u$ anti-bonding state. However, as the pulse intensity increases the gap in the avoided crossing (adiabatic picture) increases allowing for lower vibrational states to contribute to the excitation to the $2p\sigma_u$ state. Thus, the molecular dissociation, $H_2^+ \rightarrow H^+ + H$, proceeds via a one-photon process by the vibrational states in the neighborhood of the crossing point. The



one-photon dissociation process is known as *bond-softening* (BS). It should be pointed out that even though the process is termed as one-photon, it is not a weak field process. The molecule interacts with the strong field exchanging numerous of photons with the field of the pulse but at the end the outcome is that the molecule dissociates using the energy of only one photon. The two pictures shown in Fig. 10.14 are considered energetically equivalent.

Above threshold dissociation

The process of *above threshold dissociation* (ATD) is similar to BS. It involves the crossing of the three-photon crossing of the $|2p\sigma_u - 3\omega\rangle$ and $|1s\sigma_g\rangle$ (see Fig. 10.14). It needs stronger fields than the BS process in order to absorb three photons at the crossing point and get excited to the $|2p\sigma_u\rangle$ anti-bonding state. However, as the molecule nuclei are moving apart the system goes by the strong coupling of the one-photon crossing and emits one photon. Finally, the ATD process is termed a two-photon process due to energy considerations.

Charge resonance enhanced ionization

It is instructive to see this process in a hydrogen molecule rather than in a molecular ion. The process of charge resonance enhanced ionization (CREI) leads to double ionization of the diatomic molecule but not in a typical multiphoton absorption. It occurs in three steps as shown in Fig. 10.15. Initially during the rise of the laser pulse, the first electron is ejected nearly instantaneously via tunneling. Next, the process of dissociation is launched via the strong coupling between the $|1s\sigma_g\rangle$ and $|2p\sigma_u\rangle$, much similar to the ATD process. As the dissociation process evolves reaching a critical nuclear distance R_c , the molecular ionization rate exceeds the atomic rate by several order of magnitudes. This is due to the localization of the electron to one of the nuclei. The enhanced ionization occurs from the higher, σ^+ up-hill, quasi-static electronic energy state from which the force from the laser electric field and the force from neighboring nuclei add up leading to a much lower barrier to overcome or even to overbarrier ionization.

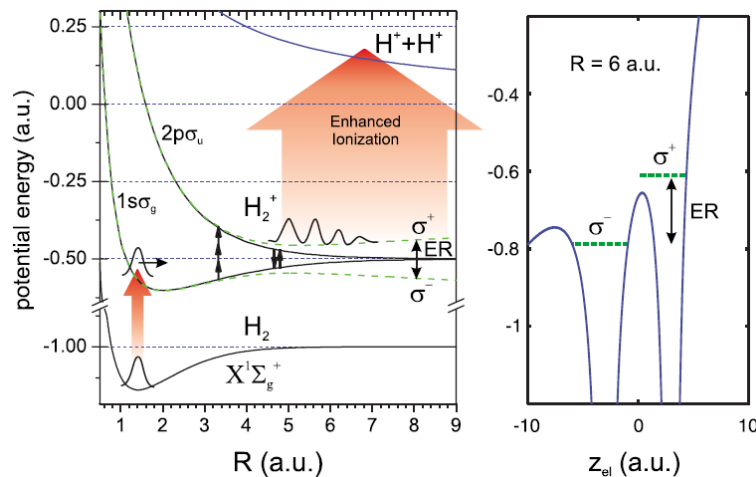


Figure 10.15 Energy diagram for the process sequence leading to CREI (Phys. Rev. A 76, (2007) 013405).

Rescattering

The rescattering process (RES), as described earlier, can be considered also for the double ionization of diatomic molecules. As mentioned in CREI the first step is the ejection of the first electron via tunneling. However, the electron will recollide with the parent molecular ion, according to the dynamics described earlier, and may cause a direct emission of the second electron in an electron collision type of interaction.

A typical time-of-flight (TOF) spectrum showing the ionization and dissociation processes of the D_2 molecule is shown in Fig.10.16. The processes of BS, ATD, CREI and RES are seen as double peaks in the TOF spectrum. The larger the TOF distance the higher the dissociation energy known as kinetic energy release (KER). RES is a quite broad peak not visible in the TOF spectra. It can be only recorded in coincidence measurements.

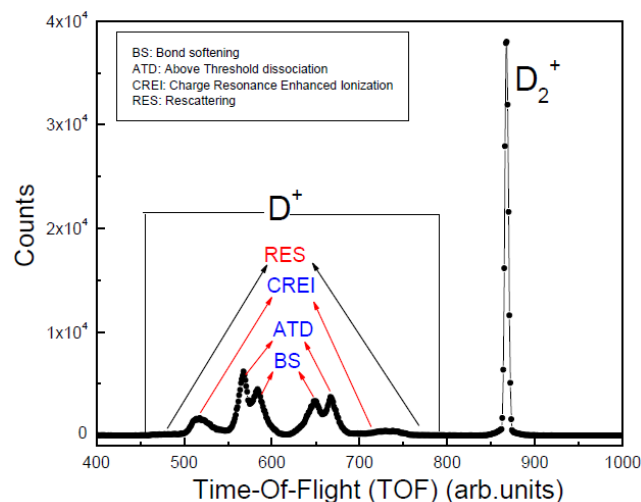


Figure 10.16 Time-of-flight spectrum of the ionization and dissociation of the D_2 molecule in intense laser fields ($\sim 10^{14}$ W/cm²). The processes of BS, ATD, CREI and RES are depicted.

in order to explicitly include the wavefunction dependence on the wave vector k . The general solution can be written in an integral form known as the *Lippmann-Schwinger equation*

$$\psi_k(\mathbf{r}) = \Phi_k(\mathbf{r}) + \int G_0(k, \mathbf{r}, \mathbf{r}') U(\mathbf{r}') \psi_k(\mathbf{r}') d\mathbf{r}' \quad (10.76)$$

where $\Phi_k(\mathbf{r})$ is the solution for the homogeneous equation

$$(\nabla^2 + k^2)\Phi_k(\mathbf{r}) = 0 \quad (10.77)$$

that is the known plane wave $e^{i\mathbf{k}\mathbf{r}}$, and $G_0(k, \mathbf{r}, \mathbf{r}')$ is the *Green's function* satisfying the equation

$$(\nabla^2 + k^2)G_0(k, \mathbf{r}, \mathbf{r}') = \delta(\mathbf{r} - \mathbf{r}') \quad (10.78)$$

Requiring that the wavefunction $\psi_k(\mathbf{r})$ describes outgoing scattering waves, the Green's function can be obtained as

$$G_0(k, \mathbf{r}, \mathbf{r}') = -\frac{1}{4\pi} \frac{e^{ik|\mathbf{r}-\mathbf{r}'|}}{|\mathbf{r}-\mathbf{r}'|} \quad (10.79)$$

which indeed describes outgoing waves generated at the point \mathbf{r}' and approximating spherical waves of the form of Eq. 10.65 for large $|\mathbf{r}|$, i.e. for $|\mathbf{r}| \gg |\mathbf{r}'|$, as depicted in Fig. 10.18

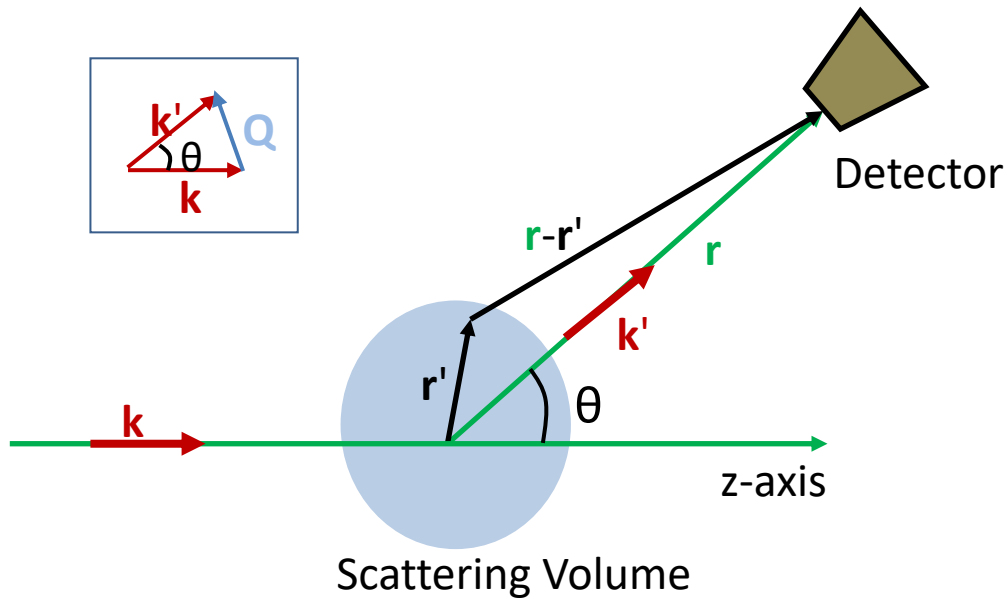


Figure 10.18 Scattering geometry corresponding to the outgoing waves described by the Green's function of Eq. 10.79.

Then the final form of the integral equation 10.76 is written as

$$\psi_k(\mathbf{r}) = e^{i\mathbf{k}\mathbf{r}} - \frac{1}{4\pi} \int \frac{e^{ik|\mathbf{r}-\mathbf{r}'|}}{|\mathbf{r}-\mathbf{r}'|} U(\mathbf{r}') \psi_k(\mathbf{r}') d\mathbf{r}' \quad (10.80)$$

which in the asymptotic form of $|r| \rightarrow \infty$ (after approximating $\frac{e^{ik|r-r'|}}{|r-r'|} \rightarrow \frac{e^{ikr}}{r} e^{-ik'r'}$, where $\mathbf{k}' = k\hat{r}$) is reduced to

$$\psi_{\mathbf{k}}(\mathbf{r}) = e^{ikr} - \frac{1}{4\pi} \frac{e^{ikr}}{r} \int e^{-ik'r'} U(\mathbf{r}') \psi_{\mathbf{k}}(\mathbf{r}') d\mathbf{r}' \quad (10.81)$$

Thus, by comparing Eqs 10.81 and 10.66 we obtain the scattering amplitude as

$$f(\theta, \varphi) = -\frac{1}{4\pi} \int e^{-ik'r'} U(\mathbf{r}') \psi_{\mathbf{k}}(\mathbf{r}') d\mathbf{r}' \quad (10.82)$$

However, the solution is still not reached since the wavefunction $\psi_{\mathbf{k}}(\mathbf{r})$ is unknown. Its solution can be obtained in a series of iterations for the integral Eq. 10.76. Indeed, starting from an incident plane wave as the zeroth order approximation then the next iterations are structured as follows

$$\psi_{\mathbf{k}}^{(0)}(\mathbf{r}) = e^{ikr} \quad (10.83a)$$

$$\psi_{\mathbf{k}}^{(1)}(\mathbf{r}) = e^{ikr} - \frac{1}{4\pi} \frac{e^{ikr}}{r} \int e^{-ik'r'} U(\mathbf{r}') \psi_{\mathbf{k}}^{(0)}(\mathbf{r}') d\mathbf{r}' \quad (10.83b)$$

$$\psi_{\mathbf{k}}^{(2)}(\mathbf{r}) = e^{ikr} - \frac{1}{4\pi} \frac{e^{ikr}}{r} \int e^{-ik'r'} U(\mathbf{r}') \psi_{\mathbf{k}}^{(1)}(\mathbf{r}') d\mathbf{r}' \quad (10.83c)$$

$$\psi_{\mathbf{k}}^{(n)}(\mathbf{r}) = e^{ikr} - \frac{1}{4\pi} \frac{e^{ikr}}{r} \int e^{-ik'r'} U(\mathbf{r}') \psi_{\mathbf{k}}^{(n-1)}(\mathbf{r}') d\mathbf{r}' \quad (10.83d)$$

This approach is actually a perturbation expansion in powers of the interaction potential $U(\mathbf{r})$ known as the *Born expansion* or *Born series*. The first order term $\psi_{\mathbf{k}}^{(1)}(\mathbf{r})$ is the *first Born approximation* or simply *Born approximation*, resulting for the scattering amplitude in

$$f^{(1)}(\theta, \varphi) \equiv f_{B1} = -\frac{1}{4\pi} \int e^{-i(\mathbf{k}-\mathbf{k}')r'} U(\mathbf{r}') d\mathbf{r}' \quad (10.84)$$

It is interesting to note that the quantity $\mathbf{k} - \mathbf{k}' = \mathbf{Q}$ is the momentum transfer as depicted in Fig. 10.18 and that the scattering amplitude is the Fourier transform of the potential.

The physical meaning behind the Born series is that each term corresponds to a scattering process inside the scattering volume. The zeroth order corresponds to no scattering, the first order to a single scattering process, and the second order to a double scattering process and so on and so forth. Usually higher orders than the first require arithmetical approaches and even though the convergence is not guaranteed depending on the potential and the collision energy. Thus, only the first Born approximation is taken into account which gives good results for high collision energies and weak potentials as expected.



10.2.4 Electron-atom collisions

In this last subsection, we will describe the approach on a realistic problem that of an electron beam colliding with an atom. We shall examine the elastic scattering from a hydrogen atom for simplicity. Let us call electron 1 the electron of the beam and electron 2 the electron of the atom in its ground state. Then the asymptotic wavefunction for $|\mathbf{r}_1| \gg |\mathbf{r}_2|$ of the system is written as

$$\psi_{\pm}(\mathbf{r}_1, \mathbf{r}_2) \sim F_1^{\pm}(\mathbf{r}_1)\psi_{100}(\mathbf{r}_2) \quad (10.85)$$

where \pm corresponds to the singlet (+) and triplet (-) spin states of the two electron system. The function $F_1^{\pm}(\mathbf{r}_1)$ is the known scattering wavefunction of Eq. 10.66

$$F_1^{\pm}(\mathbf{r}_1) = e^{ik_1z} + f_1^{\pm}(k_1, \theta, \varphi) \frac{e^{ik_1r_1}}{r_1} \quad (10.86)$$

Due to the symmetry of the wavefunction it can also be written as (interchanging \mathbf{r}_1 and \mathbf{r}_2 should not affect the wavefunction)

$$\psi_{\pm}(\mathbf{r}_1, \mathbf{r}_2) \sim F_1^{\pm}(\mathbf{r}_2)\psi_{100}(\mathbf{r}_1) \quad (10.87)$$

Therefore a correctly antisymmetrized wavefunction for the problem of the electron elastic scattering from the ground state of the atomic hydrogen can be written as

$$\psi_{\pm}(\mathbf{r}_1, \mathbf{r}_2) = [F_1^{\pm}(\mathbf{r}_1)\psi_{100}(\mathbf{r}_2) + F_1^{\pm}(\mathbf{r}_2)\psi_{100}(\mathbf{r}_1)] \quad (10.88)$$

This is known as the *static exchange method*. In case where the collision energy is high enough to excite or even ionize the hydrogen atom then all the open channels should be included in an appropriately antisymmetrized wavefunction which would be then written as

$$\psi_{\pm}(\mathbf{r}_1, \mathbf{r}_2) = \sum_{q=1}^N [F_q^{\pm}(\mathbf{r}_1)\psi_q(\mathbf{r}_2) + F_q^{\pm}(\mathbf{r}_2)\psi_q(\mathbf{r}_1)] \quad (10.89)$$

where N is the number of states allowed by the collision conditions. This is also known as the *close coupling approximation*. It is instructive to realize that these wavefunction are actually approximations of the "real" wavefunction and not the only solutions to the problem.

10.3 Bibliography

The following bibliography is only indicative containing books, chapters and review articles. The reader is referred to the references within for further reading.

1. B. H. Bransden, C.J. Joachain

Physics of Atoms and Molecules



- Longman Group Limited, 1983. ISBN 0-582-44401-2
2. M. Scully and S. Zubairy
Quantum Optics
Cambridge University press, 2008. ISBN 0521434580
 3. J. H. Posthumus
The dynamics of small molecules in intense laser fields
Rep. Prog. Phys. 67 (2004) 623–665
 4. F. Krausz and M. Ivanov
Attosecond Physics
Rev. Mod. Phys. 81 (2009) 163-234
 5. S. Blüegel
Scattering Theory: The Born Series
Lecture Notes of the 43rd IFF Spring School, 2012. ISBN 978-3-89336-759-7
 6. A. Müller
Electron-Ion Collisions: Fundamental Processes in the Focus of Applied Research
Advances in Atomic, Molecular and Optical Physics, Vol. 55, (2008) 293-417, Elsevier Inc.
 7. N. Stolterfoht, R. D. DuBois, R.D. Rivaola
Electron Emission in Heavy Ion-Atom Collisions
Springer-Verlag Berlin Heidelberg 1997, ISBN 978-3-642-08322-8
 8. R. K. Janev
Atomic and Molecular Processes in Fusion Edge Plasmas
Springer Science+Business Media, LLC, 1995. ISBN 978-1-4757-9321-5
 9. Y. Itikawa
Molecular Processes in Plasmas. Collisions of Charged Particles with Molecules
Springer, 2007. ISBN 978-3-540-72609-8
 10. G.B. Rybicki, A.P. Lightman
Radiative Processes in Astrophysics
WILEY-VCH Verlag GmbH & Co. KGaA, 2004. ISBN-13: 978-0-471-82759-7.



HELLENIC
MEDITERRANEAN
UNIVERSITY



universit 
BORDEAUX



Erasmus+

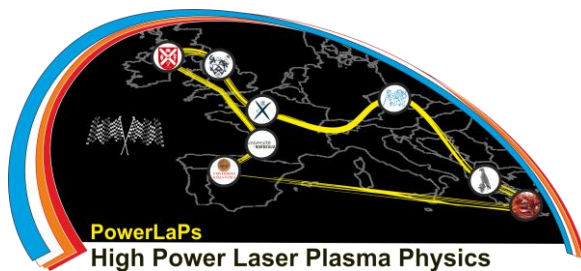
PowerLaPs

Innovative Education & Training in High Power Laser Plasmas

High Power Laser Matter Interactions/High Energy Density Physics - Theory and Experiments

Chapter 11: Inertial Confinement Fusion implosion hydrodynamics and indirect drive

J. Pasley





11. Inertial Confinement Fusion implosion hydrodynamics and indirect drive

The subject of inertial confinement fusion centres around the achievement of ignition and propagating burn in a fuel mass that has been imploded by some form of driver. Whether this driver is a laser, a hohlraum radiating soft x-rays, or a charged particle beam, this theme of implosion followed by ignition and propagating burn is a common one. In this chapter we shall consider some of the requirements placed upon the implosion and show that in order to achieve the required high densities in the imploded fuel it is necessary to employ a series of shock waves to accelerate the shell. We shall also briefly consider the role of the hohlraum in the indirect drive approach to ICF.

11.1 Implosion

The goals of the implosion in ICF include, at least, compression of the bulk of the fuel to a high density. In the conventional central hotspot ignited approach to ICF, another aim of the implosion is to form a central hotspot, which satisfies the ignition ρr criterion. The implosion is a complex process, which we must simplify substantially in order to bring some degree of sense to it.

During the implosion, the outermost regions of the capsule are ablated by the driver. The rest of the material is accelerated inward. This is often termed rocket-like acceleration, and indeed this is a fair analogy. However, the student should be careful not to extend the analogy of a space rocket too far! For instance, there is a significant delay between the commencement of the ablation of the exterior of the capsule, and the time at which the inner surface of the capsule begins to implode, due to the time taken for the shock waves that are accelerating the material to pass through the thickness of the shell.

The bulk of the compression in an ICF implosion actually occurs at late times, as the fuel stagnates against itself in the centre. While the shock waves which are driven through the capsule do indeed result in significant compression, the key criteria for an implosion are the final implosion velocity and the adiabat of the fuel [1, 2]. The first parameter determines how much energy there is available during stagnation for driving the compression. The second parameter determines the degree to which the fuel will resist compression; essentially it is a measure of how much the fuel has been heated during the implosion. Hot fuel is harder to compress. Therefore, all efforts must be made to limit the heating of the fuel during the implosion, be this through excessive shock heating (which we shall discuss shortly) or other forms of preheat (radiative/hot particle). So, one could paraphrase and suggest that the ICF



capsule designer must go to great lengths to ensure that the fuel remains cold. The question that we must address first then is that of “how cold is cold?”

Cold fuel and Fermi-degeneracy

It turns out that the answer to our question of “how cold is cold?” lies in an area of physics that one might not necessarily expect to have great relevance to ICF. Electrons are fermions, and fermions cannot occupy the same state as one another. They must remain degenerate, or in different states. Fermi statistics dictate that if a large number of electrons occupy a given volume, then many of them must be in higher energy states in order to remain degenerate [3]. If the volume of the gas is reduced, and the number of electrons remains the same, then the electrons will be forced to ever higher energies. What this implies is that compressing an electron gas inevitably requires at least the energy required to force the electrons into the higher energy states dictated by Fermi statistics. There is no way around this. The mean energy of electrons in such a system is given by:

$$E_{Favg} = \frac{3}{5} E_{Fermi} \quad (11.1)$$

where,

$$E_{Fermi} = 3.65 \times 10^{-15} n^{2/3} \text{ eV} \quad (11.2)$$

One can also associate a pressure and a temperature with the degenerate electron gas:

$$P_{Fermi} = \frac{2}{5} n E_{Fermi} = 2.34 \times 10^{-39} n^{5/3} \text{ Mbar} \quad (11.3)$$

and,

$$T_{Fermi} = E_{Fermi} / k \quad (11.4)$$

And this presents us with an answer to our question: if the temperature of the dense fuel in an ICF capsule is kept well below this Fermi temperature, then it can be compressed without significant extra work being required than that which is unavoidable. Putting numbers into equation 4 we can also see that, for example, the Fermi temperature of deuterium at 1000 gcm^{-3} is around 18.5 Million Kelvin. The answer to our question “how cold is cold?” is therefore “very hot!”

Implosion velocity

It is actually quite straightforward to obtain a simple estimate of the required implosion velocity for an ICF capsule, by equating the kinetic energy of the imploding shell to the required total Fermi energy (the average Fermi energy of an electron in the imploded state, multiplied by the



total number of electrons in the dense fuel core). Doing this for fuel at around 1000 gcm^{-3} leads to an estimate of the implosion velocity of around $2.7 \times 10^7 \text{ cm/s}$. As would be expected, this is an underestimate. Typical implosion velocities for central hotspot ignition are close to $4 \times 10^7 \text{ cm/s}$, however much of the energy in that scheme is required to heat the hotspot.

While not the topic of this chapter, the reader is probably aware that hydrodynamic instabilities, in particular the Rayleigh-Taylor instability [4], make it unfeasible to implode a capsule whose initial thickness is an extremely small fraction of its initial radius. This limits the distance over which the fuel can be accelerated, and therefore means that the acceleration must be quite violent in order that the fuel reaches the required final implosion velocity. This in turn suggests that the pressure required to accelerate the fuel must be very large. An alternative way to look at this would be to say that if we set the PV work done on the capsule equal to the required total Fermi Energy of the fuel, then the pressure required to accelerate the fuel will be large: around 20 Mbar. However, as will be shown in the following sections, applying such a large pressure suddenly will result in the fuel being heated dramatically, preventing efficient compression to high density.

Shock waves

A shock wave [5] is a discontinuity in the gas dynamic variables which propagates through the fluid at a velocity that is greater than the speed of sound ahead of the wave, and less than the speed of sound behind the wave. Such waves form inevitably from pressure disturbances in fluids, except in the case where the disturbances are very weak (such weak disturbances are known as sound waves). If we imagine the situation of a sinusoidal pressure disturbance propagating in a fluid, the cause of the formation of such waves can be seen by examining how the sound speed in the wave varies with position. Regions of the wave that are at a higher pressure have associated with them a higher local sound speed than regions that are at a lower pressure. This results in progressive steepening of the wave front, and finally the formation of a sudden jump in the pressure from peak to trough. This sudden discontinuous jump in pressure is known as a shock wave. It can be shown that the density and temperature follow a similar trend, passing from the low to the high pressure portions of the wave. The degree to which the shock wave front is actually discontinuous is dependent upon the dominant mode of energy transport across the wave front. At low temperatures viscosity and thermal conduction dominate the energy transport, and therefore the shock front thickness is governed by relevant electron mean free paths. At low temperatures, in high density fluids, these mean free paths are on the order of nanometers, and therefore the jump does, from a macroscopic standpoint, indeed appear to be discontinuous. At very high temperatures, however, radiation can play a dominant role, and therefore the shock front thickness can be

better approximated by the much longer mean free paths of the relevant photon populations that are conveying the energy from the hot to the cold region of the fluid. In this latter case the discontinuous nature of the shock front transition tends to disappear [5].

Hugoniot curves [5] represent the locus of all possible final states (pressure P_1 , and specific volume V_1) that may be produced by the passage of a single shock wave, from some initial state (P_0, V_0):

$$V_1 = \left[\frac{P_0 V_0 (\gamma - 1) + P_1 V_0 (\gamma + 1)}{P_0 (\gamma - 1) + P_1 (\gamma + 1)} \right] \quad (11.5)$$

where γ is the adiabatic exponent of the fluid, such that $P_1 V_1^\gamma = P_0 V_0^\gamma$. If P is plotted against V then, from some initial state, the Hugoniot curve lies above the isentropic compression curve, but diverges significantly from it only if the ratio of P_1 to P_0 is large. It is also simple to show from equation 1.5 that the limiting compression produced by a single shock wave is given by the ratio $(\gamma+1)/(\gamma-1)$ by suggesting that the initial pressure is negligible.

Some insight can be gained by considering the relationships between initial and final temperatures and entropies generated by the passage of a single shock wave:

$$\frac{T_1}{T_0} = \frac{P_1 V_1}{P_0 V_0} \quad (11.6)$$

$$S_1 - S_0 = c_V \ln \frac{P_1 V_1^\gamma}{P_0 V_0^\gamma} \quad (11.7)$$

These two relationships suggest that the parameter that is critical in determining the degree of any heating which takes place due to the passage of a shock wave is the ratio of post- to pre-shock pressure, P_1/P_0 and not the absolute magnitude of the final pressure. This is critical since it suggests that we might reduce the amount of heating required to achieve a given final pressure by using a series of shock waves; each shock wave limiting the ratio of P_x to P_{x-1} , however the final pressure after many shocks being allowed to reach a high value. Since, in ICF, we need to apply very large pressures to our fuel, without heating it excessively, this suggests that we must resort to the use of multiple shock waves.

Use of Hugoniot curves in ICF target design

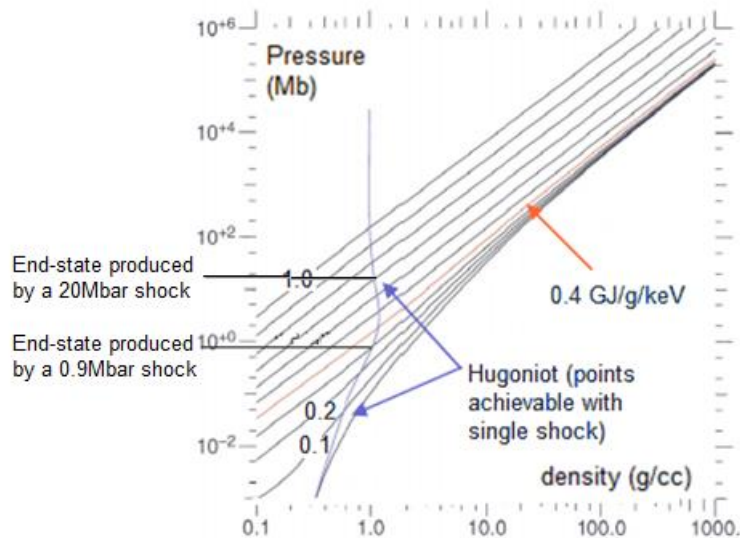


Figure 11.1 A set of isentropes for DT are plotted (black lines), with the Hugoniot curve for a single shock from DT-ice at normal solid densities (purple line) overlaid. The extent to which it is acceptable to raise the fuel pressure by the passage of a single shock going into DT-ice is limited. At high densities the cold, quasi-Fermi-degenerate curve lies very close to isentropes with a specific entropy of less than 0.4GJ/g/keV. Therefore, since entropy cannot be lost from the fuel during the implosion, we must aim to maintain the dense imploding fuel below this isentropes (red line) throughout the implosion.

Figure 11.1 illustrates the difficulty in accelerating the fuel by application of a sudden pressure jump from zero to tens of Megabars, as might be suggested by our simple previous calculation. Looking at the isentropes for DT fuel, it can be seen that at very high densities isentropes with a specific entropy of less than 0.4GJ/g/keV lie very close to the cold quasi-Fermi-degenerate curve (represented by a specific entropy of 0.0 in figure 11.1). Therefore, since it is not possible to lose entropy from the fuel during the course of the implosion, it is necessary to maintain the dense fuel below this value of specific entropy during the course of the implosion. By considering the hugoniot curve from cold-DT ice (plotted as a purple line in figure 11.1), it can be seen that a single shock of strength ~ 20 Mbar, leaves the fuel with a very much higher specific entropy than this (approximately 0.7GJ/g/keV). This implies that substantially more work than necessary will need to be performed upon the fuel in order to compress it to the desired density (thereby invalidating the simple calculation performed previously and encouraging us to go to even higher pressures- which would exacerbate the problem further). By consideration of figure 11.1, it can be seen that an acceptable strength for the first shock wave going into the fuel might be around 0.9Mbar. This is approximately the strength of the first shock employed at the National Ignition Facility [1]. Figure 11.2 illustrates how this

principle is extended to the second shock wave. A new hugoniot curve is plotted from the fuel conditions created by the passage of the first 0.9Mbar shock wave.

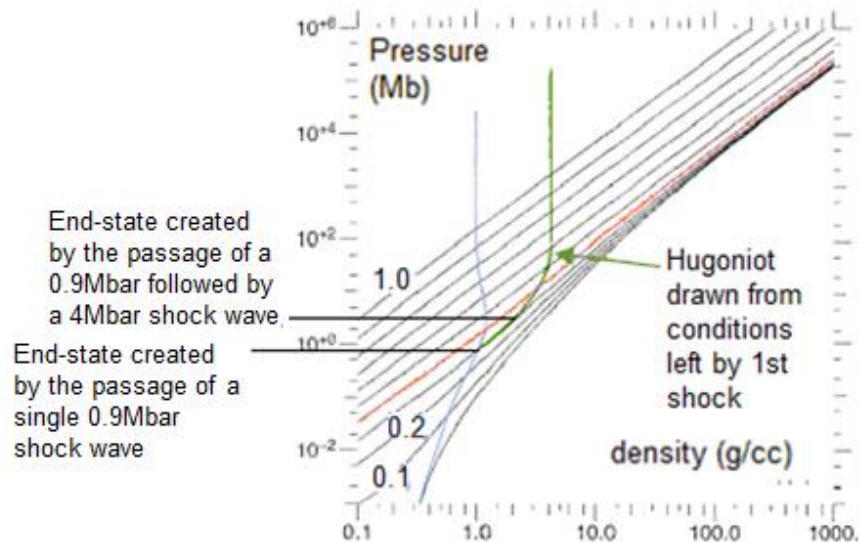


Figure 11.2 This figure builds upon the information contained in figure 12.1, showing the hugoniot curve for a 2nd shock wave starting from the conditions created by the passage of a 0.9Mbar shock wave into cold DT-ice. It can be seen that this second shock can have a strength of approximately 4Mbar without raising the entropy of the fuel above the critical 0.4GJ/g/keV level.

It is found that the shock pressure may be increased by approximately a factor of four by each successive shock wave, without raising the fuel entropy significantly above the level “set” by the first shock wave. NIF uses a series of four shock waves [1], to raise the pressure to the levels required to achieve a satisfactory implosion velocity. In reality, for central hotspot ignition, this implosion velocity is on the order of 4×10^7 cm/s. In central hotspot ignition, the velocity is required to be significantly higher than in the case of fast ignition, since the stagnation of the shell is required to heat the central hotspot, in addition to compressing the dense fuel. Figure 11.3, taken from reference 1 shows the complete trajectory of the dense fuel and hotspot in a NIF-like central hotspot ignited target.

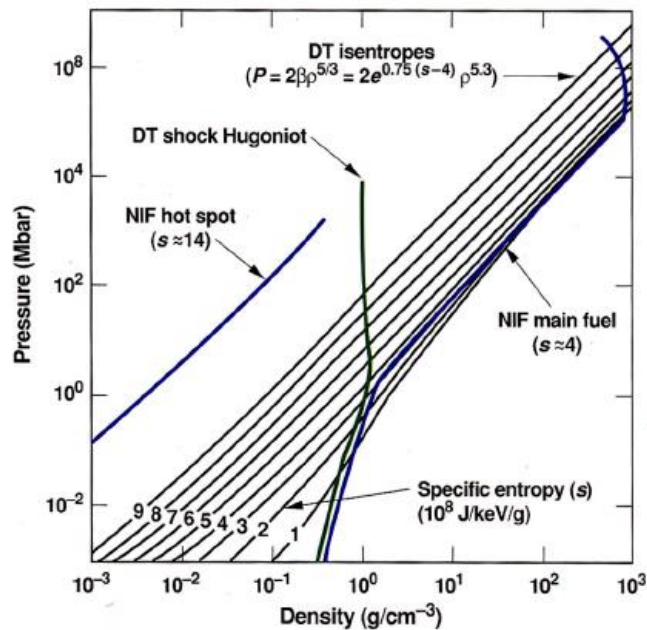


Figure 11.3 Shows the trajectories of the dense fuel and central hot-spot in a NIF-like implosion, taken from reference 1. Notice that the entropy units are in 10^8 J/keV/g unlike in the previous two figures.

11.2 Indirect-drive ICF

In the indirect-drive approach to inertial confinement fusion, the fuel capsule surface is heated by soft x-rays. These soft x-rays emanate from a so-called hohlraum in which the capsule is located centrally. The key advantage to this approach is that it enables a driver that cannot be readily applied with a high degree of uniformity to a spherical surface to be used in driving the implosion of the fuel capsule. The energy from the driver is firstly captured by the hohlraum, which heats up, and the thermal emission from this hohlraum drives the capsule. By having a hohlraum that is large relative to the fuel capsule, the radiation falling on the capsule may become quite uniform, even if the deposition of energy at the hohlraum wall is relatively non-uniform. This is for two reasons. Firstly, the thermal emission from the hot plasma at the inner surface of the hohlraum is isotropic. This results in the non-uniformity in the radiation field leaving the wall being smoothed out by the time it reaches the capsule surface. A similar effect may be observed in most lecture theatres. In a lecture theatre there are usually multiple lights on the ceiling, such that the emission is quite non-uniform e.g. if you looked at a large piece of cardboard, held close to the ceiling, from above, you would see alternating regions of light and dark, depending on whether or not the card was below a lamp or not. However if one were to examine the floor of the lecture theatre, these spots of light would no longer be so visible, having merged with neighboring spots due to the fact that the emission from each individual lamp is not particularly beam-like (this is not to say that it is truly isotropic, but a substantial



difference would be observed if the lamps were replaced with spot-lights or downward-pointing laser beams!) Secondly the radiation from the regions of the hohlraum wall that are heated directly by the driver falls not only upon the capsule but also on other regions of the hohlraum wall – both those regions that exposed to the driver, and those that are not. The whole interior of the hohlraum wall is thereby raised to a high temperature, and therefore the entire wall is also responsible for heating the capsule. The non-uniformities in the radiation drive at the capsule surface are reduced even further by this process. To continue our analogy of the lecture theatre and the lamps, we could suggest that this is somewhat like the effect of painting the walls of the lecture theatre white – so that the light reaching the floor comes not only directly from the lamps, but also indirectly via the walls. (Whilst these analogies may seem somewhat naïve it is worth noting here that the numerical simulation codes used to model hohlraum radiation uniformity, so called “view-factor codes”, are very similar to those used by architects to ensure that buildings and their sur-rounding environs are adequately lit!).

Inevitably indirect-drive ICF has a substantially lower coupling efficiency between the driver and the capsule than in the case of direct-drive (*Though note that the x-rays are absorbed more effectively by the capsule than laser radiation at optical wavelengths. The loss of efficiency is down to the fact that only a relatively small fraction of the x-rays interact with the capsule approximation to such a system, and the emission often departs quite significantly from a planckian emission spectrum– partly due to the fact that the system is constantly being driven out of equilibrium by the driver, and partly because the opacity of the wall varies significantly across the frequency spectrum of the photons contained by the hohlraum*). This is due to the fact that energy must be provided to raise the entire interior surface of the hohlraum to a high temperature, and this surface is many times larger than that of the capsule. In laser-driven indirect drive, a substantial amount of energy also flows out of the Laser Entrance Holes (some ion-beam and pulsed-power driven indirect drive concepts do not require such openings to the vacuum chamber).

$$\eta_{c.e.} E_{laser} = E_{capsule} + E_{wall} + E_{L.E.H.} \quad (11.8)$$

Equation 11.8 gives the hohlraum energy-balance for a laser-driven hohlraum, where $\eta_{c.e.}$ is the laser to x-ray conversion efficiency, and the other terms are the energy from the laser, the energy going into the capsule, the energy going to heat the hohlraum wall, and the energy escaping from the laser entrance holes (LEH) accordingly. Each of the terms on the right-hand side of equation 11.8 is proportional to the surface area of the component (or simply the area in the case of the LEHs). The dominant term in the hohlraum energy balance is the wall term. This describes the energy that goes into heating the hohlraum wall. The hohlraum wall is heated by a diffusive radiative heat-wave known as a Marshak wave. What this means is

that (except at very early times) the radiative heat-flow that is going into the cold, unheated regions of the wall is not coming directly from the radiation field in the interior void of the hohlraum, but rather it is coming from adjacent hot material. This adjacent hot material is in turn heated by even hotter material closer to the central void of the hohlraum. This behaviour is illustrated in figure 11.4. Note that this is a different process than that responsible for heating the fuel capsule ablator – in that case the heated material is sufficiently transparent to the x-ray drive that the cold material can be thought of as being heated directly by the x-rays coming from the body of the hohlraum.

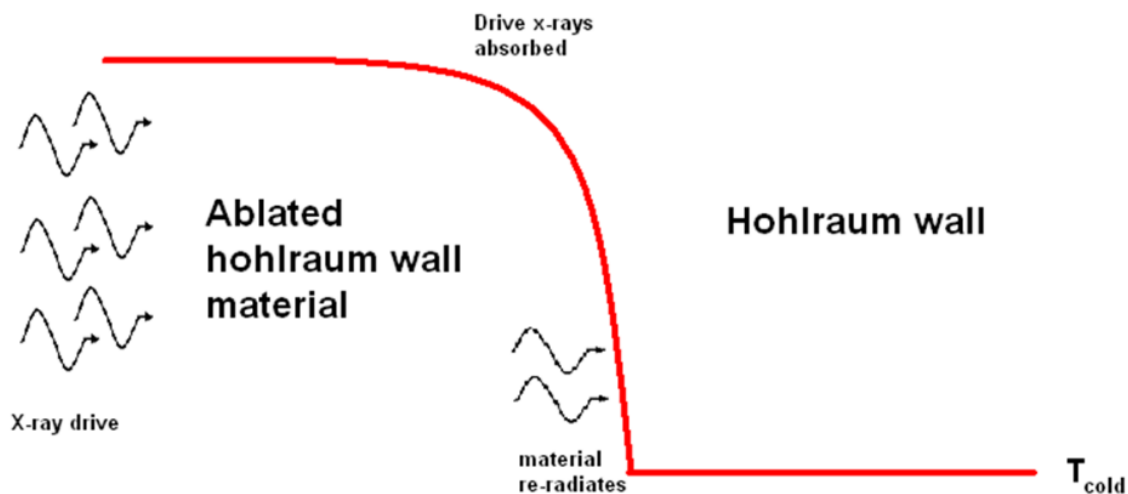


Figure 11.4 A Marshak wave is a diffusive heat-wave that is responsible for heating the hohlraum wall interior. Note that this is a different process than that responsible for heating the fuel capsule ablator – in that case the heated material is sufficiently transparent to the x-ray drive that the cold material is heated directly by the x-rays coming from the body of the hohlraum.

As noted in the previous paragraph, the heating of the hohlraum wall is diffusive. This is due to the fact that the hohlraum wall has a high opacity to the radiation field inside the hohlraum. The hohlraums used in laser-driven indirect drive ICF typically operate at a temperature up to around 400eV. At such temperatures the only materials that have a relatively high opacity to the radiation field contained by the hohlraum are those with a high atomic number (high-Z) such as gold and uranium (both of which are used in the construction of the hohlraum wall used at the National Ignition Facility). The reasoning behind the use of a high-Z wall can be encapsulated in several different ways. One way to consider it is in terms of the Marshak wave. If the wall opacity is high then the Marshak wave will proceed relatively slowly into the unheated wall material, and therefore the total amount of energy expended in heating the wall



material will be limited. Another way to look at it is in terms of Kirchhoff's radiation law which states that in thermal equilibrium, the emissivity of a body (or surface) matches its absorptivity. This comes from the principle of detailed balancing. The meaning of this is relevant to the question in hand since it implies that the opaquer our hohlraum wall is, the more it will emit at a given temperature. Clearly, in order to be efficient, one objective of the hohlraum is to illuminate the capsule as intensely as possible for a given driver intensity, and so Kirchhoff's law points us toward using a high-Z wall material in order to achieve this.

Substantially more information on hohlraum physics, with specifics of relevance to the laser-driven approach to indirect drive ICF, may be found in reference 1.

11.3 Conclusions

In this chapter, we considered the requirements placed upon the implosion in order to render the fuel in the desired state. We showed that it is important to limit the entropy of the fuel by accelerating it with multiple shock waves, such that the fuel pressure during stagnation does not significantly exceed the unavoidable Fermi back-pressure, thereby limiting the compression. We have also briefly considered the role of the hohlraum in the indirect drive approach to ICF.

References

- [1] J. D. Lindl, *Phys. Plasmas* **2** (11), pp. 3933-4024, 1995 or "Inertial Confinement Fusion – The quest for ignition and energy gain using indirect drive", J. D. Lindl, pub. Springer, 1998
- [2] "The Physics of Inertial Fusion", S. Atzeni and J. Meyerter-Vehn, pub. Oxford, 2004
- [3] "Thermal Physics", H. Kroemer and C. Kittel, pub. Freeman, 1980
- [4] R. Betti et al, *Phys. Plasmas* **5**, 1446, 1998
- [5] "Physics of shock waves and high-temperature hydrodynamic phenomena", Ya.B. Zel'dovich and Yu.P. Razier, pub. Academic Press, 1966 and Dover Press, 2002.



HELLENIC
MEDITERRANEAN
UNIVERSITY



université
BORDEAUX



UNIVERSITY
of York



Erasmus+

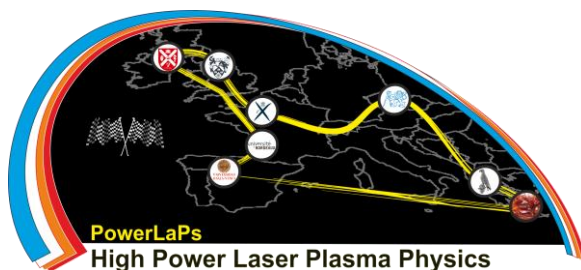
PowerLaPs

Innovative Education & Training in High Power Laser Plasmas

High Power Laser Matter Interactions/High Energy Density Physics - Theory and Experiments

Chapter 12: Generation and characterisation of warm dense matter in the laboratory

D. Riley



Erasmus+



12. Generation and characterisation of warm dense matter in the laboratory

12.1 Introduction

The study of warm dense matter (WDM) in the laboratory has matured into a well-developed field with many active researchers [e.g. 1-7]. The reason for this is a combination of the exciting and interesting academic challenges inherent and also the important application to understanding the structure and formation of planets and other astrophysical objects, such as brown dwarfs. There have been many scientific questions posed regarding the structure of planets over the last 30 or more years. For example, it has been suggested that the extreme conditions inside planets such as Neptune and Uranus may cause carbon to form into diamond layers [8]. It has been further shown by Nettelmann et al [9] that different models of the interior of Jupiter can be created that predict quite different internal structures and yet both predict gravitational moments and other parameters that agree with observation. The key difference is the equation of state used to describe the relationship between pressure, density and temperature for the hydrogen and helium. Such questions can only be resolved once a firmer understanding of warm dense matter has been established.

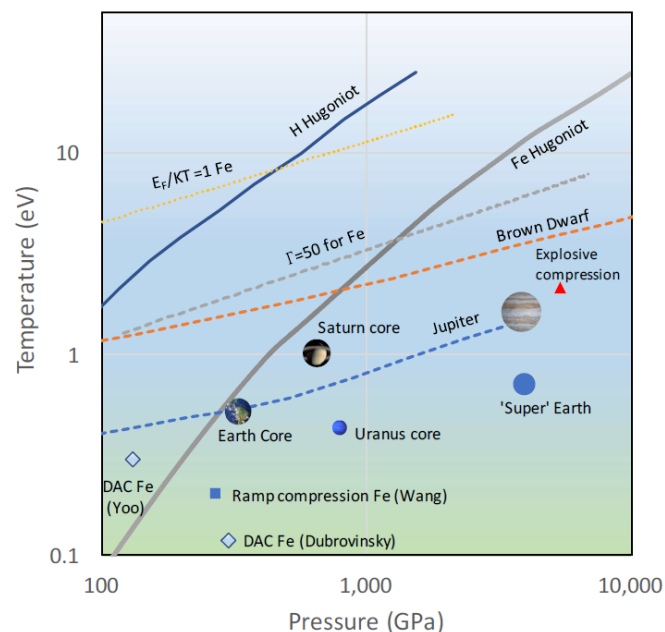


Figure 12.1 Mapping of the warm dense matter region. The boundaries are a broad guide. We can see the way in which conditions in Jupiter as a function of depth (dashed blue line) pass through the WDM regime as well as conditions in a Brown Dwarf (dashed orange line). We note that static methods of compression and heating such as diamond anvil cells (DAC) only probe the bottom left corner of our regime.

We can see, in figure 12.1, a mapping of warm dense matter conditions in terms of the temperature-pressure space occupied. The challenges faced can be described by reference

to some of the key properties of warm dense matter. These include strong inter-particle correlation often expressed through the parameter;

$$\Gamma = \frac{q^2}{akT} \quad (12.1)$$

where q is the charge on a particle and a is some characteristic distance (in the case of ions, the ion- sphere radius). For ions, in high temperature, low density plasmas such as the solar corona or a tokamak, this parameter is much smaller than unity indicating that the Coulombic interactions can be looked at as a small perturbation on the random thermal motion, albeit a perturbation that leads to rich physics. At the other extreme, in solid matter, values of Γ for ions are well in excess of 100 and the thermal motion represents a perturbation about a fixed lattice position. For warm dense matter, we are often in an intermediate regime where neither Coulomb interaction nor thermal energy are a small perturbation of the other. This presents a challenge in theoretical modelling of WDM.

Another important characteristic is partial degeneracy. For low density classical plasmas, electron degeneracy is not a feature and for cold solids and even liquid metals we can usually approximate that the electrons are in the ground configuration. For WDM we can often have $\mu/kT \sim 1$, where μ is the chemical potential. This means that whilst Pauli blocking will play a role in determining, for example, the electron-ion equilibration time and plasma resistivity, we cannot approximate that all electrons are in the ground state. Finally, we can note that partial ionisation is a key aspect of WDM, especially for mid to high- Z elements. This has a significant effect on the microscopic arrangement of ions within the sample as the strong short-range repulsion between bound electron shells might play a part in the interionic potential [10]. In turn, the microscopic structure has profound effects on macroscopic quantities such as the resistivity, compressibility and internal energy of a sample, as we shall discuss further below.

There are some general requirements we can consider in evaluating methods of generating WDM samples. The first of these is the need, in many cases, for a uniform sample. This is important as strong gradients in density and temperature can mask physical effects and make comparison with modelling and theory problematical. Sometimes, we may of course be interested in non-equilibrium situations where heat flows and currents may be generated by gradients but resolving those gradients in itself becomes a challenge to be met. For this reason, direct heating of a solid by laser-irradiation is generally ruled out as a useful method. Whilst high intensities lead to a hot plasma on the surface and strong electron



thermal conduction inwards from the laser-plasma can create WDM conditions in the solid, this is invariably accompanied by very strong density and temperature gradients. The use of very high intensity, short pulse irradiation to create a population of super-thermal electrons that can penetrate a solid and create warm dense matter is a possible exception that will be discussed below.

There are also considerations of timescale. As noted above, static methods such as diamond anvil cells cannot probe most of the WDM regime and we resort to dynamic methods where a sample is created rapidly and stays in a WDM condition due to inertia for long enough for it to be probed. Take for example a sample heated to around 10eV at close to solid density. The speed of expansion can be roughly approximated to the sound speed, which is of order 10^4 ms^{-1} depending on the material. This implies that for millimetre scale targets we can have decompression timescales of order 10^{-8} - 10^{-7} s. This is a distinct advantage in terms of probing opportunities. As we shall see, however, such samples present the issue that, for some methods of generation and probing, we would be limited to lower Z materials. This is due to the high opacity for x-rays with higher Z materials and thus smaller samples with consequently faster evolution would be needed.

The timescale is also important from the point of view of equilibration. As noted above, we will sometimes be interested in the process of equilibration in dynamic systems. However, we would often like to compare our data to what may happen inside, for example, a planet where timescales are extremely long. In these cases, when we create a sample, we need to concern ourselves with the rates at which electron-ion exchange of energy, melting and phase changes might occur and compare these to the timescale of our experiment.

In the following sections we will discuss the generation and diagnosis of warm dense matter by a variety of means, addressing generation and diagnosis together in some cases as some experiments lend themselves to particular diagnostic techniques. We broadly categorise the methods as shock/ramp compression and volumetric heating, both of which can be achieved by a range of means.

12.2 Shock or ramp compression

The generation of a shock wave by the sudden application of a high pressure has been discussed and described very well elsewhere [11]. For the purpose of this discussion we will observe that the shock generates a sudden jump in the pressure, density and temperature of a sample. This process is described by the Rankine-Hugoniot equations which consider the conservation of mass, momentum and energy;

$$\rho_0 v_s = \rho v_p$$

$$P_0 + \rho_0 v_s^2 = P + \rho v_p^2 \quad (12.2)$$

$$E_0 + \frac{P_0}{\rho_0} + \frac{v_s^2}{2} = E + \frac{P}{\rho} + \frac{v_p^2}{2}$$

There are thus five unknowns, which are the pressure, P , density, ρ , and internal energy, E of the shocked matter and the velocity of the shock, v_s and the particle velocity of the matter after it has been shocked, v_p . If we measure any two of these parameters, we can, in principle, solve for the others. We can see, in figure 13.1, the so called Hugoniot curves for Fe and Hydrogen taken from the SESAME database [12]. These show how the temperature of the shocked matter is related to the shock pressure. We can also see a point labelled ramp compression. This results from a more gentle compression where pressure is applied in a smooth way rather than a sudden jump. The principle on which this is based can be understood by considering that, for an ideal gas, the entropy created by a single shock is given by [see e.g. 11];

$$\Delta S = C_V \ln \left(\frac{P V^\gamma}{P_0 V_0^\gamma} \right) \quad (12.3)$$

For strong shocks, it is well known that the maximum compression in an ideal gas is a factor of 4 (given by $(\gamma + 1)/(\gamma - 1)$). If we consider a final shock pressure P , then we can show that by reaching it in a series of shocks of increasing pressure rather than a single jump from P_0 to P , we create less entropy and can, in the limit of specially shaped drive, achieve close to isentropic compression. This permits the exploration of a wider range of conditions away from the shock Hugoniot [e.g. 13,14], although in many cases we should note that this includes matter below the temperature that we would normally consider as being in the WDM regime.

Directly laser driven shocks

Figure 12.2 shows a much-simplified schematic of laser-shock drive [15-17]. An intense laser incident on a solid surface creates a plasma in which laser light is further absorbed by mechanisms such as inverse bremsstrahlung. Thermal transport into the target creates a dense high temperature ablation surface where the pressure created drives a shock inwards. There are several scaling laws in the literature that describe the pressure of the shock as a function of the laser intensity and wavelength. For example [17];

$$P(\text{Mbar}) = 8I_{14}^{3/4} \lambda^{-1/2} \quad (12.4)$$

where the laser intensity is in units of 10^{14} Wcm^{-2} and the wavelength is in microns. The shock speed depends on the material, being faster for lower density but is generally in the regime of 10s km/s. This implies that for a typical drive duration of 1ns, a sample of 10s μm thickness can be compressed before the pressure source is removed. For direct drive of lasers in this manner, this can create an issue of radiative pre-heating. The keV temperature plasma created in the surface laser-solid interaction will radiate x-rays at several keV. These x-rays can penetrate the solid and heat the material ahead of compression, for example, at 5keV x-rays have an attenuation length in Al of 20 μm . This in turn can alter the Hugoniot so that it is no longer possible to apply the Rankine-Hugoniot equations without knowledge of the pre-heated conditions.

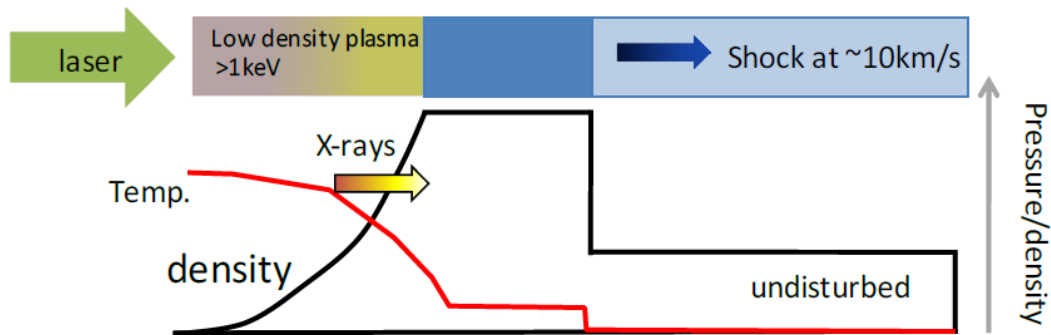


Figure 12.2 Schematic of a laser driven shock. The incident laser creates a hot plasma on the surface of a solid target. The hot plasma ablates from the surface, exerting a Mbar level pressure that drives a shock into the solid.

In addition to radiative pre-heating there can also be electron pre-heating. This can originate in fast electrons created by processes such as filamentation or stimulated Raman scatter in the coronal plasma. The threshold intensity for the latter instability depends of the spatial scale-length of the plasma, L [e.g. see 18]

$$I > \frac{5 \times 10^{16}}{L^{4/3} \lambda^{2/3}} \text{ Wcm}^{-2} \quad (12.5)$$

where L and the wavelength of the laser, λ are in microns. For a keV coronal plasma expanding at sound speed of $2 \times 10^5 \text{ ms}^{-1}$, we expect $L > 200 \mu\text{m}$ after 1ns and thus the threshold is below 10^{14} Wcm^{-2} for $0.527 \mu\text{m}$ laser light. The issue of pre-heating by supra-thermal electrons in shock experiments was discussed by, amongst others, Trainor and Lee [19].

An important consideration in the generation of such laser-driven shocks is the quality of the focal spot. For some years now optical devices such as random phase plates [20] have

been available to counter this problem. There are now several varieties [e.g. 21] of such devices. The basic principle is that the beam is broken into a number of smaller beamlets, for each of which a randomly assigned phase change is introduced, either π or 0. This creates a high frequency interference on the target surface that can be smoothed out via lateral thermal transport in the coronal plasma. The speckle size is typically a few microns and depends on the f-number of focusing and the wavelength. The size of the elements needed is inversely proportional to the size of the focal spot required. This means that for a given f-number and focused intensity, it may be considered that a larger system has some advantages. Firstly, for a larger beam there will be a larger number of elements and so statistical averaging of intensity is more effective. Secondly, with a larger system, a larger focal spot can be used and the ratio of speckle size to focal spot is smaller. Thus, generally higher energy systems (>100J) are to be preferred for this work. Other methods of beam smoothing such as smoothing by spectral dispersion (SSD) [22] have also been considered, sometimes in conjunction with a phase plate, although these require modifications to the laser, whilst a phase plate is simply inserted into the beam. An example of a focal spot created with a phase plate is shown in figure 3. In addition to the focal spot issue, there are other considerations such as the shaping of the laser pulses and the structure of the target. The first of these has been alluded to above in the context of isentropic compression. Prior to the advent of laser pulse shaping technologies, use of multiple beams to create coalescing shocks was considered to obtain higher compression with lower heating [e.g. 23,24]. Pre-stressed targets have also been used in conjunction with shock waves so that with a different P_0 , a different Hugoniot curve is explored. For example [25], compressed helium at up to 60 GPa contained in a diamond anvil cell has been shock compressed with a pulsed laser driving a shock through the diamond into the sample.

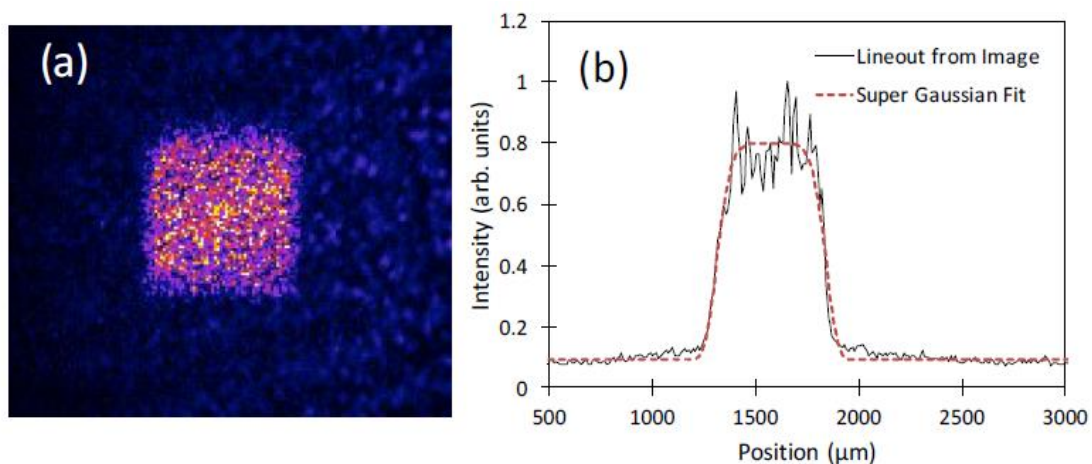


Figure 12.3 Example of a focal spot shape possible with phase plate technology. (a) Square focal spot with nominal 0.5mm sides. A low level plateau around the focal spot is due to higher order diffraction and imperfection in manufacture. (b) Lineout average across central



part of the spot with a super-Gaussian fit.

Shaping of the shock drive is not just a way to gain a more isentropic compression but, as discussed by Swift and Kraus [26], can be used to maintain a more constant shock driving pressure. As a plasma is created on the surface of the solid, the critical density, at which the laser is absorbed, moves outward and the distance over which thermal conduction needs to deliver energy to the ablation front increases. This generally means a drop in the applied pressure and a rising intensity pulse can help mitigate this factor. We can note, however, that as the scale-length of the coronal plasma increases, the threshold for parametric instabilities such as stimulated Raman scattering (SRS) becomes lower. The use of an ablator layer, such as CH to absorb the laser light and help form the shock driving pressure has also been discussed [26]. The impedance mismatch between a CH layer and a metal sample leads to a higher shock pressure imposed on the metal than would otherwise be generated by the ablation pressure. This comes at the price of a shorter duration of application peak pressure that comes about as a result of the series of shock reflection and release waves that occur between the plasma-vacuum interface and the CH-metal interface.

Indirectly driven shocks

Intense lasers incident on high Z materials can be efficient sources of X-rays, especially in the sub-keV regime with conversions up to 80% level [27-29]. With sub-keV x-rays the absorption length in a solid can be generally sub-micron and thus they can in principle be used to ablate the surface, exerting an ablation pressure in order to drive a shock. This is often achieved by irradiation of the inside of a gold cavity (hohlraum) with intense laser pulses (see figure 4). The x-ray emission, which can have an equivalent black body temperature of over 200 eV, is allowed to fall onto a shock target which may have an “ablator” layer, consisting of a low Z material such as CH [30]. In this way, shocks of over 20 Mbar have been generated [31]. In such experiments care has to be taken to ensure that harder x-rays do not penetrate and pre-heat the sample. For example, when using Au as the x-ray sources, the M-band radiation is broadly in the 2-4 keV photon energy range and conversion efficiency to M-band from laser energy can easily be a couple of percent [28,29]. A low Z ablator may need to be of order 100 μ m to avoid significant pre-heating of the shocked sample. A key advantage of this method is that nonuniformities in the optical laser profile can be smoothed out by conversion to x-rays and a more uniform shock can be generated. In addition to this, electron pre-heating is mitigated as faster electrons created in the optical laser-plasma interaction may not escape the x-ray generation target.

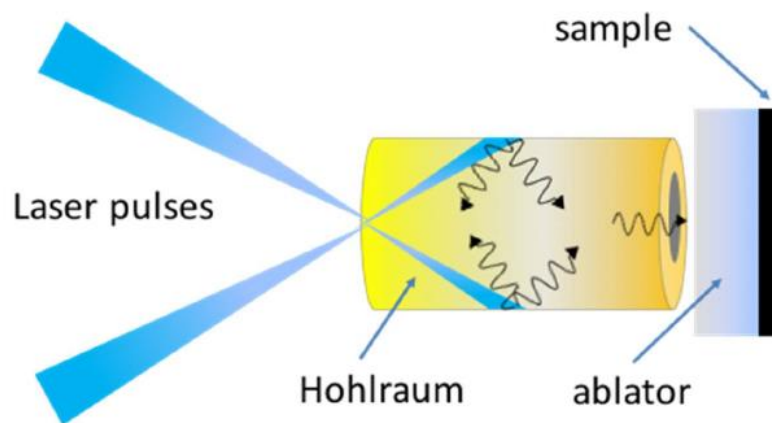


Figure 12.4 Schematic of a hohlraum target used to create an intense quasi black-body radiation field. Peak radiation is typically about 0.5keV which has an attenuation length of order 1 micron in CH.

Flyer plates

An alternative method for shock production is to use an accelerated foil as a ‘flyer plate’. For laser facilities, this flyer plate can be either directly illuminated with a laser beam or indirectly driven with an intense x-ray source. An example of the latter is [32] in which 25kJ of laser light in 1ns drive was focused into a gold hohlraum to create an intense x-ray drive in a that was incident on a foil consisting of a 50 μm polystyrene ablator on a 3 μm Au flyer plate. Collision with a further stepped Au foil generated a shock of Gbar (100TPa) pressure. The pressure was inferred from the speed of the shock measured by observing the optical emission from the rear of the Au steps as the shock emerged from the rear. Such experiments have the advantage of potentially removing radiative and electron pre heating but are susceptible to hydrodynamic instability as the flyer is accelerated and this issue along with any non-uniformity in irradiation can lead to a non-flat impact and thus non-uniform shock drive.

12.3 Volumetric heating

X-ray heating

As indicated above, the conversion of laser light to sub-keV x-ray and XUV radiation can be very efficient, reaching 10s of percent for high Z elements. For volumetric heating we are generally more interested in the harder (>1keV) X-ray regime as the photons can penetrate a sample and deposit energy uniformly, for example the M-band of Au [33]. Naturally, good uniformity requires a photon absorption length somewhat greater than the sample dimension and this also implies a low efficiency, thus a high available energy is desirable. For mid- Z materials we can create L-shell spectra in the few keV range with several percent conversion of laser light to x-rays [34,35]. An example spectrum for Pd is shown in figure 12.5.

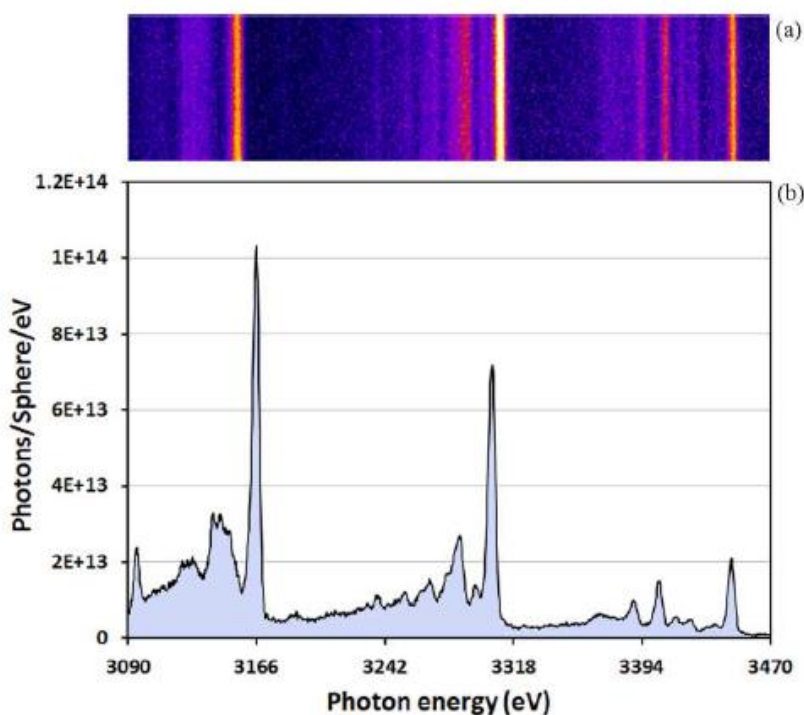


Figure 12.5 Experimental L-shell emission spectrum from a 50nm Pd foil irradiated with 527nm wavelength laser beams with 200ps FWHM duration. Intensity on target was $\sim 10^{15} \text{Wcm}^{-2}$ and conversion to L-shell X-rays was estimated at 4%. Similar data can be seen in [35].

An example of the use of volumetric heating with L-shell radiation can be seen in the work of Glenzer et al [36] who demonstrated X-ray Thomson scattering (discussed below) using a sub-millimetre scale Be target heated by L-shell x-rays in the 2.7-3.4 keV range from a Rh shell around the sample. They were able to achieve relatively uniform electron density of over $3 \times 10^{23} \text{cm}^{-3}$ at a temperature of 53eV. The ion-ion coupling parameter is of order unity. Furthermore, the Fermi energy of the electrons should be 15eV and thus $EF/kT \sim 0.3$, illustrating both strong coupling and partial degeneracy; two of the key features of WDM. More recently, Kettle et al [37] have used volumetric x-ray heating using Pd L-shell emission to heat Al to WDM conditions of $\sim 1\text{eV}$ and solid density in order to probe free-free opacity in the XUV radiation. The foils in this case were sub-micron in thickness and thus with a sound speed of $\sim 6000 \text{ms}^{-1}$ the decompression time was of order 30-50ps meaning that rapid heating ($< 50\text{ps}$ rise time) and fast probing with sub-ps high harmonic radiation was required. In this case, the ion-ion coupling achieved was of order $\Gamma \sim 50-80$ with $EF/kT \sim 0.1-0.15$. A further important consideration in this type of experiment is the effect of softer x-rays. If these have a very short absorption length in the solid target then they can result in non-uniform heating as only the outer layers absorb energy. A filter layer, typically a material such as CH is employed as it is relatively transparent to the desired keV heating x-rays whilst reducing the softer x-rays significantly. We are not dealing specifically with x-ray free-electron lasers



in this paper, but it is worth noting that a key advantage of such facilities is that they produce an intense beam tunable to over 10keV that can be used for uniform volumetric heating [e.g. 38], without an unwanted softer x-ray component.

Proton and fast electron heating

The use of intense short pulse lasers (picosecond and below) to create beams of accelerated protons by mechanisms such as the target-normal-sheath-acceleration (TNSA) mechanism has been well documented for over a decade now [39]. Proton energies up to 10s of MeV have been routinely achieved. Conversion efficiencies of up to 10% with proton energies in excess of 85 MeV have been reported [40]. The beams typically have some divergence of about a radian and so schemes have been proposed to focus these for warm dense matter creation [41].

A key experimental feature is that there is a spectrum of protons (see example in figure 6). If we consider protons from 5-10 MeV in the heating beam as playing the significant role in heating, then we can readily calculate that even at only 1mm from the target the temporal dispersion will be approximately 10ps. If we consider both the issue of divergence and time of flight, then it is evident that, for now, experiments using these beams to create warm dense matter require a small (mm scale) offset between the intense laser-plasma used to create the beam and the warm dense matter sample. Focusing of the proton beam has been attempted. For example, a hemispherical target has been used, such as described in Patel *et al* [41] to create a WDM sample at 20eV and solid density. This is well into the WDM regime. However, the sub-mm proximity of the intense laser plasma interaction at $>10^{18}$ Wcm⁻² complicates probing of the sample and it is only from the optical emission from the sample surface that the temperature is diagnosed.

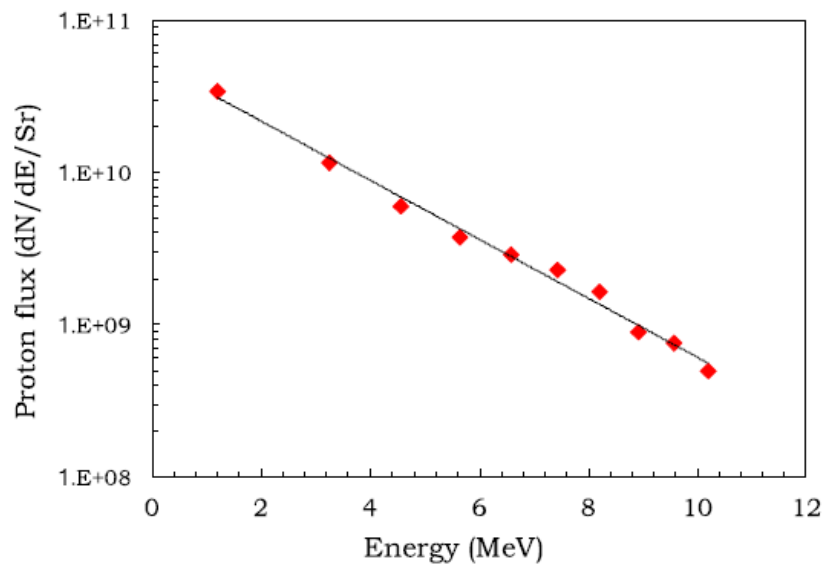


Figure 12.6 Experimental proton spectrum from the TARANIS laser facility. The 1.053 μm wavelength laser pulse was 7.5J energy, 1ps duration focused to about 10 μm focal spot onto a 10 μm thick Au foil. The solid line is a fit to an exponential showing an effective temperature of $\sim 2.2\text{MeV}$. The latest work in this area has achieved proton energies in excess of 85 MeV [40]

The TNSA mechanism relies on the generation of supra-thermal electrons. The efficiency of conversion into such *fast* electrons can be 10s of percent with temperatures according to the scaling of Beg *et al* [42] given by

$$T_{ho} = 100(I\lambda^2)^{1/3} \text{ keV} \quad (12.6)$$

The range of such electrons in solids can be 100s of microns. As discussed by Bell *et al*, [43] the current generated by fast electrons alone would exceed the Alfven limit and a balancing return current of electrons at lower energy is present. The return current electrons are more collisional and resistive heating of the sample can occur. This process has been used to create warm dense matter, e.g. [44] at temperatures of 10s eV and solid density, leading to ion-ion coupling parameters of >1 and partial degeneracy. Even more than the proton heating discussed above, a potential limitation of this technique is that the warm dense matter is necessarily in close proximity to a very high temperature non-uniform plasma created by the intense laser interaction and this can create problems with hard x-ray background in diagnostics as well as electromagnetic pulse interference with electronics, which is a known problem with intense laser-plasma experiments.



12.4 Diagnostics

Emission spectroscopy is often of limited value in WDM research as the high density and low temperature will combine to make the sample opaque to the wavelengths we would expect from thermally excited emission and so we generally only observe surface emission. We will discuss, below, how this can be used in some diagnostics. There are some exceptions to this case where non-thermally stimulated emission can originate from within the bulk of a sample and analysis can tell us something about density and temperature as well as ionization. First, we discuss some other key diagnostic methods.

X-ray scattering

X-ray scattering from dense plasmas and WDM has been developed experimentally over the past 20 years [e.g. 36, 45-50] and now sophisticated experiments and analysis can be applied to explore key questions in warm dense matter theory. The basic formulation can be expressed in the following equation

$$I(k, \omega) = I_T(k) \left[(f(k) + q(k))^2 S_{ii}(k, \omega) + Z_b \int S_b(k, \omega - \omega') S_i(k, \omega') d\omega' + Z_f S_{ee}(k, \omega) \right] \quad (12.7)$$

We can see that there are three contributions to the scattering which are scaled by $h(k)$ which is the Thomson scattering cross section as a function of angle, or expressed in this case as a function of scatter wave-vector k . For laser-plasmas, the source is generally unpolarised so this scaling is slightly different than for a polarised source such as an x-ray free electron laser. The first term inside the square bracket is quasi-elastic scattering from bound electrons. The second is bound-free Compton scatter whereby the scattering photon imparts sufficient momentum to a bound electron to cause ionisation. Finally, we have the free-electron scattering. These contributions have been reviewed in detail elsewhere [48,50]. For the first term $f(k)$ is the ionic form factor and $q(k)$ accounts for correlation between free electrons and ions. The term, $S_u(k, \omega)$ is the ion-ion form factor and is connected to the microscopic arrangement of the ions through the pair correlation function $g(r)$. This term is, in principle, dynamic and has a frequency dependence due to motion of the ions. However, most experiments cannot resolve this and we generally expect to measure the related quantity $S_a(k) = \int S_a(k, M) dM$. In figure 13.7a, we see a scatter cross section as a function of angle for shock compressed Fe, taken with the LCLS x-ray laser operating at 7keV photon energy. The scattering has been fitted using a hyper-netted chain approach [see e.g. 51] that uses a screened Coulombic potential between the ions supplemented by a short range repulsive term that accounts for the interaction between the shells of bound electrons. An important role of such measurements is that it can connect the microscopic structure of the

WDM sample to bulk properties such as the thermal and electrical conductivity as well as compressibility and internal energy. For example [52] the resistivity of a plasma can be expressed as

$$\rho_e = \frac{m_e^2}{12 \pi^3 \hbar^3 e^2 n} \int_0^{2k_F} dk k^3 |V_{ei}(qk)|^2 S_{ii}(k) \quad (12.8)$$

As we can see, the ion-ion structure factor and thus the pair correlation function $g(r)$ for the sample has a key role.

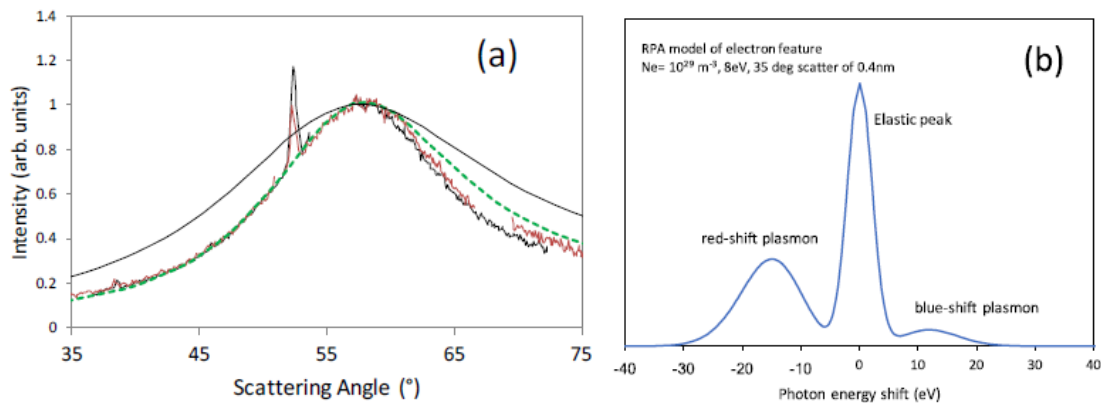


Figure 12.7 (a) Elastic scatter data as a function of angle for a shock compressed Fe target. The probe photon energy was 7keV. The black curve is a fit using a simple screened Coulombic potential whilst the green dashed curve is a fit that uses a short range repulsive term of form a/r^4 that accounts for the repulsion between shells of bound electrons. The fit conditions are density of 11.1gcm^{-3} and $T=1.5\text{eV}$. (b) Schematic of the expected spectrum from X-ray Thomson scattering. The plasmon ratio can be linked directly to temperature and the spectral position of the peaks to the electron density. The strength of the elastic peak will depend on the number of bound electrons and so we can see that this is a very powerful diagnostic that can link ionisation state, electron density and temperature.

The second term is the bound-free Compton scatter term [53] and is present when Compton scatter of a photon from a bound electron imparts sufficient recoil energy to an electron to ionise it. The scattered x-ray energies are not simply dependent on the scatter angle as in the usual Compton scatter from free electrons at rest but show a spectrum that depends on the orbital and the ionisation energy [53]. The final term is the free-electron Thomson scatter. As with optical Thomson scatter this can occur in either the collective or non-collective modes. We see in figure 7b a schematic of the collective mode where we see plasmon features either side of the central peak due to elastic scatter. We note that there is an asymmetry in peak intensity governed by the principle of detailed balance such that there is a ratio of

$$I(\omega, k) = I(-\omega, k) \exp\left(-\frac{\hbar\omega}{kT}\right) \quad (12.9)$$

This asymmetry is typically not noticeable in optical Thomson scatter as the exponential term is very close to unity. In WDM this is a possible temperature diagnostic that does not depend on the damping of the plasmons or detailed understanding of the plasmon dispersion. Examples of such data can be found in [54,55].

K-edge and XANES measurements

Since WDM samples are often transparent to X-rays, a key diagnostic is absorption spectroscopy. The existence of edges in the absorption spectra of materials is, of course, well known since the advent of X-ray physics. A key feature for WDM research is that the position of the K-edge, corresponding to the binding of the K-shell electrons, is not fixed but depends on conditions of density and temperature. This dependence arises in simple terms from three factors. The first is continuum lowering or ionisation potential depression (IPD) [e.g. 56] through which the energy levels of bound electrons are raised by interaction with the ambient plasma electric micro-field. This tends to shift the edge position to lower energy. The second term is the shift due to ionisation as a result of the elevated temperature and compression of WDM. This tends to move the edge back to higher energy. Finally, there is the change in degeneracy. Pauli blocking causes the effective edge position to be at a higher energy than would otherwise be the case, this term can shift to either higher or lower energy depending on the temperature and density reached. In the first experimental work using this diagnostic for WDM, Bradley *et al* [57] estimated a shift of -3.7eV for a KCl sample that was estimated to be at 6.2gcm⁻³ and 19eV. This, however, was predicted to be comprised of a continuum lowering of -45.2eV, an ionisation shift of +47.6eV and a change due to degeneracy of -6.2eV. This illustrates a challenge of this diagnostic in that a small net shift is seen and relatively small changes in theory of IPD or estimates of the ionisation can have a large proportional effect on the final result. This issue of IPD is currently a field of renewed interest since recent experimental data from X-ray laser facilities and large laser facilities disagree on which model is appropriate [see 58 and references within].

A more detailed analysis of the edge that looks at oscillations in absorption close to the edge as well as the position can be carried out. These techniques are called EXAFS (extended x-ray absorption fine structure) or XANES (x-ray absorption near edge structure) depending on how far from the edge we are working. The oscillations in absorption coefficient near an edge are caused by quantum mechanical interference. As an electron is ionised in the absorption process, the wave-function of the free state can scatter off nearby ions or

atoms and cause oscillations in the final state amplitude that leads to structure in the absorption spectrum. This structure in turn is linked to the microscopic arrangement of the ions. The EXAFS technique has been used in shock compressed samples [59] to look at a region relatively far ($\sim 100\text{eV}$) from the edge. The density can be deduced from the position of the ion-ion correlation peaks and the temperature will have an effect on the depth of the oscillations, which will smooth out at high temperature. The XANES technique typically looks closer to the edge. The ejected electron has lower energy and multiple scattering from nearby atoms is important. This technique, like EXAFS, is well known in solid state physics but has also been applied to warm dense matter [e.g. 60].

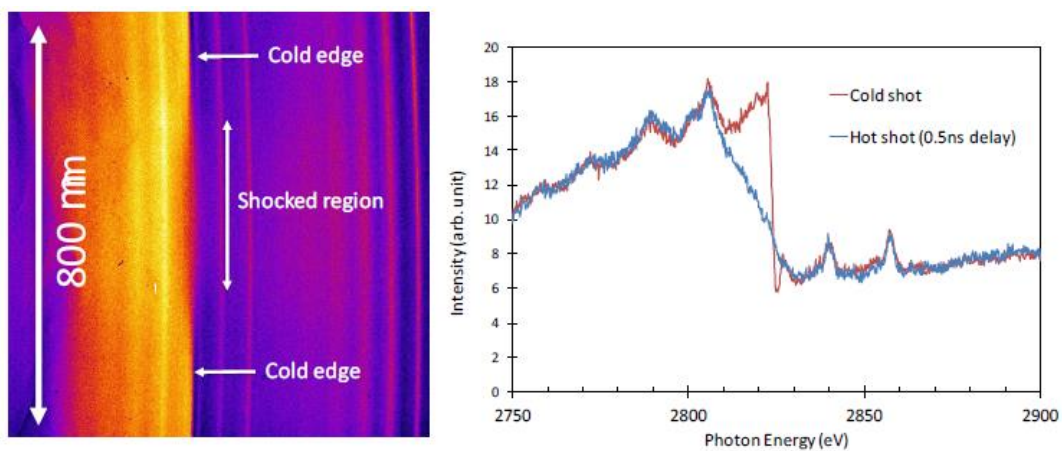


Figure 12.8 This data shows a comparison of the transmission spectrum for a cold chlorinated plastic target and a shock compressed target. A bismuth back-lighter source was used. We can see that there is good reproducibility in the spectral features of the Bi and there is a clear shift and broadening of the edge. The raw data on the left shows how the small size of the source was used to project through the target with spatial resolution, allowing comparison of the cold and compressed regions directly on each shot. The spatial scale refers to distance across the target sample.

An important experimental detail for any of the absorption techniques is the need for a smooth backlight spectrum. This is needed to see the fine structure easily. Typically, a higher Z target is used where arrays of unresolved transitions form bands of emission, commonly the M-band of transition between the $n=4$ to $n=3$ levels is used. Figure 13.8 shows an example where Bi has been used to form a K-edge in a shock compressed chlorinated plastic target. In [59] a uranium back-lighter was used as it produces a very smooth N-band spectrum in the required range around the Al K-edge.

Optical pyrometry measurements

As can be seen from the shock Hugoniot curves in figure 13.1, when a Mbar (100GPa) shock is used to compress a sample, temperatures of well over 1000K can be generated. This leads to significant emission in the optical regime, which can be viewed through a transparent



sample but also as the shock exits the rear of an opaque sample. This has been used [e.g. 32] to measure shock speeds, in particular by use of stepped target with a known step height.

In addition to the shock break-out time, the optical emission has been used to estimate the temperature. In a transparent medium such as quartz or glass, the emission can be measured before the shock has broken out. In these cases, care has to be taken to understand the optical transmission of the material ahead of the shock. At the high density of the compressed sample, the emission is generally almost black-body in nature and can be used to either measure an emission temperature, from the time resolved absolute level of emission [61] or a spectral temperature by fitting to a grey-body curve. This technique is usually called streaked optical pyrometry (SOP). A detailed discussion of the system implemented at the Omega laser facility is found in [61].

For non-transparent targets there are two options. One is to simply measure the emission as the shock exits the target. This means that there is rapid decompression of the sample as the release wave moves back into the target. The alternative is to use a transparent window. This means that the sample remains at high density as the shock is transmitted into the window material and partially reflected back into the sample. Window materials such as LiF have been shown to remain transparent at 250GPa. The quality of the interface and thermal conduction into the window are also key parameters to be considered. As with transparent targets, the optical transmission of the window as it is compressed also needs to be understood to correctly interpret the data. An alternative is to use a timing fiducial laser on an optical streak camera and compare this to the onset of rear surface emission as was done in [32]. For cases where the optical emission from the rear may be weak, we can consider VISAR as discussed in the next section.

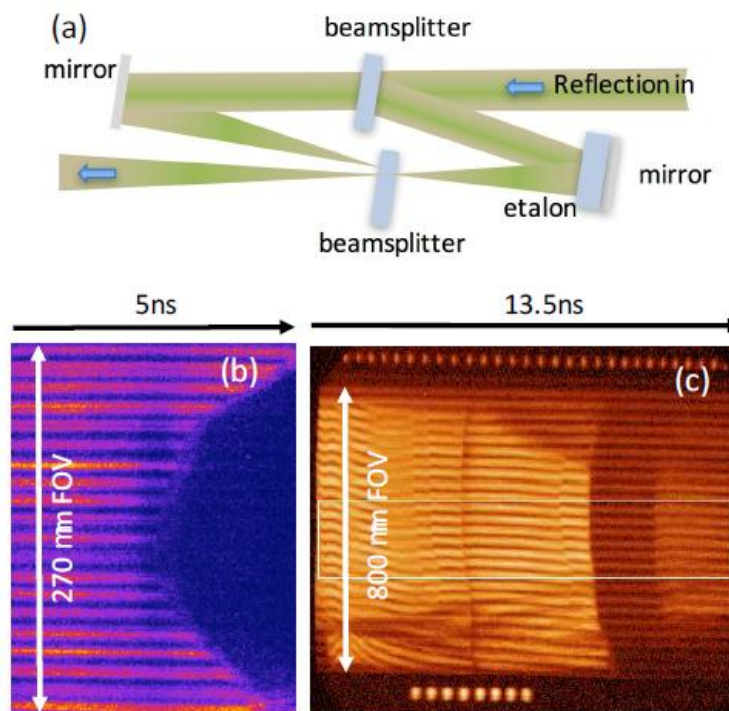


Figure 12.9 (a) Schematic of the interferometer at the heart of a VISAR system (b) Example of VISAR data showing break-out from a laser-shocked Al foil. The focal spot size was $100 \mu\text{m}$ and we can see the delayed break-out of the shock outside this central zone. The fringes disappear as the shock break out and the surface forms a highly absorbing plasma. (c) Data taken for shock break-out experiment on the Omega laser facility, with a complex layered target consisting of a CH ablator coated onto a quartz pusher with an aerogel foam target on top of that followed by a LiF window [63]. The details of the experiment can be found in [63] and references therein. Image courtesy of K Falk and colleagues.

VISAR

An important shock diagnostic commonly run alongside SOP is VISAR, [e.g. 62,63 and references within] which is an interferometric technique that uses a probe laser to monitor the motion of a surface, such as the rear of the target when a shock breaks out. Details of a design can be found in [62]. The basics are that a beam reflected from the target rear surface is collected and directed into an interferometer. By placing an etalon in one arm of the interferometer but adjusting the path, so that the effective optical path before recombination is the same, then an interference pattern can be formed without stringent coherence requirements that would necessitate a mirror like target and yet the arms sample the reflected surface at different times. The interference pattern is imaged onto the cathode of an optical streak camera, giving spatial resolution across a line on the target surface as well as temporal resolution. If the target remains stationary, then so do the fringes created. However, once the rear side accelerates, there is a shift in the fringes. If the surface velocity becomes steady, there is no further shift in fringes. Analysis of the fringe shift can be used to extract the velocity history of the surface [62]. It is common to employ two systems with different fringe



sensitivities (different etalon thicknesses) so that if shifts greater than a single fringe width occurs, then a unique solution can be found by comparing the two systems. In figure 9(b) we see what happens when a shock breaks out from the rear of a simple opaque target. The rear surface rapidly decompresses as a low density plasma/vapor that strongly absorbs the probe and the fringes disappear. For targets with windows and transparent materials we can get more complex data as in figure 9(c) which comes from an experiment in which a shock is driven through a low density aerogel foam. The laser is first incident on a CH ablator layer which is coated onto a quartz pusher. The aerogel is on top of the quartz and this is covered with a LiF window. In the data we can observe several features showing fringe shifts that occur at interfaces where the shock impedance is changing. More details of the experiment can be found in [63].

Emission spectroscopy

Although we have stated above that emission spectroscopy is of limited value, there are occasions when it can be used. For example, we have discussed the fact that fast electron heating can be used to create bulk heating of a solid due to the return current. During this process, the fast electrons can collisionally ionize the inner-shell electrons of the sample. The subsequent K- α emission will come from a range of ionization states depending on the temperature in the sample [44]. We should also acknowledge that, by its nature, this diagnostic is time integrating as the K- α emission will occur as soon as the fast electrons penetrate the sample. The K- α lines from adjacent ionization stages are close in energy and high resolution spectroscopy with $E/\Delta E > 2000$ is desirable. In addition, since we are at high density and Stark broadening may broaden the lines into each other, detailed modelling [44] capability is used to extract the information on plasma conditions.

We see, in figure 13.10, an example from a Ti sample. The foil is irradiated at $>10^{18} \text{ Wcm}^{-2}$ and subsequent analysis [64] suggested fast electrons generated via a resonance absorption process with temperatures of order 50-100keV. Analysis of the K- α spectrum created by the fast electrons suggested an ionisation spread consistent with a background temperature of up to 20eV. Even with spatially and spectrally resolving crystals, the small size of the plasma created makes it difficult to separate out contributions from regions under different conditions. In this case, the spectrum was best fitted by assuming emission coming also from a cold portion of the foil.

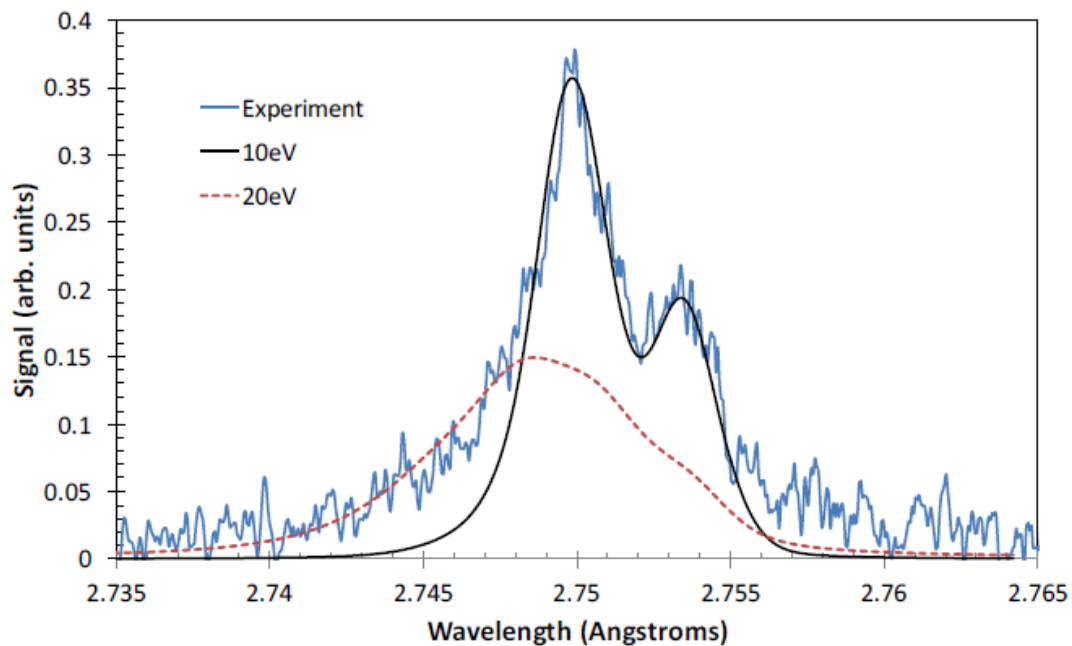


Figure 12.10 Ti K- α spectrum from a target irradiated with a sub-picosecond $1.053\mu\text{m}$ wavelength pulse at $>10^{18}\text{ Wcm}^{-2}$. Similar data can be found in [61]. The fit curves are from the SCRAM code [see 44] for different assumed background temperatures. A mixture of regions at different temperatures must contribute to the final spectrum to get the correct ratio of the K- α doublet and the shorter wavelength contribution.

As a final example, we can note that, in a recent experiment, fast electrons and shock compression were combined to investigate the issue of ionisation potential depression [65]. Laser driven shock compression with nanosecond pulses was used to create a high density sample at a few electron volts temperature. In order to stimulate x-ray emission that would originate from the bulk of the sample, an intense short pulse beam was used to create fast electron population that heated the sample to over 500eV leading to x-ray emission from He-like Al ions. Stark broadening of these lines was used to infer the density and this could be compared to the series cut-off due to the ionisation potential depression.

Summary

In this chapter are discussed several methods of creating warm dense matter with intense lasers, from picosecond to nanosecond duration and are outlined several of the common diagnostic methods for warm dense matter. Some key factors are the uniformity and lifetime of the sample as well as the accessibility to probing. A much wider ranging discussion, in addition to more extensive referencing, would take in the creation of warm dense matter with explosives, Z-pinchs, large ion-beam facilities and the relatively new x-ray free electron facilities.



References

1. RW Lee *et al*, J. Opt. Soc. Am. B, 20, 770, (2003)
2. M Koenig *et al*, Plasma Phys. Contr. Fusion, 47, B441, (2005)
3. Frontiers and Challenges in Warm Dense Matter, editors F Gaziani *et al*, (Springer 2014)
4. R More *et al*, J.Quant. Spectrosc. Radiat.Transfer, 99, 409, (2006)
5. N Nettelmann, R Redmer and D Blaschke, Physics of Particles and Nuclei 39, 1122, (2008)
6. A Ng, T Ao, F Perrot, MWC Dharma-Wardana and ME Foord, Laser and Particle Beams, 23, 527, (2005).
7. P Renaudin *et al*, Phys. Rev. Lett. 91, 075002, 2003
8. M Ross, Nature 292 435 (1981)
9. N Nettelmann *et al* Astrophys. J 683 1217, (2008)
10. LB Fletcher *et al*, Nature Photonics 9, 274 (2015)
11. Ya.B. Zel'dovich, Yu.P. Razier, Physics of Shock Waves and High-Temperature Hydrodynamic Phenomena (Academic, New York, 1966 and Dover Publications, New York, 2002)
12. S. P. Lyon, and J. D. Johnson, *SESAME: The Los Alamos National Laboratory Equation of State Database* LANL Technical Report LA-UR-92-3407, Los Alamos National Laboratory, Los Alamos, NM (1992)
13. J Wang *et al*, J. Appl. Phys. 114, 023513 (2013)
14. M Koenig *et al*, High Energy Density Physics, 6, 210, (2010)
15. RJ Trainor *et al*, Phys. Rev. Lett. 42, 1154, 1979
16. CGM van Kessel and R Sigel, Phys. Rev. Lett. 33 1020 (1974)
17. PC Thompson *et al*, J. Phys. D 14, 1215, 1981
18. EM Campbell, Phys. Fluids B 4 3781 (1992)
19. RJ Trainor and YT Lee, Phys. Fluids 25, 1898, (1982)
20. Y Kato *et al*, PRL 53, 1057, (1984)
21. DA Pepler *et al*, Proc. SPIE 2404, Diffractive and Holographic Optics Technology II, 258, (1995)
22. S. Skupsky, R. W. Short, T. Kessler, R. S. Craxton, S. Letzring, and J. M. Soures, J. Appl. Phys. 66, 3456 (1989).
23. S Jackel, D Salzmann, A Krumbein and S Eliezer, Phys. Fluids 26, 318 (1983)
24. D Riley, O Willi, SJ Rose and T Afshar-Rad, Europhysics Letters 10(2) 135 (1989)
25. JH Eggert *et al*, AIP conference Proceedings 1161, 26 (2009)
26. DC Swift and RG Kraus, Phys. Rev. E 77 066402, 2008
27. T Mochizuki *et al*, Phys. Rev. A 33, 525, (1986)
28. P Goldstone *et al*, Phys. Rev. Lett. 59, 56, (1987)
29. DR Kania *et al*, Phys. Rev. A 46 7853, (1992)
30. J Wang *et al* J. Appl. Phys., 114, 023513 (2013)
31. Th. Lower *et al*, Phys. Rev. Lett. 72, 3186, (1994)
32. R Cauble *et al*, Phys. Rev. Lett. 70, 2102, (1993)
33. TS Perry *et al* Phys. Rev. E, 58, 3739, (1998)
34. DW Phillion and CJ Hailey Phys. Rev. A 34 4886, 1986
35. B Kettle *et al* J. Phys. B 48 224002 (2015)
36. SH Glenzer *et al*, Phys. Rev. Lett. 90, 175002, 2003
37. B Kettle *et al*, Phys. Rev. E 94 023203, 2016
38. A Levy *et al*, Phys. Plasmas, 22, 030703 (2015)
39. RA Snavely *et al*, Phys. Rev. Lett. 85, 2945, (2000)
40. F Wagner *et al* Phys. Rev. Lett. 116 2005202, (2016)
41. PK Patel *et al*, Phys. Rev. Lett. 91, 125004, (2003)
42. FN Beg *et al*, Phys. Plasmas 4 447 (1997)
43. AR Bell *et al*, Plasma Phys.Control. Fusion 39 653, (1997)
44. SB Hansen *et al*, Phys. Rev.E 72 036408, 2005
45. NC Woolsey, D Riley and E Nardi, Rev. Sci. Instr. 69(2) 418-424 (1998)
46. D Riley *et al*, Phys. Rev. Lett. 84(8) 1704-1707 (2000)
47. T Ma *et al*, Phys. Rev. Lett. 110, 065001, (2013)
48. SH Glenzer and R Redmer Rev. Mod. Phys. 81, 1625, (2009)



49. G Gregori *et al*, Phys. Rev. E, 67, 026412 (2003)
50. G Gregori *et al*, Phys. Plasm. 11, 2754, (2004)
51. K Wunsch, J Vorberger and DO Gericke Phys. Rev.E79, 010201(R) (2009)
52. S. Ichimaru, Rev. Mod Phys. 54, 1017 (1982)
53. *Compton Scattering*, ed. Brian Williams, (McGraw Hill International, 1977)
54. SH Glenzer *et al*, Phys. Rev. Lett. 98, 065002, 2007
55. P Neumayer *et al*, Phys. Rev. Lett. 105, 075003, 2010
56. JC Stewart and K. D. Pyatt, Astrophys. J. 144, 1203 (1966)
57. DK Bradley *et al*, Phys. Rev. Lett. 59 2995 (1987)
58. BJB Crowley, H.E.D.P. 13, 13 (2014)
59. TA Hall *et al*, Phys. Rev. Lett. 60, 2034, (1988)
60. A Levy *et al*, Plasma Phys. Control. Fusion 51 124021, (2009)
61. JE Miller *et al*, Review of Scientific Instruments 78, 034903 (2007)
62. P. M. Celliers, *et al*, Rev. Sci. Instrum. 75, 4916 (2004)
63. K. Falk *et al*, Phys. Rev. E 90, 033107 (2014)
64. M Makita *et al*, Phys. Plasmas 21 023113 (2014)
65. D Hoarty *et al*, Phys. Rev. Lett. 110, 265003, 2013



HELLENIC
MEDITERRANEAN
UNIVERSITY



université
BORDEAUX



Erasmus+

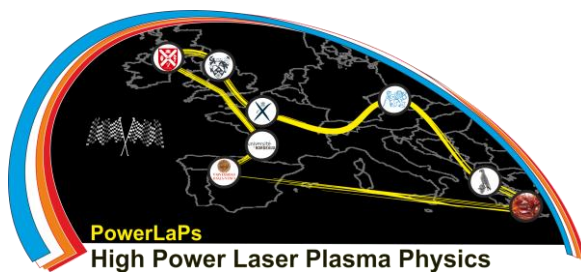
PowerLaPs

Innovative Education & Training in High Power Laser Plasmas

High Power Laser Matter Interactions/High Energy Density Physics - Theory and Experiments

Chapter 13: Fast electron beam transport

J.J. Santos



université
de BORDEAUX



13. Fast electron beam transport: theory and bibliographic overview

This textbook provides a physical description of the relevant phenomena occurring in intense laser-plasma interactions (LPI) with over-dense matter, with focus on the generation of fast-electrons and their beamed propagation through matter. It allows the non-specialist to have an overview of the subject as part of a first course on relativistic LPI.

We provide here the basic equations illustrating the experimental findings that will be presented in the lectures. Some back-of-the-envelope calculations allow to predict the typical orders of magnitude for different physical quantities of interest. For those, it has been assumed an LPI regime widely accessible in nowadays experiments. When needed, mostly for results consolidated rather empirically, a bibliographic account complements the description.

Besides the inspiration from the works and results cited thoroughly, I would like to also point out the value of textbooks by Patrick Mora [66], Vladimir Tikhonchuk [97], Paul Gibbon [38] and the review article by A.P.L. Robinson et al.: [81] published in a special topic number of Nuclear Fusion magazine.

The lectures will describe a systematic experiment-driven investigation of how intense currents of fast electrons are generated by high-intensity laser interactions and subsequently propagate and transport energy into over-dense matter – that is of density higher than the critical density for the laser propagation. We will then particularly focus on different approaches to control that propagation in order to obtain the higher energy-density flux that can be produced at the laboratory scale.

13.1 Introduction: Matter at extreme conditions driven by intense electron currents

The research topic is part of a broader discipline which is the study of plasmas at high-energy-density (HED), meaning energy-densities $> 0.1\text{MJ}=\text{cm}^3$. This corresponds to pressures > 1 Mbar, exceeding the bulk modulus of practically every material, therefore leading to strong changes in matter properties and phase changes [32]. Such states appear naturally in the interior of giant planets and in the core of earth-like planets, in compact stars such as brown and white dwarfs, as well as in supernova explosions and gamma ray bursts. Thanks to the rapid development in laser technology over the past half-century, HED matter is nowadays ubiquitous at the laboratory scale in laser-matter interactions related to inertial confinement fusion and to laser-driven secondary sources of radiation and particles. HED states of matter can indeed be reached by laser-matter interactions with high-energy or high-



intensity lasers. In the first case, shock propagation into target depth develops at a nanosecond time scale. In the second case, to which is concerned this textbook and our lectures, energy deposition by fast particle beams produces a rapid, isochoric heating at the target depths.

When the laser intensity is higher than 10^{18} W/cm², the quiver motion of electrons in the laser field is relativistic and the laser energy coupling to the plasma created in the focal spot area, in particular to the electrons (more mobile), is very rapid and efficient. For such intense laser-matter interactions at the critical density surface of dense targets, the total energy transmitted as a fast electron beam (FEB) into the target depth can amount to between 20% and 40% of the incident laser energy. We are here concerned with the understanding, the control and optimization of such energy vector. The capability of delivering energy into matter depths unreachable by laser light or other kinds of collimated electromagnetic radiation has, for the last decades, animated a broad scientific interest towards progress in the production of laser-driven intense sources of energetic particles and radiation [59], in driving matter to extreme temperatures creating state regimes relevant for planetary or stellar science [42], as well as, a major motivation within the HED-matter scientific community, in achieving high-gain laser-driven controlled thermonuclear fusion [96, 5, 71, 81, 91].

13.1.1 Fast ignition in laser-driven thermonuclear fusion for energy

Inertial Confinement Fusion (ICF) consists in compressing by its own inertia a ~ 1 mm-radius spherical capsule formed by an ablator on the exterior and a nuclear fuel layer on the inner surface. The fuel consists of a few mg of deuterium-tritium mix (DT). In the more conventional approach, the capsule implosion is driven by plasma ablation when irradiated by electromagnetic (e.m.) radiation, the more isotropically as possible, over a time-scale of ~ 20 ns. The e.m. radiation is either ~ 2 MJ-energy lasers (direct drive) or x-rays generated by those lasers in a *hohlraum* of high-atomic number Z containing the capsule (indirect drive). Typically the DT should be compressed by about 1000 times, forming at stagnation a central hot spot of density $\sim 10^{26}$ cm $^{-3}$ and temperature > 5 keV enough high to ignite and self-sustain nuclear reactions by absorption of the α -particles issuing from fusion of D and T.

The *fast ignition* (FI) scheme proposes to separate the compression and ignition phases of the capsule [96, 4], as illustrated in Fig. 1.1a). In contrast to the isobaric central hot spot ignition of the above approaches, FI would be obtained isochorically from the rapid heating of the stagnated DT core due to the lateral energy deposition of a beam of fast particles. Such particle beam is ought to be generated by a very powerful ignitor laser. Electron fast ignition is the more scrutinized scheme, but the use of protons or ions beams have also been proposed [82], representing different challenges in terms of target design [34] which are beyond the scope of this manuscript.

For the *electron-driven-FI*, Atzeni *et al.* estimated the optimal FEB parameters allowing to minimize the ignitor laser energy, upon modeling of the target hydrodynamics and burn of the nuclear fuel [4, 5]:

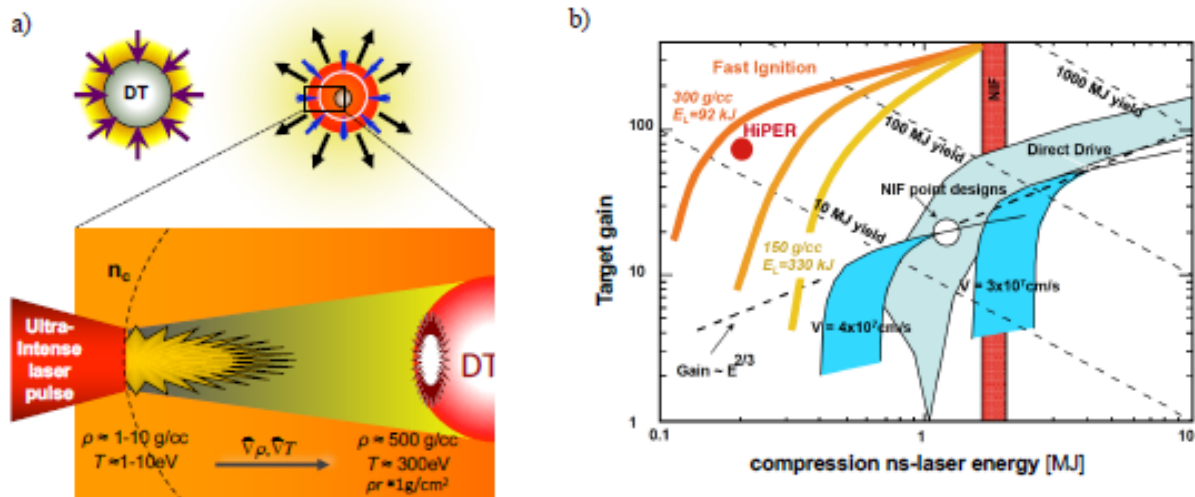


Figure 1.1: a) Illustration of the fast ignition scheme for laser fusion: the spherical target is irradiated by long-pulse lasers (top left), which produces plasma ablation and implosion by inertial effect (top right), the compressed DT core is then heated to thermonuclear temperatures by an intense beam of laser-generated particles of high energy (zoomed on the bottom diagram). b) Predictions of ICF target energy-gain as a function of the compression-laser energy. The red dot represents the prediction for a FI-target design.

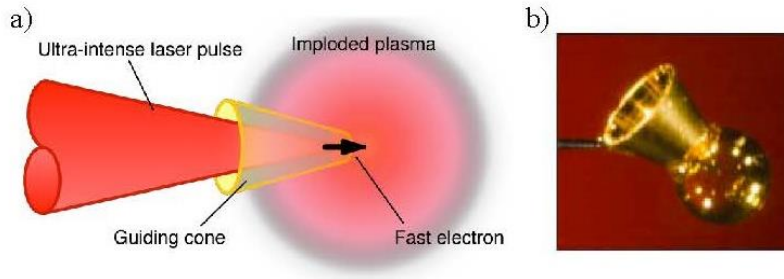


Figure 1.2: a) Schematic of cone-guided FI approach b) Photograph of cone-attached shell target used for integrated experiments on OMEGA. Figure taken from [71].

$$W_{h, \text{ign}} = 140 \rho_{100}^{-1.85} \text{ kJ} , \quad (1.1)$$

$$I_{h, \text{ign}} = 2.4 \times 10^{19} \rho_{100}^{0.95} \text{ W/cm}^2 , \quad (1.2)$$

$$\tau_{h, \text{ign}} = 54 \rho_{100}^{-0.85} \text{ ps} , \quad (1.3)$$

$$r_{hs} = 60 \rho_{100}^{-0.97} \mu\text{m} , \quad (1.4)$$

respectively for the FEB total kinetic energy, intensity and duration when reaching the DT core, and the radius of the lateral hot-spot. ρ_{100} is the density of the outer layer of the compressed core in units of 100 g/cm^3 . Expected compressed DT densities are in the range of $3 < \rho_{100} < 10$. The scaling above predicts that $W_{h, \text{ign}} \gtrsim 20 \text{ kJ}$, $I_{h, \text{ign}} \approx 10^{20} \text{ W/cm}^2$, $\tau_{h, \text{ign}} \approx 20 \text{ ps}$ and $r_{hs} \lesssim 20 \mu\text{m}$ are needed for ignition. An average electron energy in the range of 1-2 MeV would be enough energetic to cross the coronal plasma surrounding the compressed DT core, yet not too much energetic so as to be efficiently absorbed by the core $\rho r_{hs} \sim 1 \text{ g/cm}^2$ areal density.

The theory expects an advantageous ~ 10 times higher gain for FI compared to conventional direct or indirect drive schemes, while investing a significantly lower laser energy: 350 kJ instead of 2 MJ, of which 250 kJ would be used to compress the target [see Fig. 1.1b)]. The additional 100 kJ correspond to the needed 10 ps-duration ignitor pulse beam (the target stagnation lasts no longer than 20 ps), yielding 10 PW laser power and 10^{20} W/cm^2 laser intensity.

For the most developed FI-target design, the spherical target comprises a re-entrant cone embedded into the spherical shell [68, 53, 52, 51], as illustrated in Fig. 1.2. The idea is to keep a clear path for the ignition laser pulse into the inner cone tip, protected from the plasma produced during target implosion by the long laser beams. The cone walls and tip must withstand the extreme hydrodynamic conditions produced during compression, so it is foreseen to use cones of a dense material (of high atomic number Z , *e.g.* Au). The cone insertion is not of easy design as its tip should be located as close as possible to the center of the shell in order to minimize the propagation distance from the zone of the ignitor laser interaction and fast particle injection to the DT core surface [91]. For an optimum cone-in-shell target design so far, the particle beam source is at a minimum $100 \mu\text{m}$ standoff distance [90].

Besides the required lower laser energy, other advantages of FI are related to the lateral hotspot ignition, which makes the target implosion efficiency much less sensitive to the development of hydrodynamic instabilities, tolerating a certain anisotropy on the laser irradiation and on the initial rugosity state of the target surface. Moreover, the growth rate of those instabilities becomes lower than in the case of a conventional implosion, given the lower compression laser energy and the resulting lower implosion velocity. The targets' implosion is much more robust and should tolerate even the anisotropy inherent to the inserted cone.

The FEB-source needed for fast ignition

The key macroscopic parameters of the fast electron source required for fast ignition are the electrons mean energy, the fraction of energy transfer from the ignition laser to the fast electron beam, and the its angular divergence.

Fast electron energy distribution and mean energy The efficient energy coupling to the dense core requires the mean free path of those electrons to match the core's $\sim 1 \text{ g/cm}^2$ areal density at stagnation. As mentioned above, this constrains the electrons mean kinetic energy to be less than 1.5-2 MeV [5]. In turn, this constrains the ignitor laser intensity to be in the range between a few 10^{19} and 10^{20} W/cm^2 , according to the generally accepted scaling laws [11, 105] (see Sec. 1.2.2).

Fraction of laser energy transferred to fast electrons Given the stringent energy constraints in the FI scheme – specifically, the needed ignitor laser energy should by no means exceed 100 kJ, to respect reasonable predictions on the capability of laser technology – the conversion of the ignitor-laser energy into forward directed fast electrons, $\eta_{L \rightarrow e}$, should be the highest possible. In practice, only two parameters are left available to tune the most efficient source in an integrated FI experiment: these are the wavelength λ and the normalized density scale length L_n/λ in the laser interaction region. Collected different data from the literature yields $\eta_{L \rightarrow e}$ in the range of 20 to 40%, for variable laser parameters [104, 67, 102, 103] (see also Sec. 1.2.2).

Fast electron beam divergence For the present laser specifications and target design towards FI demonstration, one should expect a FEB divergence cone half-angle close to 30° [39, 71] targeting the DT core within a spot of $20 \mu\text{m}$ -radius standing at a minimum distance of $\gtrsim 100 \mu\text{m}$ from the FEB-source surface [90]. From a strictly ballistic point of view – that is, ignoring even the scattering of fast electrons with the background plasma – such broad angular distribution means that about 90% of the fast electrons generated by the ignition laser may not reach the compressed DT core within the required dimensions of the hot spot.

The *divergence issue* is considered the main bottleneck for FI feasibility. It seems to be intrinsically related to the laser-plasma interaction and the development of e.m. instabilities at the interaction surface [2, 29], and up to now there are no proposed methods to control it at the source. A major challenge is therefore to ensure a guided FEB propagation within the FI integrated target design, and indeed one of the concerns in my research has been to devise strategies to provide a FEB-transport over dense matter with a minimized radial-spread.

The extreme parameters of fast electron beams in FI

The energy requirements for fast ignition determine that a fast electrons charge of about 10 mC ought to be delivered to the $20 \mu\text{m}$ radius compressed DT core within a time shorter than 20 ps. This corresponds to currents of $\sim 1 \text{ GA}$ and current densities up to 10^{14} A/cm^2 . Even for the more modest parameters of nowadays experiments, intense laser-plasma interactions with, say 100 J, 1 ps laser pulses focused to $\sim 10^{19} \text{ W/cm}^2$, can inject into the depth of dense targets a total charge of $\sim 10 \mu\text{C}$ of MeV-electron beams, representing $\sim 10^7 \text{ A}$ currents and 10^{11} to 10^{13} A/cm^2 current densities.

These extremely intense currents largely exceed the limit of $\approx 17 \text{ kA}$ for charged particle transport in vacuum, known as the Alfvén limit [3]. Yet, in a dense plasma (or gas that is directly ionized by the incident electrons), the incident current can be neutralized by a counter-stream of electrons from the background, the so-called *return current*, and transport the energy of the electrons over large distances. But the mechanisms determining the stability of this transport are rather complex: collective mechanisms are associated with huge fields spontaneously induced by the important charge separation and currents. They contribute to the magnetic focusing or defocusing of the electron beam, to its resistive deceleration and even, in certain conditions, for the beam development into filaments. To these effects one should add the better known collisional processes of electron deceleration and angular diffusion. The deposited energy heats the propagation material, isochorically given the $\sim \text{ps}$ time-scale of the process, along with rapid transient changes on the way the material dielectrically responds to the intense e.m. perturbations, mainly as a function of the temperature. A physical description of all these processes is presented in Chapter 1.

Research challenges

From the above, four main objectives can be identified for FEB-transport investigations in the context of FI:

- To precisely characterize the FEB-source in terms of energy and angle distributions, for the wider possible range of laser parameters (energy, duration, intensity, intensity-contrast) and plasma scale-length;

- To understand the mechanisms of FEB-transport, in terms of energy losses, diffusion and guiding, either in solid-cold or in denser-warm samples (obtained by shock-compression);
- In the specific approach of FI, to study the hydrodynamics of target compression, the perturbations produced on the cone by the compression (and vice-versa) and the specific characteristics of the FEB-source issuing from laser interactions with the inner tip of the cone;
- To undertake integrated experiments (that is, comprising compression and electron transport) and assess – for the present laser capabilities, still under-scaled for FI – the compression efficiency and the efficiency of the laser energy coupling to the dense core of the compressed targets.

13.2 Intense laser interaction with over-dense matter

Consider laser light described by an electromagnetic (e.m.) mono-chromatic wave of frequency ω_0 – for now non relativistic – characterized by the electric-field (E-field) $\vec{E} = \Re(E) \exp(i(\vec{k} \cdot \vec{r} - \omega_0 t))$ and the magnetic-field (B-field) $\vec{B} = \Re(B) \exp(i(\vec{k} \cdot \vec{r} - \omega_0 t))$, where \vec{k} is the wave vector. The propagation of this e.m. wave in a plasma of density of free electrons n_e is described by the equation:

$$\nabla^2 \vec{E} - \frac{1}{c^2} \frac{\partial^2 \vec{E}}{\partial t^2} = \frac{\omega_{pe}^2}{c^2} \vec{E} \quad (1.5)$$

where c is the speed of light in vacuum, and $\omega_{pe} = (n_e e^2 / \epsilon_0 m_e)^{1/2}$ is the plasma-electron frequency, ϵ_0 is the dielectric permeability of vacuum, m_e and e are respectively the electron rest mass and elementary charge. The plasma-electron period $2\pi/\omega_{pe}$ characterizes the time-scale of the plasma dielectric response to deviations in space charge neutrality. Solving eq. 1.5 leads to the following dispersion equation:

$$\omega_0^2 = \omega_{pe}^2 + k^2 c^2. \quad (1.6)$$

We consider here *over-dense* plasmas, for which n_e is bigger than the critical density:

$$n_c = \frac{\epsilon_0 m_e \omega_0^2}{e^2} = \frac{1.1 \times 10^{21} \text{ cm}^3}{\lambda_{\mu\text{m}}^2}, \quad (1.7)$$

where $\lambda_{\mu\text{m}}$ is the laser wavelength expressed in μm . The laser cannot propagate inside such plasmas as the refraction index $N = (1 - \omega_{pe}^2/\omega_0^2)^{1/2} = (1 - n_e/n_c)^{1/2}$ becomes imaginary: the plasma polarization fields screen the laser field and this vanishes over a short *skin depth* distance $\delta_s \approx c/\omega_{pe}$. This means that interactions between the laser pulse and the plasma particles can only occur in the *under-dense* region or close to the critical surface, that is for $n_e \leq n_c$.

This picture becomes to some extent modified in the relativistic regime, that is for enough intense laser pulses such that the norm of the electron quiver velocity $\vec{v}_{osc} = e\vec{E}/m_e\omega_0$ compares to c . The ratio \vec{v}_{osc}/c corresponds also to the normalized vector potential of the laser pulse:

$$\vec{a} = \frac{e\vec{A}}{m_e c^2} = \frac{e\vec{E}}{m_e \omega_0 c}, \quad a = 0.85 \sqrt{I_{18} \lambda_{\mu\text{m}}^2}, \quad (1.8)$$

where \vec{A} and I_{18} are respectively the vector potential and the intensity of the laser light in units of 10^{18} W/cm^2 . It is then clear that for typical infra-red (IR) light lasers with $\lambda_{\mu\text{m}} \approx 1$, the relativistic regime is accessed for laser intensities above 10^{18} W/cm^2 . The electron's rest mass must then be replaced by its effective mass $m_e \rightarrow \gamma m_e$, where the correction is the relativistic factor $\gamma = \sqrt{1 + p^2/m_e^2 c^2} = \sqrt{1 + a^2}$ (p is the norm of the electron momentum). As the effective mass increases, background electrons feel less easy to follow the oscillations of the laser's e.m. field. As a consequence, the refraction index becomes

$$N = (1 - n_e/(\gamma n_c))^{1/2}. \quad (1.9)$$

Accordingly, laser propagation in the relativistic regime extends to the density range up to γn_c , an effect called *self-induced relativistic transparency*. As the laser pulse has a spatially- and temporally-varying profile, the description complicates to account for the local variation of the electron density due to ponderomotive

effects (see Sec.1.2.2). Numerical simulations have shown that, in such conditions, the laser propagation undergoes strong instabilities which lead to strong laser energy losses and strong electron heating [60].

13.2.1 Electron dynamics under a relativistic electromagnetic wave

Consider a free electron, initially at rest, under the effect of a relativistic e.m. wave propagating in vacuum. The electron motion is determined by the Lorentz force according to the following equation:

$$\frac{d\vec{p}}{dt} = -e(\vec{E} + \vec{v} \times \vec{B}), \quad (1.10)$$

where $\vec{p} = \gamma m_e \vec{v}$ is the electron momentum. As the amplitude of the wave's magnetic and electric fields are related by $B = E/c$, one understands that for relativistic velocities $v \lesssim c$, the magnetic effect on the electron's motion becomes as important as the electric effect. The following shows that indeed, due to the magnetic contribution the electron acquires motion also in the direction of the laser incidence.

As the wave electric and magnetic fields are derived from the vector potential \vec{A} : $\vec{E} = -\partial_t \vec{A}$, $\vec{B} = \nabla \times \vec{A}$, we can write the following equations respectively for the electron motion and for the transport of its kinetic energy $\varepsilon_h = (\gamma - 1)m_e c^2$:

$$\frac{d}{dt}(\vec{p} - e\vec{A}) = e(\vec{v} \cdot \vec{\nabla})\vec{A} - e\nabla(\vec{v} \cdot \vec{A}), \quad (1.11)$$

$$\frac{d\varepsilon_h}{dt} = e\vec{v} \cdot \frac{\partial \vec{A}}{\partial t}. \quad (1.12)$$

Supposing a plane e.m. wave propagating along the z -direction, $\vec{A} = \vec{A}_\perp(z, t)$, and decomposing the electron motion into the components parallel and perpendicular to the laser wave vector $\vec{k} = k\vec{e}_z$, $\vec{p} = \vec{p}_\parallel + \vec{p}_\perp$, it comes for eq. 1.11 in the perpendicular plane:

$$\frac{d}{dt}\vec{p}_\perp = e\frac{\partial}{\partial t}\vec{A}_\perp + ev_\parallel \frac{\partial}{\partial z}\vec{A}_\perp \equiv e\frac{d}{dt}\vec{A}_\perp(z_h(t), t), \quad (1.13)$$

describing the conservation of the generalized electron momentum $\vec{P}_\perp = \vec{p}_\perp - e\vec{A}_\perp$ over the electron trajectory $z_h(t) = \int_0^t v_\parallel dt$. This yields $\vec{p}_\perp(t) = e\vec{A}_\perp(z_h(t), t)$ for an electron that was initially at rest. Inserting this into the equation for the parallel motion, yields successively

$$\frac{d}{dt}p_\parallel = -\frac{e}{\gamma m_e}\vec{p}_\perp \cdot \frac{\partial}{\partial z}\vec{A}_\perp = -\frac{e^2}{2\gamma m_e}\frac{\partial}{\partial z}\vec{A}_\perp^2, \quad (1.14)$$

In the same manner, eq. 1.12 can now be written as

$$\frac{d\varepsilon_h}{dt} = \frac{e^2}{2\gamma m_e}\frac{\partial}{\partial t}\vec{A}_\perp^2, \quad (1.15)$$

and an important result yields from the subtraction of eqs. 1.14 and 1.15:

$$\frac{d}{dt}(\varepsilon_h - p_\parallel c) = \frac{e^2}{2\gamma m_e}\left(\frac{\partial}{\partial t} + c\frac{\partial}{\partial z}\right)\vec{A}_\perp^2. \quad (1.16)$$

As \vec{A} depends only on $\tau = t - z/c$, the right-hand side of the above equation is null, yielding the conservation equation $\varepsilon_h - p_\parallel c = 0$ (as the electron was initially at rest) and successively $p_\parallel = p_\perp^2/2m_e c$. This determines the angle of the electron moment with respect to the laser wave vector:

$$\tan \theta = \frac{p_\perp}{p_\parallel} = \sqrt{\frac{2}{\gamma - 1}}, \quad (1.17)$$

as schematized in Fig. 1.3 showing the electron trajectory in the focused intense laser field. Note in particular that according to eq. 1.17, in the ultra-relativistic regime, $eA \gg m_e c$, the electron momentum becomes practically longitudinal.

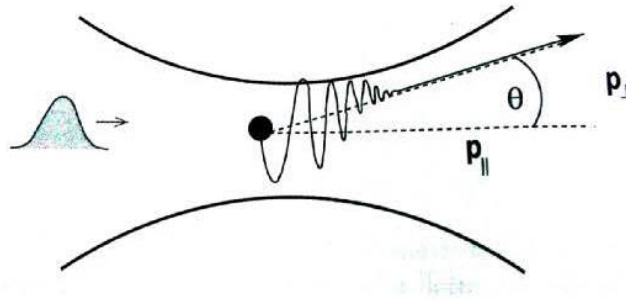


Figure 1.3: Schematics of the relativistic electron motion at the focus of a high-power laser pulse. Figure taken from [38].

Electron trajectory in a linearly-polarized e.m. field

Let us consider the case of a linearly-polarized wave, $e\vec{A}/m_e c = a \cos(\omega\tau)\vec{e}_x$, corresponding to the case of all the laser pulses of our experiments. The electron trajectory in the laboratory frame is given by [38]

$$kx = a \sin(\omega\tau) , \quad (1.18)$$

$$kz = \frac{a^2}{8} (2\omega\tau + \sin(2\omega\tau)) , \quad (1.19)$$

where $k = \omega/c$ is the wave number. The trajectory is represented in Fig.1.4a), where the abscissa coordinates for the longitudinal phase kz are shrunk by the factor a^2 . The electron movement along the laser propagation direction corresponds to a drift speed averaged over the laser period

$$\vec{v}_{\text{drift}} = \frac{a^2}{a^2 + 4} c \vec{e}_z . \quad (1.20)$$

Considering the realistic case of a laser pulse of finite duration, the electron is accelerated by the rising edge and then immediately slowed down by the decreasing edge, coming back to rest when the laser pulse has passed [38]. If the field amplitude changes slowly during a laser period, it follows from the electron adiabatic motion that the particle does not gain any energy from the laser. However, even if the electron comes back to its initial position in the perpendicular direction, it still moves along the laser propagation axis by a distance $\Delta z = \int v_{\text{drift}}(t) dt$ determined by the laser intensity and duration.¹

In the frame moving with the longitudinal drift speed (electron rest frame), the electron describes 8-shaped closed orbits, as represented in Fig.1.4b) and described by the equations:

$$k'x't' = \frac{a}{\sqrt{1 + a^2/2}} \sin(\omega'\tau') , \quad (1.21)$$

$$k'z't' = \frac{a^2}{8(1 + a^2/2)} \sin(2\omega'\tau') . \quad (1.22)$$

The *prime*-symbol refer to quantities measured in the moving frame.

13.2.2 Ponderomotive force, mechanisms of laser energy absorption and fast electron beam generation in dense plasmas

More realistically, the laser interaction processes with a plasma, not with a single electron in vacuum. Several conditions or processes can break the electron's motion adiabaticity, such as collisions with the background ions, strong density gradients or electric fields.

¹For more realistic laser beams of limited spot size, a transverse electron drift it is also predicted [77].

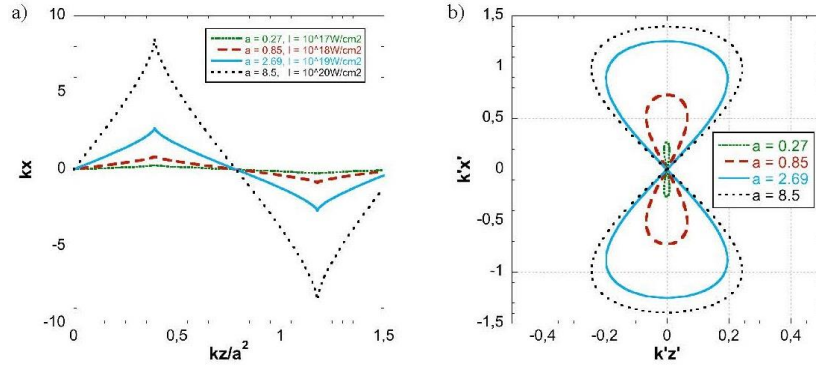


Figure 1.4: Electron orbits under a relativistic linearly-polarized e.m. wave, **a)** in the laboratory frame and **b)** in its own rest frame. The different orbits correspond to: $a = 0.27$ (dotted line), $a = 0.85$ (dashed line), $a = 2.69$ (solid line) and $a = 8.5$ (dash-dotted line), corresponding respectively to laser intensities $I_L = 10^{17}$, 10^{18} , 10^{19} and 10^{20} W/cm² (for $\lambda = 1 \mu\text{m}$).

The laser energy can be more or less efficiently transferred to the plasma electrons according to the interaction intensity regime, to the plasma density profile (often linked to the contrast in laser intensity) and to the geometry of the laser incidence. Supposing laser intensities $I_L > 10^{16}$ W/cm², the energy transfer and electron acceleration process (or processes) can be described by different collective mechanisms: resonant absorption [36], parametric instabilities such as stimulated Raman scattering (SRS), and two plasmon decay (TPD) [54], direct ponderomotive acceleration (including the so-called $j \times B$ mechanism) [55] or Brunel effect (quasi resonant absorption, also known as *vacuum heating*) [18]. The two last referred mechanisms are non-linear and for the laser intensities of interest, $\geq 10^{18}$ W/cm², are those mainly responsible for the acceleration of intense beams of supra-thermal electrons, *aka* fast electrons.

The energy distribution of the fast electrons is broad, $f(\varepsilon_h) \propto \exp(-\varepsilon_h/T_h)$, characterized by a hot electron temperature T_h typically in the range from hundreds of keV up to some MeV [105, 11]. The parameter T_h is a good approximation to the mean energy of the supra-thermal population, $\bar{\varepsilon}_h$. A further description of the fast electrons distribution is given in Sec. 1.2.3.

Relativistic ponderomotive force and potential

A general version of eq. 1.14 is $d_t \vec{p} = -\frac{e^2}{2\gamma m_e} \vec{\nabla} A^2$, meaning that the electron motion is determined by a force proportional and opposed to the gradient of the laser amplitude to the power of 2, that is of the laser intensity. Supposing again a linearly-polarized wave $\vec{A} = A \cos(\omega_0 \tau) \vec{e}_x$ of slowly varying amplitude following the laser pulse *envelope*, the electron motion equation reads:

$$\frac{d\vec{p}}{dt} = -\frac{e^2}{4\gamma m_e} \left(\vec{\nabla} A^2 + \vec{\nabla} A^2 \cos(2\omega_0 \tau) \right). \quad (1.23)$$

The applied force contains then a component with slow variations and a component oscillating at twice the laser frequency. Averaging over the laser period, we obtain the following equation for the average electron momentum $\langle \vec{p} \rangle$:

$$\frac{d\langle \vec{p} \rangle}{dt} \equiv \vec{F}_P = -\frac{e^2}{4\langle \gamma \rangle m_e} \vec{\nabla} \langle A^2 \rangle. \quad (1.24)$$

with the average relativistic factor $\langle \gamma \rangle = \sqrt{1 + \langle \vec{p} \rangle^2 / m_e^2 c^2 + e^2 \langle A^2 \rangle / m_e^2 c^2}$ [77]. This so-called *ponderomotive force* \vec{F}_P is a non-linear force associated to the slowly-varying (compared to the laser period) space and time profiles of the laser-intensity envelope. It corresponds to the laser pulse radiation pressure, as it pushes particles away of the laser pulse envelope. It acts mainly on electrons (much lighter than ions), leading to charge separation and electrostatic effects in the plasma. This can drive ion motion subsequently, but only at longer time-scales, leading for example to hole boring at the target surface [105].

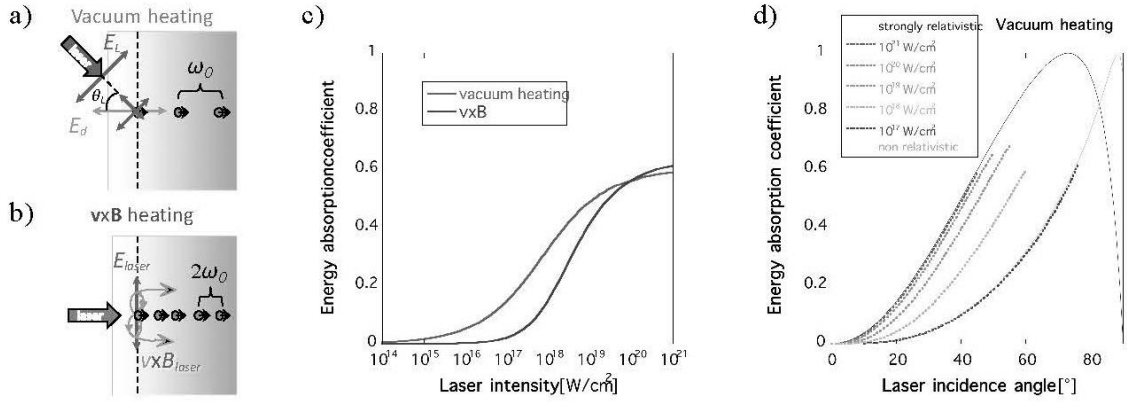


Figure 1.5: Schematics of fast electron acceleration mechanisms: **a)** vacuum heating, **b)** $\vec{v} \times \vec{B}$. **c)** Laser energy absorption coefficient for vacuum heating (eq. 1.28 with $\theta_L = 45^\circ$, in red) and $\vec{v} \times \vec{B}$ (eq. 1.29, in blue), as a function of the laser intensity. **d)** Vacuum heating absorption coefficient as a function of the laser incidence angle: eq. 1.28 for different laser intensities (colored dotted curves), and for the strongly-relativistic (thin black) and the non-relativistic (thin grey) limits.

The ponderomotive force can be expressed in a more compact way:

$$\vec{F}_P = -m_e c^2 \nabla \langle \gamma \rangle, \quad (1.25)$$

which derives from a *ponderomotive potential*:

$$W_P = m_e c^2 (\langle \gamma \rangle - 1). \quad (1.26)$$

By means of numerical simulations using variable $I_L \lambda_L^2$, Wilks *et al.* [105] have shown that the ponderomotive potential provides an approximative value for the expected mean kinetic energy or the characteristic temperature of the accelerated *fast* electrons (scaling represented by the red curve in Fig. 1.7, for $\lambda_{\mu m} = 1$):

$$T_h^{\text{Wilks}} \approx m_e c^2 (\sqrt{1 + a^2} - 1) = 511 \text{ keV} \left(\sqrt{1 + 0.73 I_{18} \lambda_{\mu m}^2} - 1 \right). \quad (1.27)$$

Vacuum heating

Vacuum heating has been first proposed by F. Brunel [18] and it is expected of very high efficiency for the laser energy absorption in intense LPI with sharp-density plasma boundaries, *i.e.* when the pre-plasma thickness (or its density scale length $L_n \equiv n_e / |\nabla n_e|$) is smaller than the electrons oscillation range in the laser field. It assumes a p-polarized laser field with non null laser incidence angle θ_L with respect to the target surface normal [see sketch in Fig. 1.5a)].

The mechanism can be described by a *capacitor-like* DC model, similarly to ref. [38]. The laser E-field, which penetrates on the dense plasma over the skin depth (enlarged in the relativistic case by the increase of the electron's mass), can extract a bunch of electrons at every cycle $2\pi/\omega_0$ over an excursion distance d into vacuum. The extracted electrons experience there a longitudinal field established by the superposition of the incident and reflected laser light, $E_d = f E_0 \sin \theta_L$, where the field amplification factor is $f = 1 + (1 - \eta_{L \rightarrow e})^{1/2}$ and $\eta_{L \rightarrow e}$ is the laser energy absorption coefficient to be estimated.

If δn_e is the electron density in the ejected bunch, on the following half-cycle the bunch is pulled back into the plasma bulk due to the space charge field of the order of $E_p = e \delta n_e d / \epsilon_0 \sim E_d$. As the space charge field fades rapidly in the plasma, the electron bunch ceases of being adiabatically coupled to the oscillation, being injected into the plasma depth. It transports part of the absorbed laser energy that has been converted into kinetic energy, consistently with the ponderomotive potential $\varepsilon_h \sim W_P = m_e c^2 (\gamma_d - 1)$ (eq. 1.26). Here the relativistic factor is $\gamma_d = \sqrt{1 + f^2 a^2 \sin^2 \theta_L}$. In principle ε_h is now much higher than the bulk electrons thermal energy.

The laser energy absorption coefficient can be estimated from the ratio of the intensity of the electron bunches injected into the plasma depth, by the intensity of the laser field projected over the target surface normal $\eta_{L \rightarrow e} = I_{\text{abs}}/I_d$. The first is related to the surface density of ejected and re-injected electrons, their kinetic energy and the characteristic time τ , $I_{\text{abs}} = \frac{1}{\tau} \varepsilon_h \delta n_e d$, and the second is $I_d = \frac{1}{2} c \varepsilon_0 E^2 \cos \theta_L$. The described *vacuum heating* (v.h.) mechanism processes at each laser cycle $\tau = 2\pi/\omega_0$, and the ratio yields:

$$\eta_{L \rightarrow e}^{\text{v.h.}} = \frac{I_{\text{abs}}^{\text{v.h.}}}{I_d} = \frac{1}{\pi a} f \left(\sqrt{1 + f^2 a^2 \sin^2 \theta_L} - 1 \right) \frac{\sin \theta_L}{\cos \theta_L}, \quad (1.28)$$

which, as $f = f(\eta_{L \rightarrow e})$, is an implicit solution for $\eta_{L \rightarrow e}$. Numerical calculations of eq.1.28 are shown in Fig.1.5c) for $\eta_{L \rightarrow e}^{\text{v.h.}}$ as a function of the laser intensity with $\theta_L = 45^\circ$ (red curve), and in Fig.1.5d) for $\eta_{L \rightarrow e}^{\text{v.h.}}$ as a function of θ_L for different values of I_L (dotted colored curves). We see that $\eta_{L \rightarrow e}^{\text{v.h.}}$ becomes greater than 10% only for $I_L > 10^{17}$ W/cm².

Equation 1.28 can be simplified in two limiting cases, the strongly relativistic $a \gg 1$, and the non relativistic $a \ll 1$, for which the dependence on the laser angle is also plotted in Fig.1.5c) [38]. At very high intensity the absorption is high over a broad angular range, peaking at $\theta \approx 70^\circ$ in the limit case. The peak narrows and shifts towards higher angles as I_L increases.

The more realistic situation with finite density gradients L_n has been simulated using particle-in-cell (PIC) codes. Several results are thoroughly discussed in [38]. The main points are that with $L_n/\lambda = 0.1$ and even for $I_L > 10^{17}$ W/cm², $\eta_{L \rightarrow e}^{\text{v.h.}}$ is always smaller than 20% and tends to peak for laser incidence near 45° , rather than for grazing incident angles as predicted by the above capacitor-model. The limitation at grazing incidence would come from the DC currents set along the target surface and the consequent additional B-field that deflects and inhibits the fast electrons from returning to the plasma bulk.

Relativistic $\vec{v} \times \vec{B}$ heating

Let us now consider a linearly-polarized laser at normal incidence ($\theta_L = 0$) into a target. As already mentioned, if the electron motion in the laser field is relativistic, the $\vec{v} \times \vec{B}$ component of the force exerted on the particles becomes as important as the electric part, yielding in particular the $2\omega_0$ -oscillating component, superposed to the ponderomotive drift associated to the inhomogeneity of the laser intensity (eq.1.23). The oscillating force driving electrons away from the laser spot combined with the electrostatic effect that pulls them back is at the origin of a laser energy absorption leading to electron acceleration.

The mechanism can be modeled by a DC model similar to the above model for the vacuum heating. Electron bunches can be extracted from the target skin depth, in this case at every half laser cycle, $\tau = \pi/\omega_0$, and are then pulled back after an excursion of distance d into vacuum. When reaching the target surface they quit the oscillation and the $\vec{j} \times \vec{B}$ -heating proceeds from their dephasing at every half laser period. The mechanism leads to the injection of a comb of electron bunches of frequency $2\omega_0$ into the target bulk, as illustrated in Fig.1.5b) and in the electrons phase space projections obtained in PIC simulations as those presented in Fig.1.6.

Again, the intensity of the electron bunches injected into the plasma depth $I_{\text{abs}} = \frac{1}{\tau} \varepsilon_h \delta n_e d$ is related to the surface density of ejected and re-injected electrons, their kinetic energy $\varepsilon_h \sim W_P$ and the characteristic time. The surface density of the oscillating electrons can be estimated from $\delta n_e d \approx \varepsilon_0 F_{\parallel} / e^2$, where the longitudinal oscillating force $F_{\parallel} \sim m_e c \omega_0 a^2 / 2\sqrt{1+a^2}$ owes to the $\vec{v} \times \vec{B}$ component of the Lorentz force. The laser energy absorption coefficient is obtained by dividing by the laser intensity $I_L = \frac{1}{2} \varepsilon_0 c E^2$:

$$\eta_{L \rightarrow e}^{\vec{v} \times \vec{B}} = \frac{I_{\text{abs}}^{\vec{v} \times \vec{B}}}{I_L} = \frac{2}{\pi} \left(1 - \frac{1}{\sqrt{1+a^2}} \right). \quad (1.29)$$

The analytical estimation of $\eta_{L \rightarrow e}^{\vec{v} \times \vec{B}}$ is plotted in Fig.1.5c) as a function of the laser intensity (blue curve), for comparison with the absorption coefficient of vacuum heating (in red). In the case of $\vec{v} \times \vec{B}$ -heating, the energy transfer goes higher than 10% only for relativistic intensities, reaching 40% at 10^{19} W/cm².

These theoretical estimations were fairly well verified by detailed PIC simulations and experiments of relativistic laser beams at normal or close to normal incidence into solid foil targets. As examples of such relatively recent experiments one may cite the works of Westover *et al.* [102, 103] and Nilson *et al.* [67], performed with $\lambda_0 = 1 \mu\text{m}$ -laser systems. The first have explored laser pulse intensities up to 10^{20} W/cm² with fixed duration $\tau_L = 1.5$ ps, estimating $\eta_{L \rightarrow e} = 30\% \pm 10\%$. The second limited the maximum laser intensity

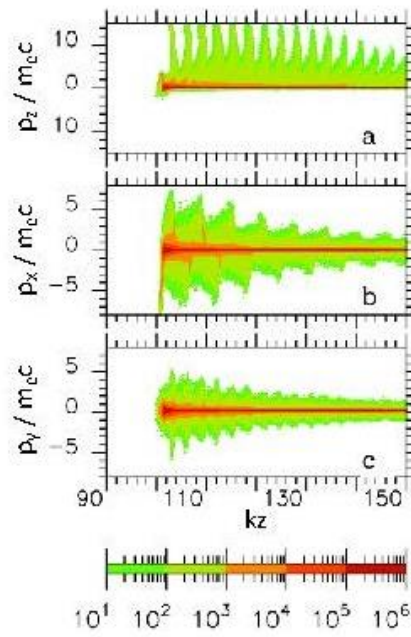


Figure 1.6: Phase space projections of the electronic distribution function. a) Longitudinal momentum. b) Transverse momentum along the direction of the laser electric field. c) Transverse momentum along the direction of the laser magnetic field. Figure taken from [2].

to 10^{19} W/cm², yet scanning the laser pulse between $\tau_L = 1$ ps and 10 ps, that is already to durations more relevant for FI: they estimated $\eta_{L \rightarrow e} = 20\% \pm 10\%$ independently of τ_L .

Each mechanism is responsible for injecting fast electron bunches into the target depth at different frequencies, the same of the laser for the vacuum heating, $\omega_b^{v.h.} = \omega_0$, and at twice the laser frequency for the $\vec{v} \times \vec{B}$ heating, $\omega_b^{v \times B} = 2\omega_0$. However, as in both cases the electrons can be injected at different phases of the laser cycle, their energy distribution is broad, with an average energy assumed to be of the order of the laser ponderomotive potential.

13.2.3 Macroscopic parameters of the FEB-source in dense targets

Laser-accelerated fast electrons have a broad distribution not only in energy, as well in angle θ between \vec{p} and the nominal direction of beam propagation. The distribution function is often represented by a Maxwell-type function for the energy dependence and by a Gaussian function for the angular dependence, as follows:

$$f_h(\varepsilon_h, \theta) \propto \exp\left(-\frac{\varepsilon_h}{T_h}\right) \exp\left(-\frac{\theta^2}{2\Delta\theta^2}\right), \quad (1.30)$$

where the characteristic dispersion angle $\Delta\theta$ is in principle a decreasing function of ε_h , according to eq. 1.17. The *hot-electrons temperature* T_h – truly speaking does not really have a thermodynamic meaning because the FEB is not at equilibrium – is a good approximation of the FEB mean kinetic energy ε_h . It is important to remind that ε_h is in general greater by several orders of magnitude than the temperature of the background thermal electrons, T_e .

As already mentioned in the Introduction, the description of the FEB-source – the population of fast electrons that are injected from the LPI-region into the target depth – is often reduced to three main macroscopic parameters: the fast electrons mean energy (or temperature), divergence (angle distribution) and the total energy (fraction of the laser pulse transferred to the fast electron population).

Fraction of laser energy transferred to fast electrons

The predominance of the different electron acceleration mechanisms and the way the efficiency of the laser energy transfer to fast electrons, $\eta_{L \rightarrow e}$, scale with the laser intensity and wavelength are still open subjects of research. Recently, it has been understood theoretically and by the support of numerical simulations that vacuum heating and $\vec{v} \times \vec{B}$ heating process simultaneously [88, 30].

These conclusions agree with experimental measurements of coherent transition radiation (CTR) spectra. CTR is emitted from the rear surface of solid foils when the comb of fast electron bunches cross the targets' rear surface: the detection of harmonics up to fifth of the laser light frequency, along with modeling of their relative intensity, are consistent with electrons being accelerated by both the laser electric field – via vacuum heating and/or even resonance absorption in the pre-plasma – and the $\vec{v} \times \vec{B}$ component of the Lorentz force [75].

Accounting for the analytical modeling and its confrontation with the PIC simulations and experimental results discussed in the lectures, it is fair to assume that $\eta_{L \rightarrow e} \approx 30 \pm 10\%$ for laser intensities in the range from 10^{18} to 10^{20} W/cm².

Fast electrons temperature

The absorption models detailed in Section 1.2.2 treat how the electron acceleration processes, but there is still some degree of debate in precisely determining the fast electrons energy spectrum from the laser pulse parameters.

The ponderomotive potential energy predicts an estimation for T_h as a function of the laser $I_L \lambda_{\mu m}^2$, eq. 1.27 (red curve in Fig. 1.7). This scaling, verified by PIC simulations [105] was soon after also observed experimentally by spectra measurements of the electrons escaping from solid targets along the laser forward direction. The targets were irradiated at normal incidence by laser pulses of intensity in the range of 2×10^{18} to 10^{19} Wcm⁻² μm^2 [63]. Other later experimental measurements verified this scaling in the same laser intensity range, this time by measurements of K-shell fluorescence [106].

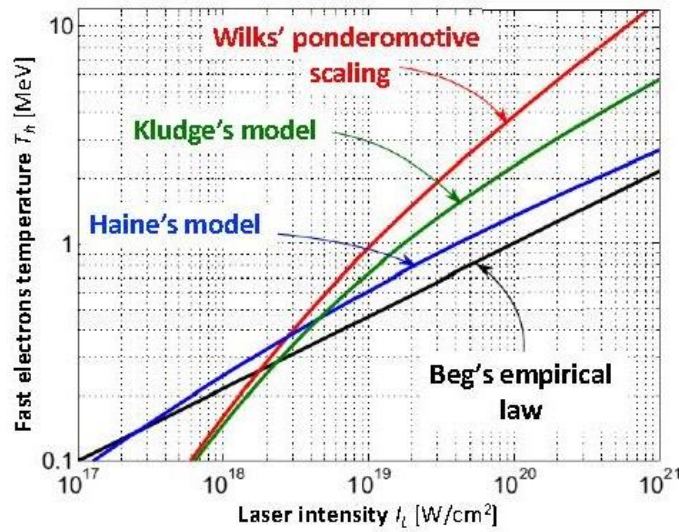


Figure 1.7: Comparison of the different scaling laws for the FEB temperature T_h (or mean kinetic energy $\bar{\varepsilon}_h$) as a function of the laser intensity.

Followed other measurements by Beg *et al.* with equivalent laser parameters but the fast electron characterization was based instead on the detection of x-ray bremsstrahlung. The results indicated a different scaling for T_h [11], the so-called *Beg's law* (black curve in Fig. 1.7):

$$T_h = 0.215(I_L \lambda_{\mu m}^2)^{1/3} \text{ MeV} . \quad (1.31)$$

More recent experiments measuring both Bremsstrahlung spectra and K-shell fluorescence yields confirmed that the Beg's empirical scaling extends to intensities $> 10^{20} \text{ W/cm}^2$ [62, 21, 20, 70].

As seen in Fig. 1.7, Beg's and Wilks' scalings disagree considerably. There is a relatively recent relativistic model by Haines *et al.* [41] predicting that for high laser intensity the electron mean energy is indeed smaller than that predicted by the ponderomotive law because of the density-profile steepening in the interaction zone. Haine's model (blue curve in Fig. 1.7) scales fairly consistently with Beg's law for I_L up to 10^{21} W/cm^2 .

Kluge *et al.* [49] proposed that the scaling of $\bar{\varepsilon}_h$ with I_L could be derived from a general Lorentz invariant electron distribution *ansatz* not relying on a specific model of energy absorption. The model assumptions were confirmed by their PIC simulations. For relativistic laser intensities, the predictions are somehow in between of those from Wilks' and Beg's scaling laws (green curve in Fig. 1.7).

The debate is not finished, and one should not forget that both Wilks' and Beg's scaling laws were established for laser parameters still quite different from the needs of fast ignition.

In the lectures we will discuss the analysis of $K\alpha$ yields from multiple laser-solid experiments, also including FEB-transport shots in shock-driven foils, in conjunction with a comprehensive set of simulations describing the hydrodynamics of the shock compression and electron beam generation and transport. That work lead to the following conclusion: the FEB-energy distribution is more complex than in eq. 1.30, often characterized by a power law $f(\varepsilon_h) \propto (\varepsilon_h/\varepsilon_0)^{-\alpha}$ for the lower energies in the spectrum, and by a Maxwell-type exponential function $f(\varepsilon_h) \propto \exp(-\varepsilon_h/T_h)$ for the higher energies.

One example is given here for the interaction conditions of one of the experiments to be discussed, using the PIC code PICLS [100] [see Fig. 1.8a)]. The FEB angular and the kinetic energy distribution functions were extracted in the overdense plasma, at $21 \leq x \leq 22 \mu\text{m}$, i.e. approximately $\sim 1.5 \mu\text{m}$ beyond the absorption region, to ensure that the electron source is not perturbed by the evanescent waves and the Weibel induced magnetic fields [2]. The computed kinetic energy distribution is temporally averaged over the entire simulation time and fitted over the range $0.01 < \varepsilon_h < 20 \text{ MeV}$ by the following normalized function:

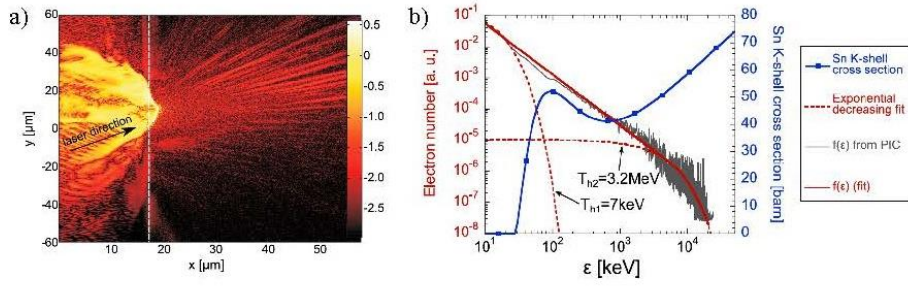


Figure 1.8: Result of a PIC simulation of the interaction of a p-polarized laser pulse with $I_L = 3 \times 10^{19} \text{ W/cm}^2$ and with $\theta_L = 45^\circ$ incidence angle into an Al plasma. The code accounts for both collisions and ionizations, with the initial ionization level self-consistently calculated using the Thomas-Fermi model. **a)** Magnetostatic field $e|B_z|/m_e\omega_0$ in logarithmic scale at the time of maximum laser field reaching the absorption region. The white dashed line at $x = 18 \mu\text{m}$ refers to the preplasma/target boundary. The fast electrons are mainly generated around the laser/plasma boundary, that separates the strong magnetostatic field in the underdense plasma region from the Weibel induced magnetic fields in the overdense region [2]. The magnetic field filaments are attributed to a resistive filamentation instability [40], with the characteristic scale length of the order of the beam skin depth. **b)** FEB energy-distribution function (gray line) and its associated fits: the red solid line corresponds to the fit $f(\epsilon_h)$ given by eq. 1.32, and the two red dashed lines to the often used exponential functions. The blue solid line with squares represents the Sn K-shell ionization cross section.

$$f(\epsilon_h) = \begin{cases} \left(\frac{\epsilon_h}{\epsilon_0}\right)^{-\alpha} & \text{for } 0.01 < \epsilon_h < 5 \text{ MeV} \\ N \exp\left(-\frac{\epsilon_h}{T_h}\right) & \text{for } 5 \leq \epsilon_h < 20 \text{ MeV}, \end{cases} \quad (1.32)$$

where $\epsilon_0 = 1.7 \text{ keV}$, $\alpha = 1.6$, $T_h = 3 \text{ MeV}$ and $N = 1 \times 10^{-5}$ correspond to the fitting parameters. This fit function is plotted on Fig. 1.8b) (red solid line) and compared to the one extracted from the particle-in-cell simulation (in gray). Because of the high number of electrons in the energy range up to $\lesssim 1 \text{ MeV}$, the electron mean kinetic energy is estimated to be $\approx 190 \text{ keV}$, a value much smaller than that given by the ponderomotive scaling, eq. 1.27, $T_h^{\text{Wilks}} \approx 1.8 \text{ MeV}$. As reported previously in the literature [79, 28], the lower energy part of the FEB spectrum is indeed best described by the decreasing power-law function, defined by the parameter α , rather than the commonly used Maxwellian functions (represented by the red dashed lines).

Note that the precaution in carefully describing the fast electrons energy spectrum is fundamental to link FEB-transport simulations to experimental data as it significantly impacts the hard X-ray fluorescence of the targets (or embedded tracer layers). This can be understood by the way the atomic K-shell ionization cross-section of most elements depends on the incident electron energy, represented for the case of Sn by the blue curve in Fig. 1.8b).

Fast electron beam divergence

It has been found in simulation studies that the FEB-source angular distribution depends upon two factors: first, the rippling of the density of the critical surface on the scale of the laser wavelength (in addition to larger scale hole boring) which is important for plasmas with a relatively large density scale length [105, 76, 57]; second, the deflections from small-scale magnetic fields generated by the filamentation instability as the fast electrons enter the target [92, 79, 2, 29].

The divergence should in principle decrease with the electron energy within the FEB, as predicted from the electron dynamics in the laser field, eq. 1.17. Yet there is no precise characterization as the FEB-source is not directly measurable on the experiments (cf. Sec. 1.4).

Most authors associate the FEB average divergence to the slope of the best linear fit to the evolution of the FEB-radius for varying target thickness, independently of the individual electron energies, taking the size of a radiative signature as the corresponding FEB-size. For example, Green *et al.* have performed spatial resolved measurements of the x-ray $K\alpha$ emission from intermediate atomic number ($Z < 10$) fluorescent layers buried at different depths on multi-layer solid targets and have compiled results from other several

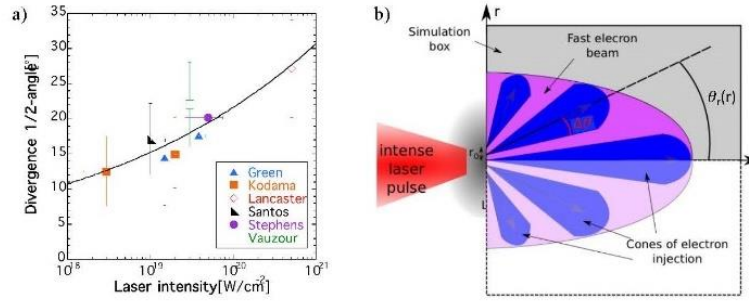


Figure 1.9: **a)** Data from the literature [39, 56, 53, 51, 83, 94, 100] for electron beam divergence (cone half-angle, HWHM) as a function of the laser intensity. The power-law fit corresponds to eq. 1.33. **b)** Illustration of the angular distribution function of fast electrons inferred from PIC simulations, eq. 1.34: for each injection radial position r , particles propagate along an axis given by θ_r with a dispersion of $\Delta\theta$ around this axis. This function is used in our studies as input of the FEB-source in transport simulations following the PIC simulations.

experiments [39]: Figure 1.9a) shows those data corresponding to the so-called *divergence-cone* half-angle (at half-width-half-height, HWHM), as a function of the laser intensity. The plot shows that the electrons diverge with angles between 10° and 30° raising with the laser intensity between 10^{18} and 10^{21} W/cm 2 . It is worth noting that the data trend is fairly regular, even if the data points are from experiments carried out in many different laser facilities, therefore acquired with different laser interaction conditions. Namely different laser focal spots were used, ranging from 3.5 to $20 \mu\text{m}$ radius, meaning this should not be a significant parameter. 2D PIC simulations presented in the same paper [39] and reproducing the trend lead to conclude that the electron beam divergence dependence on the laser intensity is a fundamental property of the laser-plasma interaction. The data of Fig. 1.9a) is fitted by the following power law (black line):

$$\theta_{1/2}^{\text{fit}} = 0.02 I_L^{0.15} . \quad (1.33)$$

In simplified rigid-models of FEB propagation [85, 87, 71], the evolution of the radial spread of the FEB against target depth z is roughly approximated by the linear law $r_h(z) = r_0 + z \tan(\theta_{1/2})$. It is also assumed, for simplicity, that $\theta_{1/2}$ is a constant value independent of ε_h and of the radial position of its injection at the target front surface.

Instead, intensive PIC simulations (as those already mentioned above) converged to the following description of the FEB-source angular distribution [29, 27], much more detailed than that in eq. 1.30:

$$f(\theta, r) = \exp\left(\frac{-(\theta - \theta_r)^2}{\Delta\theta^2}\right), \quad (1.34)$$

where $\theta_r = \theta_0 + \arctan(\tan(\theta_{r0})r/r_h)$ is the mean radial angle as a function of the injection position radius r , r_h is the initial FEB radius, and $\Delta\theta$ is the dispersion angle, as sketched in Fig. 1.9b). For the simulation presented in Fig. 1.8, the FEB angular distribution was fitted with the parameters $r_h = 20 \mu\text{m}$ (about four times larger than the laser focal spot radius), $\Delta\theta \sim 55^\circ$, $\theta_0 = 18^\circ$ and $\theta_{r0} = 30^\circ$.

As a final remark, and according to the obtained description, let us note that the electron beam in this simulation propagates with an average angle of $\theta_0 \approx 18^\circ$ from the target normal direction [see Fig. 1.8a)]. This angle is a typical feature of oblique incident laser interaction with an overdense plasma: of $\theta_L = 45^\circ$ for the considered case. Indeed, the electron beam direction is, at the lowest order, defined by transverse momentum conservation of the electrons in the boosted frame [16]. As a result, the electron propagation angle θ_0 can be estimated by [22]:

$$\sin \theta_0 = \sin \theta_L \sqrt{\frac{\gamma - 1}{\gamma + 1}} . \quad (1.35)$$

Hence, ultra-relativistic electrons would propagate along the laser incident wave direction (consistent with eq. 1.17), while the low energetic electrons would instead propagate in a direction closer to the normal to the

target surface. Considering the mean electron energy of 190 keV, characterized for the simulation in Fig. 1.8 (eq. 1.32), the associated prediction for the mean propagation angle would be of the order of $\theta_0 \sim 20^\circ$, a value consistent with the mean propagation angle $\theta_0 = 18^\circ$ measured in the simulation.

13.3 Fast electron beam transport in dense matter

Given their charge and their very small mass, electrons are easily accelerated. Yet given the total charge and currents involved in electron beam transport, their propagation is self-consistent with the generated electric and magnetic fields. If the incident charge and current are not neutralized, beams collapse under the effect of electrostatic repulsion and of magnetic pinching. The limiting current was initially estimated by Alfv n for the situation where the self-generated B-field is sufficiently strong to inverse the electron propagation [3]:

$$I_{\text{Alfv n}} \approx \frac{\gamma_h \beta_h m_e c^3}{e} \approx \gamma_h \beta_h 1.7 \times 10^4 \text{ A} . \quad (1.36)$$

where γ_h and $\beta_h = v_h/c$ are the fast electron beam average relativistic parameter and velocity normalized to the speed of light.

If the transported current is higher it will progressively converge to the *Alfv n limit*, unless the propagation medium can neutralize the incident beam. The problem appears for electron beam propagation in vacuum (obviously) and in insulator materials (where free electrons are not instantaneously available and can only be provided by material ionization). On the contrary, plasmas and metals have enough electrons available (respectively free or in the conduction band) to provide almost instantaneously the needed neutralization charge and current, a flux of thermal background electrons called *return current*. Thermal electrons are accelerated both by electrostatic field driven by the unbalanced positive charge left behind by the fast electrons, and by magnetic induction due to the variations in the fast electrons current.

13.3.1 The return current and neutralization of charge and current

Let us suppose the injection of a beam of fast electrons, of density $n_h \approx 10^{21} \text{ cm}^3$, average energy $\varepsilon_h = m_e c^2 (\gamma_h - 1) \approx 1 \text{ MeV}$ and length l_h into a dense thermal plasma of density $n_e \gg n_h$. The beam duration roughly compares to the laser pulse duration $\tau_h = l_h/v_h \gtrsim \tau_L$ (between 25 fs and 10 ps for the different laser parameters exploited in our experiments). The radius of the FEB is taken, empirically, to be 3 to 4 times the size of the intense laser focal spot radius. Let us assume $r_h \approx 10 \mu\text{m}$.

In the hypothetical case where there is no return current – which we can suppose valid only for the very first moments – the injection of the fast electron beam installs an electrostatic field $E_{\text{init}}(t) \approx j_h t / \epsilon_0$ (E-field), where $j_h = en_h v_h \approx 10^{12} \text{ A/cm}^2$ is the current density of the FEB and the numerator is the total transported surfacic charge, raising in time. E_{init} can easily reach 10^{12} V/m in just $t = 1 \text{ fs}$, which is enough to stop MeV electrons over only a $1 \mu\text{m}$ -distance.

Indeed, and according to the reduced Ohm's law, a counter-streaming current of thermal electrons can be driven by the E-field: $j_e = E_{\text{init}}/\eta$. Here we consider the Drude's model for the plasma resistivity $\eta = m_e \nu / n_e e^2$ with the collision frequency of the thermal electrons, ν . The peak resistivity of many conducting solids is $\eta \approx 10^{-6} \Omega\text{m}$, reached at Fermi temperature $T_F \approx 1\text{-}10 \text{ eV}$. The return current is spatially coincident with the fast electron current and, to a good approximation, cancels both globally and locally the incident current of fast electrons:²

$$\vec{j}_h + \vec{j}_e \approx 0 . \quad (1.37)$$

The above condition of current neutralization shows that the average speed of the electrons in the return current is $v_e \approx v_h n_h / n_e \ll v_h$, that is non-relativistic. These electrons are therefore highly collisional, which validates the resistive description of their propagation through Ohm's law.

The presence of a neutralizing return current and its implications in fast electron transport were first postulated by Bell *et al.* [13] and experimental evidence and relevance of *electric field effects* versus direct fast electron collisional effects was first inferred in [104, 48], as well as in [74]. This last work compared the propagation of fast electrons in insulators and conductors, in which by definition the target resistivity is different. In metals the return current is easily established by the free background electrons in the conduction

²Locally unbalanced current filaments lead to B-field growth that can destroy the beam.

band and this easily neutralizes the incoming fast electron current. In insulators, free electrons must be created by an initial ionization and the return current is initially weaker.

How fast is set the return current and the neutralization of the fast electrons current? It depends on the collisional nature of the material, in particular how ν compares to the plasma electron frequency ω_{pe} :

- In a **collisional medium** ($\nu > \omega_{pe}$), the characteristic neutralization time can be estimated from the continuity equation, yielding $\tau_{\text{neut}} \sim \eta \epsilon_0 \sim \nu / \omega_{pe}^2$.
- In a **non collisional medium** such an hot plasma ($\nu < \omega_{pe}$), the E-field excites electron plasma waves and the neutralization time is given by their damping time $\tau_{\text{neut}} \sim 1/\nu$.

In both cases and for typical beam and plasma parameters τ_{neut} is estimated to only a few tenths of fs, which is indeed very fast compared to the typical beam duration τ_h . The beam neutralization can therefore be considered as an instantaneous process.

The incident fast electrons current can be roughly estimated from the energy-density flux condition at the laser interaction surface $j_h \epsilon_h eV = \frac{\eta_{L \rightarrow e} W_L}{\tau_h \pi r_h^2}$, which for $\eta_{L \rightarrow e} = 0.3$, $W_L = 100$ J, $\tau_h = 1$ ps and $r_h = 10 \mu\text{m}$ yields $j_h \approx 10^{13}$ A/cm² at the source. It is reasonable to consider that j_h drops fast to $\approx 10^{12}$ A/cm² due to the natural divergence of electron beam and the collisionality of the lower energy part of its spectrum.

Assuming then the validity of eq.1.37 once the return current is set, one still gets a residual E-field $E = \eta j_h \approx 10^{10}$ V/m. This field is significantly smaller than the E_{init} estimated before but it is enough strong to still inhibit fast electron transport. From Faraday's law one can besides estimate the amplitude of the B-field associated to the neutralized electron transport and the residual E-field, $B \sim \tau_h E / r_h$, which amounts to ≈ 1 kT for $\tau_h = 1$ ps.

The setting of the return current allows the accelerated fast electrons to propagate into the dense target to depths in the range of $100 \mu\text{m}$. Still, collisions endured by the thermal electrons will deteriorate the neutralization mechanism as they diffuse both the return current and the associated B-field, as described by the resistive diffusion equation:

$$\frac{\partial \vec{B}}{\partial t} = \frac{\eta}{\mu_0} \nabla^2 \vec{B}. \quad (1.38)$$

It is worth noting that current neutralization is only maintained till a characteristic time for the B-field diffusion $\tau_{\text{diff}} \approx \mu_0 L^2 / \eta$. We can take the typical electron beam radius $L \sim r_h \approx 10 \mu\text{m}$ as the characteristic spatial scale, and $\eta = 10^{-6} \Omega\text{m}$, yielding $\tau_{\text{diff}} \sim 100$ ps. Fortunately, it is considerably larger than the electron beam duration τ_h .

13.3.2 Fast electron beam energy-loss mechanisms and induced heating

While propagating through dense matter the beam electrons will endure energy losses and diffusion through individual collisions with the background material as well as energy losses and beam tailoring by the collective effects due to self-generated fields. Altogether, these effects will determine the beam energy-density flux and the capability to efficiently transport and deliver energy into deep regions.

Stopping and scattering of individual fast electrons

We consider the collisional transport of individual fast electrons through plasmas or solid matter. Collective effects due to the presence of multiple fast electrons (correlations) can be neglected as the fast electron density is much smaller than the electron density of the crossed material, $n_h \ll n_e$ [31, 17]. Two kinds of collisions have distinct effects: elastic collisions with the background atoms and ions produce the angular scattering of the incident electrons, and consequently influence the global divergence of the beam; inelastic collisions with background bound and free electrons and plasmons are responsible for energy losses.

The following presents expressions for the collisional stopping and scattering powers, as detailed in the review ref. [81] and references therein. The results are tabulated by the International Commission on Radiation Units and Measurements (ICRUM) [95] and can be obtained using the code ESTAR, available online through the National Institute of Standard and Technology (NIST) [1].

Collisional stopping Fast electrons collisions with background bound and free electrons, as well as individual electron interactions with plasma waves (plasmons), are responsible for significant energy loss. The expression for the stopping rate of a fast electron of kinetic energy ε and momentum $\vec{p} = \gamma m_e \vec{v}$ in *all kind of matter* (solid, liquid, gas or plasma, conductor or insulator) is:

$$\frac{d\varepsilon}{dt} = -\frac{n_{et}e^4}{4\pi\epsilon_0^2 m_e v} L_d, \quad (1.39)$$

$$\text{with } L_d = \ln \frac{pv}{\sqrt{\gamma + 1} \hbar \omega_p} - \ln \frac{\ln 2}{2} + \frac{9}{16} + \frac{\frac{1}{2} \ln 2 + \frac{1}{16}}{\gamma^2} - \frac{\ln 2 + \frac{1}{8}}{\gamma}, \quad (1.40)$$

Bremsstrahlung is neglected for now. The dimensionless parameter L_d is known in plasma physics as the Coulomb logarithm $\ln \Lambda$. Z is the atomic number and n_{et} is the density of all the background electrons (not only the free electrons) which in the expression also determines the plasma frequency ω_p .

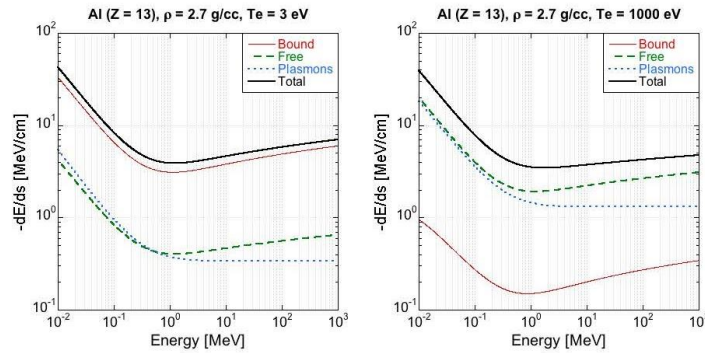


Figure 1.10: Electron collisional stopping power in solid-density Al at $T_e = 3 \text{ eV}$ (left) and $T_e = 1000 \text{ eV}$ (right), as a function of the incident electron kinetic energy. The total stopping power (black solid line) yields from the contribution of different processes: collisions with bound electrons (red thin solid line), free electrons (green dashed line) and plasmons (blue dotted line). Graphs taken from [99].

Figure 1.10 shows the different contributions to the stopping power (amount of lost energy per unit length) plot as a function of the incident electron kinetic energy in solid-density Al with background electron temperature $T_e = 3 \text{ eV}$ (left) and $T_e = 1000 \text{ eV}$ (right). The roles of the collisions with bound (solid red) and free (dashed green) electrons are inverted when the background temperature raises enough. Plasma waves (dotted blue) play an important role only for high temperature, typically for $T_e > 100 \text{ eV}$. Yet, the summed contributions into a total collisional stopping power (solid black) depends weakly on T_e .

The individual electron interactions with dense targets also goes along energy loss through the emission of radiation, a process called Bremsstrahlung. Such photon emission increases with Z^2 . In a given material it increases rapidly with ε , compared to the logarithmic dependence of the collisional stopping power, becoming the dominant energy loss mechanism for highly relativistic electrons, as seen in Fig. 1.11 for cold Al (left) or cold Au (right) targets. The radiative losses can be neglected for the typical fast electron energy range of our experiments or in a full-scale FI experiment, except for the $\sim 10 \mu\text{m}$ -thick Au cone-tip where the ignitor laser would generate the FEB.

A practical physical parameter is the fast electrons *range*, that is the maximum distance over which an electron of given initial energy ε_0 can propagate in matter before being stopped. Assuming that the electron propagates in a straight line, the range can be expressed as

$$R = -\int_0^{\varepsilon_0} \left(\frac{d\varepsilon_0}{dz} \right)^{-1} d\varepsilon_0. \quad (1.41)$$

This range is plotted in Fig. 1.12 as a function of ε_0 for solid Al (solid black) and Au (solid orange). Incident electrons with initial energies $< 40 \text{ keV}$ are stopped within less than $10 \mu\text{m}$ of Al. The same thickness of Au would absorb all electrons with $\varepsilon_0 < 80 \text{ keV}$.

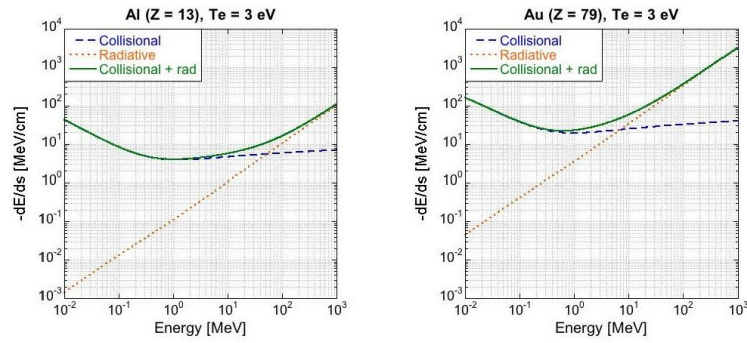


Figure 1.11: Evolution of the collisional stopping power with (green solid lines) and without (blue dashed line) taking into account the radiative effects (orange dotted lines) as a function of the incident electron energy, for Al (left) and Au (right) targets at $T_e = 3$ eV. Figure taken from [99].

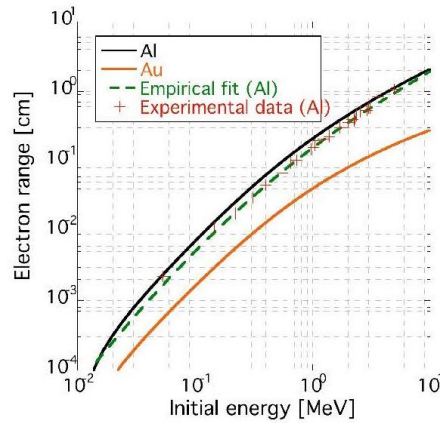


Figure 1.12: Evolution of the maximum range of fast electrons as a function of their initial energy estimated by eq. 1.41 in solid Al (black solid line) and Au (orange full line) targets. The range in Al is compared to the measurements (red crosses) and the empirical law of Katz & Penfold, eq. 1.42 (green dashed line) [47].

The above formulation over-estimates the electron range as in reality fast electrons are scattered by multiple collisions with the background atoms. Katz & Penfold established the following empirical law generalized for any material of density ρ , on the basis of experimental measurements in Al targets [47]:

$$R[\text{cm}] = \begin{cases} \frac{0.412}{\rho[\text{g/cc}]} \varepsilon_0^{1.265 - 0.0954 \ln \varepsilon_0} & \text{for } 0.01 < \varepsilon_0 < 2.5 \text{ MeV} \\ \frac{1}{\rho[\text{g/cc}]} (0.53 \varepsilon_0 - 0.106) & \text{for } \varepsilon_0 \geq 2.5 \text{ MeV} \end{cases} \quad (1.42)$$

Katz & Penfold's empirical law as well as their experimental measurements are also plotted in Fig. 1.12.

Collisional angular scattering Collisions with background ions are elastic and do not contribute to the slowing down of an electron because of a large mass difference: an incident fast electron is scattered while *practically keeping* its initial energy. The rate of angular scattering is:

$$\frac{d\langle \theta^2 \rangle}{dt} = \frac{n_{et} e^4}{2\pi \epsilon_0^2 p^2 v} \left((Z+1)L_s - \frac{1}{2} \ln \frac{\gamma+3}{2} \right), \quad (1.43)$$

$$L_s \approx \ln \frac{2\lambda_{Sp}}{\hbar} - 0.234 - 0.659\beta^2, \quad (1.44)$$

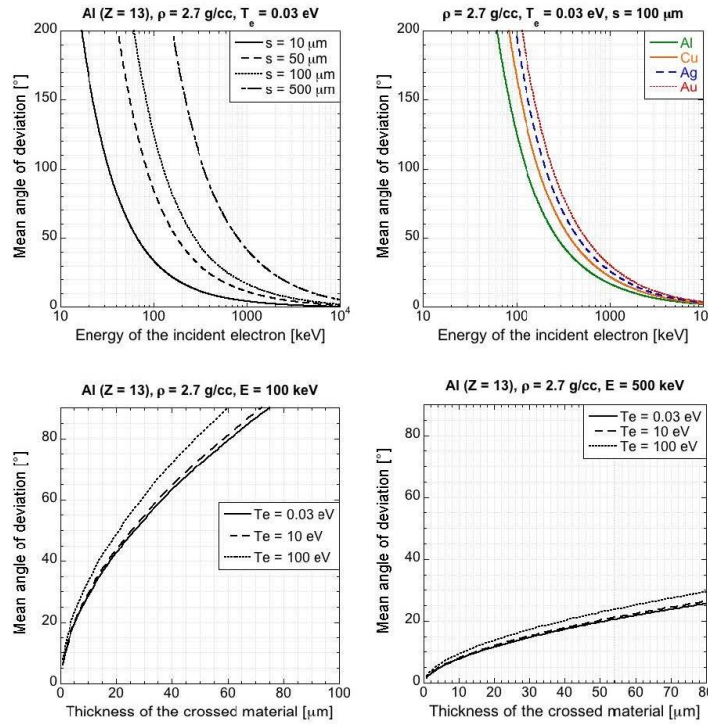


Figure 1.13: Mean angle of deviation induced by elastic scattering different path lengths in cold Al, $s = 10 \mu\text{m}$ (solid line), $s = 50 \mu\text{m}$ (dashed line), $s = 100 \mu\text{m}$ (dotted line) and $s = 500 \mu\text{m}$ (dashed-dotted line) as a function of the incident electron energy (top left). Evolution of the mean angle of deviation as a function of the incident electron energy in different cold-solid materials: Al (green solid line), Cu (orange solid line), Ag (blue dashed line) and Au (red dotted line) (Top right). Mean angle of deviation in aluminum targets for 100 keV and 500 keV electrons (bottom left and bottom right, respectively) as a function of the penetration range s for different background material temperature: 0.03 eV (solid line), 10 eV (dashed line) and 100 eV (dotted line). Figure taken from [99].

where $\langle\theta^2\rangle$ is the mean square scattering angle with respect to the electron's instantaneous direction of motion. The scattering number L_s is calculated supposing a screening distance λ_S either taken as the atomic radius for an unionized material, or as the Debye length $\lambda_D = \sqrt{(\epsilon_0 k_B T_e / n_e e^2)}$ if in a plasma.

Scattering increases the angular spread of the FEB, which can be a serious difficulty at the tip of a high- Z cone in a FI-target. The accumulated root-mean-square scattering angle over the path length s is given by:

$$\langle\theta^2\rangle^{1/2} \approx \frac{Ze^2}{\epsilon_0 p v} \sqrt{\frac{n_a s L_s}{2\pi}}, \quad (1.45)$$

where n_a is the atom number density. The evolution of the deviation angle as a function of the incident electron energy and of the penetration range is plotted in Fig. 1.13, for different materials. As expected, the mean scattering angle increases with the path range s and decreases with the energy of the incident electron. It is also shown that it increases with the background electron temperature T_e . The propagation of high energy electrons ($\gtrsim 500 \text{ keV}$) is not so much influenced by elastic collisions. In compressed targets however, as it is the case in some of our experiments and definitively in a FI-target, the increase of the material density is responsible for an enhanced diffusion, even for high energy particles.

It is worth noting that the FEB divergence is mainly determined by the laser-plasma interaction and the subsequent beam source angular distribution [29], and in a lesser extent by the elastic electron-ion collisions in the target depth just described.

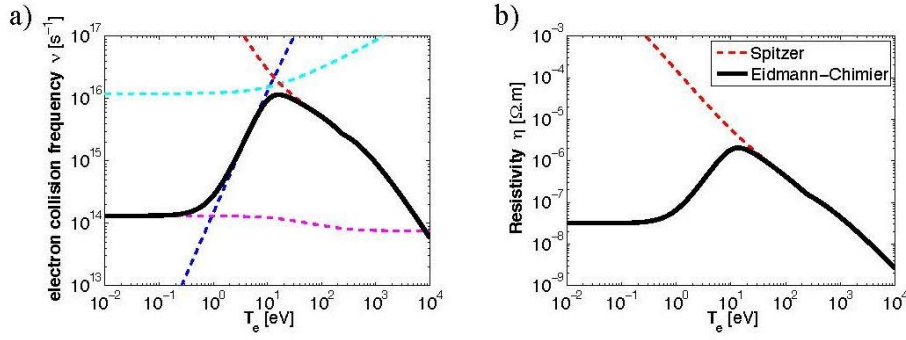


Figure 1.14: **a)** Evolution of the electron collision frequency ν_e (solid black) and its different contributions ν_{e-ph} (dashed purple), ν_{e-e} (dashed dark blue), ν_c (dashed light blue) and ν_{sp} (dashed red) as a function of the electron temperature, considering a constant cold ion temperature $T_i = 0.03$ eV. **b)** Aluminum material resistivity given by both the Eidmann-Chimier model [33, 23] and by the Spitzer model [93] for $T_i = 0.03$ eV.

Resistive losses

As the return current is mostly composed of thermal electrons, it is highly collisional and plays an important role in energy deposition. Adopting a resistive fluid description for the return current \vec{j}_e , the resistive electric field (E-field) is given by Ohm's law:

$$\vec{E} = \eta \vec{j}_e. \quad (1.46)$$

Collision frequency of the thermal particles and plasma resistivity The material electrical resistivity η is a function of the background state (electron and ion temperatures, density, ionization state) and can be computed using the classical Drude's model: $\eta = m_e \nu_e / e^2 n_e$, where ν_e is the harmonic mean of the thermal electrons collision frequency, as given by the Eidmann-Chimier model [33, 23]:

$$\nu_e^{-2} = (\nu_{e-ph} + \nu_{e-e})^{-2} + \nu_c^{-2} + \nu_{sp}^{-2}. \quad (1.47)$$

The harmonic mean resistivity and the different contributions are plotted in Fig.1.14a) for the case of solid Al, as a function of the electron temperature T_e and assuming cold ions $T_i = 0$ (following an ultra-fast non-equilibrium heating process). The terms $\nu_{e-ph} = 2g_0 e^2 T_i / 4\pi \epsilon_0 v_F \hbar^2$ and $\nu_{e-e} = g_1 T_e^2 / \hbar T_F$ refer to the electron-phonon (dashed purple line) and electron-electron (dashed dark blue) collision frequencies, respectively. $T_F = m_e v_F^2 / 2$ and $v_F = \hbar (3\pi^2 n_e)^{1/3} / m_e$ are the Fermi temperature and velocity, respectively. The parameter g_0 is calculated knowing the metal resistivity at a given temperature T_i . The parameter $g_1 \sim 1 - 10$ is approximately known for several metals. In the case of Al, $g_0 = 1.25$ and $g_1 = 1$. The electron-electron collision frequency becomes important for an electron temperature higher than a decimal fraction of the Fermi temperature. The increase of the electron collision rate with the electron temperature is saturated above the Fermi temperature because the mean time of flight between two collisions cannot be shorter than the time of flight over the interatomic distance $d_0 = (3/4\pi n_i)^{1/3}$. Consequently, the collision frequency has to be limited to the maximum rate $\nu_c = (k_B T_e / m_e)^{1/2} / d_0$ (dashed light blue). For electron temperature well above the Fermi temperature, the electron-ion collisions in a classical non-degenerated plasma become the dominant effect and the resistivity is given by the Spitzer formula: $\nu_{sp} = g_2 Z^* e^4 n_e \ln \Lambda / m_e^{1/2} T_e^{3/2}$ (dashed red), with $g_2 = 1/\sqrt{2\pi} (8\epsilon_0)^2$ [93]. Z^* is the ionization state and $\ln \Lambda$ the Coulomb logarithm. Figure 1.14b) plots the corresponding Al resistivity using Drude's law (solid black line), compared to the Spitzer resistivity (dashed red) valid only at high temperature for classical uncorrelated and non-degenerated classical plasmas.

Resistive stopping power Assuming the full current neutralization in FEB transport, $j_e = j_h$, the FEB average resistive stopping power can be expressed by:

$$\frac{d\varepsilon_h}{dz}|_{\text{ohm}} = -eE = -\eta j_h . \quad (1.48)$$

For a typical resistivity η varying between 10^{-7} and $10^{-6} \Omega\text{m}$ [see Fig.1.14b)] and a FEB current density $j_h = 10^{12} \text{ A/cm}^2$, the resistive stopping power is on the range of 1 to 10 keV/ μm

The stronger resistive losses will occur for FEB propagation in warm dense matter (WDM). This matter state stands for near solid densities ($\rho \approx 0.01\text{-}100 \text{ g/cm}^3$) and temperatures of a few eV ($1 \text{ eV} = 11604 \text{ K}$), close to Fermi temperature. In such conditions matter is too dense to be described as weakly coupled plasmas and too hot to be considered as condensed matter. It covers the transition between the *normal* behavior of matter resistivity at temperatures much below the Fermi temperature, T_F , where the electron collision rate is ruled by the *e-ph* collisions, and the Spitzer regime at high temperatures where the electron collision rate is ruled by the *e-i* collisions. WDM is a state of matter which is commonly obtained in today's experiments. It appears in the solid to plasma phase transition driven by the ns laser pulses. WDM can also be reached rapidly by rapid isochoric heating of solid-density targets, directly by a short-pulse intense laser or by the energetic particles (electrons, ions) that the laser accelerates [10, 72]. FEB transport in WDM samples is relevant for ICF as this state may correspond to several outer layers of the imploded capsules, which can be in the FEB path. Also the cone material, heated by thermal or compression waves due to the implosion or by the FEB-itself, likely corresponds to WDM. The description of this matter state is therefore essential for understanding the ongoing physics and allowing a benchmarking of simulation codes.

Resistive heating The plasma electron heating rate by resistive effect can be described by the energy conservation equation:

$$C_e \frac{\partial T_e}{\partial t} = j_e \cdot \vec{E} = \eta j_h^2 , \quad (1.49)$$

where C_e is the heat capacity of the plasma electrons at constant volume. Assuming the background material as an ideal gaz of plasma electrons, $C_e = \frac{3}{2} n_e$, Ohmic heating can heat a solid density target at a rate of 0.1 - 1 keV/ps. This introduces other important aspect following the heating induced by the fast electrons current that is the change in target resistivity $\eta = \eta(T_e)$ [26, 35, 44].

The following model, proposed in ref. [100], provides a more detailed calculation of the resistive stopping power and the induced heating, accounting for the transient behavior of η as a function of the evolving background electron temperature. As simplifications, the model neglects the evolution of the ionization state and the energy deposition by the direct collisions, as well as heat conduction (given the ps time-scale of the energy deposition).

If the FEB-current density is sufficiently intense to heat the medium to a temperature far beyond the Fermi temperature ($T_e \gg T_F$) it is possible to separate the collision frequency, eq.1.47, and hence the resistivity, into four distinct regions, each one corresponding to a temperature range where a given collision process dominates, i.e. electron-phonon (ν_{e-ph}), electron-electron (ν_{e-e}) and electron-ion (ν_{sp}) collisions as well as the saturation regime (ν_c). Hence, the resistivity can be expressed as follows:

$$\eta = \begin{cases} \eta_{e-ph} & \text{for } T_0 \leq T_e \leq T_1 \\ \eta_1 \left(\frac{T_e}{T_1} \right)^2 & \text{for } T_1 \leq T_e \leq T_2 \\ \eta_2 \left(\frac{T_e}{T_2} \right)^{\frac{1}{2}} & \text{for } T_2 \leq T_e \leq T_3 \\ \eta_3 \left(\frac{T_e}{T_3} \right)^{-\frac{3}{2}} & \text{for } T_3 \leq T_e \end{cases} , \quad (1.50)$$

where

$$\eta_{e-ph} = m_e \nu_{e-ph} / e^2 n_e \quad (1.51)$$

$$\eta_1 = m_e \nu_{e-e}(T_1) / e^2 n_e \quad (1.52)$$

$$\eta_2 = m_e \nu_c(T_2) / e^2 n_e \quad (1.53)$$

$$\eta_3 = m_e \nu_{sp}(T_3) / e^2 n_e . \quad (1.54)$$

The transition temperatures are deduced from the above equations accounting for the continuity of the resistivity evolution:

$$T_1 = (2g_0 e^2 T_i T_F / 4\pi \varepsilon_0 g_1 v_F \hbar)^{1/2} \ll T_F \quad (1.55)$$

$$T_2 = (T_F \hbar / g_1 m_e^{1/2} r_0)^{2/3} \sim T_F \quad (1.56)$$

$$T_3 = (g_2 Z^* n_e e^4 r_0 \ln \Lambda)^{1/2} \gg T_F . \quad (1.57)$$

In the following the Coulomb logarithm is assumed constant, $\ln \Lambda = 4$, as a further simplification.

In a similar way, the heat capacity is separated into two regions:

$$C_e = \begin{cases} \frac{3}{2} n_e \frac{T_e}{T_2} & \text{for } T_e \leq T_2 \\ \frac{3}{2} n_e & \text{for } T_e > T_2 \end{cases} , \quad (1.58)$$

Within this simplification, for a degenerated state, $T_e < T_2 \propto T_F$, the heat capacity is proportional to $n_e T_e / T_F$, consistent with a free fermion gas where $C_e = \pi^2 T_e n_e / (2T_F)$. For temperatures higher than T_2 , the plasma electron gas can be considered as ideal.

For an initial temperature T_0 smaller than T_1 (solid Al sample case) the integration of the energy conservation equation 1.49 provides the temporal evolution of the plasma electron temperature:

$$T_e^{\text{solid}}(t) = \begin{cases} T_0 \left(1 + \frac{2t}{\tau_0}\right)^{1/2} & \text{for } 0 \leq t \leq t_1 \\ T_1 \exp\left(\frac{t-t_1}{\tau_1}\right) & \text{for } t_1 \leq t \leq t_2 \\ T_2 \left(1 + \frac{t-t_2}{2\tau_2}\right)^2 & \text{for } t_2 \leq t \leq t_3 \\ T_3 \left(1 + \frac{5}{2} \frac{t-t_3}{\tau_3}\right)^{2/5} & \text{for } t \geq t_3 \end{cases} , \quad (1.59)$$

where the characteristic heating times are:

$$\tau_0 = \frac{3n_e T_0^2}{2\eta_{e-ph} j_h^2 T_2} \quad (1.60)$$

$$\tau_1 = \tau_0 \frac{\eta_{e-ph} T_1^2}{\eta_1 T_0^2} \quad (1.61)$$

$$\tau_2 = \tau_1 \frac{\eta_1 T_2^2}{\eta_2 T_1^2} \quad (1.62)$$

$$\tau_3 = \tau_2 \frac{\eta_2 T_3}{\eta_3 T_2} , \quad (1.63)$$

and the transition times are:

$$t_1 = (T_1^2 / T_0^2 - 1) \tau_0 / 2 \quad (1.64)$$

$$t_2 = t_1 + \tau_1 \ln(T_2 / T_1) \quad (1.65)$$

$$t_3 = t_2 + 2\tau_2 \left(\sqrt{T_3 / T_2} - 1\right) . \quad (1.66)$$

The introduction of eq.1.49 in eq.1.48, yields the following for the electron resistive stopping power averaged over the pulse duration τ_h :

$$\begin{aligned} \left\langle \frac{d\varepsilon_h}{dz} \right\rangle_t &= \frac{1}{\tau_h} \int_0^{\tau_h} e E dt \\ &= \frac{e}{j_h \tau_h} \int_{T_0}^{T_{ef}} C_e dT_e = \begin{cases} \frac{3en_e}{2|j_h| \tau_L} \left(\frac{T_2}{2} - \frac{T_0^2}{2T_2} + T_{ef} - T_2 \right) & \text{for } T_{ef} \geq T_2 \\ \frac{3en_e}{2|j_h| \tau_L} \left(\frac{T_{ef}^2}{2T_2} - \frac{T_0^2}{2T_2} \right) & \text{for } T_{ef} < T_2 \end{cases} , \quad (1.67) \end{aligned}$$

where $T_{ef} = T_e(t = \tau_h)$ is the final electron temperature, obtained from eq.1.59.

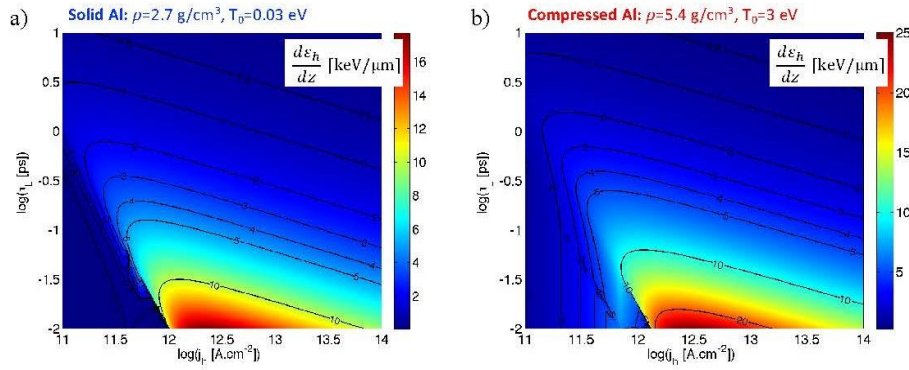


Figure 1.15: Resistive electron stopping power [keV/μm] calculated according to eqs.1.59 and 1.67 as a function of FEB current density j_h and duration τ_h : **a)** for cold Al at solid density: $Z^* = 3$, $\rho = 2.7 \text{ g/cm}^3$, $T_0 = T_i = 0.03 \text{ eV}$, **b)** for compressed and warm Al: $Z^* = 3$, $\rho = 5.4 \text{ g/cm}^3$, $T_0 = 3 \text{ eV}$, $T_i = 0.03 \text{ eV}$. The black lines represent the isocontours.

In the case of FEB-transport in pre-compressed targets, where $T_0 > T_1$, the FEB does not experience the temperature domain where the e - ph collisions occurs. Consequently, the equations are slightly modified yielding for the evolution of the electron temperature:

$$T_e^{\text{comp}}(t) = \begin{cases} T_0 \exp\left(\frac{t}{\tau_1}\right) & \text{for } t \leq t_2 \\ T_2 \left(1 + \frac{t-t'_2}{2\tau_2}\right)^2 & \text{for } t_2 \leq t \leq t_3 \\ T_3 \left(1 + \frac{5}{2} \frac{t-t'_3}{\tau_3}\right)^{2/5} & \text{for } t \geq t_3 \end{cases}, \quad (1.68)$$

with $t'_2 = \tau_1 \ln(T_2/T_0)$, and $t'_3 = t'_2 + 2\tau_2 \left(\sqrt{T_3/T_2} - 1\right)$, the other parameters remaining unchanged.

Calculations for the resistive stopping power, eq 1.67, are presented in Fig. 1.15 for the target conditions of experiments described in Chapter ??: for solid-density Al ($\rho_0 = 2.7 \text{ g/cm}^3$) with $T_0 = 0.03 \text{ eV}$ and shock-compressed Al with $\rho \approx 2\rho$ and $T_0 \approx 3 \text{ eV}$. The results are plotted for FEB current density and duration (j_h , τ_h) for a range of conditions ranging from those found in the experiments (j_h from $\lesssim 10^{11} \text{ A/cm}^2$ to $\gtrsim 10^{13} \text{ A/cm}^2$, τ_L from $\gtrsim 10 \text{ fs}$ to $\gtrsim 10 \text{ ps}$) to the full-scale FI conditions ($j_h \sim 10^{14} \text{ A/cm}^2$, $\tau_L \sim 10 \text{ ps}$).

In the case of cold solid medium, the averaged stopping power is negligible for $j_h \lesssim 10^{11} \text{ A/cm}^2$ such that the final electron temperature is much smaller than the Fermi temperature, $T_{ef} \ll T_F$. Higher values, culminating at maxima of several keV/μm, occur when $T_{ef} \approx T_F$ due to the strong increase of the resistivity averaged over the beam duration (the final value of η corresponds to its maximum). For very high currents, such that the plasma resistivity enters the Spitzer regime, the stopping power decreases again.

The above can also be understood as follows. For sufficiently high current densities, high values of the averaged resistive stopping power occur if the characteristic heating time t_2 needed to reach $T_e \sim T_F$ is of the order of $\approx \tau_h$, in which case the electrons experience the highest resistivity for longer fractions of the total heating process duration. On the other way, if the characteristic time to reach the Spitzer regime is $t_3 < \tau_h$, then the e - i collisions will dominate over time and the resistivity and the associated stopping power does not depend on the medium density and decrease rapidly with temperature. In particular for the FI conditions ($j_h = 10^{14} \text{ A/cm}^2$, $\tau_h = 10 \text{ ps}$), the result does not exceed $\sim 0.5 \text{ keV}/\mu\text{m}$.³

The comparison between the solid and the compressed targets shows a similar behavior over the range of explored (j_h , τ_h) parameters. Yet, the resistive stopping power is globally $\gtrsim 40\%$ higher in the compressed case because the electrons experience the maximum resistivity from the beginning of the FEB propagation.

³The calculations were made here for a solid or a warm-dense metal, which in the FI scenario can be representative of the cone tip material heated by thermal or compression waves.

Resistive stopping *v.s.* collisional stopping For an easier assessment of the predominant role of resistive or collisional energy losses, let us express the collisional stopping power in practical units:

$$\frac{d\varepsilon_h}{dz}|_{\text{coll}} \approx -\frac{30.7\rho[\text{g/cm}^3]}{M[\text{g/mol}]\beta_h^2} \text{keV}/\mu\text{m}, \quad (1.69)$$

where M is the propagation medium molar mass. For MeV electrons propagating in the kind of plasma explored in our experiments, Al at solid-density or two-times compressed, this yields ~ 3.5 or $\sim 7 \text{keV}/\mu\text{m}$ respectively. These values for the collisional stopping power are in the same range of the resistive stopping power predicted above by eq. 1.48 for $j_h = 10^{12} \text{A/cm}^2$, which was between 1 and $10 \text{keV}/\mu\text{m}$ for a medium resistivity between 10^{-7} and $10^{-6} \Omega\text{m}$.

According to the model's more accurate predictions in Fig. 1.15, for the laser and FEB duration of our experiments with solid Al targets, $\langle \frac{d\varepsilon}{dx} \rangle_t|_{\text{ohm}}^{\text{solid}}$ is above $\sim 1 \text{keV}/\mu\text{m}$ and likely playing an important role i) for $j_h > 5 \times 10^{11} \text{A/cm}^2$ with $\tau_h \approx 30 \text{fs}$ [85, 87] and ii) over the window $10^{11} < j_h < 5 \times 10^{12} \text{A/cm}^2$ with $\tau_h \approx 1 \text{ps}$ [101, 100, 98].

Indeed, a few experiments succeeded to evidence the role of the resistive effects in FEB-transport: shots reaching $\bar{j}_h \approx 2.4 \times 10^{11} \text{A/cm}^2$ for the FEB average current density yielded an enhancement of energy losses in more resistive warm Al compared to cold Al targets of the same areal density (that is comparing transport samples where the integrated collisional losses are equivalent) [98]. As predicted by our model, no such evidence appeared in the shots with $\bar{j}_h \approx 8 \times 10^{10} \text{A/cm}^2$ [101, 100].

It is worth to recall that the ionization as well as collisional losses are not taken into account in our resistive model. More generally, the target temperature evolves as the summed contribution from the two mechanisms:

$$C_e \frac{\partial T_e}{\partial t} = \eta j_h^2 + \frac{j_h}{e} \langle |d_z \varepsilon_h|_{\text{coll}} \rangle, \quad (1.70)$$

where the symbol $\langle \dots \rangle$ stands here for the mean over the FEB energy distribution. Hence, the collisional heating component scales as j_h while the Ohmic heating scales as j_h^2 . The dominant heating term may switch from Ohmic heating at the target front to collisional heating at the target rear as j_h drops due to both the FEB radial spread and the progressive energy loss. This was observed in our other experiments in Al-foil targets at solid density [85, 87, 86], and more recently also in Ti wires [89].

As a final remark, let us consider that when the target density is low, of density comparable to the critical density n_c , for instance in pre-plasmas created ahead of the bulk dense part of the targets by the interaction of the laser ASE-pedestal or pre-pulses. In such situations, the return current $j_e \sim en_c v_e$ may be unable to compensate the fast electron current $j_h \sim en_h c$ since $n_h \sim n_c$ and $v_e < c$. It can follow a strong electric inhibition of fast electron transport with large departures from an Ohmic behavior of the return current. The background electrons are accelerated to velocities similar to the fast electrons velocity and a number of fast electrons are *scattered* back, effectively contributing to the return current. Such mechanism with very strong electric fields associated to fast electron propagation were deliberately studied in gas media, having been evidenced by proton radiography [8, 7].

13.3.3 Effects of the self-generated magnetic-fields

Besides the energy loss of the electron beam, the resistivity of the propagation medium can generate magnetic-field (B-field) inside the dense material [12]. This is understood from the radial inhomogeneity of the return current (and the E-field), as well as from a non perfectly balanced total current density $\vec{j} = \vec{j}_h + \vec{j}_e \gtrsim 0$. Using Ampère's law for the total current density, $\vec{j} = \frac{1}{\mu_0} \vec{\nabla} \times \vec{B}$ (neglecting the displacement current on the ps time-scale of FEB transport), the generalized Ohm's law for the E-field, eq. 1.46, reads:

$$\vec{E} = -\eta \vec{j}_h + \frac{\eta}{\mu_0} \vec{\nabla} \times \vec{B}. \quad (1.71)$$

The B-field growth can then be estimated from Faraday's law $\partial_t \vec{B} = -\vec{\nabla} \times \vec{E}$, yielding:

$$\frac{\partial \vec{B}}{\partial t} = \eta \vec{\nabla} \times \vec{j}_h + \vec{\nabla} \eta \times \vec{j}_h + \frac{\eta}{\mu_0} \nabla^2 \vec{B} - \frac{1}{\mu_0} \vec{\nabla} \eta \times (\vec{\nabla} \times \vec{B}). \quad (1.72)$$

The last two terms are the MHD terms describing the resistive diffusion and the advection of B-field and are also expected to be very small over the ps-time scale of FEB transport: indeed their characteristic times $\tau_{\text{diff}} \sim \tau_{\text{adv}} \approx \frac{\mu_0}{\eta} L^2$, which again assuming the FEB radius as the typical spatial scale $L \sim r_h \approx 10 \mu\text{m}$, are of the order of 100 ps. We are here more concerned by the the first two terms which correspond to the resistive generation of B-field in presence of the FEB: the B-field generated by the first term, associated to the FEB inhomogeneity, pushes fast electrons into regions of higher current density, while the B-field generated by the second term pushes them into regions of higher resistivity. The first term is of the order of $B_1 \sim \eta j_h / r_h \approx 10^{15} \text{ T/s}$ for the usual magnitude of our parameters, meaning that the B-field can reach 1000 T in 1 ps. The second is of the order of $\dot{B}_2 \sim \eta j_h / L_\eta$ with L_η the scale length of the transition in resistivity. L_η is likely $\ll r_h$ for example at the sharp interfaces of targets with layers of different resistivity.

Such B-field strength is enough to affect the propagation of $\sim \text{MeV}$ electrons. Indeed, the Larmor radius of $\epsilon_h = 1 \text{ MeV}$ electrons embedded in a $B \approx 1 \text{ kT}$ B-field is already $r_L = \gamma_h \beta_h c m_e / e B \approx 5 \mu\text{m} < r_h$, and significant effects are expected as soon as the B-field is strong enough so that $r_L \sim r_h$.

FEB self-pinchng

The term $\eta \vec{\nabla} \times \vec{j}_h$ in eq. 1.72 grows towards the FEB self-pinchng, acting against its angular divergence. Bell & Kingham [14] proposed that resistive collimation of a FEB can occur if

$$r_h / r_L > \theta_{1/2}^2, \text{ that is} \quad (1.73)$$

$$\Gamma \equiv \frac{e r_h B}{\gamma_h \beta_h m_e c \theta_{1/2}^2} > 1, \quad (1.74)$$

where $\theta_{1/2}$ is the divergence cone half-angle of the FEB source. Their criterium is verified if the magnetic field is sufficient to bend the fast electron trajectory through an angle $\theta_{1/2}$ over the distance $r_h / \theta_{1/2}$ over which the beam radius would have doubled without B-field.

According to eq. 1.70 the plasma is heated by the FEB beyond Fermi temperature $T_F \gtrsim 10 \text{ eV}$ in $\tau_{\text{heat}} \sim 3 n_e T_F / 2 \eta j_h^2 \approx 10 \text{ fs}$, which is $\ll \tau_h \approx 1 \text{ ps}$ and definitively $\ll \tau_{\text{diff}}$. We considered here only the resistive heating for the rate of deposited energy because it is largely the dominant mechanism in the beginning of FEB propagation. So we can assume a plasma with Spitzer resistivity $\eta \sim \alpha Z^* T_e^{-3/2} \ln \Lambda$ (α is a constant), or in practical units $\eta [10^{-6} \Omega\text{m}] = \frac{Z^*}{13} \left(\frac{T_e}{300 \text{ eV}} \right)^{-3/2} \ln \Lambda$.

The integration of Faraday's equation $\partial_t B = \eta j_h / r_h$ and heating equation $\frac{3}{2} n_e \partial_t T_e = \eta j_h^2$ over the FEB pulse duration τ_h leads to:

$$T_e(t) = \left(\frac{2}{3\pi^2 n_e} \alpha Z^* \ln \Lambda \frac{P_h^2}{r_h^4 \epsilon_h^2} t + T_{e0}^{5/2} \right)^{2/5}, \quad (1.75)$$

$$B(t) = \frac{3\pi n_e \epsilon_h r_h}{2 P_h} (T_e(t) - T_{e0}), \quad (1.76)$$

where $P_h = \eta_{L \rightarrow e} W_L / \tau_h$ is the injected electron beam power, and then to the set of following equations in practical units:

$$T_e \text{ keV} = 5.8 n_{e,23}^{-2/5} Z^{*2/5} \log \Lambda^{2/5} P_{h \text{ TW}}^{4/5} \epsilon_{h 511 \text{ keV}}^{-4/5} r_{h \mu\text{m}}^{-8/5} \tau_{h \text{ ps}}^{2/5}, \quad (1.77)$$

$$B_{\text{T}} = 220 n_{e,23}^{3/5} Z^{*2/5} \log \Lambda^{2/5} P_{h \text{ TW}}^{-1/5} \epsilon_{h 511 \text{ keV}}^{1/5} r_{h \mu\text{m}}^{-3/5} \tau_{h \text{ ps}}^{2/5}, \quad (1.78)$$

$$\Gamma = 0.13 n_{e,23}^{3/5} Z^{*2/5} \log \Lambda^{2/5} P_{h \text{ TW}}^{-1/5} \epsilon_{h 511 \text{ keV}}^{-3/10} (2 + \epsilon_{h 511 \text{ keV}})^{-1/2} r_{h \mu\text{m}}^{2/5} \theta_{1/2}^{-2} \tau_{h \text{ ps}}^{2/5}, \quad (1.79)$$

where the Coulomb logarithm was taken $\ln \Lambda = 8.7$, $n_{e,23}$ is the background electron density in units of 10^{23} cm^{-3} , $P_{h \text{ TW}}$ is the FEB power in TW, and $\epsilon_{h 511 \text{ keV}}$ the FEB mean energy in units of the electron rest mass. For example, the calculation for $P_h = 30 \text{ TW}$ and $\epsilon_h = 1 \text{ MeV}$ propagating in solid-density Al with a divergence angle $\theta_{1/2} = 20^\circ$, yields $T_e \approx 5 \text{ keV}$, $B \approx 460 \text{ T}$ and $\Gamma \approx 8$.

The above three equations show that the FEB divergence angle $\theta_{1/2}$ is the more important parameter for the self-pinchng condition.

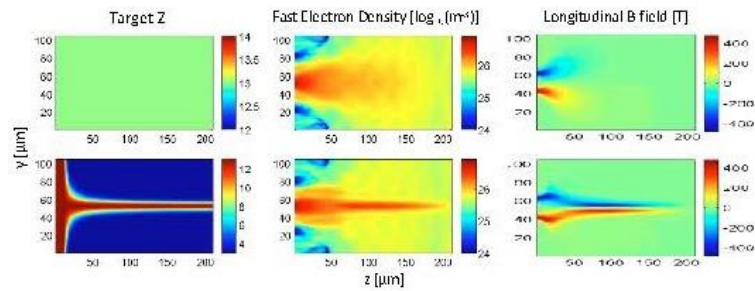


Figure 1.16: Hybrid-VFP simulations by Robinson & Sherlock [80] of the guiding effect of transverse resistive gradients on FEB-transport (bottom panels) compared to a case of an homogeneous target (top panels): Maps of the target atomic number (left column), fast electron density (middle column) at 750 ps and longitudinal B-field at 750 ps (right column).

Effect of resistive gradients

Targets presenting resistivity gradients are relatively easy to fabricate as they can be made of successive layers of different materials having different resistivity. The idea was first analyzed by Robinson & Sherlock via a hybrid-Vlasov-Fokker-Planck (hybrid-VFP) code simulating interactions of PW laser pulses (a few 100 J in about 1 ps) with solid-density foil-targets [80]. Figure 1.16 shows some of their results, evidencing the guiding effect of transverse resistive gradients on FEB-transport.

Kar *et al.* [46] performed the first experiment illustrating the mechanism. They used a 12 μm -thick Sn layer between two large Al slabs, as depicted in Fig. 1.17a): The laser was incident on the side of the Sn layer. The OTR emission at $2\omega_0$ was collected and imaged, producing images related to the transverse profile of the escaping electron beam, which appeared elongated in the direction of the Sn layer. Using comparisons to simulations, the authors concluded that the Sn-Al interfaces, having different resistivity, induced strong magnetic fields able to guide the electrons within the more resistive Sn layer.

Similarly, Ramakrishna *et al.* [78] used the cylindrical geometry illustrated in Fig. 1.17b): An Al cylinder, containing a Fe core was irradiated by the laser on one of the cylinder's faces. Electrons accelerated by the laser travel in average around the cylinder axis and upon exit, they pass through a Cu foil where they induce Cu-K α x-rays. The collected radiation indicated a smaller electron beam in the presence of the Fe core, showing that electrons were magnetically guided inside the more resistive Fe cylinder.

Resistivity gradients can also be induced by density or temperature gradients in a unique material, which is more relevant in the FI scenario where the shell implosion generates complex structures of density and temperature, especially around the compressed core. This was the case of the cylindrical compression experiment, sketched in Fig. 1.17c) [73], that is will be discussed in the lectures.

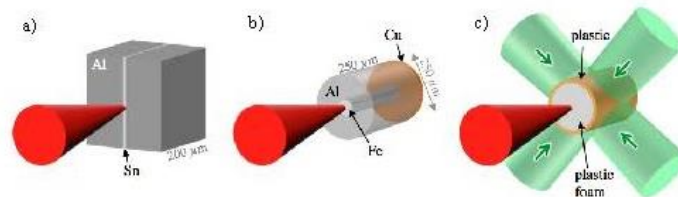


Figure 1.17: Three experimental configurations explored in refs. [46, 78, 73], respectively, for assessing the effect of transverse resistivity gradients on the electron beam guiding. Figure taken from [71].

13.3.4 Guiding of fast electron beams with imposed magnetic fields

Rather than counting on the self-generated resistive B-fields, a different approach to mitigate the FEB divergence can be to apply an exterior B-field longitudinally to the FEB propagation. Such imposed B-field

will not be able to reduce the FEB velocity-space divergence, the goal being just to spatially confine its propagation within a small radius. A simple criterium for the minimum B-field strength that is needed to confine radially a beam of MeV electrons is that the electron Larmor radius should be smaller than the initial beam radius:

$$r_L = \frac{\gamma_h \beta_h m_e c}{eB} < r_h. \quad (1.80)$$

Taking $r_h = 10 \mu\text{m}$ as before, the confinement requires a minimum of 500 T, and of course, the field should be as much uniform as possible over the FEB propagation range (or at least not too much nonuniform in order to avoid magnetic mirroring effects [45]).

Two main methods have been put forward to provide such strong B-fields in the lab: i) B-field flux compression by advection in imploding targets [90], exploring a small seed B-field, $B_0 \sim 10 \text{ T}$, delivered by a capacitor-bank discharge in a coil before driving the target [19, 43]; ii) the use of laser-driven coils [25, 24, 37, 84, 58]. We have succeeded to produce B-fields above 0.5 kT using laser-driven coils [84] and have also successfully demonstrated their efficiency to confine the propagation of $> 10 \text{ MA-FEB}$ currents, with $\approx 1 \text{ MeV}$ average energy, over $60 \mu\text{m}$ -thick plastic targets at solid density [6]. Due to the applied magnetic field, the transported energy-density and the peak background electron temperature raised by factors 5 in comparison with shots without B-field. These results thoroughly discussed in the lectures.

13.4 Detection of fast electron beams in dense matter

Devising diagnostic strategies for the characterization of the FEB source and its propagation in over-dense matter was and still is a challenge, the obvious reason for that being the physical inaccessibility of the electron beam path. Only some of the fast electrons, the relativistic tail of the FEB-spectrum, can overcome the laser target electrostatic potential barrier and be directly detected by particle spectrometers (in general based on permanent magnets). But these are representative of only the higher energy part of the FEB-source spectrum and correspond in general to a very small fraction of the total fast electrons. An additional difficulty is the short time-scale of FEB transport – of only a few ps maximum, $\lesssim 20 \text{ ps}$ for a full scale FI-experiment – mostly if one aims at time-resolving or at least isolate the electron transport from other successive phenomena of longer time-scale, typically the thermal emission associated to the target hydrodynamic evolution.

The characterization of FEB-transport in dense matter fundamentally builds upon a multitude of secondary processes produced by the interactions, either individual or collective of the fast electrons with the propagation medium. These processes involve atomic, nuclear or electrodynamic mechanisms that give rise to emission of e.m. radiation (photons) and/or secondary particles. Both can escape the target and eventually be detected, provided their respective energy is high enough to not be reabsorbed. Their detection provides signatures of the fast electrons propagation, the *figures of merit* searched by the experimentalist. The fast electrons that one aims to characterize are not the only species present in the studied plasmas. For this reason, it is very important to clearly identify mechanisms that are only or mainly related to them, but not or weakly related to the background thermal particles or other secondary sources.

Photon or neutron detection, against charged particle detection, have the advantage of being weakly disturbed by other electromagnetic, electrostatic or magnetostatic fields, may them be ambient (externally imposed), directly related to the laser or its interaction with the sample or actually self-generated by the FEB itself. A wide range of diagnostics has been developed and employed through the years, allowing to characterize the transport, and eventually the key macroscopic parameters of the FEB-source: these are based on $K\alpha$ -fluorescence [104, 94], Bremsstrahlung [11, 69], and visible emission [83], proton or heavier ion emission [61], and as well fusion-neutrons emission [53].

Producing spatially-resolved images of those emissions it is for example possible to characterize the FEB divergence. This was investigated by imaging the coherent transition radiation (CTR) emitted from the target rear side [83] or the $K\alpha$ fluorescence from an embedded tracer layer [94]. Additional experiments have shown evidence that at least the higher energy part of the fast-electrons fluxes as a comb of micro-bunches [9, 107]. By an extended spectral analysis of the CTR, looking at several harmonics of the laser light [75], it was possible to infer the relative importance of various LPI mechanisms – vacuum heating, ponderomotive $\vec{v} \times \vec{B}$ acceleration – in the laser acceleration of fast electrons in solid targets.

Moreover, experiments with laser intensities up to 10^{19} W/cm^2 have shown target heating of a few hundred eV at depths of tens of micrometers, attributed to the energy deposited by the fast electrons. These



measurements were based on the detection of x-ray thermal radiation emitted from a layer buried inside the irradiated target [50]. Such high temperatures show that the fast-electron propagation induces detectable effects on the solid rear target surface. For example, the ionization front breakout modifies the rear side electrical and optical properties [64].

If the energy deposition is large enough, the surface is ionized and heated to high temperatures, of tens of eV or more depending on the target thickness. Atoms start to ionize and proportionally reach higher ionization states as a function of the rising temperature. As a consequence of the reduced screening of the nuclear charge, the atomic energy levels rise (in absolute) and shrink. This is detectable by x-ray spectrometry in the range of the K-shell line emission: as the temperature increases from room temperature, the cold $K\alpha$ line gets broader and shifts towards higher photon energies. For further higher temperature, distinct and successively ionic $K\alpha$ lines of higher energy appear. The presence of a given line, corresponding to a precise ionization state, along the absence of the line corresponding to the next ionization state, is a very precise method of characterizing the plasma temperature, therefore the efficiency of FEB-energy transport [65].

To summarize, two of the above mechanisms that have the most efficiently allowed to unfold FEB-transport features are: hard X-fluorescence from inner atomic-shells (in the range from a few keV to few tens of keV) due to the collisions of the fast incident particles with the background atoms, and CTR produced when fast electrons cross the sharp rear surface of a target and vacuum. While X-ray fluorescence yield is roughly proportional to the number of electrons of energy above a few tens of keV [above the inner-shell ionization potential, see Fig.1.8b)], CTR is a non-linear process mainly sensitive to relativistic electrons (typically those with energy above 1 MeV) [9, 75, 85, 15]. Diagnostics based on these mechanisms are often used as complementary, yet each one has its own advantages or drawbacks according to the experimental configuration.

At a time-scale longer than FEB transport, the heated target expands into vacuum under the effect of the thermal pressure. At the same time, the surface emits a detectable thermal radiation in a spectral range going from the visible to the extreme ultraviolet. These hydrodynamic phenomena can nonetheless be related to the FEB energy deposition, and therefore analyzable as more indirect signatures of FEB energy transport. But these phenomena can also be inherent to target perturbations due to poor laser intensity contrast and the interaction of the laser pedestal or pre-pulses with the target sample prior to the interaction of the main peak of laser power. It is therefore mandatory to carefully control the exact conditions of the laser interactions in order to correctly extract the information on FEB transport.

13.5 Bibliography

- [1] <http://physics.nist.gov/PhysRefData/Star/Text/ESTAR.html> (cit. on p. 21).
- [2] J. C. Adam, A. Héron, and G. Laval, “Dispersion and transport of energetic particles due to the interaction of intense laser pulses with overdense plasmas”, *Physical Review Letters* **97**, 205006 (2006) (cit. on pp. 8, 15, 17, 18).
- [3] H. Alfvén, “On the motion of cosmic rays in interstellar space”, *Physical Review* **55**, 425 (1939) (cit. on pp. 8, 20).
- [4] S. Atzeni, “Inertial fusion fast ignitor: igniting pulse parameter window vs the penetration depth of the heating particles and the density of the precompressed fuel”, *Physics of Plasmas* **6**, 3316 (1999) (cit. on p. 6).
- [5] S. Atzeni, A. Schiavi, J. J. Honrubia, X. Ribeyre, G. Schurtz, P. Nicolai, M. Olazabal-Loumé, C. Bellei, R. G. Evans, and J. R. Davies, “Fast ignitor target studies for the hiper project”, *Physics of Plasmas* **15**, 056311 (2008) <http://dx.doi.org/10.1063/1.2895447> (cit. on pp. 6, 8).
- [6] M. Bailly-Grandvaux, J. J. Santos, C. Bellei, P. Forestier-Colleoni, S. Fujioka, L. Giuffrida, J. J. Honrubia, D. Batani, R. Bouillaud, M. Chevrot, J. E. Cross, R. Crowston, S. Dorard, J.-L. Dubois, M. Ehret, G. Gregori, S. Hulin, S. Kojima, E. Loyez, J.-R. Marques, A. Morace, P. Nicolai, M. Roth, S. Sakata, G. Schaumann, F. Serres, J. Servel, V. T. Tikhonchuk, N. Woolsey, and Z. Zhang, “Guiding of relativistic electron beams in dense matter by longitudinally imposed strong magnetostatic fields”, *Nature Communications* **9**, 102 (2018) (cit. on p. 32).
- [7] D. Batani, S. D. Baton, M. Manclossi, D. Piazza, M. Koenig, A. Benuzzi-Mounaix, H. Popescu, C. Rousseaux, M. Borghesi, C. Cecchetti, and A. Schiavi, “Laser-driven fast electron dynamics in gaseous media under the influence of large electric fields”, *Physics of Plasmas* **16**, 033104 (2009) <http://dx.doi.org/10.1063/1.3080746> (cit. on p. 29).
- [8] D. Batani, S. D. Baton, M. Manclossi, J. J. Santos, F. Amiranoff, M. Koenig, E. Martinolli, A. Antonucci, C. Rousseaux, M. R. Le Gloahec, T. Hall, V. Malka, T. E. Cowan, J. King, R. R. Freeman, M. Key, and R. Stephens, “Ultraintense laser-produced fast-electron propagation in gas jets”, *Phys. Rev. Lett.* **94**, 055004 (2005) (cit. on p. 29).
- [9] S. D. Baton, J. J. Santos, F. Amiranoff, H. Popescu, L. Gremillet, M. Koenig, E. Martinolli, O. Guilbaud, C. Rousseaux, M. Rabec Le Gloahec, T. Hall, D. Batani, E. Perelli, F. Scianitti, and T. E. Cowan, “Evidence of ultrashort electron bunches in Laser-Plasma interactions at relativistic intensities”, *Physical Review Letters* **91**, 105001 (2003) (cit. on pp. 32, 33).
- [10] S. D. Baton, M. Koenig, P. Guillou, B. Loupías, A. Benuzzi-Mounaix, J. Fuchs, C. Rousseaux, L. Gremillet, D. Batani, A. Morace, M. Nakatsutsumi, R. Kodama, and Y. Aglitskiy, “Relativistic electron transport and confinement within charge-insulated, mass-limited targets”, *High Energy Density Physics* **3**, 358 (2007) (cit. on p. 26).

- [11] F. N. Beg, A. R. Bell, A. E. Dangor, C. N. Danson, A. P. Fews, M. E. Glinsky, B. A. Hammel, P. Lee, P. A. Norreys, and M. Tatarakis, “A study of picosecond laser–solid interactions up to $1019+.1667emW.cm^2$ ”, *Physics of Plasmas* **4**, 447 (1997) (cit. on pp. 8, 12, 17, 32).
- [12] A. R. Bell, J. R. Davies, and S. M. Guerin, “Magnetic field in short-pulse high-intensity laser-solid experiments”, *Phys. Rev. E* **58**, 2471 (1998) (cit. on p. 29).
- [13] A. R. Bell, J. R. Davies, S. Guerin, and H. Ruhl, “Fast-electron transport in high-intensity short-pulse laser - solid experiments”, *Plasma Physics and Controlled Fusion* **39**, 653 (1997) (cit. on p. 20).
- [14] A. R. Bell and R. J. Kingham, “Resistive collimation of electron beams in laser-produced plasmas”, *Phys. Rev. Lett.* **91**, 035003 (2003) (cit. on p. 30).
- [15] C. Bellei, J. R. Davies, P. K. Chauhan, and Z. Najmudin, “Coherent transition radiation in relativistic laser–solid interactions”, *Plasma Physics and Controlled Fusion* **54**, 035011 (2012) (cit. on p. 33).
- [16] A. Bourdier, “Oblique incidence of a strong electromagnetic wave on a cold inhomogeneous electron plasma. relativistic effects”, *Physics of Fluids* **26**, 1804 (1983) (cit. on p. 19).
- [17] A. Bret and C. Deutsch, “Correlated stopping power of a chain of n charges”, *Journal of Plasma Physics* **74**, 595 (2008) (cit. on p. 21).
- [18] F. Brunel, “Not-so-resonant, resonant absorption”, *Physical Review Letters* **59**, 52 (1987) (cit. on pp. 12, 13).
- [19] P. Y. Chang, G. Fiksel, M. Hohenberger, J. P. Knauer, R. Betti, F. J. Marshall, D. D. Meyerhofer, F. H. Séguin, and R. D. Petrasso, “Fusion yield enhancement in magnetized laser-driven implosions”, *Phys. Rev. Lett.* **107**, 035006 (2011) (cit. on p. 32).
- [20] C. D. Chen, P. K. Patel, D. S. Hey, A. J. Mackinnon, M. H. Key, K. U. Akli, T. Bartal, F. N. Beg, S. Chawla, H. Chen, R. R. Freeman, D. P. Higginson, A. Link, T. Y. Ma, A. G. MacPhee, R. B. Stephens, L. D. Van Woerkom, B. Westover, and M. Porkolab, “Bremsstrahlung and k fluorescence measurements for inferring conversion efficiencies into fast ignition relevant hot electrons”, *Physics of Plasmas* **16**, 082705 (2009) <http://dx.doi.org/10.1063/1.3183693> (cit. on p. 17).
- [21] H. Chen, S. C. Wilks, W. L. Kruer, P. K. Patel, and R. Shepherd, “Hot electron energy distributions from ultraintense laser solid interactions”, *Physics of Plasmas* **16**, 020705 (2009) <http://dx.doi.org/10.1063/1.3080197> (cit. on p. 17).
- [22] M. Chen, Z.-M. Sheng, and J. Zhang, “On the angular distribution of fast electrons generated in intense laser interaction with solid targets”, *Physics of Plasmas* **13**, 014504 (2006) <http://dx.doi.org/10.1063/1.2167914> (cit. on p. 19).
- [23] B. Chimier, V. T. Tikhonchuk, and L. Hallo, “Heating model for metals irradiated by a subpicosecond laser pulse”, *Physical Review B* **75**, 195124 (2007) (cit. on p. 25).
- [24] C. Courtois, A. D. Ash, D. M. Chambers, R. A. D. Grundy, and N. C. Woolsey, “Creation of a uniform high magnetic-field strength environment for laser-driven experiments”, *Journal of Applied Physics* **98**, 054913 (2005) <http://dx.doi.org/10.1063/1.2035896> (cit. on p. 32).
- [25] H. Daido, F. Miki, K. Mima, M. Fujita, K. Sawai, H. Fujita, Y. Kitagawa, S. Nakai, and C. Yamanaka, “Generation of a strong magnetic field by an intense co2 laser pulse”, *Phys. Rev. Lett.* **56**, 846 (1986) (cit. on p. 32).
- [26] J. R. Davies, A. R. Bell, M. G. Haines, and S. M. Guérin, “Short-pulse high-intensity laser-generated fast electron transport into thick solid targets”, *Physical Review E* **56**, 7193 (1997) (cit. on p. 26).
- [27] A. Debayle, L. Gremillet, J. J. Honrubia, and E. dapos;Humières, “Reduction of the fast electron angular dispersion by means of varying-resistivity structured targets”, *Physics of Plasmas* **20**, 013109 (2013) <http://dx.doi.org/10.1063/1.4789451> (cit. on p. 19).
- [28] A. Debayle, J. J. Honrubia, E. d’Humières, and V. T. Tikhonchuk, “Characterization of laser-produced fast electron sources for fast ignition”, *Plasma Physics and Controlled Fusion* **52**, 124024 (2010) (cit. on p. 18).
- [29] A. Debayle, J. J. Honrubia, E. d’Humières, and V. T. Tikhonchuk, “Divergence of laser-driven relativistic electron beams”, *Physical Review E* **82**, 036405 (2010) (cit. on pp. 8, 18, 19, 24).

- [30] A. Debayle, J. Sanz, L. Gremillet, and K. Mima, “Toward a self-consistent model of the interaction between an ultra-intense, normally incident laser pulse with an overdense plasma”, *Physics of Plasmas* **20**, 053107 (2013) <http://dx.doi.org/10.1063/1.4807335> (cit. on p. 16).
- [31] C. Deutsch and P. Fromy, “Correlated stopping of relativistic electrons in superdense plasmas”, *Physics of Plasmas* **6**, 3597 (1999) (cit. on p. 21).
- [32] R. P. Drake, *High-Energy-Density physics* (Springer, 2002) (cit. on p. 5).
- [33] K. Eidmann, J. Meyer-ter-Vehn, T. Schlegel, and S. Hüller, “Hydrodynamic simulation of subpicosecond laser interaction with solid-density matter”, *Physical Review E* **62**, 1202 (2000) (cit. on p. 25).
- [34] J. Fernández, B. Albright, F. Beg, M. Foord, B. Hegelich, J. Honrubia, M. Roth, R. Stephens, and L. Yin, “Fast ignition with laser-driven proton and ion beams”, *Nuclear Fusion* **54**, 054006 (2014) (cit. on p. 6).
- [35] E. E. Fill, “Analytical theory of pulsed relativistic electron beams entering a vacuum”, *Physics of Plasmas* **8**, 4613 (2001) (cit. on p. 26).
- [36] J. P. Freidberg, R. W. Mitchell, R. L. Morse, and L. I. Rudinski, “Resonant absorption of laser light by plasma targets”, *Phys. Rev. Lett.* **28**, 795 (1972) (cit. on p. 12).
- [37] S. Fujioka, Z. Zhang, K. Ishihara, K. Shigemori, Y. Hironaka, T. Johzaki, A. Sunahara, N. Yamamoto, H. Nakashima, T. Watanabe, H. Shiraga, H. Nishimura, and H. Azechi, “Kilotesla Magnetic Field due to a Capacitor-Coil Target Driven by High Power Laser”, *Scientific Reports* **3**, 1170, 1170 (2013) (cit. on p. 32).
- [38] P. Gibbon, *Short pulse laser interactions with matter: an introduction* (World Scientific Publishing Company, 2005) (cit. on pp. 5, 11, 13, 14).
- [39] J. S. Green, V. M. Ovchinnikov, R. G. Evans, K. U. Akli, H. Azechi, F. N. Beg, C. Bellei, R. R. Freeman, H. Habara, R. Heathcote, M. H. Key, J. A. King, K. L. Lancaster, N. C. Lopes, T. Ma, A. J. MacKinnon, K. Markey, A. McPhee, Z. Najmudin, P. Nilson, R. Onofrei, R. Stephens, K. Takeda, K. A. Tanaka, W. Theobald, T. Tanimoto, J. Waugh, L. Van Woerkom, N. C. Woolsey, M. Zepf, J. R. Davies, and P. A. Norreys, “Effect of laser intensity on Fast-Electron-Beam divergence in Solid-Density plasmas”, *Physical Review Letters* **100**, 015003 (2008) (cit. on pp. 8, 19).
- [40] L. Gremillet, G. Bonnaud, and F. Amiranoff, “Filamented transport of laser-generated relativistic electrons penetrating a solid target”, *Physics of Plasmas* **9**, 941 (2002) (cit. on p. 18).
- [41] M. G. Haines, M. S. Wei, F. N. Beg, and R. B. Stephens, “Hot-Electron temperature and Laser-Light absorption in fast ignition”, *Physical Review Letters* **102**, 045008 (2009) (cit. on p. 17).
- [42] D. J. Hoarty, P. Allan, S. F. James, C. R. D. Brown, L. M. R. Hobbs, M. P. Hill, J. W. O. Harris, J. Morton, M. G. Brookes, R. Shepherd, J. Dunn, H. Chen, E. Von Marley, P. Beiersdorfer, H. K. Chung, R. W. Lee, G. Brown, and J. Emig, “Observations of the effect of ionization-potential depression in hot dense plasma”, *Phys. Rev. Lett.* **110**, 265003 (2013) (cit. on p. 6).
- [43] M. Hohenberger, P.-Y. Chang, G. Fiksel, J. P. Knauer, R. Betti, F. J. Marshall, D. D. Meyerhofer, F. H. Séguin, and R. D. Petrasso, “Inertial confinement fusion implosions with imposed magnetic field compression using the omega laser”, *Physics of Plasmas* **19**, 056306 (2012) <http://dx.doi.org/10.1063/1.3696032> (cit. on p. 32).
- [44] J. Honrubia, A. Antonucci, and D. Moreno, “Hybrid simulations of fast electron transport in conducting media”, *Laser and Particle Beams* **22**, 129 (2004) (cit. on p. 26).
- [45] T. Johzaki, K. Mima, S. Fujioka, H. Sakagami, A. Sunahara, H. Nagatomo, and H. Shiraga, “Electron beam guiding by strong longitudinal magnetic fields”, *Journal of Physics: Conference Series* **688**, 012041 (2016) (cit. on p. 32).
- [46] S. Kar, A. P. L. Robinson, D. C. Carroll, O. Lundh, K. Markey, P. McKenna, P. Norreys, and M. Zepf, “Guiding of relativistic electron beams in solid targets by resistively controlled magnetic fields”, *Physical Review Letters* **102**, 055001 (2009) (cit. on p. 31).
- [47] L. Katz and A. S. Penfold, “Range-Energy relations for electrons and the determination of Beta-Ray End-Point energies by absorption”, *Reviews of Modern Physics* **24**, 28 (1952) (cit. on p. 23).

- [48] M. H. Key, M. D. Cable, T. E. Cowan, K. G. Estabrook, B. A. Hammel, S. P. Hatchett, E. A. Henry, D. E. Hinkel, J. D. Kilkenny, J. A. Koch, W. L. Kruer, A. B. Langdon, B. F. Lasinski, R. W. Lee, B. J. MacGowan, A. MacKinnon, J. D. Moody, M. J. Moran, A. A. Offenberger, D. M. Pennington, M. D. Perry, T. J. Phillips, T. C. Sangster, M. S. Singh, M. A. Stoyer, M. Tabak, G. L. Tietbohl, M. Tsukamoto, K. Wharton, and S. C. Wilks, “Hot electron production and heating by hot electrons in fast ignitor research”, *Physics of Plasmas* **5**, 1966 (1998) (cit. on p. 20).
- [49] T. Kluge, T. Cowan, A. Debus, U. Schramm, K. Zeil, and M. Bussmann, “Electron temperature scaling in laser interaction with solids”, *Physical Review Letters* **107**, 205003 (2011) (cit. on p. 17).
- [50] J. A. Koch, M. H. Key, R. R. Freeman, S. P. Hatchett, R. W. Lee, D. Pennington, R. B. Stephens, and M. Tabak, “Experimental measurements of deep directional columnar heating by laser-generated relativistic electrons at near-solid density”, *Phys. Rev. E* **65**, 016410 (2001) (cit. on p. 33).
- [51] R. Kodama, H. Azechi, H. Fujita, H. Habara, Y. Izawa, T. Jitsuno, T. Jozaki, Y. Kitagawa, K. Krushelnick, T. Matsuoka, K. Mima, N. Miyanaga, K. Nagai, H. Nagatomo, M. Nakai, H. Nishimura, T. Norimatsu, P. Norreys, K. Shigemori, H. Shiraga, A. Sunahara, K. Tanaka, M. Tanpo, Y. Toyama, K. Tsubakimoto, T. Yamanaka, and M. Zepf, “Fast plasma heating in a cone-attached geometry—towards fusion ignition”, *Nuclear Fusion* **44**, S276 (2004) (cit. on pp. 7, 19).
- [52] R. Kodama, S. H., S. K., T. Y., F. S., A. H., F. H., H. H., H. T., I. Y., J. T., K. Y., K. K. M., L. K. L., M. K., N. K., N. M., N. H., N. T., N. P. A., S. S., T. K. A., A. Youssef, Z. M., and Y. T., “Fast heating scalable to laser fusion ignition”, *Nature* **418**, 933 (2002) (cit. on p. 7).
- [53] R. Kodama, P. A. Norreys, K. Mima, A. E. Dangor, R. G. Evans, H. Fujita, Y. Kitagawa, K. Krushelnick, T. Miyakoshi, N. Miyanaga, T. Norimatsu, S. J. Rose, T. Shozaki, K. Shigemori, A. Sunahara, M. Tanpo, K. A. Tanaka, Y. Toyama, T. Yamanaka, and M. Zepf, “Fast heating of ultrahigh-density plasma as a step towards laser fusion ignition”, *Nature* **412**, 798 (2001) (cit. on pp. 7, 19, 32).
- [54] W. L. Kruer, *The physics of laser plasma interactions* (Westview Press, 1988) (cit. on p. 12).
- [55] W. L. Kruer and K. Estabrook, “ $J \times B$ heating by very intense laser light”, *Physics of Fluids* **28**, 430 (1985) (cit. on p. 12).
- [56] K. L. Lancaster, J. S. Green, D. S. Hey, K. U. Akli, J. R. Davies, R. J. Clarke, R. R. Freeman, H. Habara, M. H. Key, R. Kodama, K. Krushelnick, C. D. Murphy, M. Nakatsutsumi, P. Simpson, R. Stephens, C. Stoeckl, T. Yabuuchi, M. Zepf, and P. A. Norreys, “Measurements of energy transport patterns in solid density laser plasma interactions at intensities of 51020 W cm^{-2} ”, *Phys. Rev. Lett.* **98**, 125002 (2007) (cit. on p. 19).
- [57] B. F. Lasinski, A. B. Langdon, S. P. Hatchett, M. H. Key, and M. Tabak, “Particle-in-cell simulations of ultra intense laser pulses propagating through overdense plasma for fast-ignitor and radiography applications”, *Physics of Plasmas* **6**, 2041 (1999) (cit. on p. 18).
- [58] K. F. F. Law, M. Bailly-Grandvaux, A. Morace, S. Sakata, K. Matsuo, S. Kojima, S. Lee, X. Vaisseau, Y. Arikawa, A. Yogo, K. Kondo, Z. Zhang, C. Bellei, J. J. Santos, S. Fujioka, and H. Azechi, “Direct measurement of kilo-tesla level magnetic field generated with laser-driven capacitor-coil target by proton deflectometry”, *Applied Physics Letters* **108**, 091104 (2016) <http://dx.doi.org/10.1063/1.4943078> (cit. on p. 32).
- [59] K. W. D. Ledingham and W. Galster, “Laser-driven particle and photon beams and some applications”, *New Journal of Physics* **12**, 045005 (2010) (cit. on p. 6).
- [60] E. Lefebvre and G. Bonnaud, “Nonlinear electron heating in ultrahigh-intensity-laser-plasma interaction”, *Physical Review E* **55**, 1011 (1997) (cit. on p. 10).
- [61] D. A. MacLellan, D. C. Carroll, R. J. Gray, N. Booth, M. Burza, M. P. Desjarlais, F. Du, B. Gonzalez-Izquierdo, D. Neely, H. W. Powell, A. P. L. Robinson, D. R. Rusby, G. G. Scott, X. H. Yuan, C.-G. Wahlström, and P. McKenna, “Annular fast electron transport in silicon arising from low-temperature resistivity”, *Phys. Rev. Lett.* **111**, 095001 (2013) (cit. on p. 32).
- [62] A. G. MacPhee, K. U. Akli, F. N. Beg, C. D. Chen, H. Chen, R. Clarke, D. S. Hey, R. R. Freeman, A. J. Kemp, M. H. Key, J. A. King, S. Le Pape, A. Link, T. Y. Ma, H. Nakamura, D. T. Offermann, V. M. Ovchinnikov, P. K. Patel, T. W. Phillips, R. B. Stephens, R. Town, Y. Y. Tsui, M. S. Wei, L. D. Van Woerkom, and A. J. Mackinnon, “Diagnostics for fast ignition science (invited)”, *Review of Scientific Instruments* **79**, 10F302 (2008) (cit. on p. 17).



- [63] G. Malka and J. L. Miquel, “Experimental confirmation of Ponderomotive-Force electrons produced by an ultrarelativistic laser pulse on a solid target”, *Physical Review Letters* **77**, 75 (1996) (cit. on p. 16).
- [64] E. Martinolli, M. Koenig, F. Amiranoff, S. D. Baton, L. Gremillet, J. J. Santos, T. A. Hall, M. Rabec-Le-Gloahec, C. Rousseaux, and D. Batani, “Fast electron heating of a solid target in ultrahigh-intensity laser pulse interaction”, *Phys. Rev. E* **70**, 055402 (2004) (cit. on p. 33).
- [65] E. Martinolli, M. Koenig, S. D. Baton, J. J. Santos, F. Amiranoff, D. Batani, E. Perelli-Cippo, F. Scianitti, L. Gremillet, R. Melizzi, A. Decoster, C. Rousseaux, T. A. Hall, M. H. Key, R. Snavely, A. J. MacKinnon, R. R. Freeman, J. A. King, R. Stephens, D. Neely, and R. J. Clarke, “Fast-electron transport and heating of solid targets in high-intensity laser interactions measured by $K\alpha$ fluorescence”, *Physical Review E* **73**, 046402 (2006) (cit. on p. 33).
- [66] P. Mora, *Introduction aux plasmas créés par laser*, Centre de Physique Théorique, Ecole Polytechnique, 91128 Palaiseau Cedex, France, Feb. 2016 (cit. on p. 5).
- [67] P. M. Nilson, A. A. Solodov, J. F. Myatt, W. Theobald, P. A. Jaanimagi, L. Gao, C. Stoeckl, R. S. Craxton, J. A. Delettrez, B. Yaakobi, J. D. Zuegel, B. E. Kruschwitz, C. Dorrer, J. H. Kelly, K. U. Akli, P. K. Patel, A. J. Mackinnon, R. Betti, T. C. Sangster, and D. D. Meyerhofer, “Scaling hot-electron generation to high-power, kilojoule-class laser-solid interactions”, *Phys. Rev. Lett.* **105**, 235001 (2010) (cit. on pp. 8, 14).
- [68] P. A. Norreys, R. Allott, R. J. Clarke, J. Collier, D. Neely, S. J. Rose, M. Zepf, M. Santala, A. R. Bell, K. Krushelnick, A. E. Dangor, N. C. Woolsey, R. G. Evans, H. Habara, T. Norimatsu, and R. Kodama, “Experimental studies of the advanced fast ignitor scheme”, *Physics of Plasmas* **7**, 3721 (2000) (cit. on p. 7).
- [69] P. A. Norreys, M. Santala, E. Clark, M. Zepf, I. Watts, F. N. Beg, K. Krushelnick, M. Tatarakis, A. E. Dangor, X. Fang, P. Graham, T. McCanny, R. P. Singhal, K. W. D. Ledingham, A. Creswell, D. C. W. Sanderson, J. Magill, A. Machacek, J. S. Wark, R. Allott, B. Kennedy, and D. Neely, “Observation of a highly directional γ -ray beam from ultrashort, ultraintense laser pulse interactions with solids”, *Physics of Plasmas* **6**, 2150 (1999) (cit. on p. 32).
- [70] P. Norreys, R. Scott, K. Lancaster, J. Green, A. Robinson, M. Sherlock, R. Evans, M. Haines, S. Kar, M. Zepf, M. Key, J. King, T. Ma, T. Yabuuchi, M. Wei, F. Beg, P. Nilson, W. Theobald, R. Stephens, J. Valente, J. Davies, K. Takeda, H. Azechi, M. Nakatsutsumi, T. Tanimoto, R. Kodama, and K. Tanaka, “Recent fast electron energy transport experiments relevant to fast ignition inertial fusion”, *Nuclear Fusion* **49**, 104023 (2009) (cit. on p. 17).
- [71] P. Norreys, D. Batani, S. Baton, F. N. Beg, R. Kodama, P. Nilson, P. Patel, F. Pérez, J. Santos, R. Scott, V. Tikhonchuk, M. Wei, and J. Zhang, “Fast electron energy transport in solid density and compressed plasma”, *Nuclear Fusion* **54**, 054004 (2014) (cit. on pp. 6–8, 19, 31).
- [72] P. K. Patel, A. J. Mackinnon, M. H. Key, T. E. Cowan, M. E. Foord, M. Allen, D. F. Price, H. Ruhl, P. T. Springer, and R. Stephens, “Isochoric heating of solid-density matter with an ultrafast proton beam”, *Phys. Rev. Lett.* **91**, 125004 (2003) (cit. on p. 26).
- [73] F. Perez, A. Debayle, J. Honrubia, M. Koenig, D. Batani, S. D. Baton, F. N. Beg, C. Benedetti, E. Brambrink, S. Chawla, F. Dorchie, C. Fourment, M. Galimberti, L. A. Gizzi, L. Gremillet, R. Heathcote, D. P. Higginson, S. Hulin, R. Jafer, P. Koester, L. Labate, K. L. Lancaster, A. J. MacKinnon, A. G. MacPhee, W. Nazarov, P. Nicolai, J. Pasley, R. Ramis, M. Richetta, J. J. Santos, A. Sgattoni, C. Spindloe, B. Vauzour, T. Vinci, and L. Volpe, “Magnetically guided fast electrons in cylindrically compressed matter”, *Physical Review Letters* **107**, 065004 (2011) (cit. on p. 31).
- [74] F. Pisani, A. Bernardinello, D. Batani, A. Antonicci, E. Martinolli, M. Koenig, L. Gremillet, F. Amiranoff, S. Baton, J. Davies, T. Hall, D. Scott, P. Norreys, A. Djaoui, C. Rousseaux, P. Fewes, H. Bandulet, and H. Pepin, “Experimental evidence of electric inhibition in fast electron penetration and of electric-field-limited fast electron transport in dense matter”, *Phys. Rev. E* **62**, R5927 (2000) (cit. on p. 20).

- [75] H. Popescu, S. D. Baton, F. Amiranoff, C. Rousseaux, M. R. Le Gloahec, J. J. Santos, L. Gremillet, M. Koenig, E. Martinoli, T. Hall, J. C. Adam, A. Heron, and D. Batani, “Subfemtosecond, coherent, relativistic, and ballistic electron bunches generated at 0 and 20 in high intensity laser-matter interaction”, *Physics of Plasmas* **12**, 063106 (2005) <http://dx.doi.org/10.1063/1.1927328> (cit. on pp. 16, 32, 33).
- [76] A. Pukhov and J. Meyer-ter-Vehn, “Laser hole boring into overdense plasma and relativistic electron currents for fast ignition of ICF targets”, *Physical Review Letters* **79**, 2686 (1997) (cit. on p. 18).
- [77] B. Quesnel and P. Mora, “Theory and simulation of the interaction of ultraintense laser pulses with electrons in vacuum”, *Physical Review E* **58**, 3719 (1998) (cit. on pp. 11, 12).
- [78] B. Ramakrishna, S. Kar, A. P. L. Robinson, D. J. Adams, K. Markey, M. N. Quinn, X. H. Yuan, P. McKenna, K. L. Lancaster, J. S. Green, R. H. H. Scott, P. A. Norreys, J. Schreiber, and M. Zepf, “Laser-driven fast electron collimation in targets with resistivity boundary”, *Phys. Rev. Lett.* **105**, 135001 (2010) (cit. on p. 31).
- [79] C. Ren, M. Tzoufras, F. S. Tsung, W. B. Mori, S. Amorini, R. A. Fonseca, L. O. Silva, J. C. Adam, and A. Heron, “Global simulation for Laser-Driven MeV electrons in fast ignition”, *Physical Review Letters* **93**, 185004 (2004) (cit. on p. 18).
- [80] A. P. L. Robinson and M. Sherlock, “Magnetic collimation of fast electrons produced by ultraintense laser irradiation by structuring the target composition”, *Physics of Plasmas* **14**, 083105 (2007) <http://dx.doi.org/10.1063/1.2768317> (cit. on p. 31).
- [81] A. Robinson, D. Strozzi, J. Davies, L. Gremillet, J. Honrubia, T. Johzaki, R. Kingham, M. Sherlock, and A. Solodov, “Theory of fast electron transport for fast ignition”, *Nuclear Fusion* **54**, 054003 (2014) (cit. on pp. 5, 6, 21).
- [82] M. Roth, T. E. Cowan, M. H. Key, S. P. Hatchett, C. Brown, W. Fountain, J. Johnson, D. M. Pennington, R. A. Snavely, S. C. Wilks, K. Yasuike, H. Ruhl, F. Pegoraro, S. V. Bulanov, E. M. Campbell, M. D. Perry, and H. Powell, “Fast ignition by intense laser-accelerated proton beams”, *Phys. Rev. Lett.* **86**, 436 (2001) (cit. on p. 6).
- [83] J. J. Santos, F. Amiranoff, S. D. Baton, L. Gremillet, M. Koenig, E. Martinoli, M. Rabec Le Gloahec, C. Rousseaux, D. Batani, A. Bernardinello, G. Greison, and T. Hall, “Fast electron transport in ultraintense laser pulse interaction with solid targets by rear-side self-radiation diagnostics”, *Phys. Rev. Lett.* **89**, 025001 (2002) (cit. on pp. 19, 32).
- [84] J. J. Santos, M. Bailly-Grandvaux, L. Giuffrida, P. Forestier-Colleoni, S. Fujioka, Z. Zhang, P. Korneev, R. Bouillaud, S. Dorard, D. Batani, M. Chevrot, J. E. Cross, R. Crowston, J.-L. Dubois, J. Gazave, G. Gregori, E. d’Humières, S. Hulin, K. Ishihara, S. Kojima, E. Loyez, J.-R. Marquès, A. Morace, P. Nicolaï, O. Peyrusse, A. Poyé, D. Raffestin, J. Ribolzi, M. Roth, G. Schaumann, F. Serres, V. T. Tikhonchuk, P. Vacar, and N. Woolsey, “Laser-driven platform for generation and characterization of strong quasi-static magnetic fields”, *New Journal of Physics* **17**, 083051 (2015) (cit. on p. 32).
- [85] J. J. Santos, A. Debayle, P. Nicolaï, V. Tikhonchuk, M. Manclossi, D. Batani, A. Guemnie-Tafo, J. Faure, V. Malka, and J. J. Honrubia, “Fast-electron transport and induced heating in aluminum foils”, *Physics of Plasmas* **14**, 103107 (2007) <http://dx.doi.org/10.1063/1.2790893> (cit. on pp. 19, 29, 33).
- [86] J. Santos, B. Vauzour, M. Touati, L. Gremillet, J.-L. Feugeas, T. Ceccotti, R. Bouillaud, F. Deneuille, V. Floquet, C. Fourment, M. Hadj-Bachir, S. Hulin, A. Morace, P. Nicolaï, P. d’Oliveira, F. Reau, A. Samaké, O. Teherbakoff, V. Tikhonchuk, M. Veltcheva, and D. Batani, “Isochoric heating and strong blast wave formation driven by fast electrons in solid-density targets”, *New J. Phys.* **19**, 103005 (2017).
- [87] J. J. Santos, D. Batani, S. D. Baton, F. N. Beg, T. Ceccotti, A. Debayle, F. Dorchies, J.-L. Feugeas, C. Fourment, L. Gremillet, J. J. Honrubia, S. Hulin, A. Morace, P. Nicolaï, F. Pérez, H. Sawada, H.-P. Schlenvoigt, V. T. Tikhonchuk, X. Vaisseau, B. Vauzour, and M. Wei, “Supra-thermal electron beam stopping power and guiding in dense plasmas”, *Journal of Plasma Physics* **79**, 429 (2013) (cit. on pp. 19, 29).
- [88] J. Sanz, A. Debayle, and K. Mima, “Model for ultraintense laser-plasma interaction at normal incidence”, *Phys. Rev. E* **85**, 046411 (2012) (cit. on p. 16).

- [89] A. Schönlein, G. Boutoux, S. Pikuz, L. Antonelli, D. Batani, A. Debayle, A. Franz, L. Giuffrida, J. J. Honrubia, J. Jacoby, D. Khaghani, P. Neumayer, O. N. Rosmej, T. Sakaki, J. J. Santos, and A. Sauteray, “Generation and characterization of warm dense matter isochorically heated by laser-induced relativistic electrons in a wire target”, *EPL (Europhysics Letters)* **114**, 45002 (2016) (cit. on p. 29).
- [90] H. D. Shay, P. Amendt, D. Clark, D. Ho, M. Key, J. Koning, M. Marinak, D. Strozzi, and M. Tabak, “Implosion and burn of fast ignition capsules—calculations with hydra”, *Physics of Plasmas* **19**, 092706 (2012) <http://dx.doi.org/10.1063/1.4751839> (cit. on pp. 7, 8, 32).
- [91] H. Shiraga, H. Nagatomo, W. Theobald, A. Solodov, and M. Tabak, “Fast ignition integrated experiments and high-gain point design”, *Nuclear Fusion* **54**, 054005 (2014) (cit. on pp. 6, 7).
- [92] L. O. Silva, R. A. Fonseca, J. W. Tonge, W. B. Mori, and J. M. Dawson, “On the role of the purely transverse weibel instability in fast ignitor scenarios”, *Physics of Plasmas* **9**, 2458 (2002) (cit. on p. 18).
- [93] L. Spitzer and R. Härm, “Transport phenomena in a completely ionized gas”, *Phys. Rev.* **89**, 977 (1953) (cit. on p. 25).
- [94] R. B. Stephens, R. A. Snavely, Y. Aglitskiy, F. Amiranoff, C. Andersen, D. Batani, S. D. Baton, T. Cowan, R. R. Freeman, T. Hall, S. P. Hatchett, J. M. Hill, M. H. Key, J. A. King, J. A. Koch, M. Koenig, A. J. MacKinnon, K. L. Lancaster, E. Martinolli, P. Norreys, E. Perelli-Cippo, M. Rabec Le Gloahec, C. Rousseaux, J. J. Santos, and F. Scianitti, “ K_{α} fluorescence measurement of relativistic electron transport in the context of fast ignition”, *Physical Review E* **69**, 066414 (2004) (cit. on pp. 19, 32).
- [95] *Stopping powers for electrons and positrons*, International Commissions on Radiation Units and Measurements, Technical Report 37, Bethesda, MD, USA, 1984 (cit. on p. 21).
- [96] M. Tabak, J. Hammer, M. E. Glinsky, W. L. Kruer, S. C. Wilks, J. Woodworth, E. M. Campbell, M. D. Perry, and R. J. Mason, “Ignition and high gain with ultrapowerful lasers”, *Physics of Plasmas* **1**, 1626 (1994) (cit. on p. 6).
- [97] V. Tikhonchuk, *La physique de l'interaction des impulsions laser relativistes avec la matière*, Centre Lasers Intenses et Applications, Université Bordeaux - CNRS - CEA, 351 Cours de la Libération, 33405 Talence Cedex, France (cit. on p. 5).
- [98] X. Vaisseau, A. Debayle, J. J. Honrubia, S. Hulin, A. Morace, P. Nicolai, H. Sawada, B. Vauzour, D. Batani, F. N. Beg, J. R. Davies, R. Fedosejevs, R. J. Gray, G. E. Kemp, S. Kerr, K. Li, A. Link, P. McKenna, H. S. McLean, M. Mo, P. K. Patel, J. Park, J. Peebles, Y. J. Rhee, A. Sorokovikova, V. T. Tikhonchuk, L. Volpe, M. Wei, and J. J. Santos, “Enhanced relativistic-electron-beam energy loss in warm dense aluminum”, *Phys. Rev. Lett.* **114**, 095004 (2015) (cit. on p. 29).
- [99] X. Vaisseau, “Experimental study of fast electron transport in dense plasmas”, PhD thesis (Université de Bordeaux, Dec. 2014) (cit. on pp. 22–24).
- [100] B. Vauzour, A. Debayle, X. Vaisseau, S. Hulin, H.-P. Schlenvoigt, D. Batani, S. D. Baton, J. J. Honrubia, P. Nicolai, F. N. Beg, R. Benocci, S. Chawla, M. Coury, F. Dorchies, C. Fourment, E. dapos;Humières, L. C. Jarrot, P. McKenna, Y. J. Rhee, V. T. Tikhonchuk, L. Volpe, V. Yahia, and J. J. Santos, “Unraveling resistive versus collisional contributions to relativistic electron beam stopping power in cold-solid and in warm-dense plasmas”, *Physics of Plasmas* **21**, 033101 (2014) <http://dx.doi.org/10.1063/1.4867187> (cit. on pp. 17, 19, 26, 29).
- [101] B. Vauzour, J. J. Santos, A. Debayle, S. Hulin, H.-P. Schlenvoigt, X. Vaisseau, D. Batani, S. D. Baton, J. J. Honrubia, P. Nicolai, F. N. Beg, R. Benocci, S. Chawla, M. Coury, F. Dorchies, C. Fourment, E. d’Humières, L. C. Jarrot, P. McKenna, Y. J. Rhee, V. T. Tikhonchuk, L. Volpe, and V. Yahia, “Relativistic high-current electron-beam stopping-power characterization in solids and plasmas: collisional versus resistive effects”, *Phys. Rev. Lett.* **109**, 255002 (2012) (cit. on p. 29).
- [102] B. Westover, C. D. Chen, P. K. Patel, M. H. Key, H. McLean, R. Stephens, and F. N. Beg, “Fast electron temperature and conversion efficiency measurements in laser-irradiated foil targets using a bremsstrahlung x-ray detector”, *Physics of Plasmas* **18**, 063101 (2011) <http://dx.doi.org/10.1063/1.3594622> (cit. on pp. 8, 14).



- [103] B. Westover, C. D. Chen, P. K. Patel, H. McLean, and F. N. Beg, “Characterization of the fast electrons distribution produced in a high intensity laser target interaction”, *Physics of Plasmas* **21**, 031212 (2014) <http://dx.doi.org/10.1063/1.4865371> (cit. on pp. 8, 14).
- [104] K. B. Wharton, S. P. Hatchett, S. C. Wilks, M. H. Key, J. D. Moody, V. Yanovsky, A. A. Offenberger, B. A. Hammel, M. D. Perry, and C. Joshi, “Experimental measurements of hot electrons generated by ultraintense ($>10^{19} \text{W/cm}^2$) laser-plasma interactions on solid-density targets”, *Phys. Rev. Lett.* **81**, 822 (1998) (cit. on pp. 8, 20, 32).
- [105] S. C. Wilks, W. L. Kruer, M. Tabak, and A. B. Langdon, “Absorption of ultra-intense laser pulses”, *Physical Review Letters* **69**, 1383 (1992) (cit. on pp. 8, 12, 13, 16, 18).
- [106] K. Yasuike, M. H. Key, S. P. Hatchett, R. A. Snavely, and K. B. Wharton, “Hot electron diagnostic in a solid laser target by k-shell lines measurement from ultraintense laser-plasma interactions ($3 \times 10^{20} \text{W.cm}^{-2}$, $\leq 400 \text{J}$)”, *Review of Scientific Instruments* **72**, 1236 (2001) (cit. on p. 16).
- [107] J. Zheng, K. A. Tanaka, T. Sato, T. Yabuuchi, T. Kurahashi, Y. Kitagawa, R. Kodama, T. Norimatsu, and T. Yamanaka, “Study of hot electrons by measurement of optical emission from the rear surface of a metallic foil irradiated with ultraintense laser pulse”, *Phys. Rev. Lett.* **92**, 165001 (2004) (cit. on p. 32).



HELLENIC
MEDITERRANEAN
UNIVERSITY



université
BORDEAUX



Erasmus+

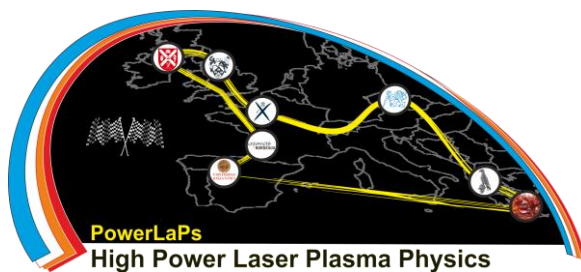
PowerLaPs

Innovative Education & Training in High Power Laser Plasmas

High Power Laser Matter Interactions/High Energy Density Physics - Theory and Experiments

Chapter 14: Laser-driven ion acceleration

M. Borghesi



Erasmus+



14. Laser-driven ion acceleration

14.1 Introduction

The first experiments reporting laser acceleration of protons with beam-like properties and multi-MeV energies were reported in 2000 [1-3]. Experiments since then have demonstrated, over a wide range of laser and target parameters, the generation of multi-MeV proton and ion beams with unique properties such as ultrashort burst emission, high brilliance, and low emittance, which have in turn stimulated ideas for a range of innovative applications. While most of this work has been based on sheath acceleration processes [3-5], a number of novel mechanisms have been at the centre of recent theoretical and experimental activities. This chapter provides an overview of the main acceleration mechanisms and the underlying physical principle, as well as a brief review of the state of the art and recent developments in the field. More extensive surveys are provided in [6-8].

14.2 Sheath acceleration

This is the acceleration mechanism active in most experiments carried out so far, and it was proposed [4] as an interpretative framework of the multi-MeV proton observations reported in [2], obtained on the NOVA Petawatt laser at LLNL (the name *Target Normal Sheath Acceleration*, TNSA, is generally used).

Acceleration through this mechanism employs thin foils (typically from a few μm to tens of μm thickness), which are irradiated by an intense laser pulse. In the intensity regime of relevance (as a guideline, $I_0^2 > 10^{18} \text{ W/cm}^2$), the laser pulse can couple efficiently energy into relativistic electrons, mainly through ponderomotive processes (e.g. $\mathbf{J} \times \mathbf{B}$ mechanism [9]). The average energy of the electrons is typically of MeV order, e.g. their collisional range is much larger than the foil thickness, so that they can propagate to the rear of the target, and drive the acceleration of ions from surface layers via the space-charge field established as they try to move away from the target. While a limited number of energetic electrons will effectively leave the target, most of the hot electrons will be backheld within the target volume by the space charge and will form a sheath extending by approximately a Debye length λ_D from the initially unperturbed rear surface. According to the model developed in [2], the initial accelerating field will be given by

$$E(0) = \frac{KT_h}{e\lambda_D} = \sqrt{\frac{n_h KT_h}{e\lambda_D}} \quad (14.1)$$

where n_h and T_h are density and temperature of the hot electrons, which for typical values at $I_0^2 \sim 10^{19} \text{ W/cm}^2$, i.e. $\lambda_D \sim 1 \mu\text{m}$ and $T_h \sim 1 \text{ MeV}$, gives field amplitudes of order TV/m. Under

the right combination of target thickness and pulse duration, the hot electrons recirculate through the target during the ion acceleration process, which can lead to an enhancement of the ion energy [10]. TNSA from the front surface has normally reduced efficiency due to the presence of a preplasma, although symmetric acceleration from front and rear has indeed been observed in ultra-high contrast interactions with moderate intensity ultrashort pulses, where front preplasma formation is effectively suppressed [11].

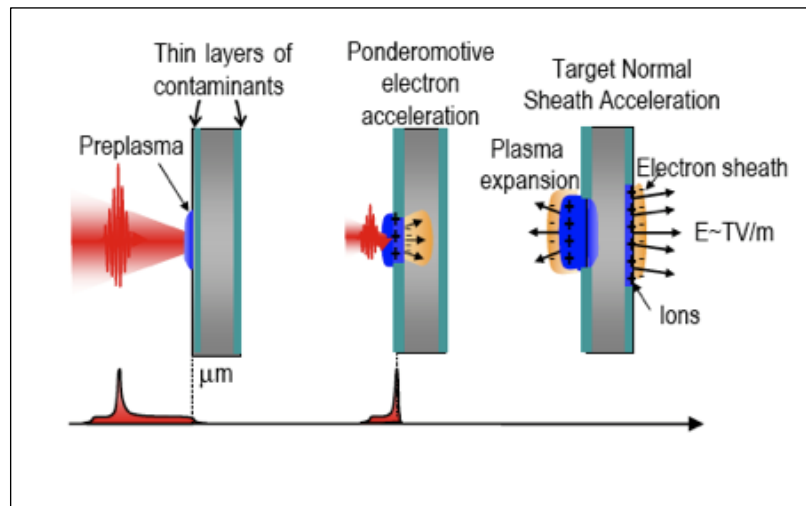


Figure 14.1 Schematics of sequential stages of Target Normal Sheath Acceleration.

While TNSA can in principle accelerate any ion species present in surface layers, in most experimental setting, this results in preferential acceleration of light ions (protons, Carbon and Oxygen ions) from contaminant layers rather than ions from the target bulk. Protons, with the highest charge to mass ratio, are therefore the dominant component of TNSA ion beams, unless the target is suitably treated prior to the laser irradiation to remove the contaminants [12].

According to (1) the field can be large enough to accelerate ions to multi-MeV energies, which have indeed been observed in a very large number of experiments. The energy spectra of the ion beams observed are broadband, typically with an exponential profile, up to a high energy cut-off, which is the quantity normally used to compare different experiments and determine experimental scaling laws for the acceleration process. The highest TNSA energies reported are of the order of 85 MeV, obtained with large PW systems, and available data (e.g. see fig. 15.2) generally shows that, at equal intensities, longer pulses (of $\sim\text{ps}$ duration) containing more energy generally accelerate ions more efficiently than 10s of fs pulses. Using state of the art fs systems has however recently allowed increasing the energies of accelerated protons up to a reported 40 MeV [13], obtained with only a few J of laser energy on target.

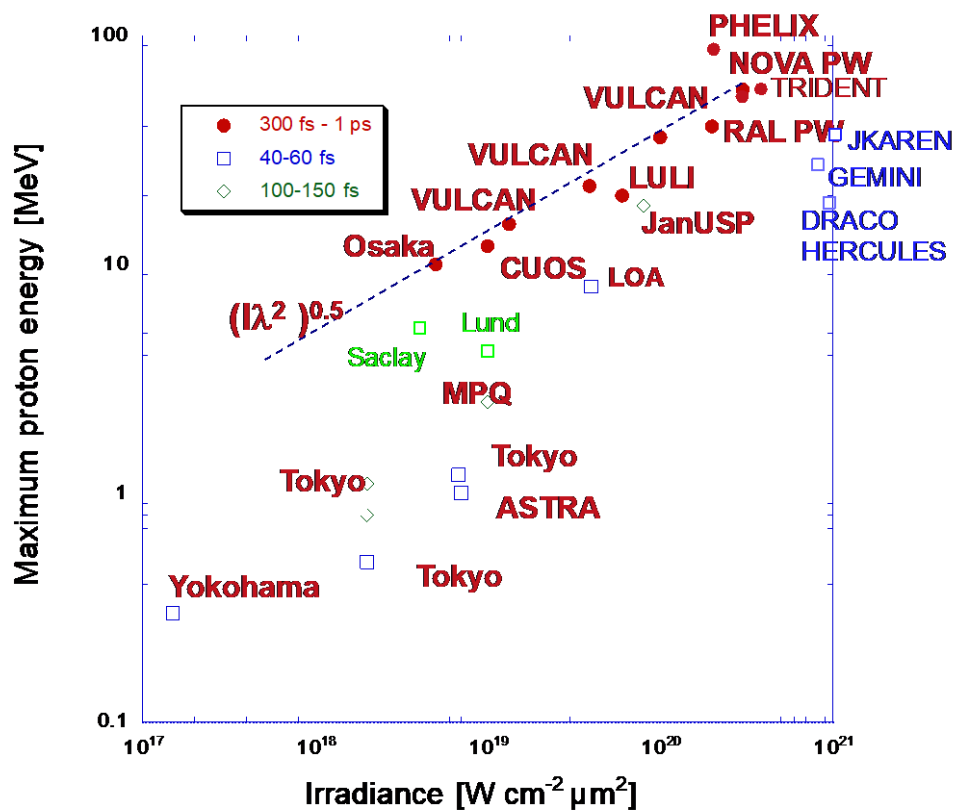


Figure 14.2 Survey of TNSA cut-off energies measured in experiments, plotted vs irradiance and labelled according to pulse duration. For references for the specific data points, see [6] and [13]. Points labelled J-Karen, DRACO and Trident refer respectively to [13], [16], [17]. The point labelled PHELIX refers to the work reported in [18].

The properties of the beams accelerated via TNSA are quite different from those of conventional RF beams, to which they are superior under several aspects. The beams are characterized by ultralow transverse emittance (as low as 0.004 mm-mrad, according to the estimate given in [14]), and by ultrashort (~ps) duration at the source. The beams are bright, with 10^{11} - 10^{13} protons per shot with energies > MeV, corresponding to currents in the kA range if co-moving electrons are removed. However, the number of protons at the high-energy end of the spectrum (i.e. the energies plotted in fig.1) can be as low as 10^7 - 10^8 particles/MeV/sr, (e.g. see [15] for a discussion related to recently published data) - with a divergence of a few degrees this gives $\sim 10^6$ - 10^7 particles/MeV. Drawbacks, as compared with conventional accelerator beams, are the larger divergence (up to 10s of degrees, and energy dependent) and, as mentioned earlier, the broad spectrum.



14.3 TNSA scaling and optimization

Increasing the laser intensity on target should generally lead to an increase of the cut-off energies of TNSA spectra, as shown in fig. 15.2. However there is still debate on what is the most appropriate scaling for ion energies as a function of irradiance, and it is also clear that, in addition to the role of pulse energy highlighted in fig.15.1, several secondary factors (e.g., such as prepulse energy and duration, target thickness) also affect the maximum energy measurable. Parametric investigations of the dependence of E_{\max} on laser pulse irradiance, duration, energy and fluence have been reported (e.g. [16-17, 19-20]). Two main classes of approaches have been developed to describe analytically the TNSA process with the aim of matching current results and predict performance at higher intensities. A first approach considers ions and hot electrons as an expanding plasma, described with fluid models [4,5,21] as an extension of the classical case of a plasma expanding into vacuum, driven by the ambipolar electric field generated in a narrow layer at the front of the plasma cloud. Simplest models are isothermal, and require that the acceleration time is artificially constrained [19-20], while more realistic adiabatic models, accounting for the finite energy of the hot electrons, have also been developed [21].

A different class of models assumes that the most energetic ions are accelerated as test particles in a *static* sheath field, unperturbed by their acceleration. These *static* models rely on an accurate description of the sheath field based on realistic assumptions on the fast electron distributions. For example, in [22], a spatial truncation of the electric potential in the sheath is introduced, and used to develop a model for the maximum ion energy as a function of the relevant laser parameters (energy and intensity). Scalings for the ion energy based on this model appear to match a large fraction of experimental results so far [23], and can be used as a predictive tool for future performance. Taking 200 MeV H^+ energy as a benchmark, predictions of the intensity requirement for reaching this cut-off value based on the two different approaches discussed above give intensities of mid 10^{21} W/cm² for ~ps pulses [22], and $\sim 10^{22}$ W/cm² for 10s of fs pulses [23].

Experimentally, several approaches have been developed to improve TNSA efficiency by acting on the characteristics of the hot electron population driving the acceleration through modifications of the target design [8]. According to (1) the accelerating field can be modified either by increasing the electron density or the temperature. The use of the so-called *mass limited targets*, aims to reduce the transverse size of the accelerating foils and concentrating the electrons in a smaller volume so that the density is increased during the acceleration process. This approach was first demonstrated in [24] where reduction of the foil down to 20 μ m x 20 μ m resulted in a 3-fold protons energy increase with respect to a large mm-size foil, jointly to a sizeable increase in conversion efficiency. A further class of experiments aims to



optimize laser energy absorption into hot electrons by structuring the target: an example of this approach is reported in [25], where foils coated with microsphere (diameter $\sim d/2$) on the irradiated surface showed, compared to uncoated foils, a clear improvement in the energy cut-off of the spectrum of the accelerated protons.

Targets with special microstructuring and/or shaping of the rear side have been also used for spectral and spatial manipulation of the proton beam. For example, target shaping to manipulate field configuration has been used for beam focusing (e.g., see [26-27]) and the highly transient nature of the TNSA field has been used for dynamic focusing with chromatic capability using a two-beam configuration [28].

A recently proposed approach employs what is a by-product of intense laser-target interactions (i.e. the generation of large amplitude electromagnetic pulses, EMP, through a process akin to ultrafast electric dipole emission), to control the properties of TNSA-accelerated ions. This is done by attaching a coiled metallic wire behind the target, and synchronizing the propagation of TNSA protons with a given energy with the EMP propagating along the coil. The strong electric field associated to the EMP can act on the protons by constraining their divergence but also by re-accelerating the protons. In proof-of-principle experiments, doubling of the energies of TNSA protons has been achieved through this process, jointly to the production of a highly collimated, narrow band proton beamlet. [29]

For a review of other approaches, including the use of foam layers, controlled pre-plasmas, or double pulses, see [8].

While experimental activity has focused until recently on the study of TNSA beams, other mechanisms have recently attracted a significant amount of theoretical and experimental attention, and some of these mechanisms are briefly discussed in the following sections. We refer the reader to [8] for a more thorough discussion. Please note that, although conceptually different, these mechanisms can coexist during an interaction, and in many experimental settings (particularly when employing ultrathin foils), ion acceleration will proceed through hybrid processes combining elements of different acceleration mechanisms, including TNSA.

14.4 Radiation Pressure Acceleration

It is well known, already from Maxwell's e.m. theory, that electromagnetic (EM) waves carry momentum, and this momentum may be delivered to a non-transparent (either absorbing or reflecting) medium irradiated by the EM wave.

In a classical approach, the momentum p carried by the wave per unit volume is given by $p=w/c$, where w is the e.m. energy density and c the speed of light. If the light strikes a surface A , it will apply a force to the surface, which is equal and opposite to the rate of change of the

momentum of the wave.

If the light is completely absorbed by the surface, the momentum change per unit time is given by the e.m. momentum contained within a volume cA , the force applied to the surface is $F = pcA$, and the pressure is $P_{rad} = F/A = w = I/c$, where I is the intensity of light.

In case of light being fully reflected from the surface, the change of momentum is double than in the total absorption case, as the momentum of the light is reversed after reflection, and the force applied to the surface would therefore be $F = 2pcA$ from which $P_{rad} = 2I/c$.

In a general case, the radiation pressure P is given by

$$P_{rad} = (1 + R_C - T_C) \frac{I}{c} = (2R_C + A_C) \frac{I}{c}$$

where R_C , T_C , A_C are the reflection and transmission and absorption coefficients (for example $R_C = I_{ref}/I$). For an intense laser pulse, such pressure can be enormous: for example for $I = 10^{20} \text{ Wcm}^{-2}$ (as achievable nowadays with state of the art lasers), the pressure $2I/c$ is of the order of 60 Gbar. Such pressure can strongly alter the dynamics of laser-plasma interaction, and can be used to accelerate and propel forward particles in the plasma.

14.4.1 Hole boring

If an intense laser pulse irradiates a dense plasma, the Radiation Pressure is coupled to the electrons via the **ponderomotive force**

$$F_{p_0} = -\frac{e^2}{4m_e\omega^2} \nabla E_0^2 .$$

Note that the expression above is obtained, for linearly polarized light, as a cycle average of the expression:

$$F_p(t) = -\frac{e^2}{2m_e\omega^2} \nabla E_0^2 \cos^2(\omega t) = -\frac{e^2}{4m_e\omega^2} \nabla E_0^2 (1 + \cos(2\omega t))$$

(e.g. see [30]). The instantaneous ponderomotive force is therefore composed of two terms, the steady ponderomotive force F_{p_0} and a term oscillating at twice the frequency of the radiation. This oscillating term is responsible for electron heating through the so-called *Ponderomotive (or JxB) heating* [9]. As we will discuss later heating electrons to high temperature is generally detrimental for radiation pressure acceleration. However, if one employs circularly polarized light at normal incidence, the oscillating component of the force is not present, and $F_i(t) = F_{p_0}$. For this reason most theoretical and numerical investigations of RPA (as well as some of the experiments) employ circularly polarized pulses.

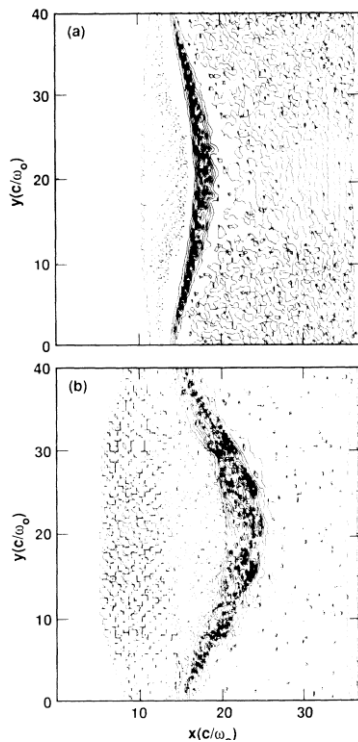


Figure 14.3 – Ion density profiles resulting from Particle in Cell simulations showing how the density is modified by the hole boring process. The laser is incident on an overdense plasma from the left, and propagates into the plasma, as the density profile is modified. The two images are two snapshots taken at different times from [34]

At the surface of the overdense plasma the electrons are pushed inward by F_{p0} , leaving a charge separation layer and creating an electrostatic, backholding field that in turn acts on the ions and leads to their acceleration. This dynamics leads to the process called *hole boring* [31], i.e. a dynamic deformation of the plasma density profile which allows the laser to penetrate into the plasma (see fig.3).

During this process the ions are compressed in a front which is pushed forward by the ponderomotive force, and the name *hole boring acceleration* is typically used to describe the ion dynamics in this process. The recession velocity of the plasma surface (i.e. the hole boring velocity u_{HB}) can be obtained from momentum balance considerations (and assuming the velocity of the ions is non relativistic) as [31]:

$$\frac{u}{c} = \left[\frac{n_{cr} Z m_e}{2 n_e m_i} \frac{I \lambda^2}{1.37 \cdot 10^{18}} \right]^{\frac{1}{2}}$$

where n_e and n_{cr} are the electron plasma density and the critical density respectively. A more complete, fully relativistic derivation of the hole boring velocity leads to a more complex dependence (e.g. see [32]), however even from this simple, 1D description some interesting features emerge:

- 1) The energy of the ions in the hole boring front ($E_i = mu^2/2$) is directly proportional to the intensity of the laser.
- 2) E_i has an inverse proportionality to the plasma density (and consequently to the mass density $\rho \sim m_i n_e / Z$), which suggests that the ion energy obtainable through this process can be optimized by choosing plasmas or targets of suitably low density (provided they are not transparent to the radiation).

A more detailed understanding of the dynamics of ion acceleration during hole boring can be had from the cartoon provided in fig. 15.4 (see also [33]), which assumes an initial step-density profile with $n_e > n_{cr}$. The ponderomotive force of the laser quickly pushes forward the electrons, which pile up, and leave behind a layer of non neutralised ions. The charge distribution creates an electrostatic field E_x , which accelerate the ions. The ions located between x_d and x_s

experience an electrostatic field which decrease with distance, meaning that the ions at the back of this layer are accelerated more than those at the front, which results in bunching of the ions, ultimately leading to a ion spike at the point where the electric field was initially zero, as shown in fig.2(c), and to an average velocity u_{HB} . Simulations [33] indicate that during this process, collapse of the electron equilibrium leads to a non-linear phase in which a narrow bunch of fast ions can be accelerated at $u \sim 2 u_{HB}$.

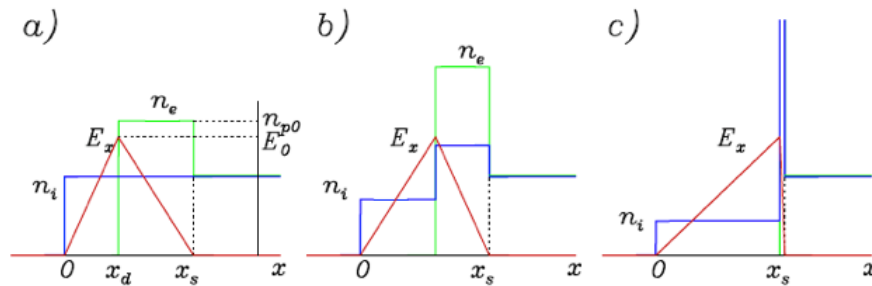


Figure 14.4 – Sketch of electron density n_e , ion density n_i and longitudinal electric field E_x at sequential stages of the hole boring process during intense irradiation of an overdense plasma

Experimental data on HB acceleration using solid density foils is limited so far, mainly because the energies of HB-accelerated ions are low due to the inverse dependence on target density and therefore ions from TNSA processes dominate experimental spectra. Most interesting for acceleration via this method are media of low density. Recent results which have highlighted HB-accelerated ions have been obtained employing CO₂ lasers ($\lambda \sim 10 \mu\text{m}$). Due to the long wavelength, the critical density is reduced by ~ 100 times with respect to the more broadly used solid state lasers (e.g. Nd:YAG or Ti:Sa systems). Therefore, even gas jet targets can be overdense for CO₂ laser pulses. For example, in an experiment employing CO₂ laser pulses and a gas jet [34], proton spectra obtained through this method showed a clean monoenergetic signal at $\sim 1 \text{ MeV}$ which was broadly consistent with hole boring acceleration in the conditions of the experiment. Although the energy observed so far through HB is modest, the dependence on both target density and laser intensity allows designing suitable acceleration scenarios for acceleration to 100s MeV/nucleon with next generation laser facilities, as suggested in [32, 35].

An acceleration scheme related to HB, but conceptually different, is the so-called **Shock Acceleration**, first proposed in [36]. In this scheme, the light pressure applied at the front surface of the target, acts as the source of a strong, collisionless electrostatic shock propagating towards the bulk of the plasma. Acceleration arises as ions present in the bulk of the target are reflected from the shock front to twice the shock velocity, in a similar fashion to acceleration scenarios thought to take place in astrophysical contexts. Results also obtained

with a CO₂ laser have been explained with this mechanism, namely monoenergetic acceleration of protons up to 22 MeV from the interaction with hydrogen gas jets at intensities in the 10¹⁶-10¹⁷ Wcm² regime [37].

14.4.2 Light Sail

Light Sail is the name currently used to define a different regime of Radiation Pressure Acceleration where the irradiated target is *thin* enough that the Hole boring process reaches the rear of the target before the end of the laser pulse [8, 38-41]. In such a case, the laser pulse is able to further accelerate ions to higher energies since the ions are not screened by a background plasma anymore. In an ideal situation, the irradiated region of the target is detached and pushed forward under the effect of the intense Radiation Pressure of the laser pulse, as sketched in fig.14.5.

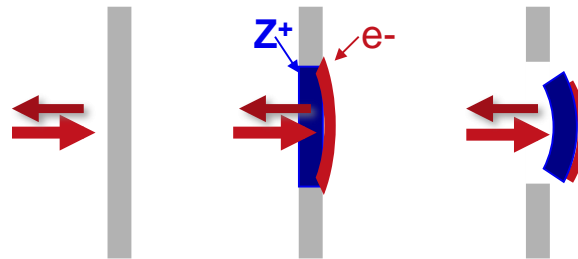


Figure 14.5 - Schematic representation of Light Sail acceleration. Reflection of light at the target surface causes a pressure on the electrons driving hole boring through the target. The target is thin enough that the laser keeps driving the irradiated portion of the target after the hole boring front has reached its rear.

An estimate of the dependence of the ion energy in this regime from the relevant parameters can be obtained from simple considerations. Neglecting absorption, the force applied by the Radiation pressure to an area A of the targets is given by

$$F = (1 + R) A \frac{I}{c}$$

The momentum acquired by the initially stationary target will be equal to the product of this force by the pulse duration τ , and the mass contained in the irradiated area of the target is given by $m_i n_i A d = \rho A d$. Therefore one has that the final velocity acquired by the target will be

$$u_i = (1 + R) \frac{1}{\rho d} \frac{I}{c} \tau$$

which gives the dependence

$$E_i \sim \left(\frac{I \tau}{\rho d} \right)^2$$

A few interesting considerations can be made on the basis of this expression:

- 1) The scaling of ion energy with laser intensity is much faster than in HB (and TNSA), which is promising for acceleration to high energy.
- 2) Due to the product Ir , the dependence is on fluence (Energy per area) rather than on intensity only.
- 3) There is an inverse dependence on the areal density $\eta = \rho d$ rather than on the density ρ which points to the advantage of using as thin targets as possible, provided that they are not so thin to be transparent to the radiation. An optimum thickness emerges if one takes transparency into consideration, as shown in [41]

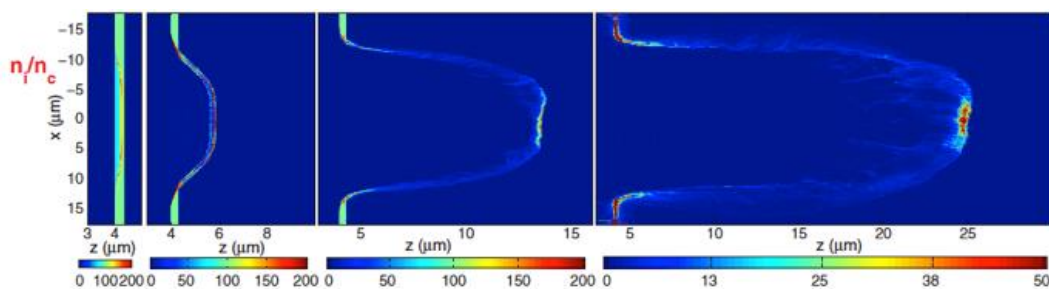


Figure 14.6 – Snapshots of 2D PIC simulations of Light Sail acceleration of protons from a thin hydrogen target. The pulse intensity employed in the simulation was circularly polarised and had intensity $\sim 5 \cdot 10^{22}$ W/cm². See [40] for further information.

The scheme has been widely investigated via numerical simulations, which, while confirming the general features above, have highlighted a complex dynamics, in which charge separation between the electron and ions is maintained by the ponderomotive force of the laser as the compressed electron ion layer becomes detached from the target. Figure 6 shows the implementation of such a scheme in 2D Particle in Cell simulations. The sequential frames show ion density plots at different stage of the process, and show how a compressed ion layer is detached and pushed forward by the radiation (the laser is still active in the last frame shown). The red curve in Fig. 14.7 is an ion energy spectrum from the same simulation, characterized by a spectral peak at very high energies ($> \text{GeV}$). A quasi-monoenergetic spectrum arises as all ions in the compressed layer share the same acceleration history (differently for example from TNSA spectra, which are typically very broad and exhibit an exponential decay at the high energy end).

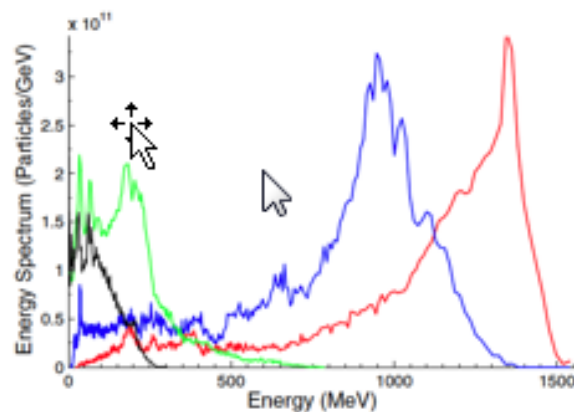


Figure 14.7 Energy spectra of protons accelerated by Light Sail in 2D PIC simulations. The red curve is from the simulation shown in fig.15.4. The green profile refers to a case in which the acceleration process is unstable (see [40])

For LS to be effective, it is essential that the radiation pressure is strong enough to overcome detrimental effects related to electron heating, such as foil disassembly under the thermal pressure of hot electrons, or debunching of the compressed foil, and to dominate over TNSA. As discussed before, the use of circularly polarized light can in principle reduce these effects, although some electron heating is unavoidable. Recent work has, however, highlighted hybrid RPA-TNSA regimes using linearly polarized pulses, where, under appropriate conditions, RPA features dominate the ion spectra [42], and has investigated the more complex dynamics associated with RPA of multispecies targets.

Experiments employing ultrathin foils have recently started to show signatures of RPA acceleration processes, namely effective acceleration of bulk species, a strong polarization dependence and the emergence of spectral peaks, as well as the observation of fast scaling consistent with theoretical predictions (see, e.g., [43-44]).

Record proton energies (approaching 100 MeV) have been reported this year (2018) in an experiment carried out on VULCAN in which an hybrid TNSA-RPA regime was optimized and enhanced by relativistic transparency processes (see next section) [45].

14.5 Relativistic transparency regimes

Acceleration regimes in which the target becomes relativistically transparent to the laser pulse are also of interest, and have been explored in a number of experiments [46-49]. In these investigations the target areal density is chosen so that the target is quickly heated by the laser pulse, and the density decreases below the relativistically corrected critical density near the peak of the pulse. In this regime the interaction leads to volumetric heating of the target electrons, and to a consequent enhancement of the field accelerating the ions. In the *Break*



Out Afterburner scenario proposed by the Los Alamos group [50], non-linear processes lead to growth of electromagnetic instabilities, which further enhances energy coupling into the ions.

Experimental spectra obtained in this regime are generally broadband, with particle numbers decreasing to a high energy plateau and show efficient acceleration of the bulk components of the target. The mechanisms of this interaction regime are rather complex, and a number of recent investigations have been devoted to the electron and ion dynamics during the interaction, as well as their dependence on laser polarization [49, 51]. Under appropriate conditions, occurrence of transparency near the peak of the laser pulse can lead to an enhancement of the energy of the accelerated ions, as well as to distinctive angular emission patterns [45,51].

References

- [1] E.L.Clark *et al*, Phys. Rev. Lett., **84** (2000) 670
- [2] A. Maksimchuk *et al*, Phys. Rev. Lett., **84** (2000) 4108
- [3] R. A. Snavely *et al*, Phys. Rev. Lett., **85** (2000) 2945
- [4] S.C. Wilks *et al*, Phys. Plasmas, **8** (2001) 542
- [5] P.Mora, Phys. Rev. Lett., **90** (2003) 185002
- [6] M.Borghesi *et al*, Fusion Sci Tech, **49** (2006) 412.
- [7] H.Daido, M. Nishiuchi and A.S Pirozhkov, Rep. Prog.Phys.,**75** (2012) 056401
- [8] A.Macchi, M. Borghesi and M. Passoni, Rev. Mod. Phys., **85** (2013) 751
- [9] W.L.Kruer and K. Estabrook, Phys. Fluids **28** (1985) 430
- [10] A.J.Mackinnon *et al*, Phys. Rev. Lett., **88** (2002) 215006
- [11] T. Ceccotti *et al*, Phys. Rev. Lett. **99** (2007) 185002
- [12] M.Hegelich *et al*, Phys. Rev. Lett. **89** (2002) 085002
- [13] K. Ogura *et al*, Opt. Lett. **37** (2012) 2868
- [14] T. Cowan *et al*, Phys. Rev. Lett. **92** (2012), 204801
- [15] A. Macchi *et al*, Plasma Phys. Control. Fusion, **55** (2013) 124020
- [16] K. Zeil *et al*, New J. Phys., **12** (2010) 045015
- [17] K.A. Flippo *et al*, Rev. Sci. Instr, **79** (2008) 10E534
- [18] F. Wagner *et al*, Phys. Rev. Lett., **116** (2016) 205002
- [19] J.Fuchs *et al*, Nature Phys, **2** (2006) 48
- [20] L.Robson *et al*, Nature Phys., **3** (2007) 58
- [21] P. Mora, Phys. Rev. E, **72** (2005) 056401
- [22] M. Passoni and M. Lontano, Phys. Rev. Lett. **101** (2008) 115001
- [23] M. Passoni, L. Bertagna and A. Zani, New Journal of Physics, **12** (2010) 045012
- [24] S. Buffechoux *et al*, Phys. Rev. Lett. **105** (2010) 015005.
- [25] D.Margarone *et al*, Phys. Rev. Lett., **109** (2012) 234801
- [26] P.K. Patel *et al*, Phys. Rev. Lett., **91** (2003) 125004
- [27] S. Kar *et al*, Phys. Rev. Lett., **100** (2011) 105004
- [28] T.Toncian *et al*, Science, **312** (2006) 410
- [29] S. Kar *et al*, Nature Comm., **7** (2016) 10792
- [30] F.F. Chen, *Introduction to Plasma Physics and Controlled Fusion*, Plenum Press (1984)
- [31] S.C. Wilks *et al*, Phys. Rev. Lett., **69** (1992) 1385
- [32] A.P.L. Robinson *et al*, Plasma Phys Control Fusion, **51** (2009) 024004
- [33] A. Macchi *et al*, Phys. Rev. Lett., **94** (2005) 165003



- [34] C. A. J. Palmer *et al*, Phys. Rev. Lett., **106** (2011) 014801
- [35] A P L Robinson, *et al*, Plasma Phys. Control. Fusion, **54** (2012) 115001
- [36] L. Silva *et al*, Phys. Rev. Lett. **92**, (2004) 015002
- [37] D.Haberberger *et al*, Nature Phys. **8**, (2012) 95
- [38] T.Esirkepov *et al*, Phys. Rev. Lett. **92** (2004)175003
- [39] A.P.L. Robinson *et al*, New J. Phys., **10** (2008) 013021
- [40] B.Qiao *et al*, Phys. Rev. Lett., **102** (2009) 145002
- [41] A.Macchi, S. Veghini and F. Pegoraro, Phys. Rev. Lett., **103** (2009) 085003
- [42] B. Qiao *et al*, Phys. Rev. Lett., **108** (2012) 115002
- [43] S. Kar *et al*, Phys. Rev. Lett, **109** (2012) 185006
- [44] C. Scullion *et al*, Phys. Rev. Lett. **119** (2017) 054801
- [45] A. Higginson *et al*, Nature Comm., **9** (2018) 724
- [46] A.Henig *et al*, Phys. Rev. Lett. **103** (2009) 045002
- [47] D.Jung *et al*, New J. Phys, **15** (2013) 023007
- [48] D.Jung *et al*, Phys. Plasmas, **20** (2013) 083103
- [49] B. Gonzalez-Izquierdo *et al*, Nature Comm., **7** (2016) 12891
- [50] L.Yin *et al*, Phys Rev. Lett **107** (2011) 045003
- [51] B. Gonzalez-Izquierdo *et al*, Nature Phys. **12** (2016) 505
- [52] H.W. Powell *et al*, New J. Phys., **17** (2015) 103033



HELLENIC
MEDITERRANEAN
UNIVERSITY



université
BORDEAUX



UNIVERSITY
of York



Erasmus+

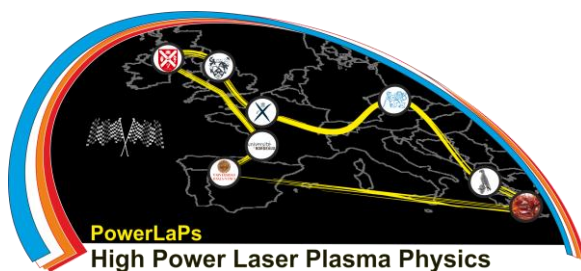
PowerLaPs

Innovative Education & Training in High Power Laser Plasmas

High Power Laser Matter Interactions/High Energy Density Physics - Theory and Experiments

Chapter 15: From perfect gas to QDM: applications to planetary physics

M. Koenig





15. From perfect gas to QDM: applications to planetary physics

In this lecture, divided in two parts: in the first one, I will present how a plasma, whatever its conditions, can be describe theoretically leading to Equation Of State (EOS) calculation. Then in the second part, I will show how EOS is important to planet formation and internal structure.

15.1 Plasma theoretical description leading to Equation Of State (EOS)

Plasma is very common state of matter in the Universe (ionized partially or completely), where particles interact through Coulomb potential. Depending on the strength of the potential and the species to which it corresponds (ions or electrons), the plasma can be described by many different theories or models. I will show that one can divide the plasmas in several "categories" first where particles can be treated as classical or quantumly. Then in each of this categories, particles can be either strongly coupled or not. Depending of its temperature and density, the plasma follow different models: perfect gas for non-interacting particles, Debye-Hückel for low interaction when classical. Thomas-Fermi when temperature is below the Fermi one that depends on density, One Component Plasma when the electrons can be considered as a uniform jellium, ... More recently ab initio methods strongly developed thanks to the new computing capabilities. Here the ions are considered as classical particles moving by following the newton laws, the electron being treated quantumly through Schrödinger equation. All these models give plasma properties (equation of state, conductivities, ...) either of extremely dense plasmas such as white dwarf or diluted one such as interstellar medium.

15.2 Description of internal structure of planets by Equation Of State (EOS)

In the second part, I will describe how equation of state is a fundamental property to describe internal structure of planets, especially for the giant ones such a Jupiter or Saturne. A quick overview of how the internal structure is determined through models (such as hydrostatic one) will be given. Here I will emphasis how by calculations and external constrains given by astronomical (telescopes, satellites, probes). The question to be answered is then how to generate pressures and temperatures that occur inside in planetary interiors. As temperature as quite low in these objects, pure shocks is not the solution but a combination of shock and isentropic compression using high energy lasers. Then having the required plasma conditions, I will present all possible/necessary diagnostics to infer fundamental parameters such as pressure, temperature, mass density, ... these are visible such as the VISAR (velocity measurement by Doppler effect), x-ray radiograph, Thomson scattering, ... finally my lecture will show a dedicated application on earth-like planets (from 1 to 10 times earth mass), using isentropic compression of iron on the LIL laser (10 kJ, 20 ns ramped pulse). The melting line of iron (fundamental property that governs all earth thermodynamics, B field generation) has been inferred for objects up to $5 M_{\oplus}$.



16.3 Exercises

Question 1

The DT fuel in ignition phase will have a mass density $\rho \approx 200 \text{ g/cc}$. As atomic number of the fuel is $A=2.5$, charge $Z=1$, what is the Fermi energy ε_F

- a) $\approx 50 \text{ eV}$
- b) $\approx 500 \text{ eV}$
- c) $\approx 5 \text{ keV}$

Question 2

What is the Fermi pressure P_F in this case

- a) $P_F \approx 0.1 \text{ Gbar}$
- b) $P_F \approx 1 \text{ Gbar}$
- c) $P_F \approx 10 \text{ Gbar}$

Question 3

In the solid phase, above 20 Gpa, iron crystal lattice is

- a) bcc
- b) fcc
- c) hcp

Question 4

What are the plasma conditions at IOB (inner-outer core Boundary) for earth?

- a) $P= 240 \text{ Gpa}$, $T= 6000 \text{ }^\circ\text{K}$
- b) $P= 365 \text{ Gpa}$, $T= 6000 \text{ }^\circ\text{K}$
- c) $P= 500 \text{ Gpa}$, $T= 8000 \text{ }^\circ\text{K}$



HELLENIC
MEDITERRANEAN
UNIVERSITY



UNIVERSITÉ
BORDEAUX



UNIVERSITY
of York



Queen's University
Belfast



Erasmus+

O2 – Experiments



HELLENIC
MEDITERRANEAN
UNIVERSITY



université
BORDEAUX



UNIVERSITY
of York



Erasmus+

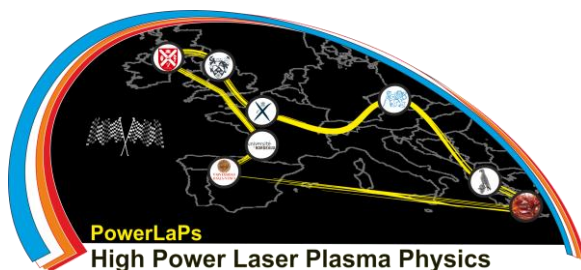
PowerLaPs

Innovative Education & Training in High Power Laser Plasmas

High Power Laser Matter Interactions/High Energy Density Physics - Theory and Experiments

EXP 1: Study of laser breakdown on solid targets

D. Batani, E. d'Humières, J.J. Santos, V.T. Tikhonchuk



Erasmus+

université
de BORDEAUX

1.1 A phenomenological approach to laser breakdown

11.1.1 Plasma ionisation

Let us begin by examining how the laser pulse ionises the irradiated material and induces breakdown. Atomic physics tells us that in order to ionise an atom at its fundamental level, we need a certain amount of energy as shown in Table 1.

Table 2: Ionisation energy values for certain elements

Atom	H	He	N	O	C	Si	Fe
Energy (eV)	13.599	24.588	14.534	13.618	11.260	8.1517	7.9024

Consider helium, for example. The energy required for ionisation at its fundamental state is 24.588 eV. For the lower-energy excited state, it is 19.96 eV. The optical ionisation of an atom (the photoelectric effect) requires high-energy photons. For the Nd-YAG laser ($\lambda_L = 0.532 \mu\text{m}$) the photon energy is 2.32 eV. This is much less energy than is required for the ionisation of helium. It is therefore impossible to create a direct photoelectric effect. In order to ionise a helium atom at its fundamental state we would need much more energy, accumulated from at least 11 photons. As we will see, this process – known as multiphotonic ionisation – does exist, yet the probability for it to occur is significantly low at the laser intensities explored here.

Now let us consider the problem from another angle. When we focus a laser beam with energy $\mathcal{E}_L = 0.005 \text{ J}$ and duration $\tau_L = 15 \text{ ns}$ on a point of diameter $50 \mu\text{m}$, the laser intensity of the beam is:

$$I_L = \frac{\mathcal{E}_L}{\tau_L S} = \frac{0.005 \text{ J}}{1.5 \times 10^{-8} \text{ s} \times 8 \times 10^{-9} \text{ m}^2} \approx 10^{13} \text{ W/m}^2. \quad (11.1)$$

According to the definition of electromagnetic wave intensity $I_L = \frac{1}{2} c \epsilon_0 E_L^2$, the amplitude of the laser's electric field is $E_L \approx 10^8 \text{ V/m}$.

To specify the orders of magnitude of the laser field, we can compare this value with that for the electric field of a hydrogen atom, for Bohr's first orbit:

$$E_H = \frac{\pi m_e^2 e^5}{4 \epsilon_0^3 \hbar^4} \approx 5 \times 10^{11} \text{ V/m}.$$

We can thus observe that, at the intensity in question, the laser field is very weak compared with the intra-atomic field. Nevertheless, we must bear in mind that this is no longer the case with today's high-intensity laser experiments, which can regularly attain intensities of over 10^{22} W/m^2 , with certain laboratories capable of attaining up to 10^{26} W/m^2 .

11.1.2 How can we ionise an atom?

In order to explain optical ionisation, we must imagine a multiphotonic process in which an atom is subjected to an intense laser field, and ionised via the "virtual" states induced by the laser field itself. This mechanism has been observed for many years in noble gases at low pressure. It is one of the mechanisms which explains the creation of the first electrons (primary electrons). The diagrams for multiphotonic ionisation and the dependency of the number of freed electrons are given in Figure 41. Other mechanisms, such as ionisation linked to cosmic radiation, but above all the ionisation of large particles on the surface of the target (dust and other pollutants, generally hydrocarbons), explain the presence of the first electrons detected in the experiment.

Indeed the ionisation of these particles (producing secondary electrons), once the first electrons have been created, is primarily a result of inelastic collisions with the primary electrons of the gas atoms. This is collisional ionisation. The electrons oscillate within the laser field and thus reach

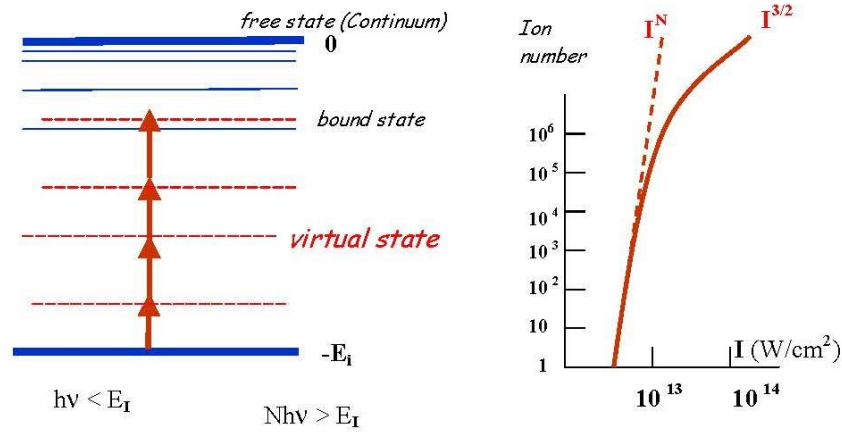


Figure 41: Multiphotonic ionisation.

a certain oscillation energy. Using the equation for electron movement in an electric field (at the intensity levels used here, we can ignore the influence of the magnetic field)

$$m_e dv_E/dt = -eE_L(t)$$

we can determine the amplitude of the oscillation speed $v_E = |eE_L/m_e\omega_L|$ where ω_L represents the laser pulse $\omega_L = 2\pi c/\lambda = 3.6 \times 10^{-15} \text{ s}^{-1}$. In practical units: $v_E = 25 \lambda_L \sqrt{I_L} \text{ cm/s}$, where laser intensity I_L is expressed in W/cm^2 and wavelength λ_L in μm . Laser intensity $I_L = \mathcal{E}_L/S_f\tau_L$, can be calculated using the equation (11.1) if we know the pulse energy \mathcal{E}_L , its duration, τ_L , and the focalisation surface area, S_f .

The oscillation amplitude is $r_L = v_E/\omega_L \approx 0.01 \text{ nm}$. The oscillation speed is low, $v_E \approx 8 \times 10^3 \text{ m/s}$, as is the oscillation energy $\varepsilon_E = m_e v_E^2/2 \approx 2 \times 10^{-4} \text{ eV}$. Nonetheless, the electron can still gain a lot more energy via elastic collisions with atoms. During an elastic collision with an atom, the energy from an electron's oscillation ε_E is converted into kinetic energy ε_e . The kinetic energy gained by the electron, per unit of time, can be expressed by:

$$d\varepsilon_e/dt = \nu_{ea}\varepsilon_E$$

where $\nu_{ea} = n_a v_e \sigma_m$ is the frequency of elastic collisions between electrons and atoms.

Assuming that the atomic density where the interaction processes is the critical density for the laser (the density above which the laser can no longer propagate) $n_a \approx n_c \sim 10^{27} \text{ m}^{-3}$, the electron thermal velocity $v_{Te} = \sqrt{k_B T_e/m_e} \approx 10^5 \text{ m/s}$ and an atomic radius equal to 2 – 3 times the Bohr radius (the Bohr radius $r_B = \hbar^2/m_e e^2 = 0.05 \text{ nm}$ is the characteristic radius of a hydrogen atom), we are left with a collisional cross-section of $\sigma_m = 4\pi r_a^2 \approx 10^{-19} \text{ m}^2$ and the collisional frequency value is therefore $\nu_{ea} \sim 10^{13} \text{ s}^{-1}$. It thus appears that for the duration of the laser pulse $\tau_L = 15 \text{ ns}$, the electron is involved in a large number of collisions, $N_{coll} \sim \nu_{ea}\tau_L \sim 150000$, and its final energy may rise to $\varepsilon_E \nu_{ea}\tau_L \sim 30 \text{ eV}$. In this way, it can exceed the ionisation energy of the atom in question. The threshold condition can therefore be expressed as: $\varepsilon_E \nu_{ea}\tau_L > E_i$.

The ionisation threshold decreases if the density of the target medium increases or if we use a gas with heavier atoms and a greater atomic radius. For example, if we focus the laser directly in the air, which has a much lower density at atmospheric pressure, approximately $\sim 10^{25} \text{ m}^{-3}$, we will need a much higher laser intensity to exceed the ionisation threshold. But when the laser intensity does exceed this threshold, ionisation occurs very rapidly.

Phenomenologically, the electron production rate, which represents the variation in electron density per unit of time, can be defined (if we ignore the recombination rate, which is relatively unimportant during the plasma creation phase):

$$dn_e/dt = (\nu_i - \nu_a - \nu_d) n_e$$

where $\nu_i n_e$ represents the ionisation rate, $\nu_a n_e$ the recombination rate and $\nu_d n_e$ the electron scattering rate outside the focal spot.

When $\nu_i > \nu_a + \nu_d$, the process expands exponentially, according to the previous equation. After around 10 successive ionisations, the irradiated zone of the target is fully ionised (on the surface of the focal spot, and to a *skin depth* of less than one micron). This condition defines the threshold for the avalanche or cascade effect.

In summary At the start of the laser pulse, when the breakdown threshold has not yet been reached, the target remains inert (if we use a glass slide, it will remain transparent to the laser beam). The amount of energy provided by ionisation is very small. The degree of ionisation (ionised atoms as a percentage of the total neutral and ionised atoms) and the plasma temperature are still very low. The small number of primary electrons in the focal volume – created by multiphotonic ionisation or produced by cosmic radiation – have a relatively low level of initial energy. They will then gain energy due to the action of the laser field.

Primary electrons which have gained sufficient energy may in turn produce secondary electrons via ionising collisions. These secondary electrons acquire their own energy and set off a cascade effect which sees an exponential increase in the number of electrons. The breakdown threshold depends on the nature and density of the target, as well as the duration and intensity of the laser pulse.

Once the avalanche effect is triggered, the electron density of the plasma grows exponentially, while the temperature still remains relatively low. The plasma thus becomes highly absorbent for the laser beam. The dominant absorption method is known as the inverse bremsstrahlung process, which is the result of electron-ion collisions and leads to the “heating” of the electrons in a similar manner to the Joule effect for electrical resistance.¹

11.1.3 Plasma expansion

Free expansion in a vacuum The plasma pressure is much greater than the ambient gas pressure, due to the high electron temperature (10^5 K). As a result, plasma expansion could occur in a similar manner to an expansion into a vacuum. Let us work on this hypothesis for the time being.

Electrons, which are lighter and more mobile than the ions, attempt to escape from the plasma, but the space-charge field holds them back. The non-neutrality scale is the Debye length λ_D . We can estimate an order of magnitude for the amplitude of the space-charge field E based on the assumption that the mean kinetic energy of the electrons $k_B T_e$ is close to their potential energy $eE\lambda_D$ where E represents the space-charge field in the vicinity of an ion. As the electrons cannot escape from the plasma, the electric field will accelerate the ions. The kinetic energy thus acquired by an ion is $m_i v_i^2/2 = ZeE\lambda_D = Zk_B T_e$. We can thus estimate the expansion velocity of the plasma front to be approximately $\sqrt{2Zk_B T_e/m_i} = \sqrt{2} c_s$ where c_s represents the velocity of sound in the plasma (in our case we can consider that $Z = 1$).

¹Bremsstrahlung is a German term meaning “braking radiation”. Inverse Bremsstrahlung is a three-body process resulting from inelastic photon-electron collisions in the presence of an ion.

Sedov-Taylor model for the expansion of plasma in a gas A more rigorous approach requires us to take the atmospheric pressure of air into account. The expanding plasma particles indeed interact with the molecules of the environment gas (the air) and the energy exchange is likely to decelerate the expanding plasma. Besides, given the plasma temperature and the neutral air pressure, the expansion is likely supersonic and leads to the formation of a shock wave and a contact front. The shock wave is the propagation of a perturbation created by the sudden impact of the expanding plasma with the gas background. It defines a boundary layer separating the unperturbed gas in front of the shock wave from the gas that went through this layer and is perturbed. The contact front is the boundary between this perturbed gas and the plasma.

One of the most used models to describe laser produced plasma expansion in a gas is the Sedov-Taylor (S-T) model.² In such model parameters such as pressure, density and temperature of the perturbed gas behind the shock wave are expressed as a function of the speed at which this wave propagates through the gas. On this subject, we recommend reading the article by E. de Posada *et al.*, in Journ. Phys.: Conf. Series **274** (2011) 012078 [doi:10.1088/1742-6596/274/1/012078].

The basic assumptions here are that (i) a large amount of energy E_s is released instantaneously from a small (negligible) volume, (ii) the mass of the energy source is negligible compared with the mass of the gas background swept by the shock wave and (iii) the pressure exerted by the explosion over the gas is greater than the pressure in the unperturbed background gas. The equations of the Sedov-Taylor define the shock radial position as a function of time:

$$R(t) = 1.08 \left(\frac{\gamma + 1}{2} \right)^{\frac{2}{2+\nu}} \left(\frac{E_s}{\rho_0} \right)^{\frac{1}{2+\nu}} t^{\frac{2}{2+\nu}} \quad (11.2)$$

where ρ_0 is the density of the gas background and γ its specific heats ratio. The parameter ν is 1, 2 or 3 for expansions with planar, cylindrical or spherical symmetry. For hemispheric expansion (3D), the S-T model predicts an expansion of $R(t) \propto t^{2/5}$.

The fluid velocity, density, maximum pressure and temperature behind the shock (bs) are given by:

$$U_{bs} = \frac{2}{\gamma + 1} \frac{dR}{dt} \quad (11.3)$$

$$\rho_{bs} = \frac{\gamma + 1}{\gamma - 1} \rho_0 \quad (11.4)$$

$$P_{bs} = \frac{2}{\gamma + 1} \rho_0 \left(\frac{dR}{dt} \right)^2 \quad (11.5)$$

$$T_{bs} = \frac{2\gamma}{\gamma + 1} \left(\frac{\gamma - 1}{\gamma + 1} M^2 + 1 \right) T_0 \quad (11.6)$$

where $M = \frac{1}{v_s} \frac{dR}{dt}$ is the Mach number with $v_s = \sqrt{\gamma P_0 / \rho_0}$.

In practice, the S-T model can be used to extract the plasma expansion velocity by fitting curves of the shock position versus time measured experimentally.

In summary Absorption is accompanied by a radial expansion as well as an axial expansion of the plasma in the sense direction opposite to the incoming laser. Absorption, which is stronger at the leading edge of the expanding plasma, leads to the formation of a hot and very highly-ionised layer. Maintained by the laser energy deposition, the leading edge of the plasma moves like a

²The S-T model was initially proposed to describe the shock waves caused by nuclear explosions.

detonation wave, followed by an expansion wave and a shock wave (which explains the distinctive sound of breakdown in the air). The temperature reached in the detonation zone is between 10^4 and 10^5 K.

From an experimental perspective, the electronic temperature of the plasma is estimated by measuring the plasma extension at different times, using shadowgraphy or strioscopy, therefore characterizing the expansion speed.

11.1.4 Plasma extinction

At the end of the laser pulse, the detonation wave is no longer maintained and gradually stops. Thermal conduction leads to a uniform distribution of temperature and pressure within the plasma. The temperature is still between 10^4 and 10^5 K.

The lifespan of the plasma created by the laser is longer than the laser pulse duration. It depends on the recombination processes, which have a much smaller cross section than the binary electron-atom collisions (elastic and inelastic). Recombination is primarily a product of three-body collisions and radiative collisions. The probabilities of these processes, which vary with the density and temperature of the plasma, are relatively small and the plasma may exist for a few dozen nanoseconds. However, the lifespan of the plasma is much shorter than the interval between two consecutive laser pulses.

1.2 A few important parameters

11.2 A few important plasma parameters

The principal quantities of plasma and the methods used to measure them are shown in figure 42.

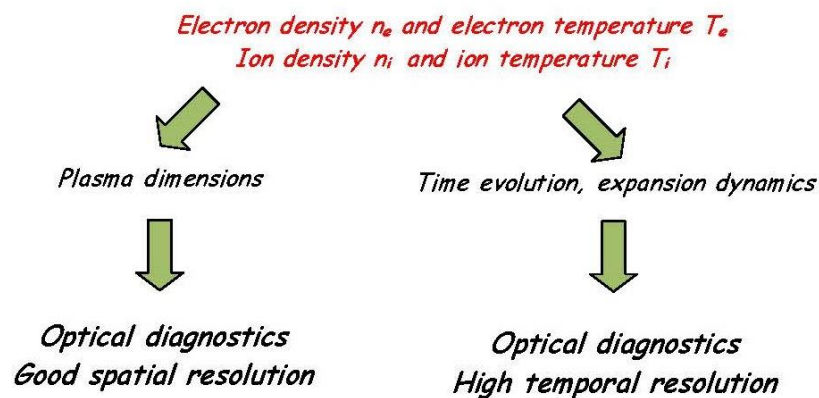


Figure 42: Plasma diagnosis diagram.

11.2.1 Refractive index for a plasma

We can express the refractive index for a plasma without collisions as follows:

$$N = \sqrt{1 - n_e/n_c}$$

where n_e is the electron density and n_c is the cut-off electron density (critical density). For $\lambda_L = 0.53 \mu\text{m}$ we get $n_c \approx 4 \times 10^{27} \text{ m}^{-3}$. With $n_e \approx 10^{25} \text{ m}^{-3} \ll n_c$. In these conditions, the plasma index can be expressed as:

$$N \approx 1 - n_e/2n_c.$$

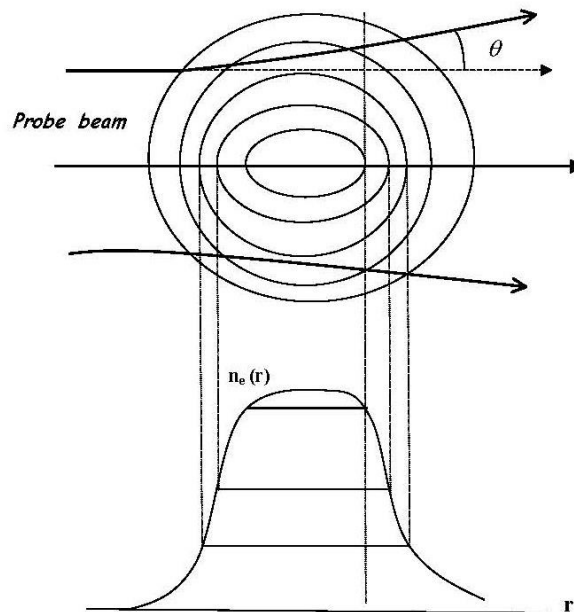


Figure 43: Refraction of the probe beam by the plasma in zones with a high index gradient ∇N or electron density ∇n_e .

In an inhomogeneous plasma, the index gradient is linked to the electron density gradient ∇n_e by the expression:

$$\nabla N \approx -\nabla n_e / 2n_c.$$

As a result, any electron density gradient induces an index gradient and thus a refraction of the light (fig. 43). High gradients exist primarily at the edges of the plasma.

Strioscopy In strioscopy, we let the refracted rays pass through, cf. figure 44. Highly refractive zones are then represented in the strioscopic image as light patches.

Shadowgraphy In shadowgraphy, the rays refracted from zones with a high index gradient are blocked and not collected by the detector (see Figure 45).

By either of these methods, we obtain an image of the edges of the plasma, either bright (strioscopy) or dark (shadowgraphy), enabling us to measure its size at different moments, by varying the delay of the probe beam. From this we can determine the plasma mean radial expansion velocity or, even better, the expansion velocity as a function of time.

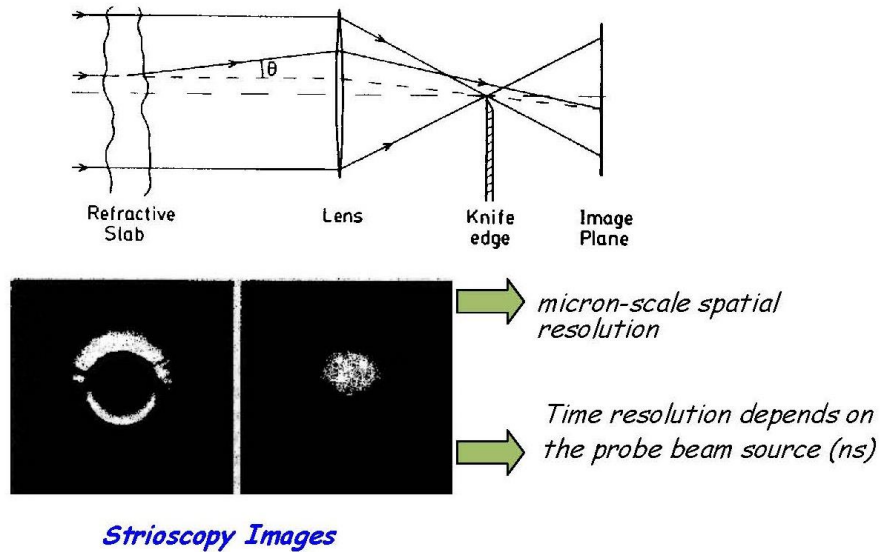


Figure 44: Diagram of strioscopic analysis and two typical images.

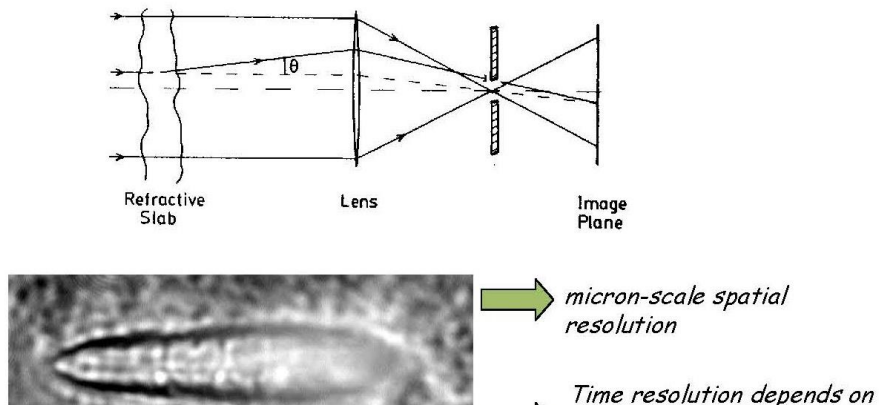


Figure 45: Diagram showing ombroscopic analysis and a typical image.

11.3 Work to be done

Our experiment will focus on two priorities: identifying the breakdown threshold and absorption of the laser pulse, and quantifying the radial expansion of the plasma.

11.3.1 Characterisation of the longitudinal and transversal expansion of the plasma and deduction of the maximum temperature attained by the plasma

The diagram for our experiment is shown in figure 46.

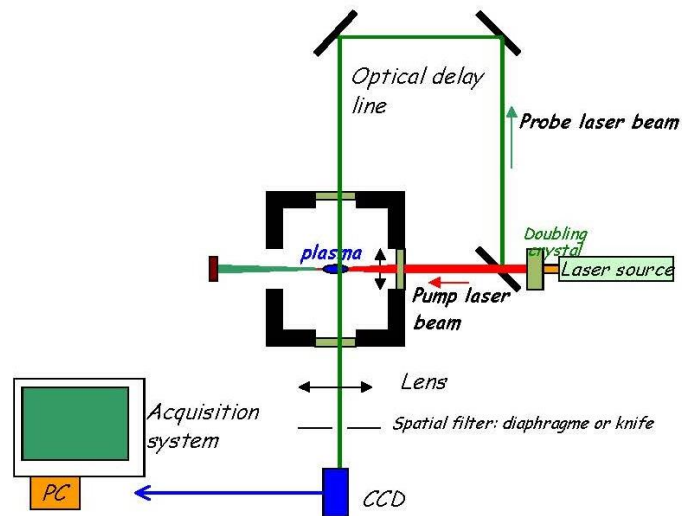


Figure 46: Strioscopy/shadowgraphy set-up diagram.

In this experiment, we will be using shadowgraphy and/or strioscopy to measure the geometric dimensions of the plasma and its evolution over time. We will proceed as follows:

- The tutor will check that the references (centring devices) used to align the Nd-Yag laser are positioned correctly. These guides determine the propagation axes of the pump and probe laser beams.
- Align the two He-Ne lasers, which simulate the pump and probe beams, on the centring devices, then adjust them so that they cross in the centre of the interaction chamber.
- Centre (using the auto-collimation function) the objective lens of the pump beam.
- Align the optical delay line using a continuous Helium-Neon laser, for all three possible configurations, corresponding to three different delays.
- Determine the optical delay by measuring the optical path length for all three delay lines.
- Draw a diagram of the experimental assembly and clearly mark the optical paths and effective temporal delays measured.
- We may also measure the effective delay between the probe laser pulses and the plasma using a fast photodiode and an oscilloscope, then comparing the results obtained (time permitting).
- Adjust the shadowgraphy/strioscopy assembly.
- Use the magnification formula to calculate the magnification (G) of the shadowgraphy/strioscopy system.
- Determine the magnification and the spatial resolution of the imaging system ($\mu\text{m}/\text{pixel}$) using the image obtained on a CCD camera with a calibration needle of known diameter (measured with a precision caliper gauge).

- Draw a diagram of the shadowgraphy and strioscopy assemblies, showing the measurements recorded.
- Acquire shadowgraphy/strioscopy images of the plasma for the three time delays (corresponding to the 3 combinations of mirrors possible for the delay line) and for 2 laser energy levels.
- Determine the radial and longitudinal dimensions of the plasma at these time delays.
- Determine the plasma's radial and axial expansion velocities. Estimate the plasma's electron temperature.

11.3.2 Measuring the absorption of laser energy by the plasma and defining the breakdown threshold and laser pulse absorption

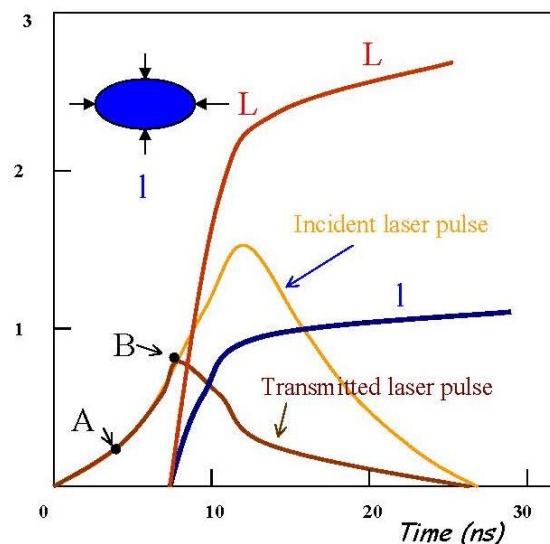


Figure 47: Characteristic variations in the transmitted laser pulse and plasma dimensions over time.

In this experiment, which can only be conducted by using glass slides as targets, we will measure the energy and temporal profile of the incident and transmitted laser pulse. We vary the intensity of the laser and observe the changes in the transmitted pulse – see fig. 47. The process is described below:

- Align the photodiodes with the incident and transmitted beams, using the He-Ne laser to reveal the high-power laser beam. Then position optical densities in front of the photodiodes in order to prevent any damage or saturation of the photodiode signal.
- Start up the high-power laser. Ask your tutor to check the alignment.
- Check that the oscilloscope is working properly, activated internally. It is better to use external activation, and to do this we will use a synchronous signal of the opening of the Pockels cell which is situated on the back of the laser.

- Measure the laser pulses (form, energy) with (transmitted pulse) and without plasma (incident pulse) at different laser power settings. Record these signals by saving the oscilloscope reading and printing it out (GPIB interface). Determine the breakdown threshold on the different kinds of used targets.

The diagram of our experiment is shown in figure 48.

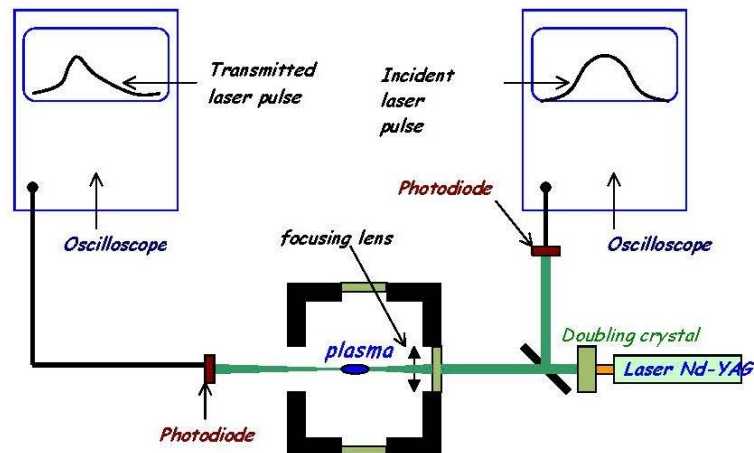


Figure 48: Experimental diagram for absorption measures.

11.3.3 How should we perform this experiment?

The working method used here must be similar to that employed in research laboratories. You will be faced with certain experimental difficulties which are inherent to this type of experiment. The tutor is available to guide you, in order to help you avoid these pitfalls and mistakes and ensure electrical and laser safety throughout the experiment.

Important precautions

- Laser risk: you must always wear the protective goggles provided when the Nd-Yag laser is in use.
- Remove any watches, rings and and other jewellery for the duration of the experiment.
- Never adjust the reference centring devices without the tutor's permission.

Before leaving the lab, please put away all equipment and leave the room as it was when you arrived, taking care to turn off all electrical devices.

Measurements The two teams will share the task of aligning the systems. They can then switch roles when it is time to modify the parameters. The findings will be shared.

Above all, this experiment uses a real measuring system, which has different limitations and disadvantages.



- Noise, spurious signals and interference affecting the signal you are trying to observe. You need to identify the origin of these problems and try to limit their impact. They often stem from a small detail (faulty ground connection, intense electromagnetic radiation, extraneous light, etc.). These phenomena may prevent you from observing the desired signal (unwanted activation of the oscilloscope), or from measuring it in the case of weak signals. They may also generate phantom images and signals.
- It is essential to understand the properties of your measuring apparatus, including its sensitivity (the minimum signal value it can measure), spatial resolution, temporal resolution of an imaging device, etc. These characteristics will determine the accuracy of your final results, which will form the basis of the interpretation of the experiment.
- You will need to choose the right experimental conditions in order to observe the desired effect. This will require you to use your expertise or otherwise your common sense.

11.3.4 Preparing the experiment report

Once you have obtained your results under very specific conditions, you should never be satisfied with your results as they stand. Wherever possible, you should seek to interpret these results: Do they seem reasonable? Is this what you expected to see? If not, how can we explain the difference? This will require you to draw upon your physical expertise, and make order of magnitude judgements wherever possible. Once you have formulated a hypothesis, you may suggest a counter-experiment that would allow you to check this hypothesis and deepen your understanding of the system in question.

In order to assess what you have learned from this experimental work, each team will be asked to draw up an experiment report. This report should reflect the educational nature of the experiment. It is very important for you to ask questions, even if you are unable to provide satisfactory answers. For all of these points, you may feel that your knowledge of this field is too limited to come up with the correct answers. But the solutions are often simpler than you might think, and the teaching staff are on hand to guide you in your search for answers. However, it is very important for you to ask yourself questions. We believe that this is where the greatest educational benefit of this work is to be found. In summary, based on your specific observations, you should be able to develop a fundamental understanding of this field, acquired through experimental experience.

The report should include all of your results, and never forget to define the symbols used and include a detailed diagram of the experiment carried out (identifying all items used). The report should include the objectives and practical aspects of your work (i.e. your methods) as well as sufficient theoretical results to interpret the results: discuss the plasma creation process, and provide relevant physical explanations. Do not forget to provide your conclusions and include a critical commentary of your work.

Here is a useful reminder:

Shadowgraphy and strioscopy:

- Explain the fundamental principles of shadowgraphy and strioscopy (spatial resolution, spatial filtering).
- Based on the images obtained, determine the temporal evolution of the actual longitudinal and transversal size of the plasma (at the laser power settings selected in the first session).
- Estimate the plasma expansion velocity in both cases, using a linear model and the Sedov-Taylor model.



- Calculate the electron temperature, the thermal velocity, the Debye length, the electron frequency of the plasma and the frequency of e-i collisions.

Characterisation of laser pulses with a calorimeter and a photodiode You will also need to define the laser intensity at the selected points by measuring the laser energy per pulse with a calorimeter and the pulse duration using a photodiode connected to an oscilloscope.

A few questions and tasks:

- What input impedance is required to observe signals that last for a few nanoseconds?
- Explain the different signals obtained with and without adapting the impedance.
- Estimate the amplitude of the laser field and the intensity of the beam according to the laser voltage.
- Calculate the oscillation of the free electrons in the laser field at the breakdown threshold.
- Obtain a theoretical estimate of the time required for a free electron to reach a level of kinetic energy approaching the ionisation threshold (~ 10 eV): take into account the collisional frequency and the initial kinetic energy of an electron oscillating in the laser field.

11.3.5 A few practical tips

Throughout the experiment, keep a "lab notebook" in which you jot down your observations - even trivial ones - as they may turn out to be key points that will help you to understand your results and compare two different sets of experimental conditions. Interpret your results as you go: if you wait until the end to write down your observations, you run the risk of forgetting essential elements of the experiment and compromising the quality of your interpretation.

11.3.6 Evaluation

Each team will be expected to submit a report on its experimental work within a few weeks after the experiment.

11.3.7 A few questions to ask yourself

- How do you adjust a lens on the optical axis?
- What is the numerical aperture of a lens?
- What is the input impedance of the oscilloscope?
- What is the pass-band of the oscilloscope?
- A fast diode is intended to measure the laser pulse. The impedance is therefore 50Ω . It is connected to the oscilloscope using a coaxial cable.
 - What should the impedance of this cable be? And the input impedance of the oscilloscope?
 - What are we measuring if the input impedance of the oscilloscope is equal to $1 \text{ M}\Omega$?



- What is the hydrodynamic expansion velocity of a laser plasma?
- How can we explain the absorption of laser radiation by plasma?
- Explain the fundamental principles of shadowgraphy and strioscopy.

BIBLIOGRAPHY

1. *Physique des Plasmas. Cours et applications*, J.-M. Rax, Dunod - Collection Sciences Sup, Paris, 2005.
2. *Introduction to Plasma Physics and Controlled Fusion*, F.F. Chen, Plenum Press, New York, 1984.
3. *Introduction to Plasma Physics*, R. Goldston and P.H. Rutherford, Institute of Physics Publishing Ltd., Bristol, 2000.
4. *Physical Kinetics*, E.M. Lifshitz and L.P. Pitaevskii, Butterworth-Heinemann Ltd., Oxford, 2002.
5. *Plasma Physics. An Introductory Course*, R. Dendy, Cambridge University Press, New York, 1993.
6. *The Physics of Plasmas*, T.J.M. Boyd and J.J. Sanderson, Cambridge University Press, New York, 2003.
7. *Physique des Plasmas*, J.-L. Delcroix et A. Bers, InterEditions, Paris, 1994, V. 1 et 2.
8. *Fundamentals of Plasma Physics*, P.M. Bellan, Cambridge University Press, London, 2006.
9. Formulaire des Plasmas, le site web du NRL: <http://wwwppd.nrl.navy.mil/nrlformulary>



HELLENIC
MEDITERRANEAN
UNIVERSITY



université
BORDEAUX



Erasmus+

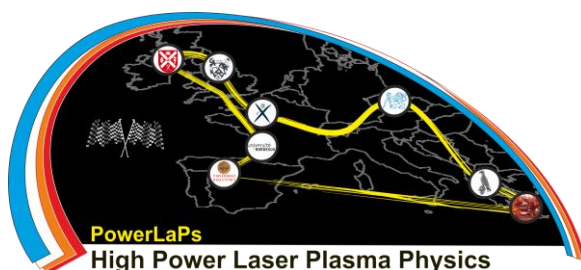
PowerLaPs

Innovative Education & Training in High Power Laser Plasmas

High Power Laser Matter Interactions - Theory and Experiments

EXP 2: Measure the coherence length/Time of flight- Determine the concentrations of metals in unknown alloys using X-ray absorption

S. White, B. Dromey



Erasmus+



Queen's University
Belfast



2 day mini experiment – larger group experiment

CCD set up and calibration

Beam expansion and collimation

Routine near field and pointing diagnostics – sensitivity and what do the results reveal

Parabola alignment and focal spot measurement

1 day experiment

Measure the coherence length/time of light

1 day experiment

I

Determine the concentrations of metals in unknown alloys using x-ray absorption.

Note: Aside from a box of components and a demonstrator in full time attendance, there will only be a list of instructions provided. The components will be sufficient but not limited to those required to do a given experiment. An “experimental recipe”, or list of instructions will not be provided.

The key learning outcome of these labs will be to work out how to use the concepts that you have been taught and combine them with asking the correct questions to achieve a defined goal.

Groups will prepare short reports on their labs outlining their results and the accuracy of these results.

The philosophy behind these labs is that in a real laser laboratory (or any experimental laboratory for that matter) there is no handbook. Therefore it is a critical step to be able to take abstract concepts from lectures and transfer them to the laboratory environment. This training week targets this through challenging lab practical sessions. Another key learning outcome will be how to quantify the results that have been obtained, what these results tell us and if it is consistent with the theoretically expected sensitivity of the diagnostic approach employed.]



HELLENIC
MEDITERRANEAN
UNIVERSITY



université
BORDEAUX



UNIVERSITY
of York



Erasmus+

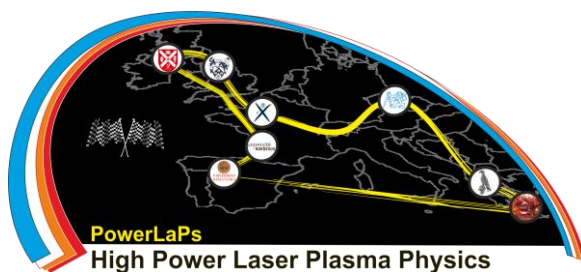
PowerLaPs

Innovative Education & Training in High Power Laser Plasmas

High Power Laser Matter Interactions/High Energy Density Physics - Theory and Experiments

EXP 3: TW ultrafast laser system and laboratories

I. Ftilis, K. Kosma, Y. Orphanos, S. Petrakis, A. Grigoriadis



Erasmus+

HELLENIC
MEDITERRANEAN
UNIVERSITY

1. DESCRIPTION OF THE 40TW LASER SYSTEM AT CPPL

The Pulsar 40TW laser system at CPPL is a compact femtosecond laser source providing more than 1J pulse energy at a 10Hz repetition rate. The pulse length is about 25fs and leads to a peak power higher than 40TW.

1.1 Chirped pulse amplification (CPA)

The system is a Titanium-Sapphire laser based on the so-called "Chirped Pulse Amplification" (CPA) technique. The system amplifies pulses from a Ti:Sapphire Oscillator and consists of a booster, a stretcher, a regenerative amplifier, 10 Hz multi-pass amplifiers with respective pump lasers, vacuum and air compressors. The CPA technique consists of temporal stretching of the ultra short pulse delivered by an oscillator (by a factor of 1000 to 10000), in order to safely amplify the pulses in solid state materials. Stretching produces a "chirped" pulse. After amplification, the laser pulse is temporally compressed back to duration as close as possible to its initial value. After the compression stage, one should obtain in principle a high intensity ultra-short pulse free of chirp (see Figure 1-1).

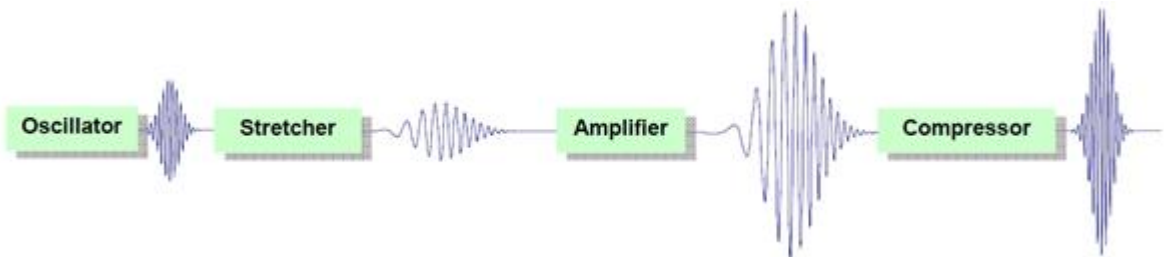


Figure 1.1 Chirped pulse amplification principle

Stretching and compression are usually achieved by means of dispersive systems such as gratings or prisms. The principle is to create different optical paths for each wavelength of the spectrum. Figure 1-2 shows a typical stretcher design using two gratings and a telescope system. As shown in this Figure, the Blue path is longer than the Red one. Therefore, Blue wavelengths take more time to travel through the system than Red ones.

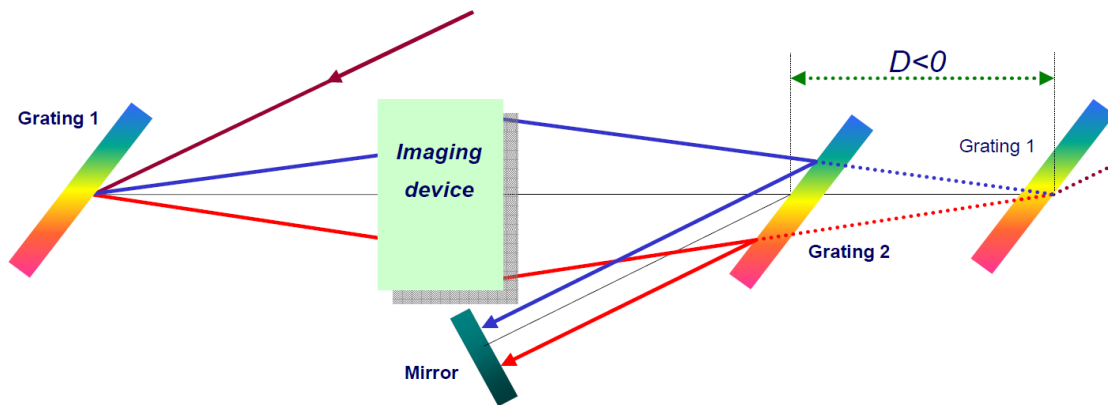


Figure 1.2 Stretcher principle

Once stretched, the pulse can be amplified in several amplification stages, using regenerative and/or single-/multi-pass amplifiers. At the output of the amplifying system, the energy does not depend on the input pulse duration delivered by the oscillator. The limit comes from possible damage that could be caused to the amplifying material. The amplified pulse energy which can be reached without damage is higher if the stretched pulse is longer.

After amplification the pulse must be compressed. A compressor device based on a wavelength dispersion system similar to the stretcher (see Figure 1-3). This compressor is theoretically able to compensate for any stretching introduced into the pulse, but the gratings need to be perfectly aligned. Particularly, the incident angle onto the compressor has to be finely adjusted in order to compensate for the stretcher and the dispersion effects through the amplifier.

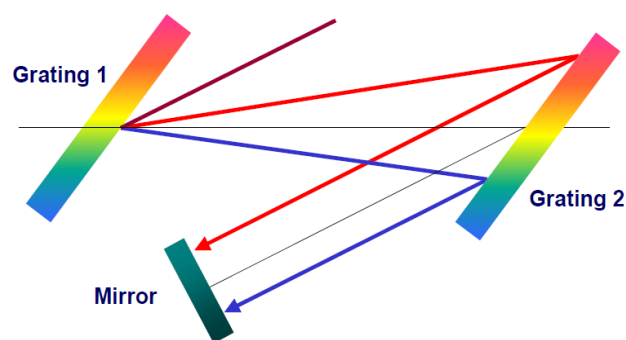


Figure 1.3 Pulse compressor principle



1.2 Oscillator

The Oscillator Femtosecond seed pulses for the CPA amplifier are provided by a laser oscillator. The femtosecond laser oscillator has four major components: the gain material, the pump laser, the feedback mirrors that form an optical resonant cavity, and the dispersion compensation optics. Femtosecond pulses from the oscillator cavity are generated by a mechanism called mode locking. To generate 10 fs pulses, the phases of $N=10^6$ modes must be the same.

1.3 Contrast Ratio Booster

In order to improve contrast ratio, an optional module is available. This module consists of a compact multipass amplifier to amplify the oscillator output up to the microjoule level. The pulse is then cleaned by a saturable absorber that removes residual ASE (Amplified Spontaneous Emission) background of the oscillator pulses before seeding. This module also contains an electro-optical device, the pulse picker, which creates a 10 Hz pulse train from the 80 MHz oscillator pulse train.

1.4 Regenerative amplifier

The first amplification stage consists of a regenerative amplifier producing around 1mJ stretched pulses at 10Hz. It includes two Pockels cells: one is used to seed the stretched pulse into the regenerative cavity and the other dumps out the pulse at the maximum energy level. High power multipass amplifiers use only flat mirrors and do not affect the beam quality. An electronic module is installed to synchronize and switch the different Pockels cells involved in the system.

1.5 Multi-pass amplifiers

The high-power amplification delivered by the system is delivered by multi-pass amplifiers. The Nd:YAG CFR200 laser produces the gain in the first multi-pass amplifier (called Pre-amplifier). The second multi-pass amplifier is pumped by 1.2J @ 532 nm delivered by one PropulseNd:YAG laser. The main amplifier is pumped by 5 J delivered by 2 Propulse+ Nd:YAG lasers. Due to the high average power of the pump beams a cryogenically cooled Ti:Sapphire mount is used in the main multi-pass amplifier.

1.6 Acousto-Optic Programmable Modulators

For Short pulse ($<30\text{fs}$) requirements, an optional AOPDF Acousto-Optic Programmable Dispersive Filter (or Dazzler) is added, right after the pulse stretcher. For standard laser systems, the *Dazzler* is used as a phase modulator to pre-compensate dispersion and phase distortions introduced throughout the laser system, but also as an amplitude modulator to optimize the laser output spectrum. In the Pulsar, the problems of phase compensation and amplitude modulation are totally de-correlated. The *Dazzler* would only be used for phase control, while another device, the *Mazzler*, would be used to optimize and enlarge the spectrum. This allows decreasing the pulse duration down to 20fs.

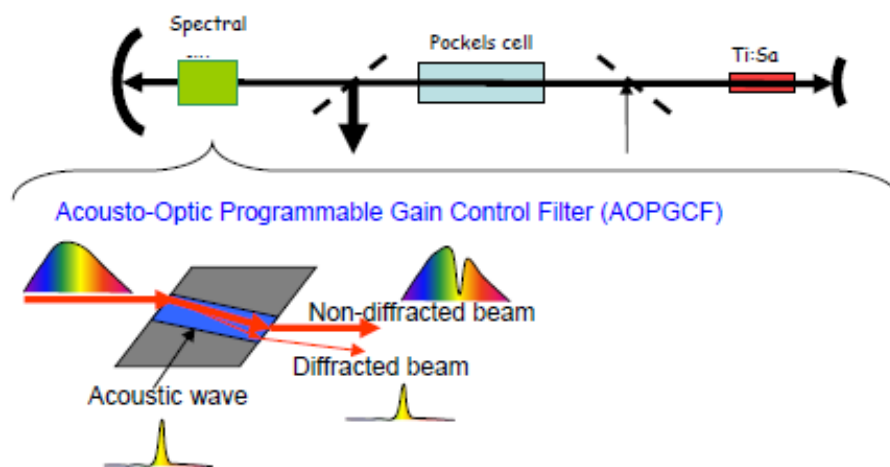


Figure 1.4 Principle of the Mazzler for a simple laser resonator

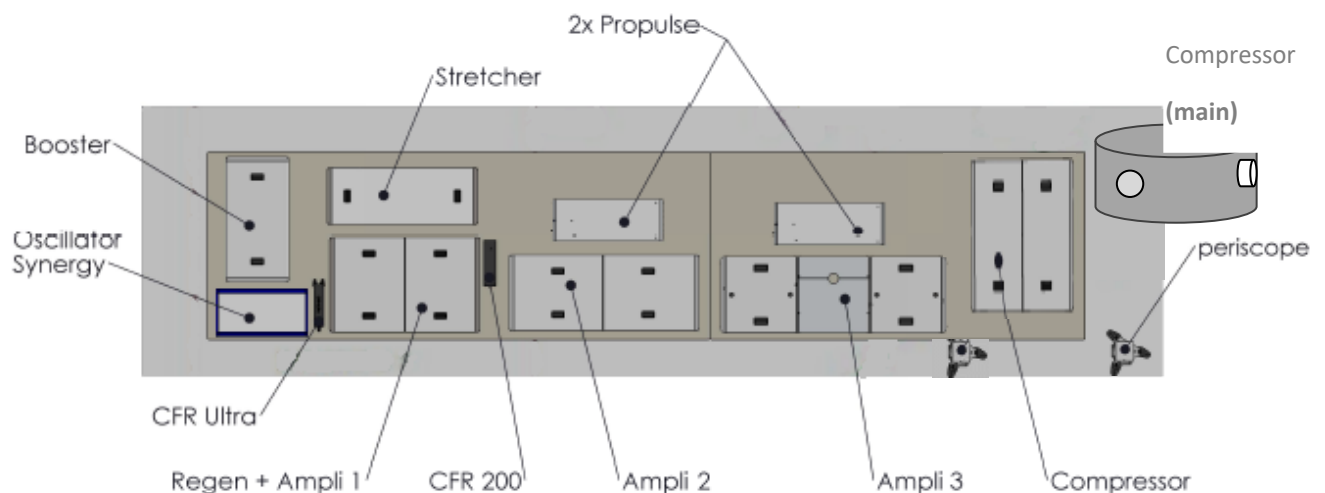


Figure 1.5 Schematic layout of the 40TW laser system arrangement

2. OPERATION OF THE 40TW LASER SYSTEM AT CPPL

Important precautions!

- 1) Make sure you wear the laser safety goggles when the laser is on.
- 2) Remove any reflective items like watches, rings, etc.
- 3) Never look at the height level of the beam propagation.
- 4) Always follow the instructions that will be given to you by the lab staff.

At the start of the session you will be asked to sign a declaration confirming that the above-mentioned instructions have been transmitted to you verbally by your tutor, and that you undertake to follow them to the letter.

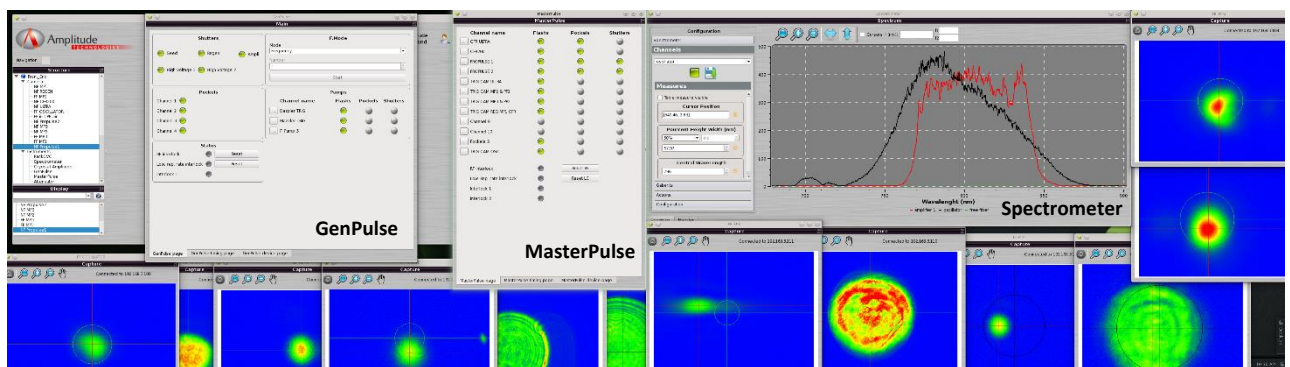


Figure 2.1 Screen capture of the main panels for controlling and monitoring the laser system

The operation of the laser system is mainly realized from a terminal computer that controls and monitors several parts of the laser system (Figure 2-1). The spectrum and the beam quality are monitored at several stages of the laser system. The main controls are at two panels.

- **GenPulse** panel communicates with the Gepulse device that
 - controls the high voltage and the trigger of the 4 Pockels Cells (**Pockels**) at the **Booster** and Regenerative Amplifier (**Regen**)
 - controls the shutter for the seed beam and for the cavity of the Regen, as well as the shutter output of Amplifier-1 (**Ampl1**)
 - controls the trigger signals for the acousto-optic modulators, **Dazzler** and **Mazzler**
 - controls the single-shot/burst-mode/frequency-divider shutter
 - generates the 10Hz clock signal, from the division of the **Oscillator's** pulse train (**RF**), that is used for all the synchronizations
 - supply power to several photodiodes of the system

- **MasterPulse** panel communicates with the MasterPulse device that



- controls the trigger signals of the flashlamps and the Pockels for all the pump laser, as well as their shutters
- generates self-clock from the RF signal and the 10Hz trigger from GenPulse to eliminate synchronization jitter
- controls the trigger signals for all the cameras of the system
- receives external interlocks from the **Cryostat** system and the **Vacuum Compressor** and checks consistency of the RF signal, to disable channels in case of fault

There are also other panels to control: the flashlamps voltage of the two **Propulse** pump laser, the Attenuator (**Atten**) of the last amplifier output (**Ampli3**), the vacuum and the motorized stages at the Vacuum Compressor chamber.

2.1 Start-up procedure of the 40TW Laser System

- The start-up procedure of the Laser System comprises of several check points and probably adjustments before the system is ready to operate at full energy. First step is to power on the Oscillator device as well as the pump laser that will be used and let them about 15' to stabilize. Also, the Cryostat system needs about 30' to reach -150 °C.
- The Oscillator's mode-locked operation and output power is the first check to make. The beam at the entrance of the Booster is monitored by a camera. The RF pulse train as well as that inside the Regen cavity is monitored by a fast oscilloscope. The proper operation of the lasing cavity (bulid-up time) is checked before seeding by the 10Hz chirped pulse output of the **Stretcher**. The beam inside the Regen cavity is also monitored by camera. After checking the operation of the seeded Regen the beam is proceeded to the first amplifier (**Ampli1**) where cameras for the near field (**NF**) and the far-field (**FF**) of the beam profile is used to monitor the amplifier output. Also, at this point is checked the spectrum of the beam that should be almost flat-top with a FWHM of ~70nm centered at ~800nm as it is properly shaped by the opto-acoustic modulator **Mazzler** inside the Regen cavity. The energy value and stability at the output of the Regen-Ampli1 unit is measured.
- Then the beam alignment at the second amplifier (**Ampli2**) unit is checked/adjusted using the installed iris and the energy output is measured. The beam alignment is also checked at the third Amplifier (**Ampli3**) and the energy is measured before the Attenuator (**Atten**) inside the Ampli3 unit. The energy after the Ampli3 unit is measured by setting in the Attenuator panel the energy value to 100% and the maximum energy is checked by adjusting the rotation offset values. After that the system is ready to operate with increased energy by pumping the last amplifiers.



- The Cryostat system has to reach -150°C before starting the first laser pump (**Propulse1**) of the last amplifiers. Furthermore, the flashlamps of the pump lasers have to operate at least for 15' to stabilize their performance. The Propulse1 laser pumps both Ampli2 and Ampli3. It is safer to block the IR seed beam, by Ampli shutter, before starting the pumping. **The covers of the amplifiers units should be in place before start pumping!** Also, always **beware of what/where will be the path/use of the high energy output.** First to check is the full energy output of Ampli2 by placing the energy meter there before enable pump. **Never place/remove anything at the beam path while the beam is on to avoid any hazard reflection!** Beware to first enable (open) the shutter of the Propulse laser before enable its Pockels and, in reverse, first disable Pockels before close the shutter. **Never move the shutter while the beam is on!** While the amplifier crystal is pumped Ampli-shutter is enabled to release the beam. After the energy/stability measurement, disable Ampli-shutter, disable Propulse1 Pockel and then disable (close) its shutter. The meter is placed before the Atten inside Ampli3 unit and the steps are repeated to enable Propulse1 pumping and the IR beam to measure the energy/stability there. Then Ampli-shutter is disabled, the second pump laser (**Propulse2**) is started and the IR is unblocked to measure the full energy of the Laser system. Following the same safety rules the energy after Atten is also measured. During the previous measurements the beam profile/position is also checked at the NF and FF cameras of each amplifier output.
- After that the high energy beam can proceed to the pulse compressor in the vacuum chamber (**Vacuum Compressor**) and utilize the diagnostics for the compressed fs pulses by exported part of the beam energy from the chamber. Also, by a beam-splitter, 5% of the Ampli2 output energy comprises the probe beam which through a similar pulse compressor provides 10mJ energy pulses of down to 25fs duration, synchronized to the main beam. The low energy probe allows the compressor (**Air Compressor**) to operate without needed to be under vacuum. The pulse duration of the probe beam is measured by a single shot autocorrelator (**Bonsai**) that can provide measurement down to 20fs pulses. For the main beam is used a more sophisticated measurement system (**Wizzler**) that provides high contrast and single shot spectral phase and intensity measurements of nearly compressed ultrafast laser pulses. The measurement technique is named "Self-Referenced Spectral Interferometry" (**SRSI**) in which a reference pulse with a flat spectral phase and a broad spectrum is collinearly generated from the pulse to measure by cross-polarized wave generation (XPW). Fourier-Transform Spectral Interferometry treatment of the single shot interferogram between the 2 delayed pulses provides high-dynamic spectral phase and intensity measurement, as well as a confirmation of the measurement validity. Wizzler provides also feedback to the **Dazzler**



opto-acoustic modulator which applies phase correction to the beam at the output of the Stretcher in order to improve the measured pulses after the Compressor. Wizzler/Dazzler feedback loops comprise a powerful compression optimization tool to achieve Fourier transform limited (FTL) pulses. Another diagnostic of the compressed main beam is the measurement of the temporal contrast of the pulses by a third-order cross-correlator device (**Sequoia**) with high dynamic range ($>10^9$). Also, a camera is used as a pointing monitor of the main beam by recording the focal spot of the partially exported beam after passing a lens. To utilize the above diagnostics the proper beam energy should be set for each of them.

2.2 Shut-down procedure of the 40TW Laser System

- Set the Attenuator at 0%. Turn of the Propulse pump lasers, initially disable their Pockels and then their Shutter. Block the seed beam by closing the Ampli-shutter.
- At MasterPulse panel: Stop the flashlamps of Propulse lasers, Stop the Pockels and flashlamps of the pump laser of Ampli1 (CFR200) and that of Regen and Booster (ULTRA). Stop the triggers (“flash” button) for all the cameras.
- At GenPulse panel: Disable the triggers of the 4 Pockels of the Booster and Regen, disable their voltage, disable the regen-shutter and seed-shutter.
- Turn off the Cryostat compressor. Turn of the power supplies and the chillers of Propulse lasers. Turn of the CFR200 and ULTRA pump lasers.
- Stop the Oscillator without turn of the power supply.
- Make sure to block the beam exit of each unit of the laser system to be safe for the next start-up.

3. LASER-MATTER INTERACTIONS EXPERIMENTS AT CPPL

In this section are briefly presented some of the experiments carried out at the CPPL regarding to the laser pulses interactions with matter.

3.1 Introduction to the pump-probe technique for “watching” the evolution of fast events

The pump-probe technique constitutes a very well established method for monitoring ultrafast phenomena. With the term “ultrafast” phenomena we refer to physical processes that evolve within times of several tens of femtoseconds to several tens of picoseconds. Therefore, the ultimate tool for achieving this goal is the femtosecond Laser, with a broad-band and therefore ultra-short output pulse.

The basic principle is depicted in Figure 3.1 and is summarized in the following: the output of a short-pulse laser is split in two parts, the pump and probe pulses. The pump hits a sample of interest and initiates a physical or chemical process. Examples of processes initiated by the laser beam include photo-chemical reactions of molecules or the generation of a mechanical wave on the surface of a metallic film. After the excitation by the pump pulse the sample is hit by a probe pulse at variable time delays (controlled with the help of a motorized optical delay line) and the corresponding resulting signal is recorded. The measured quantity recorded after the interaction of the probe pulse with the sample can be its transmission or reflection, ions that are generated due to absorption of probe photons etc and is directly dependent on the delay time upon which the probe pulse arrives to the target after the initial excitation. By monitoring the probe signal as a function of the time delay, it is possible to monitor the decay of the generated excitation and therefore obtain information on the evolution and the dynamics of the system under study and the processes initiated by the pump pulses.

The **pulse duration** of the pump and probe pulses determines the temporal resolution with which the dynamics of the phenomenon under study can be followed, while the wavelengths of the pump and probe beams do not need to be identical. In several variables of the basic experimental set up, for example, part of the pump beam is firstly up-converted to a higher frequency in a non-linear medium and this lower wavelength pulse initiates the desired process or, in the context of a two-colour pump-probe measurements, two synchronized sources of short pulses (e.g. a laser and an optical parametric oscillator, or two parametric oscillators pumped with the same laser) can also be used. These experiments have additional advantages for ultrafast spectroscopy, where electronic excitation occurs in the short-wavelength range of the spectrum.

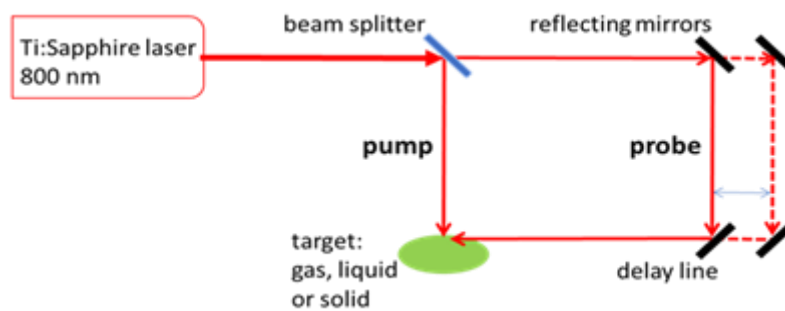


Figure 3.1 The basic experimental set-up for carrying out a pump-probe experiment. The optical delay line introduces the variable delay between the pump and the probe pulses. The measurable quantity (generated ions, probe reflectivity etc) is a fundamental parameter for the pump-probe experiment

3.2 Low intensity laser-matter interaction

3.2.1 Acoustic waves on metallic thin-film targets with pump-probe transient reflectivity method

When an intense ultra-short pulse irradiates a solid target, acoustic waves are generated. These waves are the result of the sudden and localized increase of temperature, which results in rapid thermal expansion and generation of mechanical waves propagating along the material surface. The increase of temperature arises due to the energy transfer from the electronically excited atoms of the irradiated sample to the lattice. Excitation of acoustic pulses by a pulsed laser in solid targets is of great interest due to extensive applications of pulsed laser technologies in material processing, as well as in non-destructive material characterization in the nano- and micro-scale.

The experimental set-up used for studying the evolution of the elastic waves is shown in Figure 3-2. Initially the laser pulse from a Ti: Sapphire-based amplifier laser system (1 kHz repetition rate, 35 fs pulse duration and maximum energy of 1.5 mJ at ~ 795 nm.) is split into the pump and probe beams. The pump beam hits the metal film surface perpendicularly, loosely focused by means of a spherical broad bandwidth metallic mirror to achieve a fluence, which is within the thermoelastic regime for the metals under study. The probe beam is incident at an angle of $\sim 30^\circ$ - 40° and orthogonally polarized relative to the pump beam, focused by means of a parabolic metal mirror, while its fluence is kept at significantly lower levels compared to the pump in order to avoid contribution to the excitation dynamics.

Important optomechanical components for the experiment:

1. A variable optical delay introduced between the pump and probe pulses. Here a minimum temporal delay step of 0.8 fs is achieved.
2. An imaging system used to monitor the relative position and size of the two beams on the interaction region. The probe beam spot should be kept smaller than the pump spot by a factor of ~ 4 and located at the central part of the latter.
3. A mechanical chopper modulates the pump beam at a lower frequency.
4. A small portion of the probe beam is split and is directed onto a balanced photodiode along with the probe beam reflected from the sample surface. The output of the photodiode is the difference of these two signals. The probe beams simultaneously illuminating (with ns resolution) the two inputs of the balanced photodiode should be of equal power, so that in the absence of the pump beam the photodiode output is zero. The balanced photodiode output signal is directed to a dual channel lock-in amplifier which detects signal differences at the pump beam modulating frequency. This detection scheme allows for reflectivity changes of the order of $\sim 10^{-5}$ to be resolved. Specially developed software is used to simultaneously control the temporal delay and detection instruments, and for data recording.

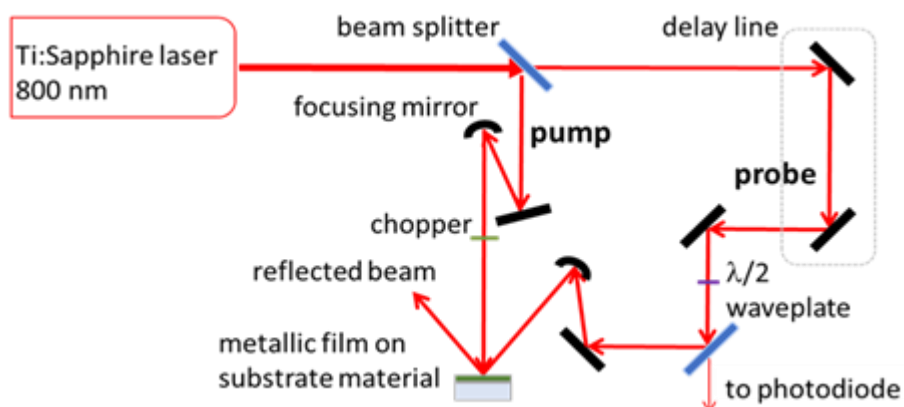


Figure 3.2 Experimental setup for the femtosecond degenerate pump-probe differential reflectivity method



3.2.2 Imaging acoustic waves on metallic thin-film targets with pump-probe full field Interferometry

Laser focusing on the metal surface leads to the absorption of energy and a local temperature increase, with the released thermal energy subsequently expanding far from the interaction area, in the form of Surface Acoustic Waves (SAWs). The wave characteristics depend on the material (thermal and mechanical properties, optical penetration depth etc.), as well as on the laser energy and pulse duration.

Laser-based interferometric detection schemes exploit the high spatial and temporal coherence of the laser radiation to record the scattered light from the distorted surface, within a formed interferometer, tracking changes in the intensity, phase, reflection angles, or spectrum. Interferometry analysis algorithms are applied to the detection of surface acoustic wave propagation and the resulting medium modifications, offer a great potential for material diagnostics due to the increased sensitivity to local features, accuracy and high spatial resolution capabilities in the nano-scale. The simplified characterization opportunities provided, have found numerous applications in a variety of research disciplines, from material science to biology and medicine.

Geometrical schemes that combine optical configurations for laser-induction and detection of the ultrasonic waves, within one integrated optical set-up, offer an ideal tool for high-resolution, minimally-invasive studies of microstructures. Figure 3.3 shows the experimental set-up for the dynamic nanoscopic characterization of thin films, with the help of SAWs, generated by laser pulses of nanosecond duration (**pump**) and characterized within a Michelson-based interferometric geometry by the generation of interferometric fringes from the **probe** pulses. The probe pulses arrive at a variable time delay, which is the result of the different combinations of the optical paths that the two beams can follow (solid and dashed lines in Figure 3.3, pump line 1, 2 and probe line 1, 2).

The objective lens (OL) is placed so as to have its back focal plane laying on the sample surface, which is then focused on the surface of the CCD. The CCD camera records interference fringe patterns with the probe beams, after BS2, traveling along the two arms of the Michelson interferometer arrangement (shown in Figure 3-3). Fringes are formed from the sample surface and the metallic mirror M. The fringe pattern reveals information about the modified scattered probe beam coming from the thin film surface, and therefore, about the effects of the laser-induced surface waves on the sample.

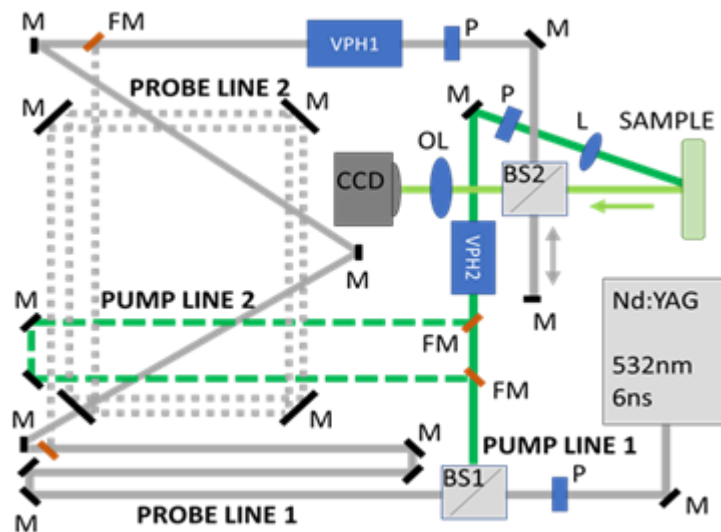


Figure 3.3

Schematic representation of the experimental set-up used for the generation and detection of SAWs with ns laser pulses at 532 nm.

M (black)-Metallic Mirrors,

FM (red)-Folding Mirrors,

P-Polarizer,

BS1,2-Beam Splitters,

OL-Objective Lens, **L**-Lens,

CCD-Camera.

3.3 High intensity laser-matter interaction

3.3.1 Target Normal Sheath Acceleration of Protons to MeV Energies

The experiments currently performed at the TW interaction chamber focus on accelerating MeV protons by taking advantage of the Target Normal Sheath Acceleration Method (TNSA). This method occurs when metal foils (in this case aluminium) with a thickness of few microns are being irradiated with ultra-intense laser pulses. The strong electric field of the laser pulse ($\cong 10^{12}$ V/m) pulls electrons from the surface of the target away from the heavy ions thus forming a strong charge separation. The electric field created by this separation accelerates the ions to kinetic energies of many MeV.

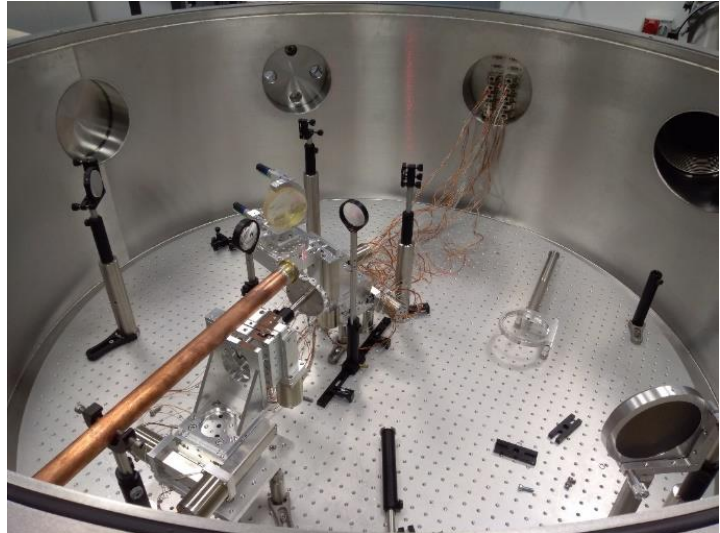


Figure 3.4 Photograph of the experimental setup for TNSA into the vacuum chamber. The re-entrant tube for proton radiation on a sample is also displayed

The energy of each pulse is up to 1 J and the pulse duration 25 fs. A 15 cm focal length parabola is focusing the beam down to a 3 μm spot resulting to peak intensity above 10^{20} W/cm². A retro reflection imaging setup is used for the optimization of the focal spot on every target before the shot.

In order to determine signal from the produced protons, stacks of radiocromic films (RCF) are being used. These films are covered with a dye, which undergoes a colour change when exposed to ionizing radiation. By using a calibrated set of RCFs an estimation of the produced protons can be made. Furthermore, this diagnostic is combined with a plastic nuclear track detector known as CR39. When protons of a few MeVs pass through this plastic, they create damage at their stopping point. In order for this damage to be revealed, the plastic needs to be placed inside a solution of sodium hydroxide at 90° for several hours. Thus, the number of protons can be measured and if it is combined with a spectrometer, the full energy spectrum can be obtained. Along with these diagnostics a novel polymer gel is used. In this gel the energy deposition is similar with the one of the human tissue. Ionizing radiation deposited in this gel can be measured after an MRI scan. This diagnostic provides vital information on using these MeV protons for medical applications. While this gel has to be kept in atmospheric pressure, a re-entrance tube is used.

Furthermore, optical probing diagnostics like shadowgraphy and interferometry are also used for characterizing the produced plasma on the surface of the aluminium foils. The synchronized probe beam originating from a fraction of the main beam before the last amplifier, is passing through a delay stage and a frequency doubling crystal (400 nm) and after probing the target, ends up to the diagnostics table.

3.3.2 Table-top XUV-source by laser-gas interaction

High-harmonic generation (HHG) provides a powerful source of ultrashort coherent radiation in the XUV and soft-x-ray range and is the main component of the of ultrafast science field. Generally, when a non-linear medium is exposed to femtosecond laser radiation with intensities $\geq 10^{14}$ Wcm⁻² the atoms are ionized and the freed electrons are accelerated by the laser field in the presence of the core potential. A small number of these electrons may recombine with the parent ions emitting the gained energy.

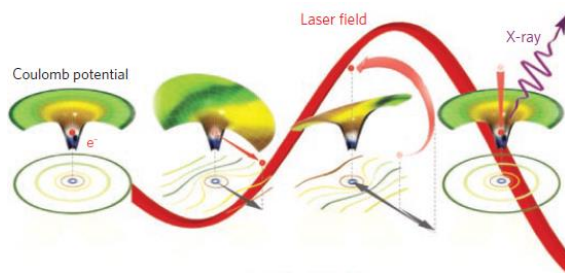


Figure 3.5 Three step model

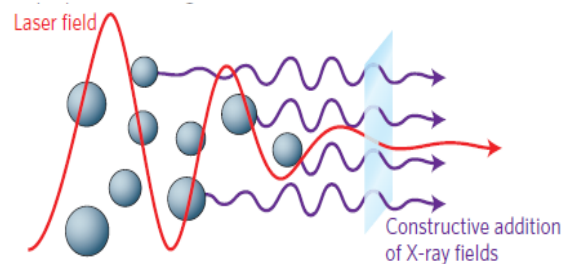


Figure 3.6 Phase matching

Changing scale from microscopic to macroscopic, the key issue for efficient HHG is the coherent addition of the generated pulses also known as phase-matching both in temporal and spatial domain. The main reasons for phase-mismatching are the dispersion, when the pulses propagate in the non-linear medium and the system geometry. In order to avoid phase-mismatching techniques have been developed such as quasi phase-matching. (e.g. gas-filled hollow capillary and multi-jet and multi-gas arrays), and loose focusing geometry.

In order to obtain clean interaction conditions, a gas target is needed that is spatially well confined so that interaction happens only at the ultrahigh intensity laser focal spot. Laser-matter interactions are strongly nonlinear processes and depend on the exact density profile of a given target and on its shot-to-shot reproducibility. This makes tailored and well characterized gas targets an essential prerequisite for these experiments.

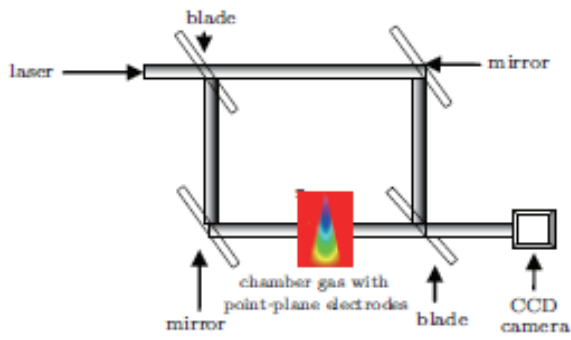


Figure 3.7 Gas jet characterization set up

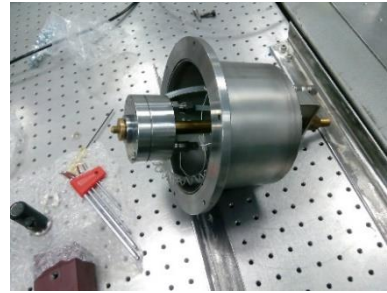


Figure 3.8 Gas jet

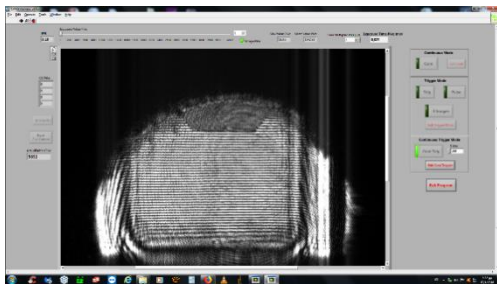


Figure 3.9 Gas jet interference imaging

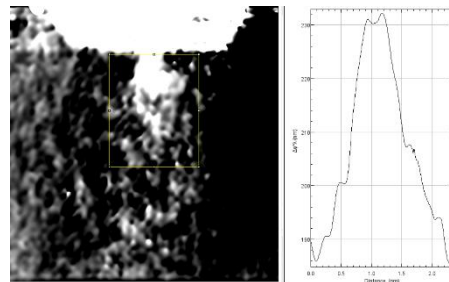


Figure 3.10 Density Profile

BIBLIOGRAPHY & REFERENCES

- User manual for the Pulsar laser system, Amplitude Technology S.A.
- <http://www.amplitude-technologies.com/?fond=produits-amplitude>
- <http://www.fastlite.com/en/al823529-Pulse-Shaping.html>
<http://www.fastlite.com/en/al823532-Measurement.html>
- <https://www.rp-photonics.com/>
- [1] Bakarezos, M. et al. Ultrafast laser pulse chirp effects on laser-generated nanoacoustic strains in silicon. *Ultrasonics*, **86**, 14-19 (2018).
- [2] Tzianaki, E. et al. Controlling nanoscale acoustic strains in silicon using chirped femtosecond laser pulses. *Applied Physics Letters*, **108**(25) (2016).
- [3] Kaselouris, E. et al. Elastoplastic study of nanosecond-pulsed laser interaction with metallic films using 3D multiphysics fem modeling. *International Journal of Damage Mechanics*, **25**(1), 42-55 (2016).
- [4] Tzianaki, E. et al. High acoustic strains in si through ultrafast laser excitation of ti thin-film transducers. *Optics Express*, **23**(13), 17191-17204 (2015).
- [5] Dimitriou, V. et al. The thermo-mechanical behavior of thin metal films under nanosecond laser pulse excitation above the thermoelastic regime. *Applied Physics A: Materials Science and Processing*, **118**(2), 739-748 (2014).
- [6] Dimitriou, V. et al. Three dimensional transient behavior of thin films surface under pulsed laser excitation. *Applied Physics Letters*, **103**(11) (2013).
- [7] Orphanos, Y. et al. An integrated method for material properties characterization based on pulsed laser generated surface acoustic waves. *Microelectronic Engineering*, **112**, 249-254 (2013).
- [8] Clark, E.L., Krushelnick, K., Davies, J.R., Zepf, M., Tatarakis, M., Beg, F.N., Machacek, A., Norreys, P.A., Santala, M.I.K., Watts, I., Dangor, A.E., Measurements of energetic proton transport through magnetized plasma from intense laser interactions with solids,(2000) *Physical Review Letters*, **84** (4), pp. 670-673.
- [9] Corkum, P. B., Plasma perspective on strong-field multiphoton ionization, *Phys. Rev. Lett.* **71**, (1994).
- [10] Corkum, P. B. and Z. Chang, The attosecond revolution, *Opt. Photon. News.* **19**, 24 (2008).



HELLENIC
MEDITERRANEAN
UNIVERSITY



universit 
BORDEAUX



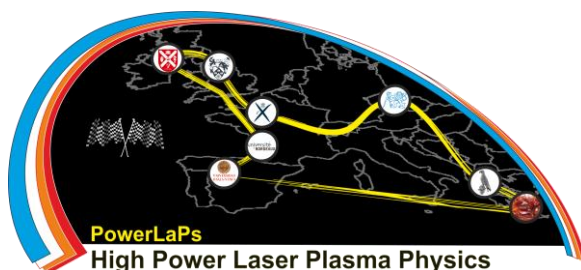
PowerLaPs

Innovative Education & Training in High Power Laser Plasmas

High Power Laser Matter Interactions/High Energy Density Physics - Theory and Experiments

EXP 4: Interaction of TW laser pulses with metal targets

I. Ftilis, A. Grigoriadis



HELLENIC
MEDITERRANEAN
UNIVERSITY



1. INTERACTION OF TW LASER PULSES WITH METAL TARGETS

1.1 Introduction

The aim of this laboratory is to give you the opportunity to get practical experience on the final preparation steps and the implementation of high power laser shots to solid targets. The solid targets to be shot, as well as the necessary auxiliary targets, have already being placed on the motorized rotational stage into the experimental chamber, which is already pumped down to low pressure, since this takes several hours. Therefore, the participant will be involved in the procedures of the experiment that can be performed with the experimental chamber under vacuum. These will be: the preparation of the imaging diagnostics shadowgraphy and interferometry, the fine synchronization of the probe with the main beam, the optimization of the main beam focal spot on the targets by retro-reflection imaging and finally the implementation of high power laser shots to solid target. The captured images of the imaging diagnostics at different shot conditions will be further analyzed to extract information of the generated plasma.

The experiments will be carried out at the 1.5 m diameter vacuum chamber utilizing the main beam output of the 40 TW laser system along with the synchronized probe beam output. The laser system provides laser pulses of up to 1 J energy into 25 fs duration and by focusing down to a 3 μm spot, intensities above 10^{20} W/cm^2 are achieved. This tight focus on the targets, of the initially 5.6 cm diameter beam, is realized by a short focal length parabola mirror installed in the experimental chamber. The laser compression chamber, that is under high vacuum, optically connects to the experimental chamber through a gate-valve with window that allows to work in air pressure at the experimental chamber without breaking the vacuum of the laser compression chamber. The main beam pulses have a spectrum of about 70 nm FWHM (full width half maximum) centered at about 800 nm wavelength. The probe beam is doubled in frequency before being used for imaging diagnostics so that it is easily filtered from the scattering light of the main beam.

Next, a brief introduction concerning basic knowledge on the laser plasma interactions is given, relevant to the experiment, along with a description of the two imaging techniques that will be used. Afterwards, are given the instructions for the experimental procedure of this laboratory session.

1.2 Basic Processes on Laser Plasma Interactions

Here we present some basic quantities and absorption processes, which are related to the experimental work.

1.2.1 Plasma frequency

In a plasma, if electrons are pulled away from the ion background, electric field will be created forcing them to return to their initial positions and restore neutrality. But due to their inertia, electrons will oscillate around their equilibrium position with a frequency known as the plasma frequency:

$$\omega_p = \sqrt{\frac{n_e e^2}{m_e \epsilon_0}} \quad (1)$$

where n_e is the electron density and ϵ_0 the vacuum permittivity.

From this equation we can see that for any radiation frequency there is a unique electron density—named critical density (n_c)—above which the wave does not propagate but rather is reflected. This critical density allows us to separate the laser-plasma interaction studies into two regions, named underdense ($n_e < n_c$) and overdense ($n_e > n_c$).

1.2.2 Ponderomotive force

An electron oscillating in the presence of a sinusoidal uniform electric field will return to its initial position after one cycle. For a laser pulse though, with an amplitude varying both in time and space, the electron will experience a larger force in the areas where the field is stronger. Therefore, the net force averaged over one cycle drives the electron away from high intensity regions. This force known as ponderomotive force can be described as:

$$\vec{F} = -\frac{1}{2} \frac{\omega_p^2}{\omega^2} \frac{dU_E}{dy} = -\frac{1}{2} \frac{n_e}{n_c} \frac{dU_E}{dy} \quad (2)$$

where $U_E = \frac{\epsilon_0 E_0^2}{2}$ is the energy density.

1.3 Laser absorption in Overdense plasma

When a laser pulse interacts with an overdense target such as a metal target, there are a few possible absorption mechanisms that might occur. The contribution for each mechanism depends on the pulse characteristics and on the laser intensity. The absorbed energy is transferred to the electrons, which accelerate away from the heavy ions thus forming a charge separation. The electric field created from this separation, forces the ions to accelerate to a wide range of kinetic energies. For protons, these kinetic energies can reach the values of many MeV.

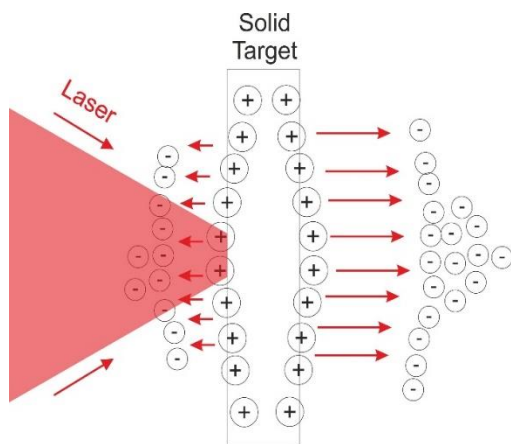


Figure 1.1 Plasma expansion on a solid target irradiated by an ultra-intense laser pulse

1.3.1 Resonance Absorption & Vacuum Heating

When a laser pulse propagates along the gradient of a plasma density, there is a point where it is reflected. The distance between this region and the critical density depends on the angle of incidence: $n_r = n_c \cos^2\theta$. At the turning point, if there is a component of the electric field along the density gradient (p-polarisation), it can excite a plasma wave on the critical surface. The field associated with this wave can accelerate electrons with energies up to hundreds of keVs.

However, this mechanism refers to situations where the scale length of the density gradient is many laser wavelengths. For density gradients less than a wavelength, no such resonance appears.

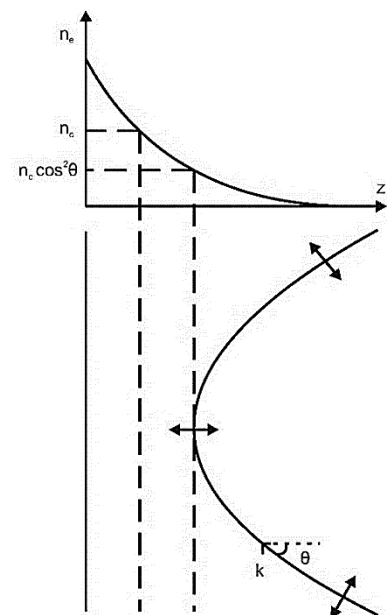


Figure 1.2 Resonance absorption

Due to the large electric fields, electrons from the surface can be pulled into vacuum and then sent into the plasma with a random phase. This mechanism called Vacuum heating is



considered to be the dominant absorption process in interactions of ultra-short and ultra-intense laser pulses with solid targets.

1.3.2 J x B Heating

The $J \times B$ term refers to the second term of the right hand side of the Lorentz equation. This term is negligible and usually crossed out for velocities much lower than the speed of light. That means that the $J \times B$ term is taken into account only in the relativistic regime. As a process it is very similar to vacuum heating, only that this time the oscillation takes place twice the laser frequency. It is accepted, that for relativistic intensities ($> 10^{19} \text{ W/cm}^2$) this absorption mechanism is the dominant one.

1.4 Plasma Diagnostics

Here we briefly describe the two imaging techniques for plasma diagnostics that will be used in this experimental work.

1.4.1 Shadowgraphy

A very common diagnostic used to image variations in space—such as plasma formation—is shadowgraphy. A light ray passing through a disturbed area experiences a different refracting index, thus it bends. This technique is sensitive to the second special derivative (Laplacian) of the medium refractive index. This implies that a disturbance with a constant gradient of the refractive index will not appear in the shadowgraph, due to the fact that all rays will bend the same way.

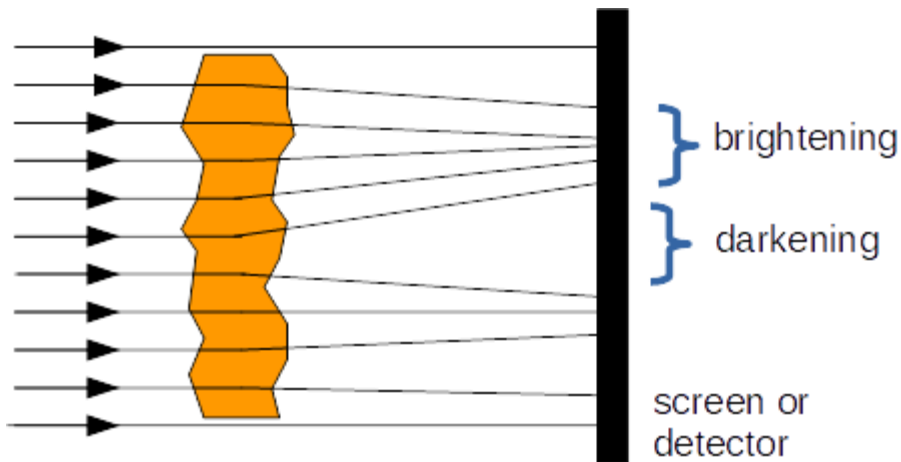


Figure 1.3 The shadowgraphy imaging technique. Parallel light rays passing through the disturbed medium deflect and arrive at different points on the screen creating brightening and darkening areas.

1.4.2 Interferometry

In order to extract quantitative results, one has to use a diagnostic sensitive to even the smallest fluctuations of the medium. One of the most popular techniques that meets this requirement is interferometry. To understand the working principle of this technique, we present the so-called Mach-Zehnder interferometer. The probe beam is split into two arms, one of which is passing through the disturbance. Then, the two beams meet again and interfere resulting in an image of bright and dark fringes due to the phase difference between the two beams. The part of the diagnostic beam passing through the disturbance will be phase shifted, resulting in a different interference pattern, compared to the one resulting from the beam propagation outside the disturbance. The phase difference between the two types of fringes is proportional to the disturbance density.

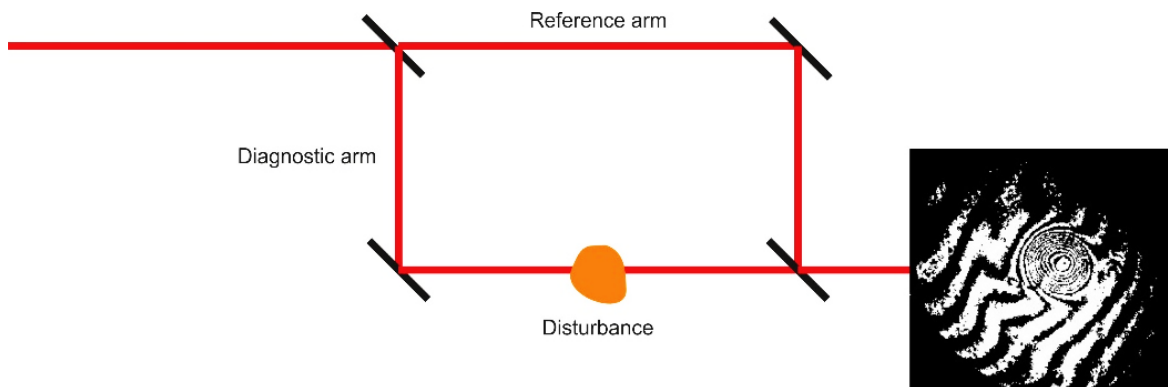


Figure 1.4 A typical Mach–Zehnder interferometer. The phase shift of the probe beam caused by the disturbance is visible due to the change of the fringes in contrast with the background ones

When the region of interest is small compared to the probe beam diameter, a Nomarski interferometer can be used. In this type of interferometer the probe beam, after the plasma region, passes through a birefringent Wolaston prism in which it splits into two beams of perpendicular polarizations that propagate at different angle. This allows the region of interest from the image of the one beam to interfere with the background from the other one. This technique has a more convenient setup and is more insensitive to external disturbances as there is not a separate reference beam path.

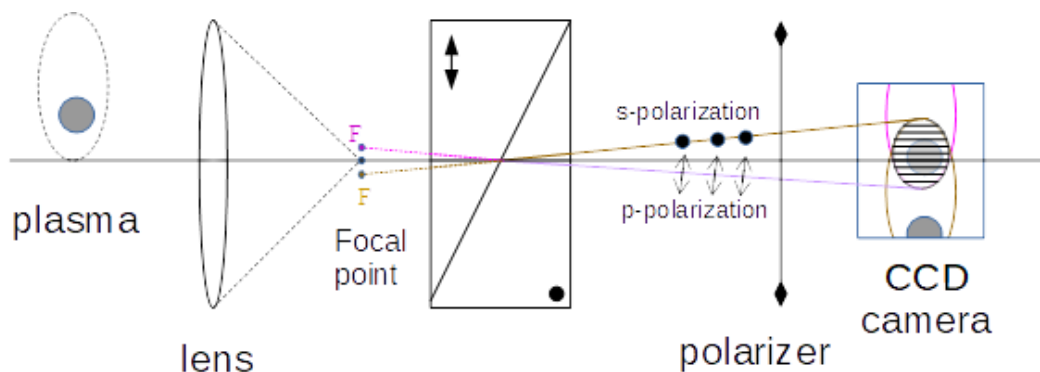


Figure 1.5 Schematic of the Nomarski interferometry principle

2. EXPERIMENTAL WORK

Important precautions!

- 5) Make sure you wear the laser safety goggles when the laser is on.
- 6) Remove any reflective items like watches, rings, etc.
- 7) Never look at the height level of the beam propagation.
- 8) None should be in the target room during the full shot experiment.
- 9) Always follow the instructions that will be given to you by the lab staff.

At the start of the session you will be asked to sign a declaration confirming that the above-mentioned instructions have been transmitted to you verbally by your tutor, and that you undertake to follow them to the letter.

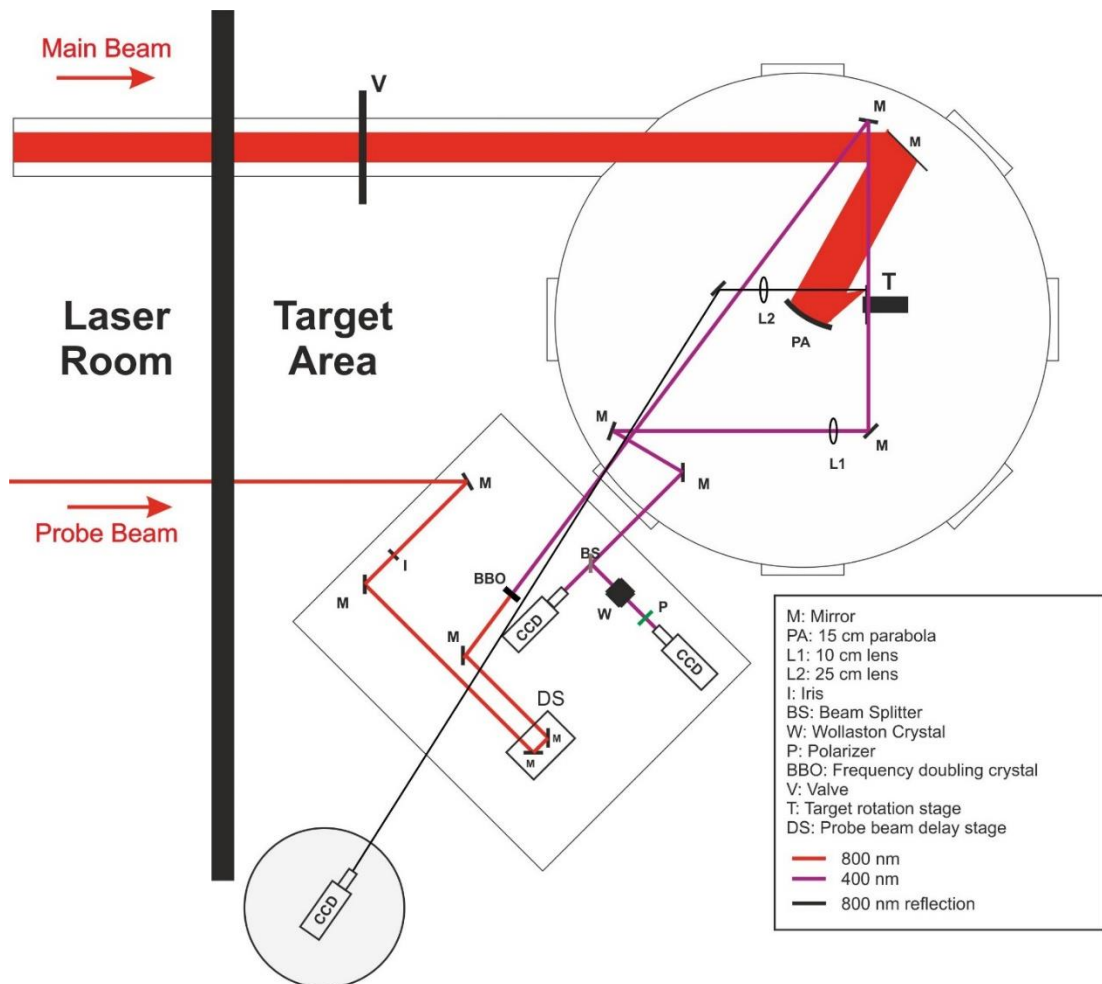


Figure 1.6 Experimental setup diagram

2.1 EXPERIMENTAL PROCEDURE

- 1) A principal advice is to make sure that you write down any value setting before and after you change it. This could save you valuable time in many cases.
- 2) Before open the gate valve that connects the laser chamber with the target chamber make sure that both pressures are below 5×10^{-6} mbar. Open gate valve.

Prepare the laser probe imaging diagnostics

- 3) Switch rotation stage to the crosswire position.
- 4) Ask from the laser-staff to provide you the probe beam at 10 Hz and low energy.
- 5) Apply to the shadowgraphy and interferometry CCD cameras the appropriate ND (neutral density) filters for the 10 Hz low energy operation of the probe beam.
- 6) Install the Wolaston prism and the polarizer to build a Nomarski interferometer.
- 7) Measure the magnification of both shadowgraphy and interferometry images.
- 8) Block the probe beam and check the retro reflection of the main beam at the respective (retro) camera. Ask laser-staff to provide you the main beam at 10 Hz and very low energy for the crosshair target. Check the retro-reflection and then ask laser-staff to block the main beam.

Synchronize the beams

- 9) Switch rotation stage to the glass slit position in order to synchronize the probe with the main beam.
- 10) Ask laser-staff to provide you the main beam at 10 Hz and appropriate energy for glass-test synchronization while also provide low energy probe.
- 11) Follow the instructions to find the T0 (tau zero) position of the probe delay line.
- 12) Ask laser-staff to block the main beam.

Preparation for the single shot experiment

- 13) Switch rotation stage to the target position.
- 14) Apply the appropriate ND filters for single shot probe beam at full energy to both shadowgraphy and interferometry CCD. Ask laser-staff to provide you single shots of the full energy probe beam (~10 times more) while the main beam is blocked.
- 15) Start the retro camera to optimize the focal spot for the first target. Ask laser-staff to provide you the main beam at 10 Hz and very low energy for the retro reflection of target. After optimizing the focal spot cover the camera entrance for full energy shot.
- 16) Set the probe delay line position to the desirable time delay for the shot.
- 17) Move to the control room and contact with the laser-staff at the laser room to collaborate for the following



Single shot experiments

- 18) Take a single shot reference image with the main beam blocked.
- 19) Take a full energy shot and save both shadowgraphy and interferometry images.
- 20) Afterward ask for laser operation at 10 Hz very low energy and repeat steps 12-16 for different delay times.
- 21) After the last shot enter the target area and check for any radiation with the Geiger Muller gauge.
- 22) Close the gate-valve and follow the final instructions from the staff.

2.2 RESULTS ANALYSIS

1. Estimate the plasma expansion velocity from the analysis of the shadowgraphs that you take at different probe delays.
2. Analyze the interferograms with the proper software that will be given to you along with all the necessary information to use it. Extract quantitatively information for the overall phase shift and the plasma density.
3. Discuss the results.

BIBLIOGRAPHY & REFERENCES

- F. F. Chen, An introduction to Plasma Physics and Controlled Fusion, Volume 1: Plasma Physics, Plenum Press, New York and London (1984).
- P. Gibbon, Short pulse laser interactions with matter, Imperial College Press (2005).
- W. L. Kruer, The Physics of Laser Plasma Interactions, Addison-Wesley Publishing Company, Redwood (1988).



HELLENIC
MEDITERRANEAN
UNIVERSITY



UNIVERSITÉ
BORDEAUX



UNIVERSIDAD
SALAMANCA



UNIVERSITY
of York



Erasmus+

O2 – Annex